SUPERFLUIDITY IN TWO-DIMENSIONAL FERMI GASES

Dissertation
zur Erlangung des Doktorgrades
an der Fakultät für Mathematik, Informatik und Naturwissenschaften
Fachbereich Physik
der Universität Hamburg

vorgelegt von
Lennart Sobirey

Hamburg, im September
2021

Gutachter der Dissertation	Prof. Dr. Henning Moritz
	Prof. Dr. Ludwig Mathey
Zusammensetzung der Prüfungskommision	Prof. Dr. Henning Moritz
	Prof. Dr. Ludwig Mathey
	Prof. Dr. Andreas Hemmerich
	Prof. Dr. Michael Potthoff
	Prof. Dr. Peter Schmelcher
Vorsitzender der Prüfungskommision	Prof. Dr. Peter Schmelcher
Datum der Disputation	22.04.2022
Vorsitzender des Fach-Promotionsausschusses Physik	Prof. Dr. Wolfgang J. Parak
Leiter des Fachbereichs Physik	Prof. Dr. Günter H. W. Sigl
Dekan der Fakultät MIN	Prof. Dr. Heinrich Graener

to my DSA group, who kept me balanced for all these years,
to my family, who were always there for me,
and to my wonderful wife, who married me.

CONTENTS

ABSTRACT

In this thesis, I present experiments that directly compare superfluid 2D and 3D Fermi gases to study the effect of reduced dimensionality on the stability of strongly correlated superfluids and superconductors. As the highest critical temperatures for superconductivity are exclusively found in layered two-dimensional materials, this is a subject of broad and immediate interest. However, changing the dimensionality of solid state materials such as superconductors is a highly non-trivial task, and it is therefore still unclear to what extent the remarkable stability of these strongly correlated 2D superfluids is related to their reduced dimensionality. For this reason, ultracold Fermi gases have emerged as clean and tunable model systems that resemble strongly correlated superconductors in many aspects, but enable the interaction strength and dimensionality of the system to be changed nearly at will.

To study the influence of reduced dimensionality on fermionic superfluidity, we therefore created such ultracold Fermi gases both in 2D and 3D in the same experimental setup, realizing homogeneous systems which are identical in their microscopic physics apart from the effects of their dimensionality. To quantify the stability of the superfluid phase in these systems, we probed their excitation spectrum over a wide range of momentum and energy using stimulated Bragg spectroscopy. Such measurements allowed us to firmly establish superfluidity in 2D Fermi gases for the first time. Using Bragg spectroscopy, we observed nonzero critical velocities below which the gas flows without friction. We investigated how the critical velocity depends on the interactions and the temperature of the system and found robust superfluidity over a wide range of interaction strengths. Our Bragg spectroscopy setup allowed us to obtain the full dynamic structure factor of 2D and 3D Fermi gases, revealing the smooth crossover between bosonic and fermionic superfluidity and allowing us to extract the superfluid gap.

These measurements enabled us to perform the first direct comparison between 2D and 3D Fermi gases. We compared our measurements of the superfluid gap in 2D and 3D using two equivalent parameterizations of the interaction strength applicable to both dimensionalities. Remarkably, we found that the superfluid gap follows the same universal function of the interaction strength in both 2D and 3D, which suggests that there is no inherent difference in the stability of fermionic superfluidity between 2D and 3D Fermi gases. This trend held even as we expanded the comparison to include different superconducting materials, indicating that the superfluid phase is unexpectedly robust with regard to the reduced dimensionality in fermionic superfluids in general.

ZUSAMMENFASSUNG

In dieser Thesis stelle ich Experimente vor, in denen ich über einen Vergleich von 2D und 3D Fermigasen den Einfluss der Dimensionalität auf die Stabilität stark korrelierter Suprafluide untersucht habe. Dies ist ein Thema von hoher Relevanz, da die Kristallstruktur von allen bekannten Supraleitern mit sehr hohen kritischen Temperaturen zweidimensionale Schichten aufweist. Da es allerdings höchst nichttrivial ist, die Dimensionalität eines Festkörpers zu ändern, ist nach wie vor ungeklärt inwiefern die Stabilität dieser stark korrelierten 2D Suprafluide mit ihrer Dimensionalität zusammenhängt. Um solche Fragen beantworten zu können haben sich ultrakalte Fermigase als Modellsysteme etabliert. Diese Systeme ähneln Supraleitern in vielerlei Hinsicht, haben aber den großen Vorteil, dass ihre Wechselwirkung und Dimensionalität kontrolliert verändert werden können.

Um den Einfluss der Dimensionalität auf fermionische Suprafluidität zu untersuchen haben wir ultrakalte Fermigase sowohl in 2D als auch in 3D im gleichen Experiment erzeugt und damit homogene Systeme geschaffen, die in ihrer mikroskopischen Physik identisch sind bis auf die Einflüsse ihrer unterschiedlichen Dimensionalitäten. Um die Stabilität dieser Systeme zu quantifizieren haben wir ihr Anregungsspektrum mithilfe von Bragg-Spektroskopie über eine weite Spanne an Energien und Impulsen untersucht. Diese Messungen erlaubten uns, zum ersten Mal Suprafluidität in 2D Fermigasen nachzuweisen. Mithilfe der Bragg-Spektroskopie konnten wir eine endliche kritische Geschwindigkeit beobachten, unterhalb derer sich das Gas dissipationsfrei um eine Störung bewegte, und die Abhängigkeit dieser kritischen Geschwindigkeit von der Wechselwirkung und der Temperatur untersuchen. Unsere Bragg-Spektroskopie erlaubte uns, die vollen dynamischen Strukturfaktoren von 2D und 3D Fermigasen zu vermessen, in welchen der graduelle Wandel von bosonischer zu fermionischer Suprafluidität sichtbar wurde und aus welchen wir die Anregungslücke im 2D sowie im 3D BEC-BCS Übergang extrahieren konnten.

Diese Messungen ermöglichten uns, den ersten direkten Vergleich von 2D und 3D Fermigasen durchzuführen. Mithilfe von zwei äquivalenten Parametrisierungen der Wechselwirkung konnten wir unsere Messungen der Anregungslücke in 2D und 3D gegenüberstellen. Wir konnten beobachten, dass die Anregungslücke sowohl in 2D als auch in 3D der gleichen universellen Funktion der Wechselwirkungsstärke folgt, was impliziert, dass kein inherenter Unterschied in der Stabilität der suprafluiden Phase von 2D und 3D Fermigasen besteht. Diese Beoachtung galt auch weiterhin, als wir diesen Vergleich auf verschiedene Supraleiter ausdehnten, was darauf hindeutet, dass fermionischen Suprafluide im Allgemeinen wenig durch reduzierte Dimensionalität geschwächt werden.

Part I

Introduction

1 INTRODUCTION

Since the initial discovery of high temperature superconductivity in the cuprates by Bednorz and Müller [1] in 1986, high temperature superconductors have been studied extensively owing to their fascinating properties and wide-ranging potential. However, while a vast number of different superconducting materials was soon discovered, the highest critical temperatures T_c remained within the cuprate family, which consist of two-dimensional (2D) copper-oxide layers stacked between insulating spacer layers [2]. This was surprising, because two-dimensional systems cannot support long range order [3], and superconductivity (as superfluidity of electrons) is only restored in a competition of quasi-long range topological order and thermal fluctuations [4–6]. Naively, one would therefore not expect two-dimensional materials to be robust superconductors - however, all known systems with high critical temperatures feature 2D structures. Many early studies therefore attempted to find a common thread that connected the vastly different superconducting materials that had been discovered.

One of the first key observations that united different superconductors was made in 1989, when Uemura and coworkers pointed out that the critical temperature of the most common cuprate superconductors increased linearly with their carrier density n_s up to some material-dependent maximum value (see fig. 1.1) [7]. They soon showed that a very similar linear scaling held for a number of non-cuprate materials, including heavy fermion superconductors and organics [8–10], whereas a different slope was observed in other materials such as conventional Bardeen-Cooper-Schrieffer (BCS) superconductors [11]. Relating the carrier density to the Fermi temperature T_F of the material, they created what has since become known as the Uemura plot, an example of which is shown in fig. 1.2.

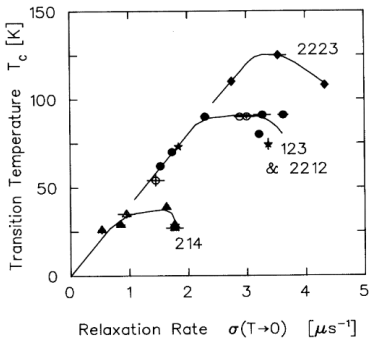

Figure 1.1: Universal relation between T_c and $n_s/m^* \propto \sigma$. Measurements of the muon-spin-relaxation rate σ, which is proportional to the carrier density n_s divided by the effective mass m^*, show a linear relation with the same prefactor for a number of different cuprate superconductors. Figure adapted from [7].

A key takeaway from the Uemura plot is that there are many different materials that reach similar values of $T_c/T_F \lesssim 0.1$, despite orders of magnitude differences in T_c. These materials, termed exotic superconductors, generally feature short coherence lengths and strong correlations, but are not limited to layered two-dimensional superconductors. In this view, the dominance of two-dimensional materials amongst high temperature superconductors might mostly be a consequence of these materials having higher Fermi temperatures at similar T_c/T_F. However, given that two-dimensional systems were expected to be inferior superconductors due to the increased phase fluctuations inherent to 2D, the question remains to what degree the reduced dimensionality of these materials influences the stability of the superconducting phase.

Nowadays, material fabrication capabilities have become more sophisticated, and it has become possible to prepare cuprates and other

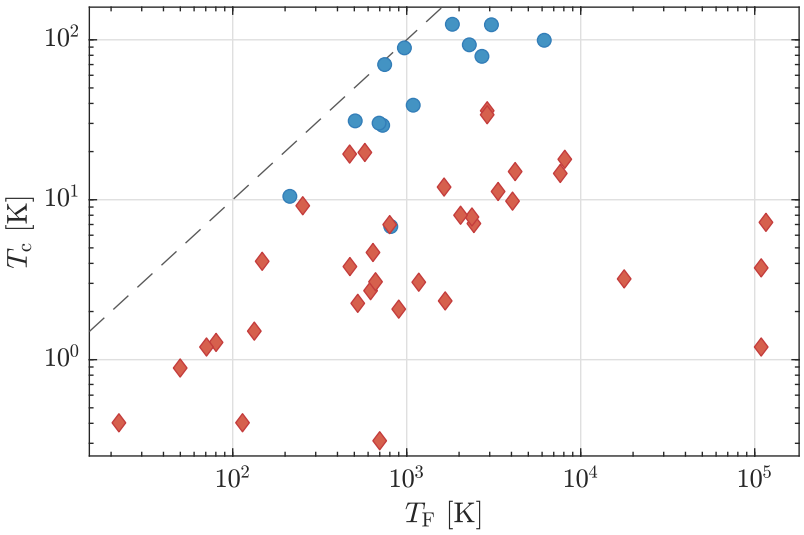

Figure 1.2: The Uemura plot. Blue points show materials with 2D structures, red diamonds show 3D bulk superconductors. The grey dashed line marks $T_c = 0.1\,T_F$. While 2D materials reach the highest critical temperatures, both 2D and 3D superconductors reach relative critical temperatures $T_c/T_F \gtrsim 0.01$. Originally shown in [8], here additional data has been added from more recent measurements [12].

2D materials such as the more recently discovered iron pnictides as a single superconducting monolayer [13, 14]. In doing so, studies have confirmed the 2D nature of these materials, and demonstrated that high temperature superconductivity requires only a single isolated 2D plane [14]. However, while such monolayer systems impressively show the robustness of 2D superconductivity, they are not well suited to investigate the influence of the reduced dimensionality on the superfluid phase itself, as the dimensionality of the monolayer is the same as that of the layers which are stacked on top of each other in the bulk material. These layers are 2D as a direct consequence of the materials chemical composition, and therefore the dimensionality of a superconductor cannot easily be changed, preventing the effect of the reduced dimensionality from being isolated.

One approach to overcome this limitation is to prepare other, comparable systems in which the dimensionality can be more easily modified. A promising candidate for such studies are ultracold Fermi gases [15–18]. These relatively simple systems consist of neutral fermionic atoms that interact via contact interactions, which are tuneable using Feshbach resonances [19]. When the temperature of an ultracold Fermi gas is lowered far enough, the fermions bind into bosonic pairs which can condense and form a superfluid, much like the electrons in superconductors.

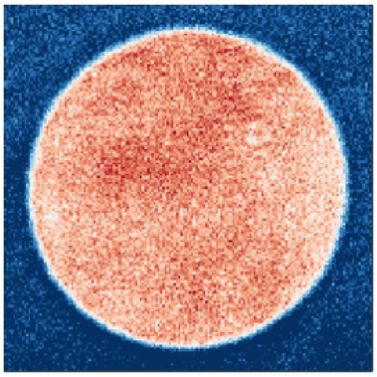

Figure 1.3: A homogeneous 2D Fermi gas. Using custom light shaping allows for the creation of homogeneous gases, imaged here using absorption imaging. Figure adapted from [20].

A key advantage of ultracold Fermi gases is the high level of control available in experiments. Besides being able to tune their interatomic interaction strength, the potential landscape the fermions experience can be manipulated using blue- or red-detuned lasers, and the internal state of the fermions can be changed using two-photon processes or radio-frequency fields. Thereby, a wide range of different systems can be prepared, from fermions in optical lattices that implement the Fermi-Hubbard model [21] to bulk systems, which will be the subject of this thesis. This high degree of control over the confining potential provides experiments on ultracold Fermi gases with the unique op-

portunity to prepare systems of different dimensionality, and hence has led to the creation of one-dimensional [22, 23], two-dimensional [24–30] and three-dimensional [17, 31–33] ultracold Fermi gases in the crossover between Bose-Einstein condensation (BEC) and BCS superfluidity.

Consequently, ultracold Fermi gases are highly controllable model systems that do not suffer from many of the intricacies of solid state superconductors, such as competing order parameters [2, 34–36] and electronic disorder [37]. These fermionic superfluids can be prepared deep in the strongly correlated regime and with arbitrary dimensionality, and thereby are ideally suited to investigate the effect of reduced dimensionality on the superfluid phase in isolation.

However, while three-dimensional Fermi gases have been the subject of intense experimental effort over the last two decades, comparatively little research has been performed with two-dimensional Fermi gases. Over the course of this work, we therefore first focused on creating and probing highly controllable homogeneous 2D Fermi gases in the BEC-BCS crossover [20, 38]. After some key upgrades to the experimental apparatus, we created a Josephson junction in our 2D Fermi gas to unambiguously show phase coherence [39] and studied the equation of state by measuring the speed and damping of sound waves in the system [40]. We implemented a moving optical lattice setup that allowed us to perform Bragg spectroscopy and hence probe the excitation spectrum over a wide range of energies and momenta, and were able to demonstrate superfluidity in the 2D BEC-BCS crossover through the observation of a critical velocity [41]. By performing Bragg spectroscopy on two- and three-dimensional Fermi gases, we measured their excitation spectrum and mapped out the evolution of the superfluid gap [12, 42]. This ultimately allowed us to perform the first comparison between ultracold Fermi gases of different dimensionalities, and to relate our results to those obtained in superconducting materials [12]. These main results are summarized in the following chapter.

2 SUMMARY OF THE MAIN RESULTS IN THIS THESIS

2.1 Observation of superfluidity in a strongly correlated two-dimensional Fermi gas

published in L. Sobirey, N. Luick, M. Bohlen, H. Biss, H. Moritz and T. Lompe, Science **372** *(6544), 844-846 (2021) [41]*

Measurement of the critical velocity

The first main result of this thesis is the direct observation of superfluidity in ultracold two-dimensional Fermi gases. We verify that 2D Fermi gases fulfill the Landau criterion by subjecting them to an optical lattice potential moving at a tunable velocity. We find that below a critical velocity v_c, no energy is dissipated by the moving lattice, heralding the presence of a superfluid.

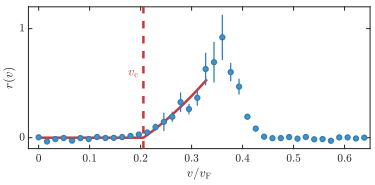

Excitations at different momenta

In Landaus gedankenexperiment, a point-like impurity is able to create excitations at any momentum. In our experiments, however, the lattice wavevector only allows for excitations at a specific momentum to be created. By changing the lattice spacing, we probe a wide range of different momenta and observe how different types of excitations set the critical velocity in bosonic and fermionic superfluids for the first time.

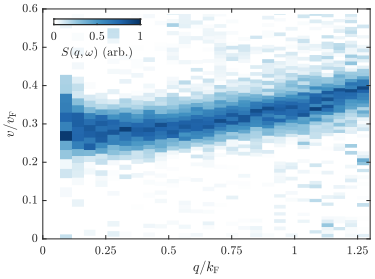

The critical velocity in the 2D BEC-BCS crossover

Tuning the interaction strength, we show that a nonzero critical velocity and therefore superfluidity is present throughout the 2D BEC-BCS crossover. We observe the expected scaling of the critical velocity with the speed of sound in the BEC regime and find a maximum of v_c in the crossover. Our momentum selective measurements demonstrate how pair breaking excitations reduce the critical velocity in the BCS regime.

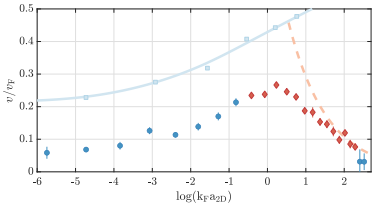

The critical temperature for superfluidity

As the temperature of the superfluid is increased, its critical velocity becomes lower, until it vanishes at the phase transition. We heat the system using the moving optical lattice and map out the temperature at which the phase transition to the normal state occurs. Tuning the interaction strength, we show that the critical entropy is roughly constant in the crossover regime.

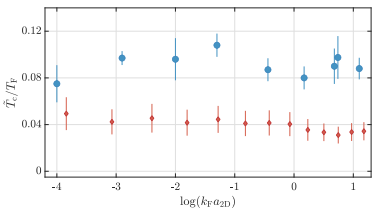

2.2 Comparing fermionic superfluids in two and three dimensions

published in L. Sobirey, H. Biss, M. Bohlen, N. Luick, H. Moritz and T. Lompe arXiv:2106.11893 (2021) [12], submitted to Nature Physics

Measuring the excitation spectrum

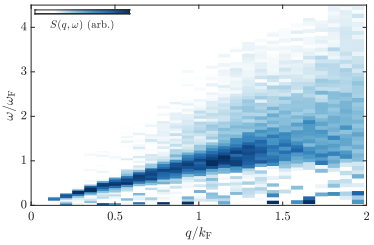

The second main result of this thesis is our measurement of the excitation spectrum. Using Bragg spectroscopy, we measure the dynamic structure factor of a two-dimensional Fermi gas over a wide range of interaction strengths. Our measurements distinctly show both phononic and pair breaking excitations as well as the interaction between the two modes, and reveal the smooth evolution from BEC- to BCS superfluidity in the crossover.

Extracting the superfluid gap

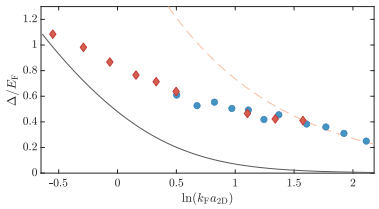

One of the key parameters in the description of fermionic superfluids is the superfluid gap. From our measurements of the dynamic structure factor, we are able extract the gap using two different methods. We compare our results with theoretical predictions and find good agreement with mean field predictions in the BCS limit, but a significant deviation from quantum Monte Carlo predictions in the strongly correlated regime.

Comparing 2D and 3D Fermi gases

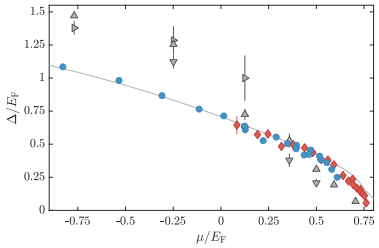

The third and most important result of this thesis is the comparison of fermionic superfluids with different dimensionality. Our measurements in two- and three-dimensional Fermi gases represent a perfect starting point to study the influence of the dimensionality on the superfluid gap, and thereby the stability of the superfluid phase. To this end, we introduce two equivalent interaction parameters which we use to compare the interaction strength in 2D and 3D. Surprisingly, we find that our measurements of the superfluid gap collapse onto a single, universal curve that depends only on the interaction strength, but is independent of the dimensionality.

Comparing ultracold Fermi gases and superconducting materials

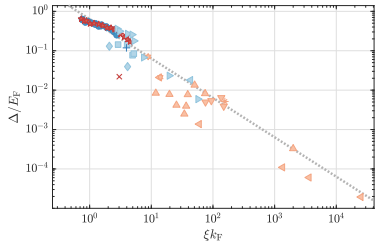

Finally, we compare our results on superfluid ultracold Fermi gases to those obtained with solid state superconducting materials. We observe a clear correlation between short coherence lengths and large superconducting gaps which holds independent of the dimensionality of the system, in excellent agreement with our results for ultracold Fermi gases. Therefore, our experiments strongly suggest that the stability of the superfluid phase is remarkably unaffected by reduced dimensionality for fermionic superfluids and superconductors in general.

2.3 Further publications obtained over the course of this thesis

An ideal Josephson junction in an ultracold two-dimensional Fermi gas

N. Luick, L. Sobirey, M. Bohlen, V.P. Singh, L. Mathey, T. Lompe, and H. Moritz
Science **369** (6499), 89-91 (2020) [39]

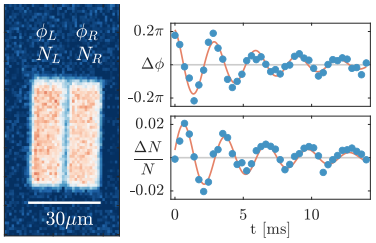

Josephson junctions are a fundamental quantum mechanical phenomenon in which a difference in relative phase between two superfluid sides of a weak link drives a current through the link without any applied voltage. Here, we implement such a Josephson junction in our ultracold two-dimensional Fermi gas and show that it follows the nonlinear relation between current and relative phase difference expected of an ideal Josephson junction. Using this junction, we show that two-dimensional Fermi gases are phase coherent throughout the 2D BEC-BCS crossover.

This project was discussed in depth in the PhD thesis of Niclas Luick [43].

Excitation Spectrum and Superfluid Gap of an Ultracold Fermi Gas

H. Biss, L. Sobirey, N. Luick, M. Bohlen, J.J. Kinnunen, G.M. Bruun, T. Lompe, and H. Moritz
arXiv:2105.09820 (2021) [42], submitted to Phys. Rev. Lett.

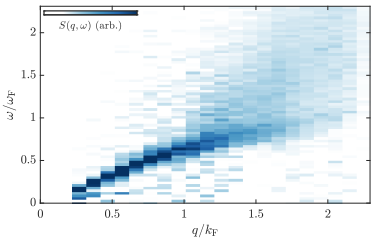

To understand correlations and quasiparticles within a system, one needs to study its excitation spectrum. Here, we use Bragg spectroscopy to measure the dynamic structure factor of a homogeneous 3D Fermi gas. We observe the different collective and quasiparticle excitations and study their evolution in the BEC-BCS crossover. From our measurements, we extract the superfluid gap and find remarkable agreement with state of the art theoretical predictions.

This project will be discussed in depth in the PhD thesis of Hauke Biss.

Sound propagation and quantum limited damping in a two-dimensional Fermi gas

M. Bohlen, L. Sobirey, N. Luick, H. Biss, T. Enss, T. Lompe, and H. Moritz
Phys. Rev. Lett. **124**, 240403 (2020) [40]

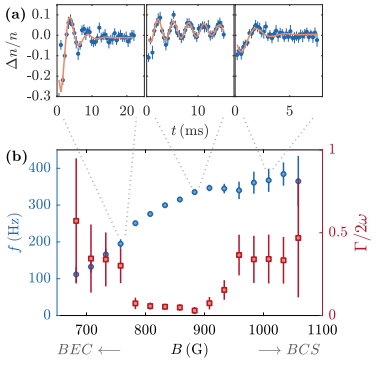

The sound modes of a system contain substantial information about its thermodynamic and transport properties, many of which are not yet known for 2D Fermi gases. Here, we measure the speed and damping of long wavelength sound waves in our homogeneous system and extract the compressibility equation of state. We find that the damping of sound waves in the 2D BEC-BCS crossover approaches the universal quantum bound of a perfect fluid.

This project was discussed in depth in the PhD thesis of Markus Bohlen [44].

Josephson junction dynamics in a two-dimensional ultracold Bose gas

V.P. Singh, N. Luick, L. Sobirey, and L. Mathey
Phys. Rev. Research **2**, 033298 (2020) [45]

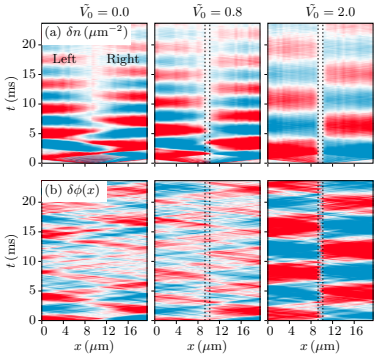

Classical field methods allow for the simulation of strongly interacting bosonic superfluids and are excellently suited to enhance our understanding of 2D Fermi gases on the BEC side of the crossover. Here, a Josephson junction in a 2D bosonic superfluid is studied to investigate the influence of BKT physics on the dynamics of the junction. We show numerically that the critical current is directly related to the condensate density and therefore the superfluid scaling exponent of the gas.

The numerical investigation was performed by V.P. Singh and L. Mathey.

Two-dimensional homogeneous Fermi gases

K. Hueck, N. Luick, L. Sobirey, J. Siegl, T. Lompe, and H. Moritz
Phys. Rev. Lett. **120**, 060402 (2018) [20]

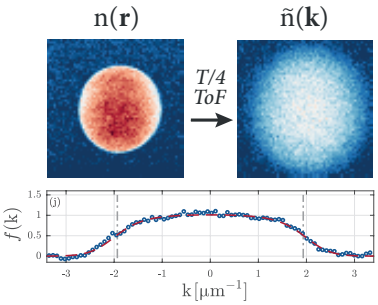

While ultracold atoms have become a flexible and powerful tool to study quantum many-body problems, the harmonic trapping potentials significantly complicate the measurement of nonlocal quantities such as the momentum distribution. Here, we present the first implementation of a homogeneous 2D Fermi gas and measure its momentum distribution. Using matter wave focussing, we demonstrate the textbook case of Pauli blocking in an ideal Fermi gas.

This project was discussed in depth in the PhD thesis of Klaus Hueck [46].

Calibrating high intensity absorption imaging

K. Hueck, N. Luick, L. Sobirey, T. Lompe, H. Moritz, L. Clark, and C. Chin
Opt. Express **25**, 8670 (2017) [38]

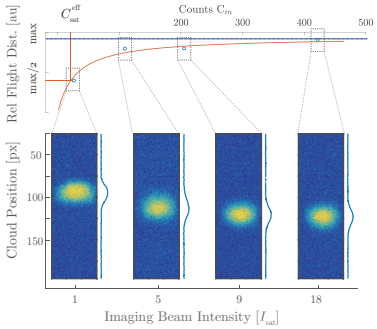

Absorption imaging is the workhorse technique to access density distributions in ultracold quantum gas experiments, but due to the low densities and masses involved in 2D ^{6}Li, its signal-to-noise ratio at low imaging intensities is not sufficient. Here, we show an extension of the usual method to higher imaging intensities that can be calibrated entirely from relative measurements. Our method results in an accurate and easy to calibrate density determination.

This project was discussed in depth in the PhD thesis of Klaus Hueck [46].

3 OUTLINE

This thesis is outlined as follows:
Part I has served to introduce the problem and the field, to summarize the main results of this work, and to provide an overview over the structure of the thesis.
Part II then provides some background to the work discussed here. First, chapter 4 introduces some key theoretical concepts, beginning with a brief overview over ultracold gases, condensation and superfluidity in section 4.1 and an introduction to superfluidity in two dimensions in section 4.2. Section 4.3 continues by introducing BEC-BCS theory, which is used in section 4.4 to derive the shape of the excitation spectrum of ultracold Fermi gases. The chapter ends with section 4.5, which discusses different ways of describing and changing the interaction strength of a system. Chapter 5 then summarizes the last decade of progress on two-dimensional Fermi gases, focusing on the different trapping geometries and measurement tools. Finally, chapter 6 describes the experimental apparatus used in this thesis.
The most essential part of this thesis is Part III, which presents our main results: Chapter 7 details measurements of the critical velocity in the 2D BEC-BCS crossover, and describes how the phase transition to the normal state can be localized. In chapter 8, the same measurement setup is used to measure the excitation spectrum of 2D Fermi gases, and these measurements are used to obtain the superfluid gap. Chapter 9 then briefly summarizes how we performed equivalent measurements on 3D Fermi gases and discusses the changes we made to the setup in order to create them. Finally, chapter 10 presents the first comparison between 2D and 3D Fermi gases, as well as between ultracold Fermi gases and superconducting materials in general.
At long last, Part IV wraps up the thesis with a conclusion and an outlook over promising future experiments.

Part II

Background

4 THEORETICAL BACKGROUND

In this chapter, I establish the theoretical background required for this thesis, introducing the relevant concepts and quantities. I will explain how condensation turns a dilute cloud of bosons into a superfluid, what consequences confining such a system into two dimensions has, and how superfluidity is maintained against all odds. I will discuss how bosonic and fermionic superfluidity are smoothly connected through the BEC-BCS crossover. Using BEC-BCS theory, I will derive the excitation spectrum of Fermi gases in the crossover region and discuss how such an excitation spectrum might be measured. Finally, I will summarize the scattering physics in 3D and 2D to establish how the interaction strength is commonly parameterized. This chapter is aimed at readers who are not already intimately familiar with the theoretical concepts discussed here. A seasoned veteran of the cold atoms community is recommended to skip ahead to chapter 5.

As this is a thesis about Fermi gases, the reader might wonder why the theory chapter begins with two sections on the physics of bosons. However, the physics of the bosons and fermions are not as different as one might initially suspect: In superfluid Fermi gases, fermions of different pseudospin form bosonic pairs which can undergo condensation. In fact, we will see in section 4.3 that by varying the strength of the pairing, a smooth transition from bosonic to fermionic superfluidity can be observed, and it is this very transition that will be studied in this thesis. Therefore, by starting with bosonic superfluidity, we are merely approaching the problem from one of its simpler limits.

4.1 Ultracold gases, condensation and superfluidity

This section follows a lecture series by G.V. Shlyapnikov on ultracold quantum gases [47], specifically on Bose condensation. It is meant as an overview of the relevant concepts, focusing on intuitive explanations.

To understand the concept of superfluidity, we start by introducing some key concepts. We will reiterate the relevant properties of ultracold quantum gases and discuss how condensates form. To describe these condensates, the Gross-Pitaevskii-equation will be introduced and motivated. By moving to a description featuring quasiparticle excitations, we then derive the quasiparticle dispersion relation and the Landau criterion.

We consider a gas of N bosonic neutral atoms at a temperature T in a three-dimensional (3D) volume Ω. There are three relevant length scales in this problem: The first is the mean interparticle separation $n^{-\frac{1}{3}}$, where $n = N/\Omega$ is the density of the gas. The second is the characteristic radius of interactions between the atoms R_e, beyond which the motion of the atoms is essentially free. We will consider only systems in the *dilute* limit, meaning $nR_e^3 \ll 1$. In this limit, the large interparticle separation suppresses three-body collisions and therefore

the formation of clusters and ultimately, a solid. The particles therefore remain gaseous, and we can neglect any short-range effects. Finally, the third length scale is the thermal deBroglie wavelength of the atoms $\Lambda_{\mathrm{T}} = \sqrt{\frac{2\pi\hbar^2}{\mathrm{m}\mathrm{T}}}$, where m is the mass of the atoms. When the degeneracy parameter $\mathrm{n}\Lambda_{\mathrm{T}}^3$ is small, the gas can be considered classical and is described by Boltzmann statistics. However, when the system is cooled to low enough temperatures (or the density increased far enough) that $\mathrm{n}\Lambda_{\mathrm{T}}^3$ approaches unity, quantum statistics start to dominate, and we refer to the system as an *ultracold quantum gas*.

If the system is cold and degenerate enough, it undergoes a phase transition to a novel phase of matter: the Bose-Einstein condensate (BEC). This phase transition is a consequence of the quantum statistics of indistinguishable particles: In a hot and dilute system, there are much more quantum states available than particles, and most quantum states are occupied by a single particle at most. In this case, the system is thermal, and the indistinguishability of the particles matters little. However, as the system becomes cold and degenerate, the number of accessible quantum states decreases, and multiple particles have to share the same quantum state. When this occurs, the indistinguishability of the particles starts to alter the distribution of particles over the available quantum states: Instead of increasingly populating all accessible states like distinguishable particles, the majority of particles will start to occupy the ground state. As the particles in the ground state thereby become completely indistinguishable in location, momentum and all relevant quantum numbers, they no longer behave as individual particles, but instead jointly become one macroscopic quantum-mechanical object: a Bose-Einstein condensate.

4.1.1 The Gross-Pitaevskii equation

How does one describe such a macroscopic quantum object? Generally speaking, it is extremely difficult to solve the Schrödinger equation for interacting quantum many-body systems, as the interaction between every combination of particles has to be considered, and the dimensionality of the Hilbert space grows exponentially with the number of particles. However, in many cases, some simplifying approximations can be made. In the following, let us consider a dilute gas which consists of a large number of atoms with weak, repulsive interactions at $\mathrm{T} = 0$, and work out the necessary equations in a mean-field picture.

We first introduce the field operator for our condensed particles $\hat{\psi}(\mathbf{r})$. In free space, the creation operator is $\hat{\psi}^\dagger = \hat{\mathrm{a}}^\dagger/\sqrt{\Omega}$, where $\hat{\mathrm{a}}^\dagger$ is the bosonic creation operator, and the annihilation operator is $\hat{\psi} = \hat{\mathrm{a}}/\sqrt{\Omega}$. In the Heisenberg representation, the operator $\hat{\psi}(\mathbf{r})$ transforms to $\hat{\Psi}(\mathbf{r}, \mathrm{t})$, and one can write down its equation of motion for a system of bosonic particles interacting via weak contact interactions

$$\mathrm{i}\hbar\frac{\partial\hat{\Psi}}{\partial\mathrm{t}} = \left(-\frac{\hbar^2}{2\mathrm{m}}\Delta_{\mathbf{r}} + \mathrm{V}(\mathbf{r}) + \mathrm{g}\hat{\Psi}^\dagger\hat{\Psi}\right)\hat{\Psi}\,, \tag{4.1}$$

where V is the external potential, m is the mass of a boson and g is a small positive coupling constant that quantifies the strength of the interactions. However, solving this equation is hardly trivial, and we will therefore introduce the mean-field approximation to simplify things.

The parameter g will be related to the microscopic properties of the system in section 4.5.

To this end, we will make use of the fact that the number of condensed particles in a bosonic condensate is usually very large compared to the number of non-condensed particles. Focusing only on the creation and annihilation operators for condensed particles $\hat{\psi}_0^\dagger$ and $\hat{\psi}_0$ and writing a state with N_0 condensed particles in a volume Ω as $|N_0\rangle$, we can write

$$\hat{\psi}_0^\dagger|N_0\rangle = \sqrt{N_0+1}|N_0+1\rangle \quad \text{and} \quad \hat{\psi}_0|N_0\rangle = \sqrt{N_0-1}|N_0-1\rangle\,. \tag{4.2}$$

If N_0 is large enough, we can therefore approximate $\sqrt{N_0} \approx \sqrt{N_0+1}$ and write

$$\hat{\psi}_0^\dagger|N_0\rangle \approx \hat{\psi}_0|N_0\rangle \approx \psi_0|N_0\rangle\,, \tag{4.3}$$

where we have introduced the complex number ψ_0 such that

$$|\psi_0|^2 = N_0/\Omega = n_0\,. \tag{4.4}$$

Here, we use n_0 to denote the density of condensed particles. ψ_0 can be interpreted as the average (or mean) of the field operator $\hat{\psi}_0$, and this approximation is therefore called the *mean-field approximation*.

We now have the tools needed to simplify eq. 4.1 by splitting the field operator into a condensate part, which we represent in the mean-field approximation, and a small non-condensed part:

$$\hat{\Psi}(\mathbf{r},t) = \Psi_0(\mathbf{r},t) + \hat{\Psi}'(\mathbf{r},t) \tag{4.5}$$

Assuming the non-condensed part represents a small correction to the physics of the system, we can omit it for now and obtain the **Gross-Pitaevskii equation**

$$\boxed{i\hbar\frac{\partial\Psi_0}{\partial t} = \left(-\frac{\hbar^2}{2m}\Delta_{\mathbf{r}} + V(\mathbf{r}) + g|\Psi_0|^2\right)\Psi_0\,.} \tag{4.6}$$

The Gross-Pitaevskii equation resembles a Schroedinger equation with a repulsive mean-field potential $g|\Psi_0|^2$ that depends on the condensate density $n_0 = |\Psi_0|^2$. In consequence, the condensate wavefunction tries to minimize its amplitude, homogeneously filling the available volume if no external potential is given. The stationary ground state is then

$$\Psi_0 = \sqrt{n_0}\exp(-i\mu t/\hbar)\,, \tag{4.7}$$

where the we have used the chemical potential $\mu \equiv \frac{\partial E}{\partial N} = gn_0$. If there is an external potential, the wavefunction will fill the *valleys* of the potential such that $V(\mathbf{r}) + \mu(\mathbf{r})$ add up to the same value everywhere, reminiscent of classical water. However, on short length scales, this will be modified by the kinetic energy term, which assigns an energy cost to the curvature of the wavefunction. As a consequence, the wavefunction does not follow changes in the potential immediately. This

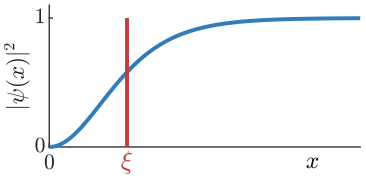

Figure 4.1: Sketch of the healing length. A condensate wavefunction (blue) close to an infinitely high potential step at $x = 0$. Due to the energy cost of the curvature of the wavefunction, it does not fall off instantaneously, but over a characteristic distance ξ called the *healing length*.

behavior is quantified by the healing length $\xi = \frac{\hbar}{m\mu}$, which is the characteristic distance over which the wavefunction falls off at a potential step (see Fig. 4.1).

4.1.2 Excitations in a bosonic condensate

The Gross-Pitaevskii equation is a zeroth order description we obtained by completely neglecting the non-condensed part of the wavefunction. However, since we wish to study excitations, we will have to go further than that and include the non-condensed part again. If we perform the replacement $\hat{\Psi}_0 \to \hat{\Psi}_0 \exp(-i\mu t/\hbar)$, $\hat{\Psi}' \to \hat{\Psi}' \exp(-i\mu t/\hbar)$ to make the wavefunction for a stationary state time independent, we can obtain an equation to first order in $\hat{\Psi}'$

$$i\hbar\frac{\partial\Psi'}{\partial t} = \left(-\frac{\hbar^2}{2m}\Delta_{\mathbf{r}} + V(\mathbf{r}) + 2\,g|\Psi_0|^2 - \mu\right)\Psi' + g|\Psi_0|^2\Psi'^{\dagger}\,. \tag{4.8}$$

Now, we make an *ansatz* for Ψ' and write it as a sum over quasiparticle excitations, for which we define the new bosonic operators $\hat{b}_\nu$ and $\hat{b}^\dagger_\nu$, and their eigenenergies ϵ_ν and eigenfunctions u_ν and v_ν:

$$\Psi' = \sum_\nu u_\nu(\mathbf{r})\hat{b}_\nu \exp(-i\epsilon_\nu t/\hbar) - v^\star_\nu(\mathbf{r})\hat{b}^\dagger_\nu \exp(i\epsilon_\nu t/\hbar) \tag{4.9}$$

This is called the Bogoliubov transformation. The functions u_ν and v_ν are normalized by the condition

$$\int (u_\nu u^\star_{\nu'} - v_\nu v^\star_{\nu'})d^2r = \delta_{\nu\nu'}\,.$$

Effectively, this approach splits the complicated effects of interactions between the atoms into two independent parts, one determining the general shape of the wavefunction at zero temperature and the other giving rise to thermal and quantum fluctuations, and allows for the two parts to be solved independently. The Bogoliubov transformation represents these fluctuations as a system of non-interacting bosonic quasiparticles that exist on top of the condensate wavefunction.

To obtain the eigenenergies ϵ_k of these quasiparticle excitations, the quasiparticle operators are inserted in eq. 4.8 and one obtains the Bogoliubov-de Gennes equations:

$$\left(-\frac{\hbar^2}{2m}\Delta_{\mathbf{r}} + V(\mathbf{r}) + 2g|\Psi_0|^2 - \mu\right)u_\nu - g|\Psi_0|^2 v_\nu = \epsilon_\nu u_\nu \tag{4.10}$$

$$\left(-\frac{\hbar^2}{2m}\Delta_{\mathbf{r}} + V(\mathbf{r}) + 2g|\Psi_0|^2 - \mu\right)v_\nu - g|\Psi_0|^2 u_\nu = -\epsilon_\nu v_\nu \tag{4.11}$$

In a uniform system, the index ν labels different excitation wavevectors k, and using the stationary solution $\psi_0 = \sqrt{n_0}$ we can write the excitation wavefunctions in a coordinate independent fashion as

$$u_\nu = \frac{u_k}{\sqrt{V}}\exp(i\mathbf{kr}) \tag{4.12}$$

$$v_\nu = \frac{v_k}{\sqrt{V}}\exp(i\mathbf{kr})\,. \tag{4.13}$$

Writing $E_k = \frac{\hbar^2 k^2}{2m}$, the Bogoliubov-de Gennes equations can then be rewritten as

$$(E_k + 2gn_0 - \mu)\, u_k - gn_0 v_k = \epsilon_k u_k \tag{4.14}$$

$$(E_k + 2gn_0 - \mu)\, v_k - gn_0 u_k = -\epsilon_k v_k\,. \tag{4.15}$$

If we assume that the system is mostly condensed, we may approximate $\mu \approx gn_0$ and write

$$(E_k + \mu)u_k - \mu v_k = \epsilon_k u_k \tag{4.16}$$

$$(E_k + \mu)v_k - \mu u_k = -\epsilon_k v_k \tag{4.17}$$

Solving these equations for ϵ_k, we obtain the well-known Bogoliubov dispersion relation

$$\boxed{\epsilon_k = \sqrt{E_k(E_k + 2\mu)}\,.} \tag{4.18}$$

This dispersion relation is linear at low momentum, when the excitation energy is lower than the interaction energy per particle μ and therefore cannot remove individual atoms from the condensate, exciting a phononic quasiparticle instead. As the energy increases and exceeds μ, the dispersion relation increasingly resembles that of free particles. It is sketched in Fig. 4.2.

Another way to interpret the Bogoliubov dispersion is to split the excitation spectrum into two contributions $\epsilon_p(k) = E_k$ and $\epsilon_d(k) = E_k + 2\mu$ such that $\epsilon_k = \sqrt{\epsilon_d(k)\epsilon_p(k)}$. The contribution ϵ_p (ϵ_d) can then be interpreted as the energy cost of creating a phase (density) fluctuation. It is straightforward to see that as $k \to 0$, the energy cost of density fluctuations does not vanish, but is set by the interaction energy per particle μ as the repulsive interactions in the system incur an energy cost to fluctuations in the local density. Because of this, density fluctuations are strongly suppressed in ultracold quantum gases. Phase fluctuations, on the other hand, are soft modes that can be excited at vanishing energy cost for $k \to 0$. Therefore, excitations at low momentum manifest almost purely as long-wavelength fluctuations of the phase of the condensate. As the momentum of the excitation increases, the energy cost of density and phase fluctuations become comparable, and quasiparticles feature characteristics of both, increasingly resembling individual atoms being excited on top of the condensate.

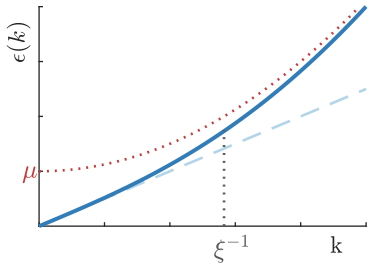

Figure 4.2: Sketch of the Bogoliubov dispersion relation. Plotted is the energy required to create an excitation in a bosonic condensate with weak repulsive interactions (solid blue line). In the linear, low-momentum part (blue dashed line), the excitations are phononic quasiparticles, but as the energy of the excitations increases, they more closely resemble single atoms being excited on top of the mean field (red dotted line).

Box 4.1: The Nambu-Goldstone mode

When a continuous symmetry is spontaneously broken in a system, a massless Nambu-Goldstone mode appears in its excitation spectrum [48, 49]. This mode corresponds to long-wavelength fluctuations of the corresponding order parameter. In the case of a Bose-Einstein condensate, the broken symmetry is that of the phase of the wavefunction: Above the critical temperature, the thermal gas has no well-defined phase, but as the phase transition is crossed, a condensate with a constant phase is formed. Therefore, the Nambu-Goldstone mode of the condensate is a long-wavelength fluctuation of the phase - the phonon.

4.1.3 The Landau criterion

Now that we have obtained the excitation spectrum of the bosonic condensate, we can study under which conditions an excitation can be created. We will do so in a classical picture, as done for the first time by Lev Landau in 1941 [50]. We consider some point-like impurity moving through a system with velocity v and imagine this impurity creating some excitation with momentum $\vec{p}$ and energy ϵ_p in the system. In the rest frame of the impurity, the energy of the system will be

$$E = \epsilon_p + \vec{p}\vec{v} + E_{kin}\,, \tag{4.19}$$

where E_{kin} is the fluids initial kinetic energy. In order for this excitation to be created by the impurity, it has to be energetically favorable compared to not creating one. Thus, at the minimum, the velocity needs to be such that

$$\epsilon_p - pv < 0 \rightarrow v > \frac{\epsilon_p}{p}\,. \tag{4.20}$$

If this condition is not fulfilled, no excitations will be created, and the system moves around the impurity without friction. This phenomenon is called superfluidity.

We can restate the expression above by defining a *critical velocity* v_c and stating the **Landau criterion for superfluidity**:

$$\boxed{v_c = \min_p \left\{ \frac{\epsilon_p}{p} \right\} > 0} \tag{4.21}$$

In words, a system is considered to be superfluid if there is some nonzero critical velocity v_c below which a moving impurity does not create any excitations in the system.

It is straightforward to see that the Landau criterion is not fulfilled by an ideal gas, as $\epsilon_p = \frac{p^2}{2m}$ and thus $v_c = \min_p\{\frac{p}{2m}\} = 0$. However, we obtain a different result when calculating the critical velocity for a bosonic condensate where the excitation spectrum is described by the Bogoliubov dispersion relation (eq. 4.18). We find that

$$\boxed{v_c = \sqrt{\frac{\mu}{m}} = c_s\,,} \tag{4.22}$$

showing that the weakly interacting bosonic condensate is superfluid, with its critical velocity set by the speed of sound c_s. This is a very intuitive result: As the lowest-energy excitations in the Bogoliubov dispersion relation are phonons, the minimum velocity for an impurity to create such an excitation must be the phonon velocity, which is the speed of sound.

4.2 Two-dimensional superfluidity

This section summarizes some parts of the lecture "Two-dimensional Bose fluids: An atomic physics perspective" by Zoran Hadzibabic and Jean Dalibard [51]. It is intended to provide an overview over some of the peculiarities of two-dimensional superfluidity without going into much detail, as the topic will not be discussed much in future chapters.

So far, our discussion of condensation and superfluidity was limited to describing three-dimensional systems of bosons. However, only a single argument in the discussion so far relied on the dimensionality of the system: Where in an ideal 3D Bose gas, statistical physics predicts the presence of a Bose-Einstein condensate at zero temperature, the modified density of states in 2D prevents such a phase transition from occurring. In fact, it was shown by Hohenberg [3] that true long-range order such as the constant phase of the macroscopic wavefunction cannot exist in 1D and 2D systems, interacting or not.

The proof of this statement is rather lengthy, relying on carefully constructed operators and use of the Bogoliubov inequality to show that the assumption of long-range order leads to a contradiction if the dimensionality $d < 3$. Here, we merely motivate the statement by trying to estimate the variance of the phase of the wavefunction in an infinite homogeneous system following [52]: Let $\theta(\mathbf{r})$ be the phase of the macroscopic wavefunction such that $\theta(\mathbf{r}) = 0$ without fluctuations, and let θ_k be the Fourier components of $\theta(\mathbf{r})$. The energy of a mode of phase fluctuations is given by $E \propto \epsilon_k^2 |\theta_k|^2$ [51]. Assuming that the system is condensed, we follow the arguments given in section 4.1 to arrive at the Bogoliubov dispersion (eq. 4.18). At low momentum up to some $k^\star$, the dispersion is thus linear with $\epsilon_k \propto k$. Therefore, the degree of freedom due to phase fluctuations enters quadratically in the energy, and their average energy in thermal equilibrium is given by the equipartition theorem such that $k_B T = E \propto \epsilon_k^2 |\theta_k|^2$. We can then calculate the variance of the phase as

$$\langle |\theta|^2 \rangle = \sum_k |\theta_k|^2 \,. \tag{4.23}$$

In an infinite homogeneous system, we replace the sum by an integral which we can without loss of generality evaluate in polar coordinates and find

$$\langle |\theta|^2 \rangle \propto k_B T \int_0^{k^\star} k^{d-3} dk \,, \tag{4.24}$$

which is divergent for dimensions $d < 3$, showing that no well-defined phase exists in infinite 1D and 2D systems at nonzero temperature.

While the contribution of phase fluctuations to the integral is constant for any dimensionality, we see that the additional factor of k^{d-1} resulting from the integration in polar coordinates causes the integral to diverge for 1D and 2D systems.

However, this divergence occurs due to the lower bound of the integral, which is the smallest momentum that an excitation in the system can have. This smallest momentum is that of an excitation with a wavelength equal to the system size and thus only equal to zero in a truly infinite system. For finite-size systems, the variance of the phase can thus be finite, and if the system is small and cold enough, this might suffice to give rise to condensation again.

4.2.1 The BKT transition

Even though true long-range order is not possible in two-dimensional systems, superfluidity can still persist in systems with quasi-long-range order. The microscopic theory of this phenomenon was developed by Berezinskii, Kosterlitz and Thouless [4–6] and has been studied in great detail over the last decades. Here, we will not go through the complicated thermodynamic description of the two-dimensional Bose gas, focusing more on some of the key takeaways. In the following, we will first discuss what it means for superfluidity and condensation to have quasi-long-range order instead of long-range order, and then motivate the presence of a superfluid jump as one of the more striking differences between 2D and 3D superfluids.

For a recent review of BKT physics, see [53]

Quasi-long-range order

To quantify the differences in superfluid order between 2D and 3D, we introduce the one-body correlation function $g_1(r) = \langle \psi^\star(r)\psi(0)\rangle$, which is the Fourier transform of the momentum distribution n_k. In a homogeneous system, g_1 describes how the phase of the condensate is correlated over a distance r. Let us neglect short-range physics and consider only the behavior of g_1 over distances $r \gg \xi$ in the following. In a uniform 3D BEC as discussed in section 4.1, the phase of the condensate is constant, and we find $g_1(r \to \infty) = n_0$. This is the Penrose-Onsager definition of the condensate density, and a finite value at infinite distance indicates that the gas is phase coherent and has off-diagonal long-range order. For comparison, we can calculate g_1 for a thermal Bose gas far from degeneracy in 2D or 3D, where occupation of momentum states is given by the Boltzmann distribution and we find

$$n_k \approx n\lambda_T^2 \exp\left(-\frac{\hbar^2 k^2}{2mk_B T}\right) \implies g_1(r) \approx n \exp\left(-\frac{r^2}{\lambda_T^2}\right). \qquad (4.25)$$

Note that if the Bose gas is degenerate, but above T_{BKT}, Bose-Einstein statistics modify g_1 from a Gaussian decay of correlations to an exponential one over some length scale ℓ as $g_1(r) = \exp(-\frac{r}{\ell})$. This length scale ℓ diverges as the BKT transition temperature is approached, smoothly increasing the range of correlations as the BKT phase transition is crossed.

This is the expected result: a system far above the superfluid transition temperature has no long-range order, and no condensate is present as $g_1(r \to \infty) = 0$. The phase is uncorrelated on length scales larger than the thermal de-Broglie wavelength.

In a uniform 2D superfluid, the phase is not constant - as we have

discussed above, long-range order is not possible in 2D. Instead, the one-body correlation function is found to be

$$\boxed{g_1(r) = n_s \left(\frac{a}{r}\right)^{\frac{1}{n_s \lambda_T^2}}}, \tag{4.26}$$

where the short-range cutoff a is approximately equal to the healing length ξ and n_s is the superfluid density. As we will see, the exponent of this algebraic decay is smaller than $1/4$, leading to a slow decay of correlations. While the phase is no longer correlated over large distances, the correlations decay slow enough that the system can still be considered locally phase coherent. As was shown in [54], if the correlations decay only on very large length scales, one can still perform the Bogoliubov analysis performed in section 4.1 and find that the two-dimensional Bose gas indeed is superfluid below some transition temperature T_{BKT}.

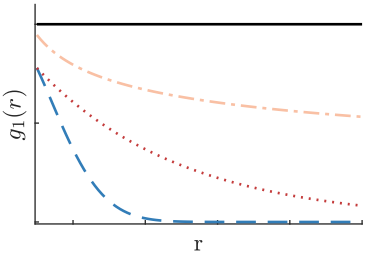

Figure 4.3: One-body correlation functions for different systems. Shown are sketches of the one-body correlation function g_1 for a 3D Bose condensate (solid black line), a thermal gas (dashed blue line), a degenerate Bose gas above the transition temperature (dotted red line) and a BKT superfluid (dash-dotted orange line). Short-range effects at small r have been neglected.

The superfluid jump

Next, let us motivate a very peculiar feature of BKT superfluids: the superfluid jump. Let us consider a two-dimensional BKT superfluid and first remember that a *vortex* is a point around which the phase of the superfluid $\theta(\mathbf{r})$ rotates by a multiple of 2π. For simplicity, we will only consider vortices with charge ± 1 here, that is with phase winding $\pm 2\pi$ around the core. The magnitude of the velocity field $\frac{\hbar}{m}\nabla\theta$ around a single vortex at the origin is therefore $\frac{\hbar}{mr}$. Due to the singularity at the origin, the superfluid density there is suppressed, and a vortex core forms which has the size of the healing length ξ. Vortices are an additional source of phase fluctuations in the system and can scramble the phase of the two-dimensional superfluid, leading to a destruction of quasi-long-range order and superfluidity above a critical temperature T_{BKT} as shown below.

We now estimate whether vortices naturally occur in the 2D superfluid by calculating their free energy F as a function of temperature. To do so, we first estimate the kinetic energy of a single vortex in a disk with radius R as

$$E = \int_\xi^R \frac{1}{2} n_s \left(\frac{\hbar}{mr}\right)^2 d^2r = \frac{\hbar^2 \pi}{m} n_s \ln\left(\frac{R}{\xi}\right). \tag{4.27}$$

We make the very rudimentary assumption here that the superfluid density is zero inside the vortex core of size ξ and n_s outside of the core. Of course, in a realistic system, the superfluid density decays smoothly to zero, but we will neglect such details for the sake of a simple argument.

Here, n_s is the density of the superfluid component of the gas far away from the vortex, and we have assumed that the normal component is unaffected by the vortex. We can furthermore estimate the entropy associated with a single vortex by adding up the number of distinct positions a vortex of radius ξ can have in the disc of radius R and find

$$S = k_B \ln\left(\frac{\pi R^2}{\pi \xi^2}\right) = 2 k_B \ln\left(\frac{R}{\xi}\right). \tag{4.28}$$

Then, ignoring any edge effects, the free energy is found to be

$$F = E - TS = \frac{k_B T}{2}(n_s \lambda_T^2 - 4) \ln\left(\frac{R}{\xi}\right). \tag{4.29}$$

As we can see, there is a distinct point when $n_s \lambda_T^2 = 4$ where the free energy changes sign. When $n_s \lambda_T^2 > 4$, the free energy increases when adding a vortex to the system, making it unlikely for vortices to be present. However, for $n_s \lambda_T^2 < 4$, it becomes energetically favorable for a vortex to be created. As this reduces the phase coherence in the gas, however, it will further reduce n_s, increasing the gain in free energy when vortices are created. Thus, an avalanche effect occurs as more and more vortices appear, reducing the superfluid density to 0. Therefore, the 2D superfluid is unstable when the superfluid density is between $4/\lambda_T^2$ and 0 - it must suddenly jump from $4/\lambda_T^2$ to 0 instead. This phenomenon is called the superfluid jump.

However, while this simple estimation correctly predicts the presence of a superfluid jump, one should not assume that vortices can thus not be present in a system cold enough to be below the BKT transition temperature T_{BKT} where the superfluid density becomes nonzero. Instead, vortices of opposite charge form tightly bound pairs. Their effect on the phase of the system is negligible on length scales larger than their pair size, which is also on the order of ξ. Repeating the arguments above for vortex pairs, one finds a negative free energy for any non-zero temperature, showing that these pairs are always present as a result of thermal fluctuations. However, while their presence lowers n_s somewhat, it does not qualitatively change the nature of the superfluid. Instead, it is the unbinding of these pairs at T_{BKT} into the suddenly more energetically favorable free vortices that destroys superfluid order in 2D.

Box 4.2: Finite-size condensation

While in an infinite homogeneous 2D system, superfluidity occurs without condensation, this is not really the case in realistic systems like those implemented in ultracold quantum gas experiments. This can be understood from the Penrose-Onsager definition of the condensate density given above: In a two-dimensional box of length L, the condensate density is

$$n_0 = g_1(L) > 0\,, \tag{4.30}$$

as the phase correlations have not decayed to zero across the disk. For a BKT superfluid, the condensate density is therefore

$$n_0 \approx n_s \left(\frac{\xi}{L}\right)^{\frac{1}{n_s \lambda_T^2}} \tag{4.31}$$

In fact, even for a degenerate Bose gas above T_{BKT}, condensation and therefore superfluidity are possible in 2D as long as the size of the system is small enough that g_1 remains sizable throughout the system. This phase is called a finite-size condensate.

4.3 The BEC-BCS crossover

In this section, I will show the derivation of BEC-BCS theory, following the derivation given in [55]. As the BEC-BCS crossover is a central aspect of this thesis, this section covers the topic more in-depth, and the derivation will be rather extensive, aiming to be useful to a reader not yet familiar with BCS theory or the BEC-BCS crossover.

We finally turn to the discussion of superfluid Fermi gases. Of course, it is not immediately obvious how a gas of fermionic atoms should become superfluid, as Bose-Einstein condensation does not occur in fermions. This question about the origin of fermionic superfluidity was at the heart of the quest to understand superconductivity, which puzzled scientists after its discovery in 1911 by Onnes [56]. However, it took a full 45 years before the microscopic theory of superconductivity was discovered by Bardeen, Cooper and Schrieffer (BCS) in 1957 [11].

The central assumption of BCS was that fermions of opposite spin and momentum form bosonic pairs. To motivate this assumption, we consider a system of two fermions in the vacuum at $T = 0$ with contact interactions. If the two fermions are of the same spin, they cannot scatter due to Pauli blocking. Therefore, to obtain anything else than an ideal Fermi gas, we have to consider fermions of different spin. Now, assuming weak attractive interactions between the fermions, the question of whether the fermions pair is equivalent to the question of whether a bound state exists in the interatomic interaction potential. We can assume this potential to be a square well, as the short-range details of the interactions should not matter on the relevant length scales for our discussion. From simple quantum mechanics, we know that a square well always features a bound state in 1D and 2D, but not in 3D, where the bound state is only present after a certain minimum well depth is reached. Does this mean that fermions in 3D usually do not pair? In 1956, Cooper realized that the situation changes significantly when the fermions considered are not in a vacuum, but part of a larger system [57]. At low temperatures, the momentum states below the Fermi wavevector k_F are already occupied and not available for particles to scatter into. Thus, the interacting particles must do so in a narrow region above the Fermi surface, which is effectively a two-dimensional system in momentum space if the system is cold enough. Therefore, a bound state will always exist for these fermions which is stabilized by the presence of the Fermi sea, and they pair for arbitrarily weak attractive interactions even in 3D.

The focus on pairing at opposite momentum stems from a simple phase-space argument (see Fig. 4.4). We can safely assume that pairs for which many states are available to scatter from and into (those with a large available phase-space volume) are more relevant for the behavior of the system than those with few states available. Because only states above the Fermi surface are available, we can also assume that both fermions have momenta close to $\hbar k_F$, as higher momenta are energetically unfavorable. If the pair of fermions now has a nonzero

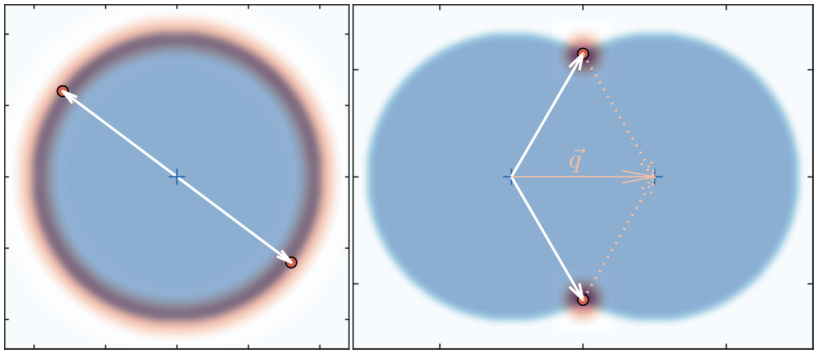

Figure 4.4: Phasespace available for pairing at zero and non-zero momentum. When two particles of opposite spin and opposite momentum of $|k| = k_F$ form a pair (left panel), the phase space available for them to scatter into (red) consists of the entire surface of the Fermi sphere (blue). When the two particles have a non-zero center-of-mass momentum $\vec{q}$, pairing is possible, but the phase space available to scatter into is severely limited as few other combination of two momenta at the Fermi surface add up to the same center-of-mass momentum. Figure adapted from [55].

total momentum, there are only few states available in the vicinity of the Fermi surface that add up to this total momentum, and their phase-space volume is small. Therefore, we can see that the relevant scattering processes should occur between fermions with equal and opposite momentum of $|\mathbf{k}| \sim \pm\hbar k_F$.

Since strong interactions can lead to significantly modified momentum distributions with holes even at low momenta, we will not restrict ourselves to momenta close to k_F in the following derivation, only maintaining that the momenta need to be equal and opposite.

The success of BCS theory in explaining conventional superconductivity led to the theory being thoroughly discussed in a wide range of different scenarios. In 1980, A. Leggett pointed out [58] that simply by relaxing the restriction that the attractive interaction has to be weak, the BCS wavefunction we will derive below naturally transforms into a wavefunction describing a Bose condensate of tightly bound pairs in the limit of strong attractive interaction. In the intermediate regime, he postulated a smooth transition from a BCS superfluid to a Bose-Einstein condensate of molecules. This extended BCS theory, which became known as BEC-BCS theory, has proven to be extremely successful and has become a core concept of ultracold Fermi gases. Due to its importance, we will show the full derivation of this theory in detail in the following.

4.3.1 Pairs and holes: the ansatz

Our goal is to find the many-body wavefunction $\Psi(\mathbf{r}_1, \dots, \mathbf{r}_N)$ describing a condensate of paired fermions. We will write down the Hamiltonian of the system and use the BCS ansatz for the wavefunction to solve it. This ansatz assumes that the system consists of $N/2$ bosonic pairs, which consist of two fermions of opposite spin and momentum. As we will see, the key parameter that describes the system will be the quantity v_k^2, which describes the occupation of states with momentum $\pm\hbar k$. By minimizing the free energy, we will obtain a set of coupled equations for v_k and the energy of these states E_k as a function of the chemical potential μ and the interaction parameter g that need to be solved. From these equations, we will calculate all relevant quantities of the system, from its momentum distribution to the excitation spectrum.

To start, we define the pair creation (annihilation) operator $b^\dagger$ (b) in terms of the creation (annihilation) operators $c^\dagger_{k,\sigma}$ ($c_{k,\sigma}$) for single

fermions with momentum $\hbar k$ and spin $\sigma = \uparrow, \downarrow$:

$$b^\dagger = \sum_k \phi_k c^\dagger_{k,\uparrow} c^\dagger_{k,\downarrow} \tag{4.32}$$

This operator creates a pair consisting of two fermions of opposite spin and momentum, as motivated above. The N-particle state can then be written as

$$|\psi\rangle_N = {b^\dagger}^{N/2} |0\rangle \,. \tag{4.33}$$

Now, we will rewrite this state in a fashion similar to the Bogoliubov transformation used in section 4.1, using two variational parameters u_k and v_k. This will allow us to write the Hamiltonian as a system of two coupled equations later and enable us to find solutions.

Moving to the grand canonical ensemble, we consider a coherent state with a mean of $N/2$ Cooper pairs and write

$$\begin{aligned} \mathcal{N}|\Psi\rangle = \sum_N \frac{1}{(N/2)!} |\Psi\rangle_N = \sum_N \frac{1}{(N/2)!} {b^\dagger}^{N/2} |0\rangle = e^{b^\dagger} |0\rangle \\ = e^{\sum_k \phi_k c^\dagger_{k,\uparrow} c^\dagger_{k,\downarrow}} |0\rangle = \prod_k e^{\phi_k c^\dagger_{k,\uparrow} c^\dagger_{k,\downarrow}} |0\rangle = \prod_k (1 + \phi_k c^\dagger_{k,\uparrow} c^\dagger_{k,\downarrow}) |0\rangle \,. \end{aligned} \tag{4.34}$$

In the last step, we made use of the fact that the operators $c_{k,\sigma}, c^\dagger_{k,\sigma}$ are fermionic and thus $c^\dagger_{k,\sigma} c^\dagger_{k,\sigma} = 0$. The normalization constant $\mathcal{N}$ must then be

$$\mathcal{N} = \prod_k \sqrt{1 + \phi_k^2} \tag{4.35}$$

so that $|\Psi\rangle$ is properly normalized. We now define the variational parameters u_k and v_k such that

$$\begin{aligned} u_k = \frac{1}{\sqrt{1+\phi_k^2}} \quad , \quad v_k = \frac{\phi_k}{\sqrt{1+\phi_k^2}} \quad , \\ \mathcal{N} = \prod_k \frac{1}{u_k} \quad \text{and} \quad |u_k|^2 + |v_k|^2 = 1 \,. \end{aligned} \tag{4.36}$$

Now, we can write down the BCS wavefunction, originally derived for electrons in a superconductor:

$$\boxed{|\Psi\rangle = |\Psi_{BCS}\rangle = \prod_k (u_k + v_k c^\dagger_{k,\uparrow} c^\dagger_{k,\downarrow}) |0\rangle} \tag{4.37}$$

However, as we see here, it applies generally for systems consisting of bosonic pairs, formed from fermions of opposite spin and momentum.

It is straightforward to see that the variational parameters u_k and v_k have physical meaning: We calculate the occupation of a state with momentum $\hbar k$ and find

$$\begin{aligned} n_k &= \langle \Psi | c^\dagger_{k,\uparrow} c_{k,\uparrow} | \Psi \rangle = \langle \Psi | c^\dagger_{k,\downarrow} c_{k,\downarrow} | \Psi \rangle \\ &= \langle 0 | \prod_k (u_k + v_k c_{k,\uparrow} c_{k,\downarrow}) \; c^\dagger_{k,\uparrow} c_{k,\uparrow} \; \prod_k (u_k + v_k c^\dagger_{k,\uparrow} c^\dagger_{k,\downarrow}) |0\rangle \\ &= v_k^2 = 1 - u_k^2 \end{aligned} \tag{4.38}$$

Therefore, if a state with momentum $\hbar k$ is occupied by a pair, $|v_k|^2 = 1$ and $|u_k|^2 = 0$, whereas in an unoccupied state $|v_k|^2 = 0$ and $|u_k|^2 = 1$. We see that v_k (u_k) describes the average occupation of a momentum state with pairs (holes). As states quite often will have both $u_k, v_k > 0$, they can be viewed as being occupied by a superposition of pairs and holes.

4.3.2 Gap and number equation

To obtain solutions for the parameters u_k and v_k, we write down the many-body Hamiltonian of the system in a uniform system of volume Ω as

$$\boxed{\hat{H} = \sum_{k,\sigma} \epsilon_k c^\dagger_{k,\sigma} c_{k,\sigma} + \frac{g}{\Omega} \sum_{k,k'} c^\dagger_{k,\uparrow} c^\dagger_{-k,\downarrow} c_{k',\downarrow} c_{-k',\uparrow}\,,} \tag{4.39}$$

where we used $\epsilon_k = \frac{\hbar^2 k^2}{2m}$, once again parametrized the interaction strength with g and are neglecting interactions between pairs at non-zero momentum as explained above. The first term simply describes the kinetic energy of the fermions, while the second term describes the interactions in the system through scattering processes in which a pair with momentum $\pm k$ scatters into unoccupied states at momentum $\pm k'$ (see fig. 4.5). With $\xi_k = \epsilon_k - \mu$ and letting $u_k, v_k \in \mathbb{R}$, we can calculate the free energy of the system as described in the box below:

$$\mathcal{F} = \sum_k \mathcal{F}_k = \sum_k 2\xi_k v_k^2 + \frac{g}{\Omega} \sum_{k,k'} u_k v_k u_{k'} v_{k'} \tag{4.40}$$

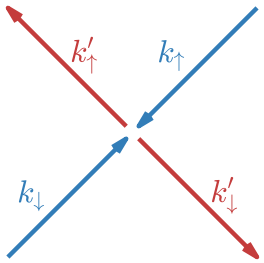

Figure 4.5: Illustration of the scattering process. Note that no scattering processes with a non-zero center of mass momentum are considered.

Box 4.3: Calculating the free energy $\mathcal{F}$

To calculate $\mathcal{F}$, we split the calculation into three parts:

$$\mathcal{F} = E - \mu N = \langle\Psi|\hat{H} - \mu\hat{N}|\Psi\rangle = \langle\Psi|\hat{H}_{kin}|\Psi\rangle + \langle\Psi|\hat{H}_{int}|\Psi\rangle - \langle\Psi|\mu\hat{N}|\Psi\rangle$$

We first solve the kinetic energy part of the Hamiltonian:

$$\langle\hat{H}_{kin}\rangle = \langle 0|\prod_k (u_k + v_k c_{k,\uparrow} c_{k,\downarrow}) \sum_{k,\sigma} \epsilon_k c^\dagger_{k,\sigma} c_{k,\sigma} \prod_k (u_k + v_k c^\dagger_{k,\uparrow} c^\dagger_{k,\downarrow})|0\rangle = \sum_{k,\sigma} \epsilon_k v_k^2 = \sum_k 2\epsilon_k v_k^2$$

For the kinetic energy term to be non-zero, the state at momentum $\hbar k$ needs to be occupied, and we obtain simply the occupation of momentum states $n_k = v_k^2$. Next, we solve the interaction part of the Hamiltonian

$$\langle\hat{H}_{int}\rangle = \langle 0|\prod_k (u_k + v_k c_{k,\uparrow} c_{k,\downarrow}) \frac{g}{\Omega} \sum_{k,k'} c^\dagger_{k,\uparrow} c^\dagger_{-k,\downarrow} c_{k',\downarrow} c_{-k',\uparrow} \prod_k (u_k + v_k c^\dagger_{k,\uparrow} c^\dagger_{k,\downarrow})|0\rangle = \frac{g}{\Omega} \sum_{k,k'} v_{k'} u_k u_{k'} v_k$$

For the interaction term to be nonzero, the states at momentum $\pm\hbar k'$ need to be occupied while the states at momentum $\pm\hbar k$ must not be, so we collect a mix of u_k and v_k. Finally, the number operator term is very similar to the kinetic energy term and we obtain

$$\langle\mu\hat{N}\rangle = \langle 0|\prod_k (u_k + v_k c_{k\uparrow} c_{k\downarrow}) \sum_{k,\sigma} \mu c^\dagger_{k,\sigma} c_{k,\sigma} \prod_k (u_k + v_k c^\dagger_{k\uparrow} c^\dagger_{k\downarrow})|0\rangle = \sum_k 2\mu v_k^2$$

We can obtain a solution for the parameters u_k and v_k by minimizing the free energy while simultaneously fulfilling the normalization constraint $u_k^2 + v_k^2 = 1$ using the method of Lagrange multipliers. We make use of equation 4.36 to write down the Lagrangian function

$$\mathcal{L} = \mathcal{F} - E_k(u_k^2 + v_k^2 - 1)\,, \tag{4.41}$$

where E_k is the Lagrange multiplier at momentum $\hbar k$. Now, the minimum of $\mathcal{F}$ can be found by solving

$$\nabla\mathcal{L} = 0 \implies \frac{\partial\mathcal{L}}{\partial u_k} = 0\,,\ \frac{\partial\mathcal{L}}{\partial v_k} = 0 \tag{4.42}$$

For each momentum $\hbar k$, we carry out the derivatives and find

We write $2v_k^2$ as $v_k^2 + 1 - u_k^2$ here as it results in a cleaner, more symmetric solution later.

$$\frac{\partial}{\partial u_k}\sum_{k'} 2\xi_{k'}v_{k'}^2 = \frac{\partial}{\partial u_k}\sum_{k'}\xi_{k'}(v_{k'}^2 + 1 - u_{k'}^2) = -2\xi_k u_k \tag{4.43}$$

$$\frac{\partial}{\partial v_k}\sum_{k'} 2\xi_{k'}v_{k'}^2 = \frac{\partial}{\partial v_k}\sum_{k'}\xi_{k'}(v_{k'}^2 + 1 - u_{k'}^2) = 2\xi_k v_k \tag{4.44}$$

$$\begin{aligned}
&\frac{\partial}{\partial u_k}\frac{g}{\Omega}\sum_{k',k''} v_{k''}u_{k'}u_{k''}v_{k'} \\
&= \sum_{k',k''}\delta(k-k')v_{k''}u_{k''}v_{k'} + \delta(k-k'')v_{k''}u_{k'}v_{k'} \\
&= 2v_k\frac{g}{\Omega}\sum_{k'} v_{k'}u_{k'}
\end{aligned} \tag{4.45}$$

$$\begin{aligned}
&\frac{\partial}{\partial v_k}\frac{g}{\Omega}\sum_{k',k''} v_{k''}u_{k'}u_{k''}v_{k'} \\
&= \sum_{k',k''}\delta(k-k')v_{k''}u_k u_{k''} + \delta(k-k'')v_k u_{k'}u_{k''} \\
&= 2u_k\frac{g}{\Omega}\sum_{k'} v_{k'}u_{k'}
\end{aligned} \tag{4.46}$$

$$\frac{\partial}{\partial u_k}E_k(u_k^2 + v_k^2 - 1) = 2E_k u_k \tag{4.47}$$

$$\frac{\partial}{\partial v_k}E_k(u_k^2 + v_k^2 - 1) = 2E_k v_k \tag{4.48}$$

By defining

$$\Delta \equiv -\frac{g}{\Omega}\sum_k v_k u_k \tag{4.49}$$

we can therefore write equation 4.42 as

$$\begin{pmatrix} \xi_k - E_k & \Delta \\ \Delta & -\xi_k - E_k \end{pmatrix}\begin{pmatrix} u_k \\ v_k \end{pmatrix} = 0\,. \tag{4.50}$$

It is now straightforward to calculate the eigenvalues of this matrix, and we arrive at

$$\boxed{E_k = \sqrt{\xi_k^2 + \Delta^2}\,.} \tag{4.51}$$

Furthermore, we can calculate the eigenfunctions and obtain

$$u_k = \sqrt{\frac{1}{2}\left(1 + \frac{\xi_k}{E_k}\right)} \tag{4.52}$$

$$v_k = \sqrt{\frac{1}{2}\left(1 - \frac{\xi_k}{E_k}\right)}. \tag{4.53}$$

From expression 4.53, we can directly obtain the momentum distribution $n_k = v_k^2$ of the system.

We have now found solutions that minimize the free energy, but there are two unknowns remaining that depend on the specifics of the system: the chemical potential μ and the parameter Δ, which is referred to as the **gap** (or pairing gap). To obtain μ and Δ, we need to find equations that relate these two unknowns to the parameters of the system we are trying to describe, namely the total particle number N and the interaction parameter g.

First, we will derive the **number equation**, which relates the chemical potential μ to the density n, as the density is usually easily measurable in cold atom experiments. From equation 4.38, it is straightforward to write

$$\begin{aligned} n &= \sum_{k,\sigma} n_k = \sum_{k,\sigma} v_k^2 = \sum_k 2v_k^2 \\ \implies n &= \sum_k \left(1 - \frac{\xi_k}{E_k}\right). \end{aligned} \tag{4.54}$$

A second equation can be obtained from definition 4.49 and is called the **gap equation**:

$$\begin{aligned} \Delta &= -\frac{g}{\Omega}\sum_k u_k v_k = -\frac{g}{\Omega}\sum_k \sqrt{\frac{1}{4}\left(1 - \frac{\xi_k}{E_k}\right)\left(1 + \frac{\xi_k}{E_k}\right)} \\ &= -\frac{g}{\Omega}\sum_k \sqrt{\frac{1}{4}\left(1 - \frac{\xi_k^2}{E_k^2}\right)} = -\frac{g}{\Omega}\sum_k \sqrt{\frac{1}{4E_k^2}\left(E_k^2 - \xi_k^2\right)} \\ &= -\frac{g}{\Omega}\sum_k \sqrt{\frac{\Delta^2}{4E_k^2}} \\ \implies -\frac{\Omega}{g} &= \sum_k \frac{1}{2E_k} \end{aligned} \tag{4.55}$$

Now, it is simply a matter of solving these two equations in a self-consistent fashion to obtain μ and Δ, which is usually done numerically.

Box 4.4: Intuitive meaning of the gap

It is worthwhile to spend a moment to consider the physical meaning of the gap by looking at its extreme cases. A system with very weak interactions must approach the case of a free Fermi gas, meaning that we will find that all momentum states below k_F are occupied with a pair while all momentum states above are occupied by holes. Therefore, for any k, we will find $u_k v_k \approx 0$ and therefore $\Delta \approx 0$ - an ideal Fermi gas does not have a pairing gap. The maximum possible value of Δ would be achieved if for any occupied momentum state $u_k = v_k$, where we would find $\Delta = gn$, the interaction energy of the system. Therefore, we can see that Δ quantifies the mixing between holes and pairs.

4.3.3 The BEC-BCS crossover in 2D

To provide an intuition for the expressions derived above, we calculate the momentum distribution and single-particle excitation spectrum for the case of a two-dimensional Fermi gas relevant in this thesis. Here, we will neglect the peculiarities of two-dimensional systems discussed in section 4.2 and merely note that they change very little in the case of a system at zero temperature as discussed in the following.

The BEC-BCS crossover problem in 2D was first considered in 1989 by Mohit Randeria and coworkers using a T-matrix approach at zero temperature [59]. The parameterization of the 2D BEC-BCS crossover used is somewhat more complicated than the simple parameterization by some coupling constant g shown in the previous section, since Randeria and coworkers take into account that a realistic two-body potential is repulsive at very short distances in addition to the usual attraction at longer distances. They find, however, that the problem can be neatly parametrized by the two-body binding energy E_B, which increases monotonously with g. Here, we will not derive an expression for E_B as a function of g, since we will see in section 4.5 that the actual expression for E_B in realistic 2D Fermi gases is more complicated anyways. Instead, we will simply take E_B to be some parameter that scales with g and spans a wide range from weakly bound Cooper pairs for $E_B \ll E_F$ to tightly bound bosonic molecules for $E_B \gg E_F$, where $E_F = \frac{\hbar^2 k_F^2}{2m}$ is the Fermi energy. The results for μ and Δ Randeria and coworkers obtained were remarkably simple. Solving the gap and number equations analytically in the mean-field approximation, they found

$$\Delta = \sqrt{2 E_F E_B} \tag{4.56}$$

$$\mu = E_F - E_B/2\,. \tag{4.57}$$

We emphasize that these simple results are only valid on the mean-field level. Going beyond the mean-field approximation, the effect of fluctuations must be accounted for, see e.g. [60–62].

It is worth a moment to emphasize that these simple equations are all that is needed to calculate the entire crossover from BEC-like superfluidity of molecules to BCS superfluidity. Their simple structure not only confirms that the two-body binding energy E_B parameterizes the

BEC-BCS crossover in 2D, but also indicates a close relation between the trivial two-body bound state and many-body pairing in the crossover region.

With these expressions, we can now demonstrate the smooth evolution from BEC to BCS type superfluidity in two dimensions. We will consider the momentum distribution n_k as well as the single-particle excitation spectrum, which describes the energy required to add or remove a single fermionic atom. When adding or removing a single fermion at momentum $\hbar k$, the number of atoms in both spinstates is no longer equal, and one atom is unable to find a partner to pair with. Its contribution to the free energy is therefore only ξ_k, its kinetic energy, and we can calculate the energy difference to a system where all atoms are paired up as

$$\Delta\mathcal{F} = \mathcal{F}_k^{\text{single atom}} - \mathcal{F}_k = \xi_k - \mathcal{F}_k \tag{4.58}$$

We can evaluate this expression using equations 4.53 and 4.55:

$$\begin{aligned}
\mathcal{F}_k &= 2\xi_k v_k^2 + 2\frac{g}{\Omega} u_k v_k \sum_{k'} u_{k'} v_{k'} \\
&= \xi_k \left(1 - \frac{\xi_k}{E_k}\right) - 2\Delta u_k v_k \\
&= \xi_k \left(1 - \frac{\xi_k}{E_k}\right) - 2\Delta \frac{\sqrt{E_k^2 - \xi_k^2}}{2E_k} \\
&= \xi_k - \frac{\xi_k^2}{E_k} - \frac{\Delta^2}{E_k} \\
&= \xi_k - \frac{\xi_k^2}{E_k} - E_k + \frac{\xi_k^2}{E_k} \\
&= \xi_k - E_k \\
\implies \Delta\mathcal{F} &= E_k
\end{aligned} \tag{4.59}$$

Note that the results for other dimensionalities will qualitatively be very similar, except for the parameterization by the two-body binding energy.

Therefore, the single-particle excitation spectrum is simply given by the Lagrange multiplier E_k, and can be calculated using equation 4.51.

The evolution of u_k^2, $n_k = v_k^2$, E_k and ξ_k in the 2D BEC-BCS crossover is shown in Fig. 4.6. The momentum distribution, which resembles that of an ideal Fermi gas in the limit of negligible binding energy, shows how holes and pairs gradually hybridize more and more as the interaction strength is increased. In the BEC limit of strong binding energies, pairs occupy states up to very high momentum, with each individual momentum state mostly being occupied by holes. The single-particle excitation spectrum undergoes a similar evolution from that of free atoms in the far BCS limit to that of free molecules in the BEC limit. However, its shape in the intermediate region is very interesting, with a minimum at $k_{\min} = \sqrt{2m\mu/\hbar^2}$ that is slowly moving from $k = k_F$ to $k = 0$ as E_B is increased.

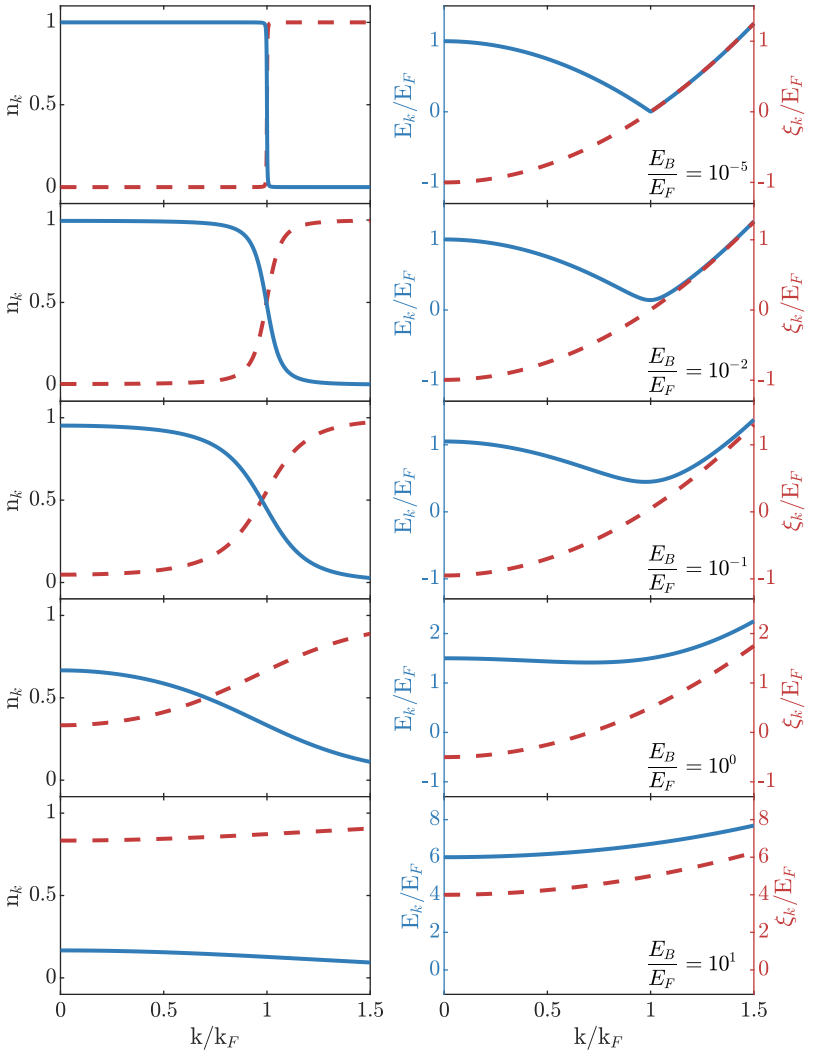

Figure 4.6: n_k and E_k in the 2D BEC-BCS crossover. Left panels: Distribution of pairs $n_k = v_k^2$ (blue line) and holes u_k^2 (red line) as a function of momentum $\hbar k$, for different interaction strengths. The momentum distribution resembles the ideal Fermi gas result at weak interaction (top row). As the binding energy increases, pairs and holes begin to mix around k_F, smoothing out the momentum distribution until no similarities with the free fermion result remain. Right panels: Single-particle excitation spectrum E_k (blue line) and free energy of the added fermion ξ_k (red line) as a function of momentum $\hbar k$, for the same interaction strengths. At low interaction strengths, $E_k \approx |\xi_k|$, but as pairs and holes start to hybridize, the pairing gap opens at k_F and excitations at energies lower than Δ are suppressed. As the gap increases, the minimum energy for excitations is found at smaller and smaller momentum, until the parabolic dispersion of free molecules is recovered when $E_B \gg E_F$.

4.4 The dynamic structure factor

In this section, we introduce the dynamic structure factor and derive a simple representation in BEC-BCS theory. We will calculate the dynamic structure factor in 1D, 2D and 3D and discuss additional contributions, as well as methods of measuring the dynamic structure factor.

While E_k describes the cost of adding (or removing) a particle at a given momentum $\hbar k$, not all excitations change the number of particles. In fact, the particle number is usually conserved in cold atom experiments, and special schemes like hiding atoms in (nearly) non-interacting spinstates have to be used to measure E_k directly. Therefore, in this thesis, the focus is on a different kind of excitation spectrum: the **dynamic structure factor**, which we will introduce in the following.

The derivation of the dynamic structure factor given here follows [63].

First, we need to introduce the concept of a density fluctuation in our BEC-BCS picture. If the density of a Fermi gas is given by $\rho(\vec{r})$, we write its Fourier components as ρ_q. In a uniform system with no excitations, the density is constant with $\rho(\vec{r}) = \rho_0$ for any $\vec{r}$. However,

if excitations are present in the system, the density fluctuates around this value, and we write $\delta\rho_q = \rho_q - \rho_0$. In our fermionic basis, a fluctuation at momentum $\hbar q$ must correspond to some state where a fermion at momentum $\hbar k$ is removed and recreated at momentum $\hbar k + \hbar q$ - a single-particle excitation that maintains the number of particles. These processes are described by the density fluctuation operator

$$\delta\rho_q^\dagger = \sum_{k,\sigma} c_{k+q}^\dagger c_k \,, \tag{4.60}$$

which describes the creation of such a density fluctuation with momentum $\hbar q$.

We now let the Fermi gas be perturbed by some weak external probe with a well defined momentum $\hbar q$ and energy $\hbar\omega$. The interaction Hamiltonian is

$$H_{int} = \frac{V_q}{2}(\delta\rho_q^\dagger e^{-i\omega t} + \delta\rho_q e^{i\omega t}) \,, \tag{4.61}$$

where V_q is a small parameter describing the strength of the perturbation. H_{int} couples weakly to the ground state $|\Psi_0\rangle$ of the system, meaning that the eigenstates are not modified by the perturbation. If $|\Psi_0\rangle = |\Psi_{BCS}\rangle$ is the ground state of the system and $|\Psi_n\rangle$ are the excited states, we can write

$$\langle\Psi_n|H_{int}|\Psi_0\rangle = V_q\langle\Psi_n|\delta\rho_q^\dagger|\Psi_0\rangle \equiv V_q(\delta\rho_q^\dagger)_{n,0} \,. \tag{4.62}$$

At this point, the excited states $|\Psi_n\rangle$ are quite generic and feature all possible excitations, but we will derive results for a specific basis of excited states later. The probability $W(q,\omega)$ for the probe to transfer momentum $\hbar q$ and energy $\hbar\omega$ to the system can now be calculated in a straightforward fashion from Fermi's golden rule as

$$W(q,\omega) = 2\pi V_q^2 \, S(q,\omega) \,, \tag{4.63}$$

where $S(q,\omega)$ is the **dynamic structure factor** with

$$S(q,\omega) = \hbar \sum_n |(\delta\rho_q^\dagger)_{n,0}|^2 \delta(\omega - \omega_{n,0}) \,, \tag{4.64}$$

writing $\omega_{n,0} = \omega_n - \omega_0$ for the difference in energy between the states $|\Psi_n\rangle$ and $|\Psi_0\rangle$. The dynamic structure factor is therefore the fundamental quantity that determines for which combinations of energy and momentum such excitations can be created in the system. It fully describes the spectrum of excitations that maintain the number of particles.

Box 4.5: $S(q,\omega)$ *and correlation functions*

By Fourier-transforming $S(q,\omega)$ in time and space, one obtains the van-Hove function $G(\vec{r},t)$ [64], which is defined as

$$G(\vec{r},t) = \left\langle \frac{1}{N} \int \rho(\vec{r}'+\vec{r},t)\rho(\vec{r}',0)d\vec{r}' \right\rangle . \tag{4.65}$$

$G(\vec{r},t)$ is the time-dependent pair distribution function of the system, which describes how interactions change the probability of finding a particle at a position $\vec{r}$ and time t after another particle was at a position $\vec{r}=0$ and time $t=0$. Therefore, measuring $S(q,\omega)$ is directly equivalent to measuring the time-dependent correlation function between particles in a system.

In the following, we will derive a simple expression for the dynamic structure factor in the framework of BEC-BCS theory. We will restrict ourselves to excitations of single particles, since BEC-BCS theory does not support collective excitations as it neglects pairs at nonzero momentum. Therefore, we can construct our basis of excited states by writing down wavefunctions where a single particle has been excited, meaning it has been removed at momentum $\hbar k$ and re-created at $\hbar(k+q)$:

$$|\Psi_n\rangle \equiv |\Psi_{k,\sigma}\rangle \equiv c^\dagger_{k+q,\sigma} c_{k,\sigma} |\Psi_0\rangle \tag{4.66}$$

Note that this is not strictly a basis of excited states, as it only contains the excited states that can be reached from the ground state by excitations created by the external probe. However, as other states do not couple to the density fluctuation operator anyways, we can safely neglect them.

From these states, all others can be constructed as linear combinations.

Since we know the energy cost of adding and removing fermions to the BCS wavefunction, it is also straightforward to write down the energy of such a state relative to the ground state:

$$\hbar\omega_{n,0} = E_k + E_{k+q} \tag{4.67}$$

With the excited states known, it is now straightforward to write

$$\begin{aligned}
(\delta\rho^\dagger_q)_{n,0} &= \sum_\sigma \langle \Psi_{k,\sigma}| \sum_{k',\sigma'} c^\dagger_{k'+q,\sigma'} c_{k',\sigma'} |\Psi_0\rangle \\
&= \sum_\sigma \langle \Psi_0| c^\dagger_{k,\sigma} c_{k+q,\sigma} \sum_{k',\sigma'} c^\dagger_{k'+q,\sigma'} c_{k',\sigma'} |\Psi_0\rangle \\
&= \sum_\sigma \langle \Psi_0| c^\dagger_{k,\sigma} c_{k+q,\sigma} c^\dagger_{k+q,\sigma} c_{k,\sigma} |\Psi_0\rangle \\
&= 2\, v_k u_{k+q} \,.
\end{aligned} \tag{4.68}$$

The dynamic structure factor is therefore given as

$$\begin{aligned}
S(q,\omega) &= \hbar \sum_n |(\delta\rho^\dagger_q)_{n,0}|^2 \delta(\omega - \omega_{n,0}) \\
&= \hbar \sum_k |2\, v_k u_{k+q}|^2 \, \delta(\hbar\omega - E_k - E_{k+q}) \\
&= 4\hbar \sum_k n_k(1-n_{k+q}) \, \delta(\hbar\omega - E_k - E_{k+q})
\end{aligned} \tag{4.69}$$

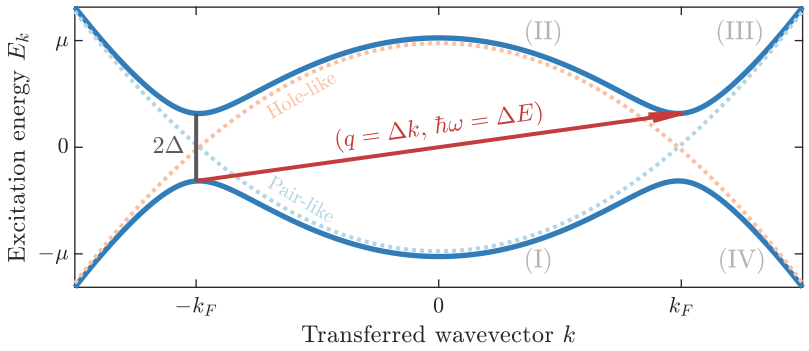

Figure 4.7: Unfolded single-particle excitation spectrum By mirroring E_k on both the k- and the E-axis, one obtains the full energy spectrum of particle- and hole excitations, here shown for $E_B/E_F = 0.05$. The solid lines show E_k, the dashed lines shows ξ_k. At negative energies and $k < k_F$, the curve describes an excitation where a hole in the Fermi sea is filled by an atom (I). As this process is energetically favorable, its energy is negative. At the same k, the same curve at positive energies corresponds to replacing an atom in the Fermi sea with a hole, which is energetically costly (II). Above k_F, replacing a hole with an atom is costly, as this corresponds to adding a highly energetic atom to the system (III). Therefore, the energy cost of this process is positive. However, if an atom is already present, it is energetically favorable to replace it with a hole (IV). Any vector $(\hbar q, \hbar\omega)$ (red arrow) that connects a (partially) occupied state with a (partially) unoccupied state results in a nonzero $S(q, \omega)$. Note that while at $T = 0$, all states at $E_k < 0$ are occupied and all states at $E_k > 0$ are empty, thermally occupied states have to be considered once the temperature becomes comparable to Δ.

As eq. 4.69 shows, two things have to be fulfilled to have a nonzero dynamic structure factor at some (q, ω): First, there need to be occupied momentum states at some $\hbar k$ ($n_k > 0$ for some k) that can be transferred into initially empty momentum states at $\hbar k + \hbar q$ ($n_{k+q} < 1$). Second, for at least one of these momentum states, the transferred energy $\hbar\omega$ needs to match the energy required to create a hole at $\hbar k$ and a particle at $\hbar(k + q)$. This condition can be visualized in a simple way by mirroring the single-particle excitation spectrum E_k on both axes, as done in Fig. 4.7, where the statement above corresponds to finding a (partially) occupied state and a (partially) unoccupied one at a distance of $(\Delta k, \Delta E) = (\hbar q, \hbar\omega)$.

4.4.1 The dynamic structure factor from BEC-BCS theory

In the following, we will calculate the dynamic structure factor from BEC-BCS theory in 1D, 2D and 3D to show how the results depend on the dimensionality of the system. In Fig. 4.8, we show the evolution of the dynamic structure factor across the BEC-BCS crossover in 1D. Instead of parameterizing the crossover with some interaction parameter, we simply set Δ to some value and solve the number equation to obtain the corresponding μ. We then numerically solve equation 4.69 and obtain the plotted $S(q, \omega)$.

In weakly interacting Fermi gases, the shape of $S(q, \omega)$ is straightforward to predict using the visual method outlined above: The lowest energy excitations transfer $\hbar\omega = 2\Delta$ to an atom sitting at the Fermi edge with either $q = 0$ or $|q| = 2k_F$, such that the atom is still at the Fermi edge after the excitation. As $\hbar\omega$ is increased, excitations away from the Fermi edge become possible as more unoccupied states are available to scatter into. The onset of $S(q, \omega)$ therefore has two distinct minima. Additionally, excitations at higher $\hbar\omega$ require some transferred momentum because the only states where such a transfer would be possible without a momentum transfer are at very large values of $\hbar k$ and therefore initially unoccupied, creating a region with negligible weight at small q and large ω.

As the strength of interactions and therefore the pairing gap increases, pairs and holes begin to mix even deep in the Fermi sea, and

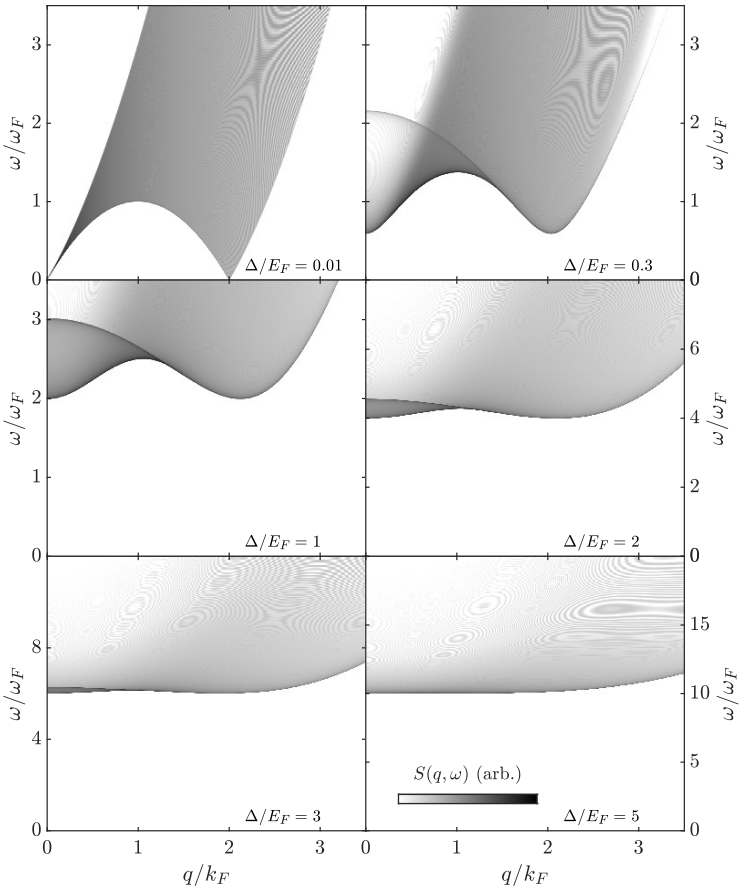

Figure 4.8: Evolution of the dynamical structure factor in a 1D Fermi gas. Plotted is $\mathrm{S}(\mathrm{q},\omega)$ for a range of different interaction strengths as quantified by the pairing gap Δ. The dynamic structure factor smoothly transforms from the two distinct features at $\mathrm{q} = 0$ and $\mathrm{q} = 2\mathrm{k_F}$ expected for a Fermi gas to the quadratic dispersion expected for bosonic molecules. The colormap shown is scaled logarithmically to increase the visibility of the continuum; the striped patterns are numerical artifacts.

the low-momentum, high-energy features of $\mathrm{S}(\mathrm{q},\omega)$ begin to wash out. Initially, excitations at low momentum transfers still mostly occur within the Fermi sea and therefore in a limited range of energy transfers, but with increasing interactions, higher momentum states also become partially occupied, allowing for excitations at $\mathrm{q} = 0$ even at large energy transfers. Additionally, the distinct minima of the onset broaden as the pairing gap increases, and the minimum initially found at $\mathrm{q_{min}} = 2\mathrm{k_F}$ starts to move to lower momentum transfers as $\mathrm{q_{min}} = \sqrt{2\mathrm{m}\mu/\hbar^2}$. Finally, for strong interactions, the two minima merge, and $\mathrm{S}(\mathrm{q},\omega)$ henceforth has only a single minimum at $\mathrm{q} = 0$, reproducing the quadratic increase expected for a gas of bosonic molecules. This merging occurs once $\mu = 0$, and the new onset of excitations is found at $\sqrt{\Delta^2 + \mu^2}$ at $\mathrm{q} = 0$.

When the geometry of the system is two-dimensional, the dynamic structure factor changes (Fig. 4.9).

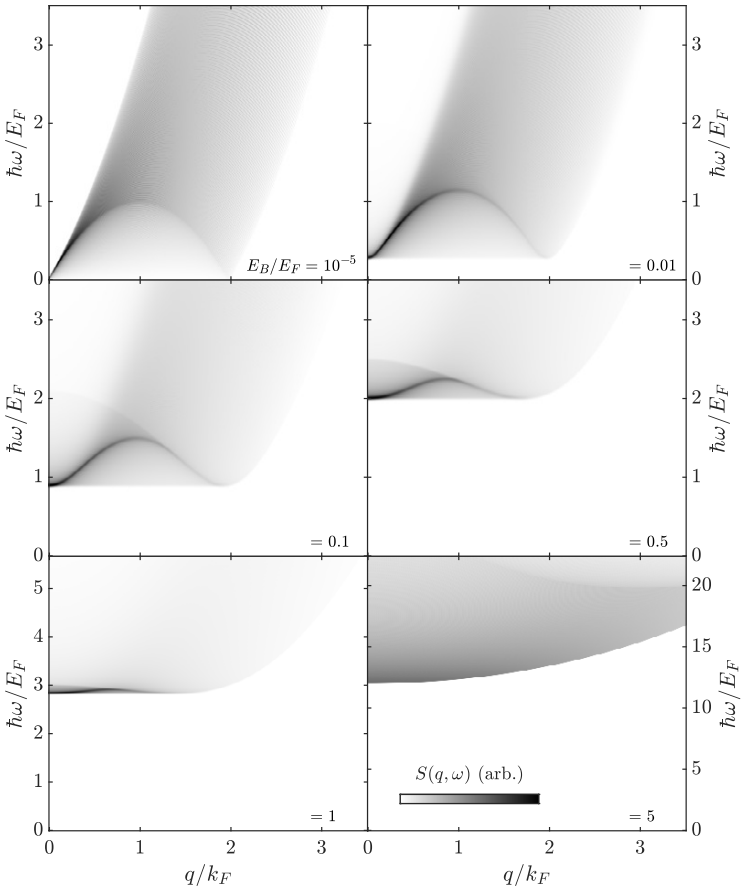

Figure 4.9: Evolution of the dynamical structure factor in a 2D Fermi gas. Plotted is $S(q,\omega)$ for a range of different interaction strengths, parametrized by the two-body binding energy E_B as described in the text. While the 2D-$S(q,\omega)$ resembles the result for the 1D Fermi gas, the minimum energy of excitations is 2Δ anywhere from 0 to $2k_F$ as excitations can occur between any two points on the Fermi surface. However, due to the available phasespace, excitations at low q are more likely than those at higher q.

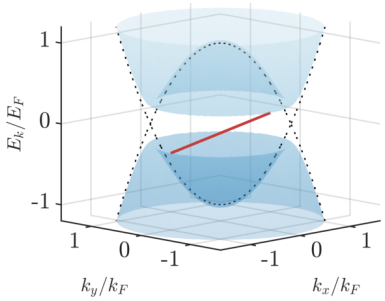

Figure 4.10: Two-dimensional excitation spectrum. In two-dimensional systems, excitations can happen for any angle between $\vec{k}$ and $\vec{q}$ (red line), leading to a modified dynamic structure factor.

Because excitations at 2Δ can occur from any point on the Fermi surface to any other (see Fig. 4.10), the onset of excitations no longer shows two distinct minima. Instead, excitations can occur at 2Δ at any transferred momentum between $q = 0$ and $\hbar q_{\mathrm{min}} = \sqrt{2m\mu}$. Additionally, the momentum-dependent weight of $S(q,\omega)$ changes: As the system is excited along one fixed direction, there is still only one point on the Fermi edge where excitations to the other side of the Fermi surface can occur. However, excitations with $q = 0$ can happen everywhere on the Fermi surface, leading to a higher probability and more weight at low q.

Fig. 4.11 shows the simulated $S(q,\omega)$ for the three-dimensional Fermi gas. Here, the solution for the gap and number equations are found as described in [55] and parametrized by the interaction parameter $-1/k_F a$ (see section 4.5). Generally, the dynamic structure factors in 2D and 3D are quite similar: From 1D to 2D, the possibility of exciting atoms along a direction not aligned with their momentum significantly changed $S(q,\omega)$, leading to a constant onset at 2Δ instead of two distinct minima. However, from 2D to 3D, no qualitative change in the possible excitations occurs. Instead, the weight of such non-aligned excitations merely increases further, leading to an even higher weight at low q but no qualitative changes to $S(q,\omega)$.

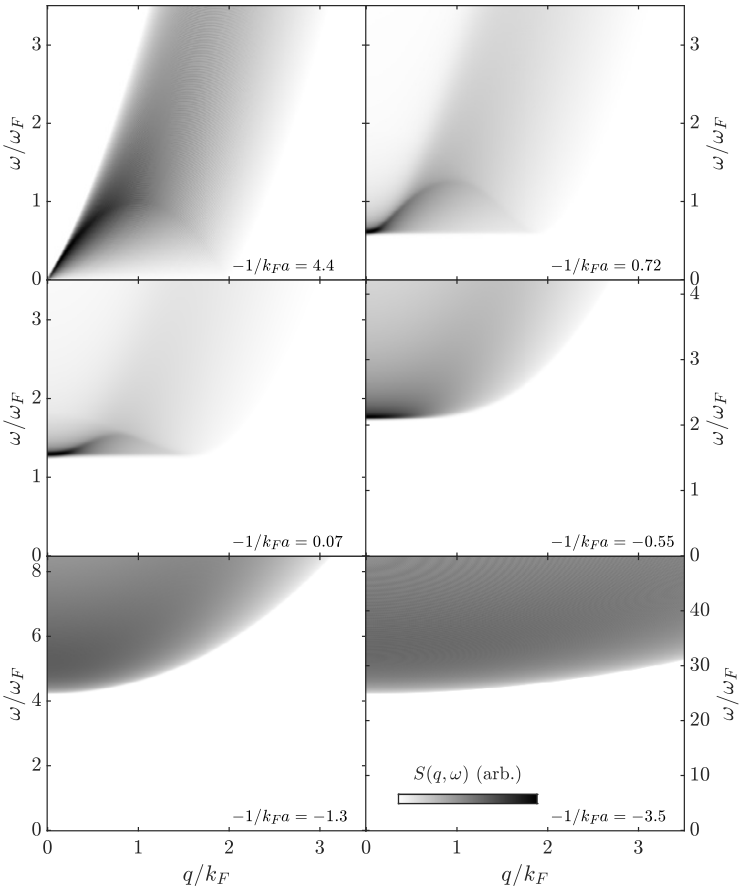

Figure 4.11: Evolution of the dynamical structure factor in a 3D Fermi gas. Plotted is $S(q, \omega)$ for a range of different interaction strengths, parametrized by the commonly used $-\frac{1}{k_F a}$. The obtained dynamic structure factors are very similar to those found for a 2D Fermi gas, except for an even stronger decrease in probability towards higher momentum.

4.4.2 Other contributions to the dynamic structure factor

In subsection 4.4.1, we calculated the dynamic structure factor $S(q, \omega)$ from BEC-BCS theory in one-, two- and three-dimensional Fermi gases. However, our results miss some crucial contributions. In section 4.1, we established that the excitation spectrum of a weakly interacting, condensed system is given by the Bogoliubov dispersion, which features a linear branch of phononic excitations at low momentum. In fact, we argued that such a linear branch should be present in any neutral condensate in the form of a Goldstone mode, leading to excitation spectra as shown in Fig. 4.12. As we have assumed the BEC-BCS ground state to consist of a condensate of bosonic pairs, it is natural to ask why our calculations do not find such a Goldstone mode at low energy and momentum.

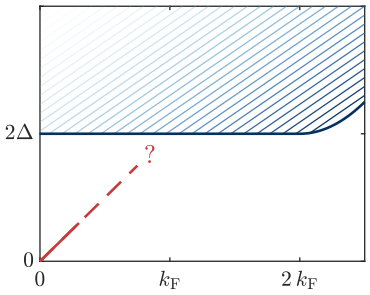

Figure 4.12: Sketch of the Goldstone mode in the dynamic structure factor In a superfluid, a linear Goldstone mode should be present at low momentum that is not found in the calculated spectra as they only contain single-particle excitations.

The answer to this question lies in the fact that the calculated excitation spectrum found above is that of single-particle excitations of the fermionic atoms that form the bosonic pairs, as can be seen from equation 4.60. Therefore, the $S(q, \omega)$ we calculated shows the probability of creating a single-particle pair breaking excitation. However, the Goldstone mode consists of long-wavelength fluctuations, which are collective excitations in which many pairs participate. To obtain these collective excitations, our initial assumption of BEC-BCS theory to consider only pairs consisting of atoms of equal and opposite mo-

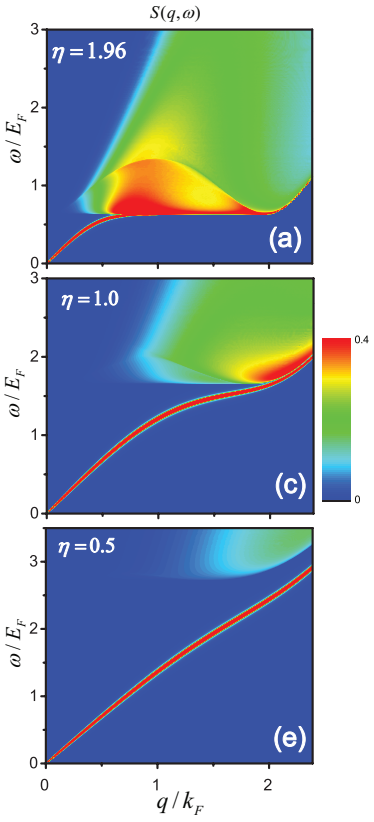

Figure 4.13: Dynamic structure factors from RPA. Calculated dynamic structure factors of the two-dimensional Fermi gas for three different interaction strengths, taken from [66]. These spectra were obtained using a method called quasi-random phase approximation, which allows for the calculation of both the single-particle excitations as well as the collective modes.

mentum would have to be relaxed, and the resulting equations are no longer easy to solve.

One method to approach this problem is the random-phase approximation (RPA), by means of which some of the contributions for pairs with finite momentum that were neglected in BEC-BCS theory are recovered. RPA was already used by Anderson in 1958 to calculate the collective mode of a BCS superconductor [65], and has recently been applied to the two-dimensional Fermi gas by Huaisong Zhao and coauthors [66], who calculated the dynamic structure factors shown in Fig. 4.13. A clear Goldstone mode is visible in these spectra. Interestingly, the Goldstone mode appears to bend down as it approaches the continuum, indicating some interaction between the collective and single-particle excitations. This effect had previously been predicted for 3D Fermi gases [67], but has not been observed experimentally so far. The single-particle continuum found using RPA is very similar to those we obtained from BEC-BCS theory above, besides a reduction of spectral weight at low momentum. This effect will be discussed further in later sections of this thesis. Similar calculations have previously been carried out for three-dimensional Fermi gases and found comparable results [68, 69].

In addition to these higher-order excitations, an obvious contribution to the dynamic structure factor that we have ignored so far is that of finite temperature, which is unavoidable in experiments. In a system at $T > 0$, some of the excited states in the system will be thermally occupied, meaning that they cannot be scattered into anymore. As described in detail in [63], one can calculate the effect of these thermally occupied excitations on the measured excitation spectrum by detailed balancing, and finds that the density-density response function $X''(q, \omega)$ one measures in the experiment changes with temperature as

$$X''(q, \omega) \propto S(q, \omega) \left(1 - e^{-\frac{\hbar\omega}{k_B T}}\right) . \tag{4.70}$$

However, in our experiments in the crossover region and in the superfluid phase, $T < 0.1 T_F$ while $\Delta \sim E_F$, leading to a negligible effect of thermal excitations on the measured excitation spectrum. Therefore, throughout the thesis, we will use $X''(q, \omega) \approx S(q, \omega)$ and neglect the small correction due to finite temperature.

Finite temperature can, however, also change $S(q, \omega)$ in other ways. For example, the sound velocity which sets the slope of the Goldstone mode is not independent of temperature, but will increase due to the increased mobility of hotter particles. The pairing gap also has a temperature dependence, decreasing in magnitude as temperature increases until it vanishes at some critical temperature for pair formation T^*. Additionally, the linewidth of the Goldstone mode increases with hotter temperatures through a process called Beliaev damping, where phonons scatter off thermal excitations, in addition to the finite linewidth already given by scattering off other phonons called Landau damping [70, 71].

Encouragingly, these quantities do not appear to depend too strongly on the temperature as long as one is close enough to $T = 0$: Accord-

ing to [72], the speed of sound is mostly constant at $T < 0.1T_F$, and according to [73], the pairing gap shows a wide plateau as long as $T < 0.5T^*$, which is usually fulfilled in the crossover as $T^* > T_{BKT}$. Therefore, one can be optimistic that dynamic structure factors measured in the BEC-BCS crossover will be in good approximation of the zero-temperature result at experimentally achievable temperatures, albeit the finite temperature will certainly lead to a thermal broadening of features which might complicate the interpretation of the measured spectra.

4.4.3 Measuring the dynamic structure factor

To measure the dynamic structure factor of a system, one needs a method of transferring a known energy and momentum to the system without changing the number of constituent particles. In solid state physics, this is commonly done by inelastic scattering of neutrons or X-ray photons, where a sample is illuminated with a beam of e.g. neutrons with a well-defined momentum and energy [74]. By measuring the angle and velocity with which the scattered neutrons leave the sample, the energy and momentum that were transferred to the system can be inferred, and one obtains the dynamic structure factor.

In cold atom experiments, the high level of control and access allow for a different approach: In Bragg spectroscopy, the system is allowed to undergo stimulated scattering processes at a well-defined momentum and energy. To do so, two laser beams are overlapped in the ultracold gas, such that the wavevector of their interference pattern is $q = |\vec{k}_1 - \vec{k}_2| \propto 1/\sin(\alpha)$, where $\vec{k}_1$ and $\vec{k}_2$ are the wave vectors of the two laser beams and α is the angle under which the beams intersect. The energy selectivity is obtained by detuning one of the two beams with respect to the other by ω. For an illustration of the process, see Fig. 4.14.

During Bragg spectroscopy, atoms can virtually absorb a photon from one beam and emit it into the other, which transfers momentum $\pm\hbar q$ and energy $\pm\hbar\omega$ to the system. The probability of this process to occur is then proportional to $S(q, \omega)$ as explained above. To measure the dynamic structure factor using Bragg spectroscopy, one therefore only has to detect the momentum transferred to the system, which is directly proportional to $S(q, \omega)$.

The most common approach to do so is to expose the system to the Bragg beams for a very short time and record the transferred momentum directly. This method has been used extensively and produced important results such as the velocity distribution in 3D BECs [75, 76] and Tan's contact and the pairing gap in 3D Fermi gases [69, 77]. Alternatively, it is possible to let the system equalize and record the transferred momentum by observing the resulting increase in temperature in the system. Using this method, the band structure in optical lattices was measured [78] and the transition from the Mott-insulating to the superfluid state in one-dimensional Bose gases was investigated

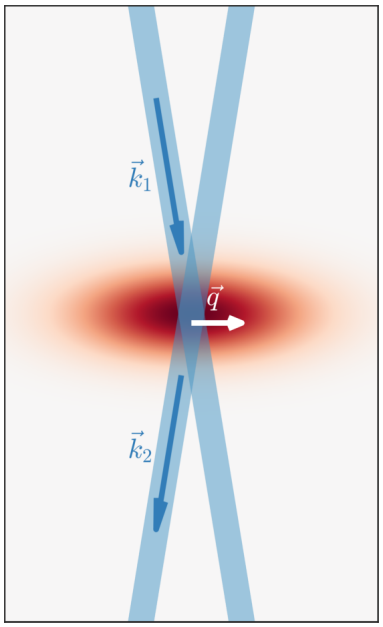

Figure 4.14: Sketch of Bragg scattering. Two laser beams (blue) interfere in the center of an atomic gas (red). In a stimulated process, a particle can virtually absorb a photon with wavevector $\vec{k}_1$ and energy $\hbar\omega_1$ from one beam and immediately emit it into the other beam with wavevector $\vec{k}_2$ and energy $\hbar\omega_2$. In the process, the particle absorbs momentum $\hbar\vec{q} = \hbar(\vec{k}_1 - \vec{k}_2)$ and energy $\hbar(\omega_1 - \omega_2)$. If no excitation at this combination of energy and momentum can be created, the stimulated process cannot occur.

It would also theoretically be possible to measure the number of photons scattered from one beam into the other, but the low amount of scattered photons makes this very challenging experimentally.

[79, 80]. Both methods have their advantages: While measuring the transferred momentum allows for some differentiation between different kinds of excitations created [69], the Bragg pulse has to be kept short, and a high signal to noise ratio is needed to detect small values of $S(q, \omega)$. Measuring the temperature after equilibration enables longer exposures of the system to the Bragg beams, which increases the signal while keeping the perturbation from the beams small. In this thesis, we make use of the second method, as is it more conveniently applied to low-density systems.

4.5 The length scale of interactions

In this section, we provide a brief overview over the parametrization of interactions in two-dimensional Fermi gases by discussing their relevant length scales. The aim here is not to provide a rigorous derivation of scattering physics, but rather a somewhat intuitive idea of how the different parameterizations are related. First, we will establish the concept of scattering lengths in three-dimensional systems and discuss how they are tuned using Feshbach resonances. Next, we will discuss how scattering is modified when confining a system into a two-dimensional geometry before discussing corrections due to the imperfect confinement. Finally, we will discuss the nature of the bound state and calculate its binding energy.

As we have seen so far, ultracold quantum gases are simple systems, consisting of a number of (nearly) identical particles and not much else. We generally assume (and hope) that they are closed systems, meaning that the particles do not interact with anything we do not explicitly want them to interact with. Therefore, there are only very few things that can contribute to the sometimes quite complicated many-body physics we want to study. To understand which effects matter for what type of system, let us consider their characteristic *length scales*.

There are three relevant scales which determine the physics of a quantum gas. Going from small to big, the first important scale is R_e, the characteristic radius of interparticle interactions. This is the length scale on which the bound states that occur in nature are decided. The second important scale is $k_F^{-1} \sim n^{\frac{1}{d}}$, with the Fermi wavevector k_F, density n and the dimensionality d, which is just the average interparticle separation. This is quite commonly the most important scale: In a quantum gas, this is the length scale of the thermal deBroglie wavelength λ_T and therefore the scale on which most of the quantum effects occurs. As we will see, it is also the length scale on which Fermi gases pair, and therefore of pretty much any of the interesting many-body effects, and in our system also the scale of the two-dimensional confinement. Since the systems we consider are *dilute*, k_F^{-1} is much larger than R_e, and this separation of length scales means that we do not have to concern ourselves with the details of short-range physics when discussing phenomena that occur on the scale of k_F^{-1}. The final length scale is $L = \Omega^{\frac{1}{d}}$, the size of the system. This length scale is not too important for the purpose of this thesis, but it is the scale on which

collective modes like the breathing or sloshing mode of a harmonically trapped system occur and on which sound waves are reflected. In a many-body system, L will again be much larger than k_F^{-1}, which is why the shape of the trap volume generally does not enter into a system's many-body physics.

However, there is one length scale which we have not yet discussed: the characteristic length scale of interactions. This is because depending on the system, this length scale can fall in any of these categories, leading to fundamentally different regimes into which quantum gases can fall. This section discusses these different regimes and their characteristic length scales.

4.5.1 Scattering in 3D

This section mostly follows the discussion in [81]. *The reader might turn to* [82] *for a more in-depth derivation.*

First, we will introduce the concept of a *scattering length*, which will provide us with a first length scale for interactions that is then later modified by other effects. We will start by imagining two distinguishable particles colliding in the vacuum and neglect all effects that might occur on the length scale of R_e. In the center-of-mass frame, the incoming wavefunction is a plane wave $\Psi_{in} \sim e^{ikx}$, while the outgoing wavefunction is a spherical wave $\Psi_{out} \sim f(\theta, k)\frac{e^{ikr}}{r}$. The scattering amplitude $f(\theta, k)$ depends on the angle θ and the relative momentum k of the scattering particles and is directly related to the differential scattering cross section as $d\sigma/d\Omega = |f(\theta, k)|^2$. Now, the scattering wavefunction $\Psi = \Psi_{in} + \Psi_{out}$ can be expanded in the basis of Legendre polynomials $P_\ell(\cos\theta)$ as

$$f(\theta, k) = \frac{1}{2ik}\sum_{\ell=0}^{\infty}(2\ell+1)(e^{2i\delta_\ell(k)} - 1)P_\ell(\cos\theta)\,. \tag{4.71}$$

Here, $\delta_\ell(k)$ is the phase shift between the incoming and the scattered wave and contains all nontrivial information about the scattering process. In dilute, ultracold systems, all but the lowest partial wave can be neglected, and after integrating out the angular dependence we obtain the scattering amplitude

$$f_0(k) = \frac{1}{2ik}(e^{2i\delta_0(k)} - 1)\,. \tag{4.72}$$

The phase shift δ_0 is now expanded in a power series of k^2 and can be written as

$$k\cot(\delta_0(k)) = -\frac{1}{a_{3D}} + \frac{1}{2}r_e k^2 + \mathcal{O}(k^4)\,, \tag{4.73}$$

If the momentum dependence of the phase shift becomes important, the effective range provides the first correction term. However, it is only rarely necessary, and we will not further consider it in this thesis.

where we have defined the scattering length a_{3D} and the s-wave effective range r_e. In most systems, $r_e \approx R_e \ll k^{-1}$ and the series can be truncated after the first term, writing

$$a_{3D} = \lim_{k \ll 1/r_e}\left(-\frac{\tan\delta_0}{k}\right)\,. \tag{4.74}$$

The scattering length is then a single scalar quantity that describes all relevant details of the scattering between the two particles, and therefore fully quantifies their interactions. Finally, we insert this expression into the expression for the scattering amplitude above and integrate to obtain the cross section for s-wave scattering of distinguishable particles:

$$\sigma = \frac{4\pi a_{3D}^2}{1 + k^2 a_{3D}^2} \tag{4.75}$$

In most ultracold systems, $k a_{3D} \ll 1$ and the cross section is simply given by $\sigma = 4\pi a_{3D}^2$. In this case, a_{3D} is typically on the order of R_e, which is quite reasonable given that the interatomic interaction potential is the microscopic origin of the scattering length. However, as we will see below, it is also possible to increase a_{3D} to arbitrarily high values. When $k a_{3D} \gg 1$, the scattering cross section becomes independent of a_{3D} and is only limited by the relative momentum of the scattering particles as $\sigma = \frac{4\pi}{k^2}$.

When the two scattering particles are no longer distinguishable, the expression for the cross section is modified by the symmetry of the wavefunction, and one needs to calculate

$$\frac{d\sigma}{d\Omega} = |f(\theta, k) \pm f(\pi - \theta, k)|^2 , \tag{4.76}$$

where the plus sign refers to bosons and the minus sign refers to fermions. Due to the symmetry of the expansion in Legendre polynomials, the cross section is therefore twice as large for scattering between two bosons, but zero for scattering between fermions. Therefore, gases of indistinguishable (and therefore spin-polarized) fermions at ultracold temperatures are essentially non-interacting. To overcome this limitation, ultracold Fermi gases generally work with mixtures of two different spin states, such that scattering can still occur between fermions of different spin.

Note that case of indistinguishable particles discussed here therefore also implies that the spin-wavefunction is symmetrical, and therefore for fermions the spatial wavefunction needs to be antisymmetrical.

At this point, it is natural to ask how this scattering length a_{3D} is related to the coupling constant g we have used previously to quantify the interactions between particles. The relation between the two quantities becomes clear when considering a system of ultracold, dilute, distinguishable particles with mass m and density n. We will look at the wavefunction of a probing particle with momentum $\hbar k$ which moved a distance l through this system. In the far field, its wavefunction will be a superposition of all possible scattered waves, which results in a phase shift of the incoming wave of

$$\delta = -\frac{4\pi a_{3D} n l}{k} . \tag{4.77}$$

We can view this phase shift as the probing particle temporarily having changed its momentum while traversing the system. The change in momentum due to the surrounding gas is $\Delta k = \delta / l$, equivalent to a change in the kinetic energy of the particle of

$$\frac{\hbar^2 (k^2 - (k - \Delta k)^2)}{2m} \approx -\frac{4\pi \hbar^2 a_{3D} n}{m} . \tag{4.78}$$

We can now see that the gas the probing particle interacts with acts exactly like an additional potential the probing particle moves through. Therefore, the change in energy above is simply the mean-field energy gn we obtained in section 4.1, and

$$g = \frac{4\pi\hbar^2}{m} a_{3D} \,. \tag{4.79}$$

In weakly interacting systems, a_{3D} and g are therefore equivalent parameters to quantify the interaction strength.

4.5.2 Feshbach resonances

This section follows the discussion in [81]. [19] is recommended for more details on Feshbach resonances in ultracold gases.

As the scattering length a_{3D} that quantifies the interaction strength is usually on the same length scale as R_e and therefore much smaller than k_F^{-1}, most systems are quite weakly interacting. This can be very convenient for theoretical descriptions, as na_{3D}^3 becomes a small parameter and the effects of interactions can be treated perturbatively. However, if we wish to realize strongly correlated systems, we will have to increase the magnitude of a_{3D} such that it reaches the length scale of k_F^{-1}. To do so, we turn to Feshbach resonances.

To understand what a Feshbach resonance is, we first have to recall the shape of the interatomic interaction potential (see fig. 4.15). The van-der-Waals force between the particles leads to an attractive force at low distances, meaning that the potential is negative. Therefore, this potential is able to support bound states, in which the particles form a stable dimer. Usually, these bound states do not affect the scattering behavior, because spontaneous decay into one of these lower-lying states would require a three-body collision to conserve energy and momentum. For gases of fermions, this would require an s-wave collision between two atoms of the same spin, which is not possible due to Pauli-blocking. Even in bosonic quantum gases, such events are rare due to the diluteness, which results in a low probability to find three of the particles close to each other. Therefore, the scattering particles are not affected by the bound states, and remain free.

The situation changes drastically once the particles are put in the presence of an external magnetic field. In the high field regime, which is the only regime relevant in this thesis, the electron spin becomes polarized, and scattering between particles happens almost exclusively in a triplet configuration as the singlet state is energetically highly unfavorable. However, the singlet interatomic interaction potential still exists, it is merely shifted to higher energies. There is a stark difference between the singlet and triplet potentials, though: The energy of the singlet does not tune as the strength of the external magnetic field is increased. The triplet, on the other hand, tunes with $2\,\mu_B \approx h \cdot 2.8\,\mathrm{MHz/G}$, where μ_B is the Bohr magneton. Therefore, as the magnetic field strength is increased, the two interaction potentials are shifted with respect to each other.

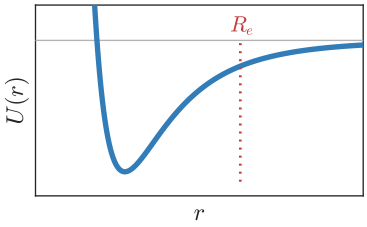

Figure 4.15: Sketch of the interatomic interaction potential. At very short distances, the particles repel each other due to the Coulomb force. At intermediate distances, the van-der-Waals force leads to a mutual attraction. Finally, at distances larger than the characteristic length R_e, the movement of the atoms is free.

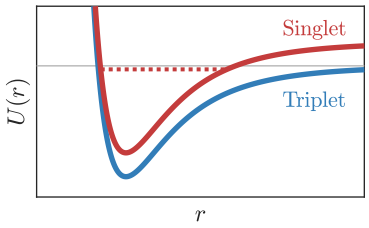

Figure 4.16: Triplet and Singlet interaction potentials. Because the singlet and triplet potentials react differently to magnetic fields, bound states of the singlet potential (dashed red line) can be brought into resonance with the continuum of the triplet potential (grey line). This phenomenon is called a Feshbach resonance.

It is interesting to note that both in the regime of weak and strong interactions, the parameterization of the interaction strength ultimately results in a parameter $\propto \sqrt{\sigma}$, where we remember that σ is the scattering cross-section.

Once the continuum of the triplet becomes degenerate with a bound state of the singlet, a Feshbach resonance occurs (see fig. 4.16). The triplet and singlet states begin to mix, and an avoided crossing occurs between the continuum and the bound state. One important consequence of this is that by preparing a system at a magnetic field above the Feshbach resonance and then slowly lowering the magnetic field strength, the previously free particles can be adiabatically converted into bound pairs. The second important consequence is that the coupling to the bound state modifies the scattering length. In the vicinity of the resonance, the scattering length is modified as

$$a_{3D} = a_{BG} + a_{BG}\frac{\Delta B}{B - B_0}\,, \tag{4.80}$$

where a_{BG} is the background scattering length far from the resonance and ΔB is the width of the resonance centered at B_0.

By tuning the magnetic field strength close to a Feshbach resonance, ultracold gases can therefore realize arbitrary scattering lengths. This is a remarkable feature: Increasing the scattering length to values on the order of or even above the interparticle spacing realizes a strongly correlated many-body state. However, as R_e is still much smaller than k_F^{-1}, the system remains dilute, resulting in a strongly interacting system with point-like interactions, a regime so far unique to ultracold atoms. In this regime, the strength of interactions can be quantified by comparing the scattering length to the interparticle spacing. As the scattering length diverges, a smooth parameterization can be obtained from its inverse, resulting in the parameter $-\frac{1}{k_F a_{3D}}$ commonly used in publications on ultracold Fermi gases.

We now see the connection between Feshbach resonances and the BEC-BCS crossover discussed in section 4.3: The further the magnetic field is increased above the resonance, the smaller a_{3D} and the weaker the interactions. There is no two-body bound state, and pairing would have to be a purely many-body effect - the system is in the BCS limit. Below the resonance, where the scattering length is positive, a bound state exists and the atoms form pairs. Their binding energy is simply given by

$$E_B = \frac{\hbar^2}{m a_{3D}^2}\,, \tag{4.81}$$

and the system approaches the BEC limit. In between those limits, the system smoothly interpolates between the BEC and the BCS limits, featuring aspects of both. In fact, at $B = B_0$, a very special case is realized: the unitary Fermi gas. As the scattering length diverges, the only length scale that remains to dictate the thermodynamic and many-body properties is k_F^{-1}, the average interparticle separation. The unitary Fermi gas is therefore a scale-invariant system with the strongest possible interactions.

In this thesis, the atoms in question will be fermionic Lithium-6 atoms, for which the background scattering length is only $a_{BG} = 45\,a_0$, close to the characteristic length scale of interparticle interactions $R_e = 31\,a_0$ [19]. The interatomic interaction potential features a total of 39

bound vibrational states, with the dissociation energy of the ground state at an impressive 12253 K [83]. The Feshbach resonance we will make use of is particularly broad due to the presence of a virtual bound state close to the triplet continuum: In a balanced spin mixture of the lowest two hyperfine states, $B_0 = 832.2\,G$ and $\Delta B = -262.3\,G$ [84]. This makes is straightforward to tune the scattering length a_{3D} over a wide range of values, as shown in Fig. 4.17. The virtual bound state also leads to a particularly high triplet background scattering length, leading to unusually strong interactions at magnetic fields above the Feshbach resonance. Finally, we note that at magnetic fields below the broad Feshbach resonance discussed above, there is a second, narrow resonance at $B_0 = 543\,G$ as well as a zero-crossing of the scattering length at $B = 527\,G$. However, these features as well as the scattering behavior at low magnetic fields are not relevant to this thesis and will not be discussed further.

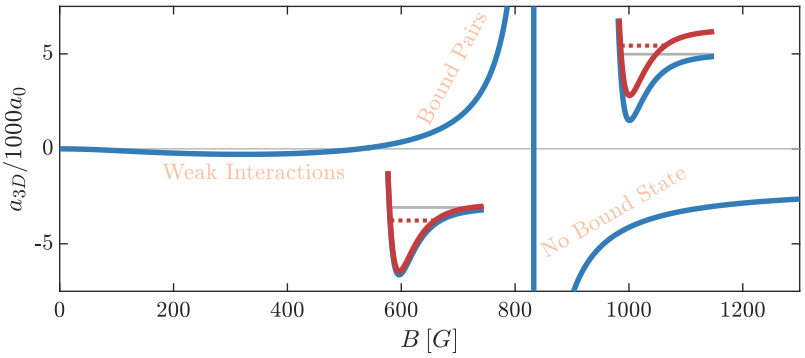

Figure 4.17: Feshbach resonances in Lithium-6. Scattering length in a mixture of the lowest two hyperfine states of Li_6 as a function of magnetic field, in units of the Bohr radius a_0. The scattering length a_{3D} is positive when there is a singlet bound state below the continuum of the triplet, and negative otherwise (see insets). The values of the scattering length are obtained from [84].

4.5.3 Scattering in 2D

Let us consider a system of fermionic particles that is tightly confined into a two-dimensional plane. While the confinement constrains the kinematics of the fermions, it also introduces a new length scale. As the bound states stem from the shape of the interatomic interaction potential, the size of which is still much smaller than any realistic size of the system in the axial direction, they will be unaffected by the confinement, and we therefore expect the Feshbach resonance to remain at the same magnetic field. However, the wavefunctions of the scattering particles will be significantly affected by the reduced dimensionality since the harmonic oscillator length in the axial direction l_z is close to the length scale of the interparticle spacing k_F^{-1}. Therefore, the parameterization of the scattering physics must take into account both the three-dimensional scattering behavior and the tight confinement.

Often, such systems are referred to as quasi-2D systems, while the term 2D is reserved for purely two-dimensional systems. However, as we will mostly talk about the realistic quasi-2D case, we will usually omit the *quasi-* and refer to purely 2D systems as *true 2D*.

In a true 2D system, the scattering amplitude is given as a function of the two-dimensional scattering length a_{2D} by

See for example [29, 30].

$$f_{true2D}(k, a_{2D}) = \frac{4\pi}{-\log(k^2 a_{2D}^2) + i\pi}\,. \tag{4.82}$$

The scattering length and scattering momentum therefore enter only

logarithmically into the scattering amplitude. In the experimentally relevant case of tight harmonic confinement in the axial direction, the scattering problem in quasi-2D was solved in 2001 by Petrov and Shlyapnikov [85]. They showed how the scattering amplitude is related to the three-dimensional scattering length and the confinement by

$$f_{2D}(k) = \frac{4\pi}{\sqrt{2\pi}\frac{l_z}{a_{3D}} + w(\frac{k^2 l_z^2}{2})}\,, \tag{4.83}$$

where $w(x)$ is a function that describes the momentum-dependent contributions to the scattering amplitude:

The notation $-i0$ denotes an infinitesimal imaginary contribution which is required due to the pole at $x = j$.

$$w(x) = \lim_{J\to\infty}\left\{\sqrt{\frac{4J}{\pi}}\log\left(\frac{J}{e^2}\right) - \sum_{j=0}^{J}\frac{(2j-1)!!}{(2j)!!}\log(j - x - i0)\right\} \tag{4.84}$$

One can now obtain a_{2D} by requiring that

$$f_{true2D}(k, a_{2D}) = f_{2D}(k)\,. \tag{4.85}$$

To solve this equation, we write the function $w(x)$ as

$$w(x) \equiv w_{lim}(x) + \Delta w(x) \qquad \text{with}$$

$$w_{lim}(x) = -\log\left(\frac{2\pi x}{A}\right) + i\pi\,, \tag{4.86}$$

where $A \simeq 0.905$. w_{lim} therefore approximates $w(x)$ at small values of x and the filling correction Δw is the error of this approximation, which becomes relevant for larger momenta. Therefore,

$$\begin{aligned} f_{true2D}(k, a_{2D}) &= \frac{4\pi}{-\log(k^2 a_{2D}^2) + i\pi} \\ &= \frac{4\pi}{\sqrt{2\pi}\frac{l_z}{a_{3D}} - \log\left(\frac{\pi k^2 l_z^2}{A}\right) + \Delta w + i\pi} \end{aligned} \tag{4.87}$$

In the zero momentum limit $w_{lim} \gg \Delta w \approx 0$ and we arrive at

$$a_{2D,k\to 0} = l_z\sqrt{\frac{\pi}{A}}e^{-\sqrt{\frac{\pi}{2}}\frac{l_z}{a_{3D}}}\,. \tag{4.88}$$

However, experiments are usually not performed in the zero momentum limit, as the experimentally achievable values of l_z are limited. Therefore, the scattering length cannot be evaluated using the simple limiting behavior of $w_{lim}(x)$, and the filling correction Δw has to be evaluated. The simplest correction to the scattering length can be obtained by evaluating the w-function at a characteristic momentum $k = k_0$ instead of $k = 0$, obtaining once again a single parameter a_{2D} that describes the scattering behavior of the system. This correction does not fully capture the momentum-dependence, but extends the validity of the parametrization using a single scattering length to higher momenta. In a many-body system, this characteristic momentum k_0 is generally given by the chemical potential μ, and we write

Note that the majority of publications in 2D Fermi gases still omit the Δw correction even though it would result in a significant shift in the interaction parameter used, often of comparable magnitude to the size of the features reported (see e.g. [86, 87]).

$$\hbar k_0 = \sqrt{2m\mu} \quad \text{and}$$

$$\frac{k_0^2 l_z^2}{2} = \frac{\mu}{\hbar\omega_z}\,, \tag{4.89}$$

where $\hbar\omega_z$ is the harmonic oscillator spacing in the axial direction. The corrected scattering length can then be written as

$$a_{2D} = a_{2D,k\to 0} e^{-\frac{1}{2}\Delta w\left(\frac{\mu}{\hbar\omega_z}\right)} . \tag{4.90}$$

Box 4.6: Parameterizing scattering with an effective range

There is an alternative approach to take into account the finite momentum correction, which introduces an effective range of interactions R_s in the definition of the true 2D scattering amplitude, similar to eq. 4.73. This approach is discussed in detail in [62]. In essence, the scattering amplitude is modified to read

$$f_{true2D}(k, a_{2D}, R_s) = \frac{4\pi}{-\log(k^2 a_{2D}^2) + R_s k^2 + i\pi} . \tag{4.91}$$

In a true 2D system, $R_s = 0$, and eq. 4.82 is recovered. However, when solving eq. 4.85, the effective range absorbs the momentum dependence of the scattering amplitude, and the scattering physics of the system can be well described without evaluation a characteristic momentum, at the cost of having to parametrize the system by a set of two parameters. In this thesis, we will nevertheless use eq. 4.90, as it is the standard in experimental publications.

An interesting consequence of the interplay of 2D and 3D scales can be seen when considering the bound state in two-dimensional systems. The 2D scattering length a_{2D} we have derived above must by definition always be positive. Therefore, we can always calculate a nonzero binding energy from the scattering length:

$$E_{B,2D} = \frac{\hbar^2}{m a_{2D}^2} \tag{4.92}$$

This is a natural consequence of the fact that an attractive potential must always feature a bound state in two dimensions, and in stark contrast to the three-dimensional case, where a bound state is only present on one side of the Feshbach resonance. However, eq. 4.92 is only valid in a true 2D system. In a quasi-2D geometry, the binding energy has to interpolate between two very different cases: Where a_{3D} is small and negative, no bound state exists in 3D, and the binding energy obtained with eq. 4.92 will describe the bound state well, as it is a purely 2D phenomenon. However, for small positive a_{3D}, one would expect the atoms to form very tightly bound pairs already from three-dimensional scattering physics. As the size of these pairs will be small compared to l_z, the confinement should no longer modify this bound state, and the binding energy should purely be the three-dimensional one. The correct interpolation between these limits is shown in [29]. To obtain the binding energy, one needs to solve the transcendental equation

$$\frac{l_z}{a_{3D}} = \int_0^\infty \frac{du}{\sqrt{4\pi u^3}} \left(1 - \frac{e^{\frac{-E_B u}{\hbar\omega_z}}}{\sqrt{\frac{1}{2u}\left(1 - e^{-2u}\right)}} \right) . \tag{4.93}$$

The resulting values of E_B are plotted together with the limiting cases in true 2D and 3D in Fig. 4.18.

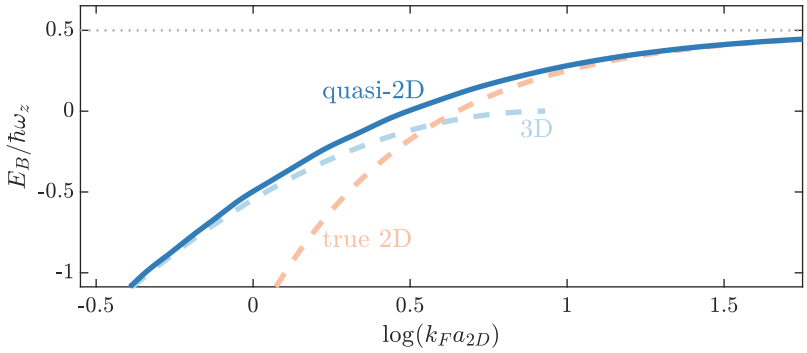

Figure 4.18: Binding energy in 2D. Plotted in solid blue is the binding energy as a function of the interaction parameter. For comparison, the dashed lines show the binding energies computed from a_{2D} (orange) and a_{3D} (light blue). The two-dimensional binding energies (blue) have been shifted by $\frac{\hbar\omega_z}{2}$ to account for the ground state energy of the confining harmonic oscillator. Figure adapted from [43].

We point out that in true 2D, eq. 4.92 shows that an alternative parameterization of interactions can be obtained by $\log(E_B/E_F)$ (or just E_B/E_F), where instead of comparing length scales, the energy of the two-body bound state is compared to the energy associated with the interparticle separation. However, as the two-body binding energy is modified by the confinement in quasi-2D, this parameterization is generally not recommended, although it is still commonly used in theoretical works.

A good parameterization of interactions in the vicinity of a Feshbach resonance for a two-dimensional system must once again stem from comparing the length scale of scattering (and therefore interactions) to the length scale of interparticle separation k_F^{-1}. However, as we have seen, a_{2D} does not feature a singularity at the Feshbach resonance: The presence of an additional length scale in l_z leads to a smooth evolution of a_{2D} as the resonance is crossed. Therefore, the interaction parameter does not need to be defined using the inverse of the scattering length $-\frac{1}{k_F a_{2D}}$ as in the three-dimensional case. Instead, one notes that the scattering amplitude depends logarithmically on the scattering length as shown in eq. 4.82 and arrives at $\log(k_F a_{2D})$ as a good parameterization of interactions in the 2D BEC-BCS crossover.

We note that some authors (see e.g. [30]) use a slightly modified expression of the scattering length $a_{2D'} = a_{2D}\frac{2}{e^{\gamma_E}}$ where $\gamma_E \approx 0.577$, leading to a small shift in the interaction parameter (see below) of $\Delta\log(k_F a_{2D}) \approx 0.05$.

Fig. 4.19 shows the correction to the interaction parameter due to the finite scattering momentum. When the Fermi energy becomes comparable to the harmonic oscillator spacing, the filling correction becomes relevant, shifting the interaction parameter $\log(k_F a_{2D})$ by the plotted value. While experiments are generally performed at as low values for $E_F/\hbar\omega_z$ as are realistically achievable, corrections of up to $-0.5\,\Delta w \sim 0.5$ are often unavoidable when working in the BCS regime due to the high chemical potential.

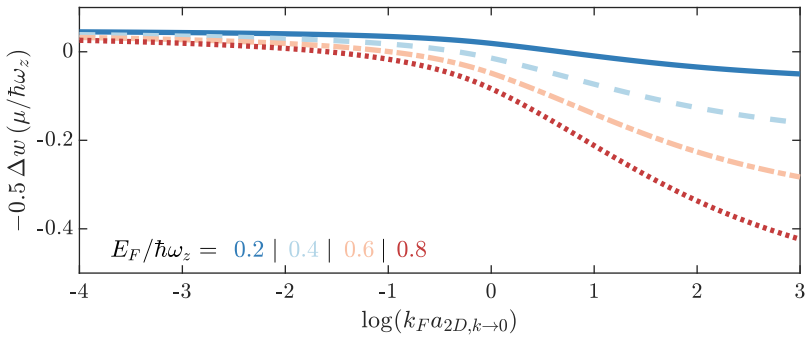

Figure 4.19: Magnitude of the filling correction Δw. Plotted is the difference between the interaction parameter $\log(k_F a_{2D})$ with filling correction and without for different ratios of $E_F/\hbar\omega_z$. The larger the Fermi energy is compared to the harmonic oscillator spacing, the more the momentum dependence of scattering modifies the scattering properties. This effect becomes significant as the chemical potential increases towards the BCS side of the crossover.

Finally, we take a moment to point out that the entire discussion above is essentially the result of the introduction of a third length

scale by the confinement. This not only fundamentally shakes up the scattering physics of the system, it also has another interesting consequence: In two-dimensional Fermi gases, there cannot be a unitary point, as even on the Feshbach resonance, there is always another length scale that the interparticle separation can be compared with. Therefore, the scale invariance of the unitary 3D Fermi gas is not found in 2D Fermi gases. However, interestingly, the 2D Fermi gas is already expected to be scale invariant due to a symmetry of its classical Hamiltonian, and in fact this scale invariance only gets broken in close vicinity of the Feshbach resonance in a so-called quantum anomaly [86, 88, 89].

5 STATE OF THE FIELD

This chapter is intended to give a short summary of the current state of experiments on 2D Fermi gases. I will discuss the historic development of the different trapping setups that were used to study these systems and discuss their advantages and disadvantages. While explaining the different ways by which measurements are made and what kind of information they yield, I will give a short overview over the most relevant results obtained in 2D Fermi gases so far.

5.1 Trapping geometries

To create a two-dimensional Fermi gas, the most important ingredient must be the confinement that brings the system into the kinematic 2D regime. This confinement needs to be strong enough such that all motion in the confined direction is frozen out. This is not exactly trivial: To be able to create degenerate Fermi gases, the density per spin state needs to be on the order of $n \sim 1\,\mu m^{-2}$ at experimentally achievable temperatures. However, the Fermi energy of a system with such a density is on the order of $h \cdot 10\,kHz$, requiring a confining potential where the first excited state is also at the least around $h \cdot 10\,kHz$ above the ground state. This requires tightly focused traps and a significant amount of laser power.

The first realizations of such deep confining potentials made use of a retro-reflected red-detuned laser beam, creating deep optical traps that provided harmonic confinement along all directions, with high trap frequencies in the axial direction [24–26, 90] (see e.g. fig. 5.1 A). The advantage of this approach is that it allows one to use widely available CO_2 or Nd:YAG lasers to create the tight confinement. However, unless significant effort is made to manipulate the geometry of the system before loading into the confining potential, many layers of the trap will be populated at once. As a consequence, measurements along the axial direction will average together many different systems with different densities and complicate both the interpretation of data and control over the density distribution.

Soon, optical lattices created by interfering two beams under a shallow angle became common. The highest flexibility here is achieved by making the angle between the two beams adjustable [91], but high trap frequencies can be reached also with a fixed angle while maintaining enough separation between the maxima to be able to load a single layer with negligible population of the surrounding ones [28] (see fig. 5.1 B). Since the curvature of the magnetic offset field can be used to provide the harmonic confinement along the radial direction, the confining lattice can also be created from blue-detuned light, resulting in less radial confinement [20]. As an alternative to optical

lattices, it is furthermore possible to achieve a single layer, harmonically trapped 2D Fermi gas by using a blue-detuned TEM_{01}-mode [92] (see fig. 5.1 C).

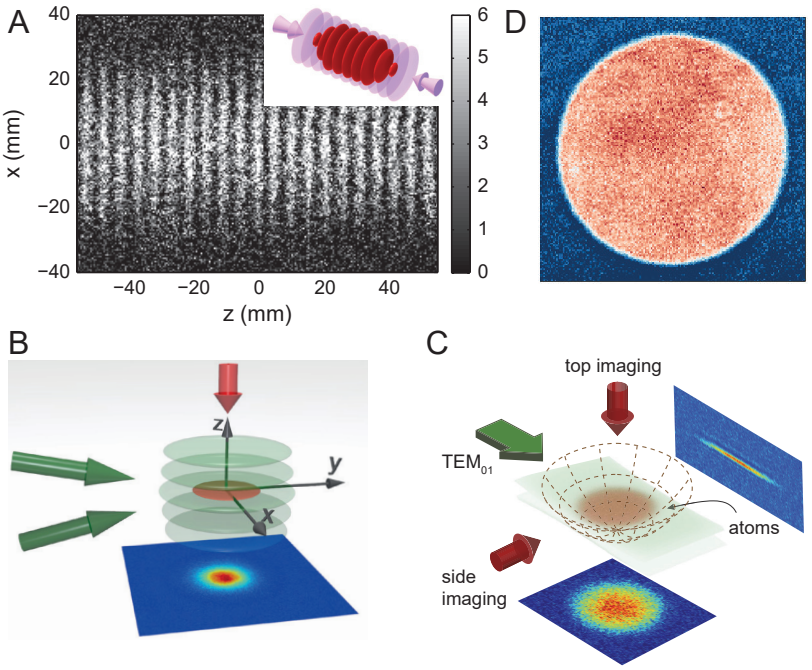

Figure 5.1: Overview over different trapping geometries. **A**: The first realization of 2D Fermi gases features many layers prepared in a red-detuned optical lattice. Shown is the density distribution, integrated along one direction perpendicular to the lattice, with the many layers clearly visible. Figure adapted from [24]. **B**: Schematic showing a 2D Fermi gas (red) trapped in a single node of a red-detuned optical lattice (green). By populating only a single layer, the integrated column density measured (image on the bottom) corresponds directly to the density of the system. Figure adapted from [28]. **C**: Schematic showing a 2D Fermi gas confined in a blue-detuned TEM_{01}-mode, demonstrating how a higher Hermite-Gaussian mode can be used instead of an optical lattice. Figure adapted from [93]. **D**: Density distribution of a homogeneous 2D Fermi gas. Here, the radial confinement is provided by a sharp blue-detuned wall instead of the curvature of the magnetic field or a red-detuned dipole trap. Figure adapted from [46].

However, the harmonic confinement in the radial direction will always result in an inhomogeneous density distribution, with a cold, high density region in the center of the trap and hot, thermal low-density regions in the regions of higher potential. This is not always an issue, and can even be desirable in measurements where data at many different densities is required. However, when measuring non-local quantities such as the momentum distribution, the inhomogeneous density distribution complicates the interpretation of the results, as it will inevitably average together the different regions in the trap. To address this problem, we combined the low radial trapping frequencies achievable with blue-detuned confining lattices with beam shaping using axicons or spatial light modulators [20]. This results in homogeneous density distributions in arbitrary geometries in the radial direction, while the axial direction is still frozen out by the confining lattice (see fig. 5.1 D).

5.2 Measurement tools

Generally, measurements on two-dimensional Fermi gases are performed by taking an absorption image of the density distribution of the system. However, there are different manipulation techniques that can be used prior to imaging to modify the information that can be obtained from the resulting images. In the following, we will discuss the most common techniques and highlight important results.

In the early years, the measured density distributions were complicated to interpret due to the averaging of multiple layers as explained above. As a consequence, most measurements were performed using radio-frequency (RF) spectroscopy, where the pseudospin of atoms resonant with a RF pulse is changed to an undetected third state. By recording the apparent atom loss, the fraction of atoms resonant with the energy of the RF photons can be inferred. Over the years, such measurements were used to study the evolution of the two-body bound state as a function of the interaction strength [25, 94] and in the crossover from 3D to 2D [26]. By studying the line shape of the RF spectrum, polaron physics were investigated the strongly interacting regime [90], and measurements above the critical temperature for superfluidity were performed to search for a Fermi gas equivalent of the pseudogap phase originally described in cuprate superconductors [87, 95].

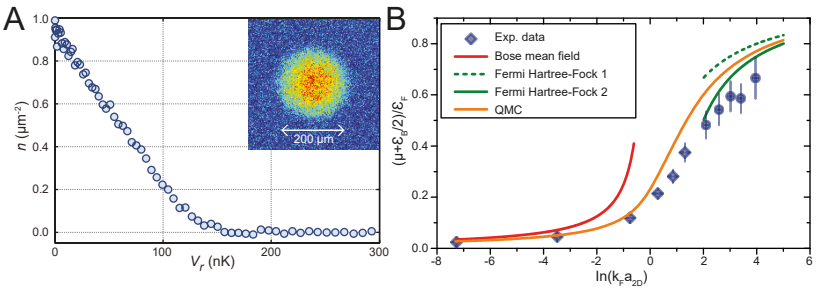

Figure 5.2: Equation of state obtained from the in-situ density distribution A: The density distribution of a harmonically trapped 2D Fermi gas (inset), plotted as a function of the potential energy, can be used to extract the density equation of state. Figure adapted from [93]. **B**: Reduced chemical potential $\tilde{\mu} = \mu + E_B/2$ as a function of interaction strength, compared with theoretical predictions. $\tilde{\mu}$ increases from values close to 0 in the BEC limit to E_F in the BCS limit. Figure adapted from [96].

However, the unperturbed density distribution itself already contains valuable information about the equation of state of the system. Especially once single-layer systems were available, precision measurements of the local density as a function of the trapping potential were used to map out the thermodynamic properties of the system (see fig. 5.2). Such measurements were used to determine the pressure [97] and the density equation of state [93, 96] and revealed the presence of a spin-balanced core in spin-imbalanced systems above a critical polarization [27, 91].

Another scheme to obtain a different set of information from the system is to record the density distribution after switching off most trapping potentials and waiting for a set amount of time. If the only remaining trapping potential is the harmonic trap in the radial direction and the expansion time is chosen to be a quarter of its trapping period, such a scheme performs a rotation in phase-space that allows for a measurement of the momentum distribution of the system [98]. Such measurements of the momentum distribution were used to show the presence of a pair condensate in spin-balanced [28] and spin-imbalanced [91] systems. Furthermore, from the Fourier transform of the momentum distribution, the spatial coherence properties can be inferred and compared to predictions from BKT theory [86, 99] (see fig. 5.3).

It is also possible to observe the behavior of a system after a sudden change in the trapping potential, for example by measuring the width

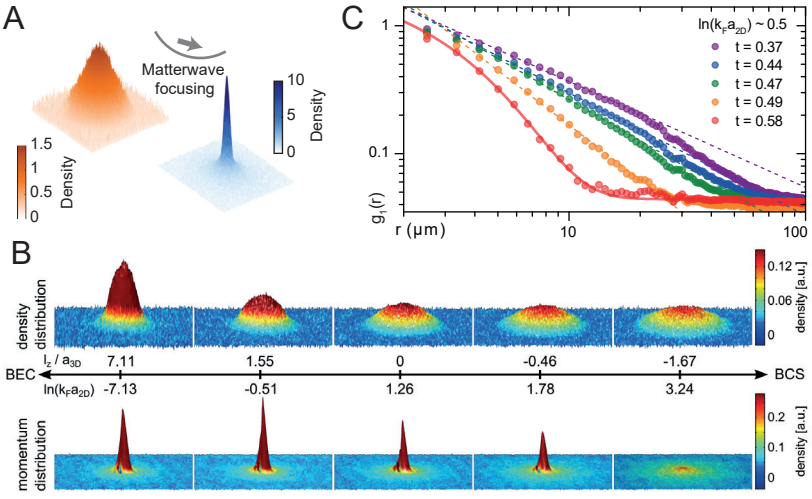

Figure 5.3: Observing pair condensation and coherence properties in the momentum distribution A: Schematic of matter wave focusing, adapted from [86]. A harmonic confinement is used for a rotation in phase space that allows for measurements of the momentum distribution, here shown for a system in the BEC limit. **B**: Experimental evidence for pair condensation in 2D Fermi gases, obtained by rapidly ramping the system into the BEC regime while matter wave focusing is performed. The macroscopic occupation of low momentum modes indicates the presence of a pair condensate. Figure adapted from [28]. **C**: Experimental evidence for algebraically decaying correlations in a 2D Fermi gas, adapted from [99]. The first-order correlation function $g_1(r)$, obtained by Fourier-transforming the momentum distribution, is plotted for different reduced temperatures $t = T/T_{BEC,0}$, where $T_{BEC,0}$ is the condensation temperature of an ideal 2D Bose gas. For cold temperatures, algebraically decaying correlations are observed.

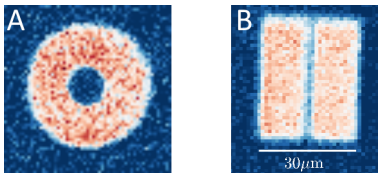

Figure 5.4: Creating custom potentials using spatial light modulators. A: Homogeneous Fermi gas with a potential step in the center used to measure the density equation of state, adapted from [20]. **B**: Homogeneous Fermi gas with a narrow potential barrier used to observe Josephson oscillations, adapted from [39].

and center-of-mass of the cloud in response to the change. Such measurements have been used to study whether the kinematics of the system are truly two-dimensional [92] and have investigated the broken scale invariance in the crossover [88, 89].

Finally, recent measurements have started to employ spatial light modulators to manipulate the system prior to measuring. The ability to freely manipulate the trapping potential can not only be used in a static fashion to probe the response of the system to a well-defined potential. The potential can also be switched on faster than the timescales of the system. As the density distribution cannot follow the change of potential this fast, the phase of the wavefunction is modified instead, allowing for the imprinting of phase differences that then evolve into custom-designed dynamics. Using such methods enabled us to perform measurements of the equation of state in homogeneous systems [20] and to observe Josephson oscillations across a narrow potential barrier [39] as well as perform quantitative measurements of sound waves [40].

6 THE EXPERIMENTAL APPARATUS

In this chapter, I will describe the experimental sequence, following one complete path of the atoms through the apparatus. Upgrading and maintaining the experimental setup has been one of the core components of my work over the last years. However, as the setup is already well-documented by the previous PhD students, I will limit myself here to a general overview. The interested reader may find a detailed description of the apparatus including the initial design and commissioning in [100, 101], with some more recent improvements described in [46, 102]. Especially the PhD thesis of Niclas Luick [43] documents in detail the improvements we made over the last years. More information on the techniques employed can be found in [103] or [104].

In our quantum gas apparatus, fermionic ^{6}Li atoms are cooled to degeneracy. ^{6}Li is one of the only two reasonably radioactively stable fermionic isotopes of alkali atoms, which are strong candidates for ultracold atom experiments due to their simple, hydrogen-like electronic structure, the other one being ^{40}K. It features a broad Feshbach resonance (see section 4.5.2), and lasers with wavelengths resonant to the D_2 transition from the $2S_{\frac{1}{2}}$ to the $2P_{\frac{3}{2}}$ electronic states at $\lambda = 671\,\mathrm{nm}$ are commonly available. As collisions with room-temperature atoms make cooling to the nanokelvin temperatures we require impossible, the entire cycle must occur in an ultrahigh vacuum environment, with any manipulation of the atoms occurring through electromagnetic fields. In our apparatus, a combination of ion-getter pumps and titanium sublimation getter pumps maintains a vacuum pressure of roughly $1.5 \cdot 10^{-11}$ mbar, low enough that the characteristic time in which an individual atom collides with a non-^{6}Li particle is on the order of minutes and therefore much longer than our experimental cycle of $\sim 15\,\mathrm{s}$. To manipulate the atoms, a combination of magnetic fields, resonant and non-resonant laser light, and radio-frequency photons is used. In the following, we will discuss the different steps that are performed as the fermionic atoms travel through the experimental apparatus, from the oven chamber to the science cell.

From Kelvin to millikelvin

The path of the atoms begins in a pool of ^{6}Li in the oven chamber. The oven is a cylindric steel container that was filled with unoxidized ^{6}Li before being mounted to the vacuum chamber. As the vapor pressure of ^{6}Li at room temperature is negligible, the oven chamber is heated to $710\,\mathrm{K}$ ($440^\circ\mathrm{C}$) to achieve a vapor pressure of $p \approx 2.5 \cdot 10^{-4}\,\mathrm{mbar}$ [105]. At some point, the hot atoms leave the oven chamber through a series of apertures leading to a decreasing-field Zeeman slower, in which a counter-propagating resonant laser beam scatters photons off the atoms, reducing their overall velocity from $\sim 1000\,\frac{\mathrm{m}}{\mathrm{s}}$ to $\sim 50\,\frac{\mathrm{m}}{\mathrm{s}}$. To compensate for the considerable Doppler-shift due to the velocity of

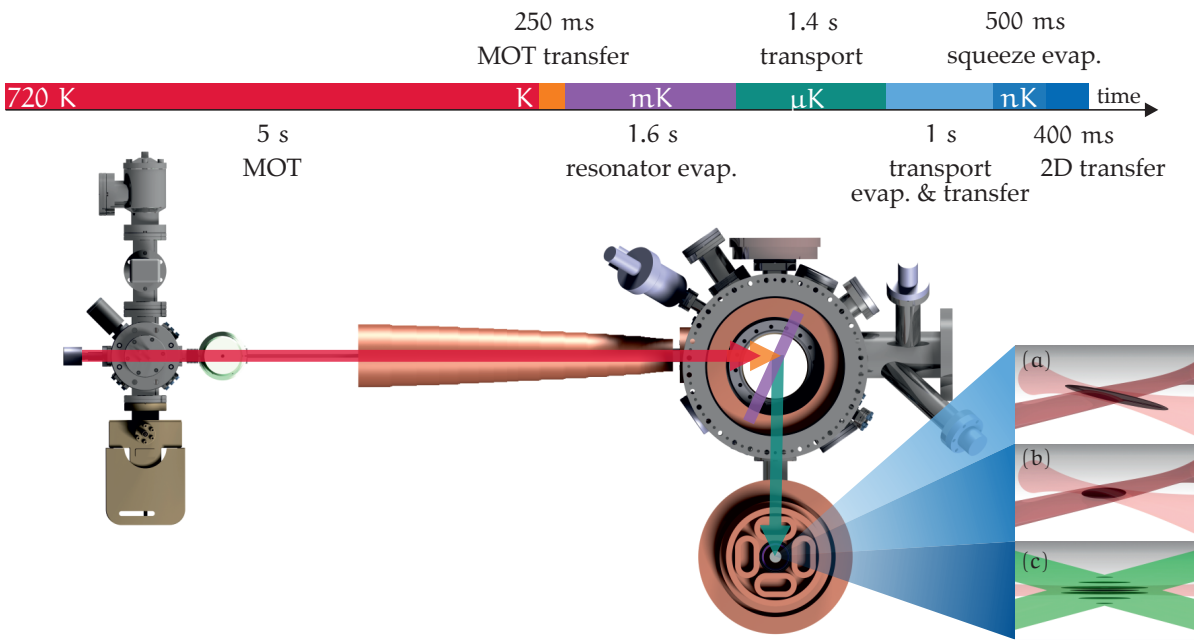

Figure 6.1: Overview of the experimental cycle to create an ultracold 2D Fermi gas. Fermionic ^{6}Li atoms are ejected from the oven, decelerated in a Zeeman slower (**red arrow**) and captured in a MOT. After loading the MOT for about 5 s, we shift the MOT (**orange arrow**) to transfer atoms to a deep optical dipole trap created by the standing wave of two counter-propagating far detuned beams inside a high-finesse cavity (**purple**). After evaporative cooling in this resonator, the gas is transported to the resonator focus position and loaded into an elongated dipole trap which is focused to the resonator waist. By moving the focus position (**green arrow**) of the elongated dipole trap, the gas is transported to the science chamber, where we apply a magnetic offset field close to the Feshbach resonance to perform efficient evaporative cooling. Finally, we create a two-dimensional system by squeezing the gas in a highly elliptical dipole trap (**a,b**) and transferring the gas into a single layer of a repulsive 1D optical lattice (**c**). Figure and caption adapted from [101].

During my PhD, we invested a significant amount of time in improving the stability of the resonator setup as recently described in [43]. We redid the entire beam path and fiber-coupled both beams to increase the passive stability of the setup. Significant upgrades to the lock setup, such as a feed-forward compensation that keeps the amount of light on the lock photodiode constant as well as optical isolation of the lock beam path improved the stability of the resonator to the point where it can be relied on to lock automatically within the first second of the MOT phase in virtually any run. In fact, in the beginning of 2020, the apparatus ran uninterrupted for three months straight, during which the resonator did not require human attention a single time. This significant improvement to the stability has been instrumental for allowing measurements of large datasets like the ones shown in this thesis.

the atoms, a decreasing magnetic field is used. The resulting Zeeman-shift brings the initially fast atoms into resonance with the laser beam, and keeps them at resonance as both the velocity and the strength of the magnetic field decrease. When the atoms reach the exit aperture of the Zeeman slower, they have scattered approximately 14000 photons, bringing their temperature all the way from 710 K to approximately 1 K. As the atoms enter the main chamber of the vacuum system, they are captured in a magneto-optical trap (MOT), consisting of a spatially varying magnetic field with a gradient of $\approx$ 17 G/cm and six resonant laser beams that act similarly to the Zeeman slower, but from all directions. Confined in the MOT, the atoms are cooled down to a temperature on the order of the Doppler temperature of about 1 mK, set by the finite linewidth of the D_2 transition of $\Gamma = 6$ MHz.

From millikelvin to microkelvin

Once approximately 10^8 atoms are trapped in the MOT, we switch on a resonator enhanced dipole trap (REDT). This trap consists of

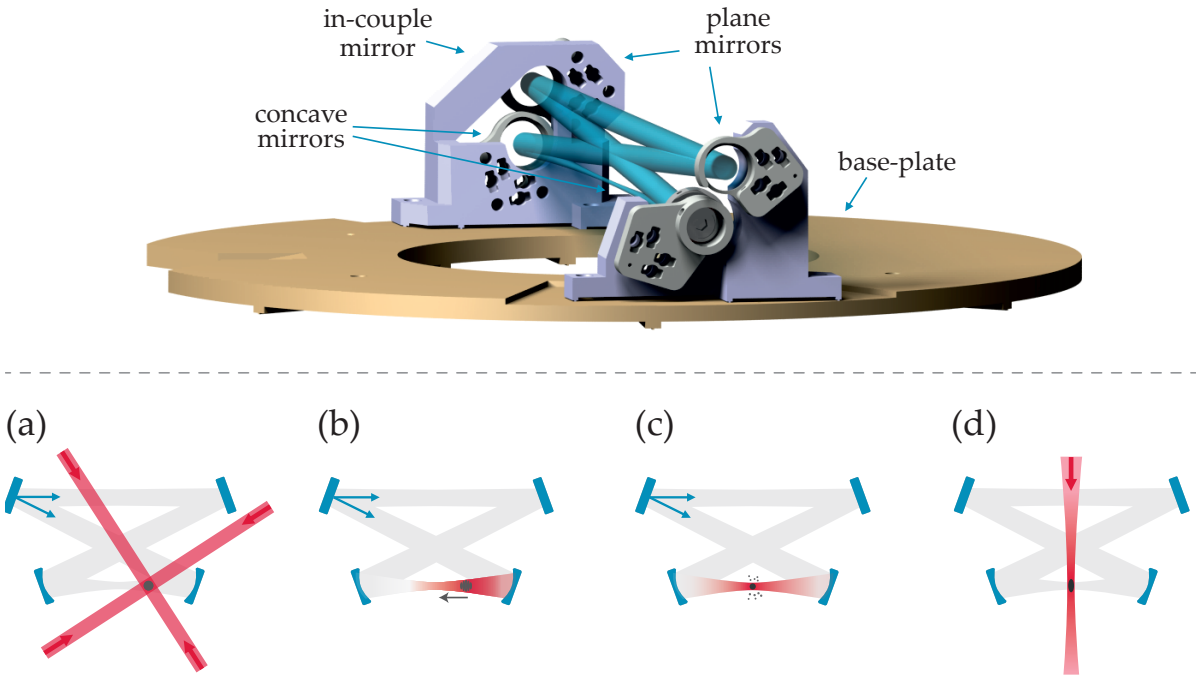

Figure 6.2: The cooling resonator. (**top panel**) CAD model of the bow-tie resonator. (**bottom panel**) Schematic of the loading scheme. (**a**) We load atoms from the MOT (red beams) into the standing wave of the resonator (grey) by shifting the MOT to a position about 3cm from the focal plane of the TEM_{00} mode, where the increased radial waist of about 200−300 µm ensures a high transfer efficiency. (**b**) We detune the secondary beam by a fixed frequency offset of 200 kHz, which moves the standing wave at a velocity of $2\,\frac{\text{cm}}{\text{s}}$ and transports the atoms within 137.5 ms to the focus of the bow-tie resonator. (**c**) We switch off the secondary beam completely and evaporatively cool the gas in this running wave trap at a magnetic offset field of 300 G by ramping down the power of the primary beam by a factor of 100. (**d**) At the end of this evaporation, the atoms are trapped inside the elongated dipole trap (red beam) and transported to the science chamber. Figure and caption adapted from [43, 101].

two counterpropagating $\lambda = 1064\,\text{nm}$ beams with a laser power of $P \approx 1\,\text{W}$ which are coupled into a bow-tie resonator with a finesse of ≈ 10000, realizing a deep optical standing-wave potential without requiring excessive laser power (see fig. 6.2). The MOT beams, initially detuned by $4\,\Gamma$, are then brought closer to resonance, compressing the trap to transfer as many atoms as possible into the REDT at a position 3 cm away from the focus position of the bow-tie geometry. Once the atoms have been transferred, the magnetic field is switched from the quadropole field required for the MOT to a homogeneous offset field used to manipulate the scattering length of the atoms. At a magnetic field of $B = 300\,\text{G}$, the scattering length of $a_{3D} \approx -280\,a_0$ is large enough to enable reasonably fast thermalization. The frequency of one of the REDT-beams is then detuned by 200 kHz, which causes the standing-wave potential to move towards the focus of the bow-tie geometry, moving and compressing the atoms (see fig. 6.3). Once the atoms reach the focus position of the resonator, forced evaporation is performed, first reducing the power in both beams and then in a running wave trap after one of the beams has been switched off.

In the focus position located in the center of the chamber, the minimum beam waists of the bow-tie resonator are $(17.5 \times 30)\,\mu\text{m}$.

The capability to move the atoms into the focus position of the resonator was another one of the important improvements to the functionality of the REDT we implemented over the last years.

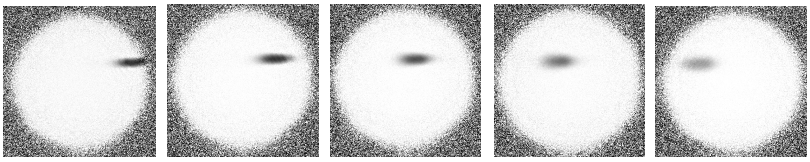

Figure 6.3: Transport inside the REDT. By detuning one of the beams that form the REDT, the standing wave pattern starts to move, and the atom cloud is transported into the focus position. The compression of the trap during movement heats the cloud, causing the waist of the cloud after time of flight to increase. However, this heating is acceptable because of the more efficient evaporation and loading in the focus position. Figure adapted from [43].

Finally, the atoms are loaded from the REDT into an elongated dipole trap (EDT) created by focusing a single $\lambda = 1064\,\mathrm{nm}$ beam with $P \approx 4\,W$ onto the REDT focus position. The EDT has a depth of a few $100\,\mu K$, a tight focus with beam waists of $(25 \times 25)\,\mu m$ and captures nearly all of the $\sim 2 \cdot 10^6$ atoms remaining in the evaporated resonator. After performing another evaporation step, the focus position of the EDT is moved from the REDT center position through a vacuum tube into the science cell using a translation state over $1.4\,s$.

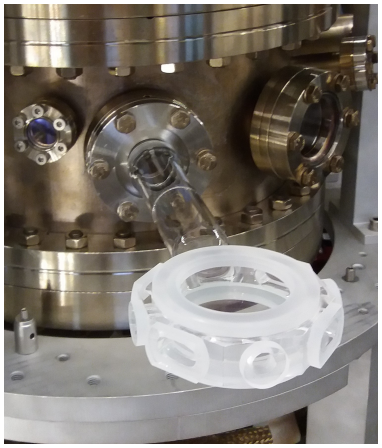

Figure 6.4: The new glass science cell. One of the largest upgrades to the apparatus during my PhD was performed by switching from a steel science cell to a glass cell. This increased the vacuum-limited lifetime in the science cell from 8 s to 120 s, eliminating the large heating rates we had previously struggled with.

Figure 6.5: The old steel science cell.

From microkelvin to nanokelvin

The science cell is a thin glass cell situated between stacks of magnetic field coils and two high-resolution microscope objectives. After the atoms are transported into the cell, the current in the coils is switched on, creating a magnetic offset field of $B = 824\,G$, close to the Feshbach resonance. At these fields, the atoms collide rapidly, enabling thermalization within a few milliseconds.

Before further evaporation, the atoms are subjected to a $200\,ms$ radio-frequency pulse resonant to the transition between the two lowest hyperfine states of ^6Li at $\nu \approx 78\,MHz$. The pulse is long enough so that the atoms decohere, creating a balanced mixture of the two pseudospin states. This balanced mixture is then evaporated further. While this evaporation can be used to obtain a cigar-shaped degenerate Fermi gas, its geometry is not well suited for the transfer into the tight harmonic confinement used to reach the 2D regime. Therefore, the atoms are transferred into a highly elliptic dipole trap (HEDT) with a laser power of $P \approx 0.8\,W$ and an aspect ratio of 40:1:1, corresponding to beam waists of $(8 \times 320 \times 320)\,\mu m$. Here, another evaporation step is performed during which a magnetic gradient is applied along the z-direction and the magnetic offset field is lowered to $B = 730\,G$, resulting in an almost pure BEC of around 3000-30000 atoms at a temperature of a few ten nanokelvins.

From 3D to 2D

To create homogeneous 2D Fermi gases, we first need to provide radial confinement. For most of our experiments, this confinement is provided by a ring-shaped beam (ring) created by a combination of axicons as detailed in [46]. The ring is ramped on during the last steps of evaporation in the HEDT to a potential height significantly larger

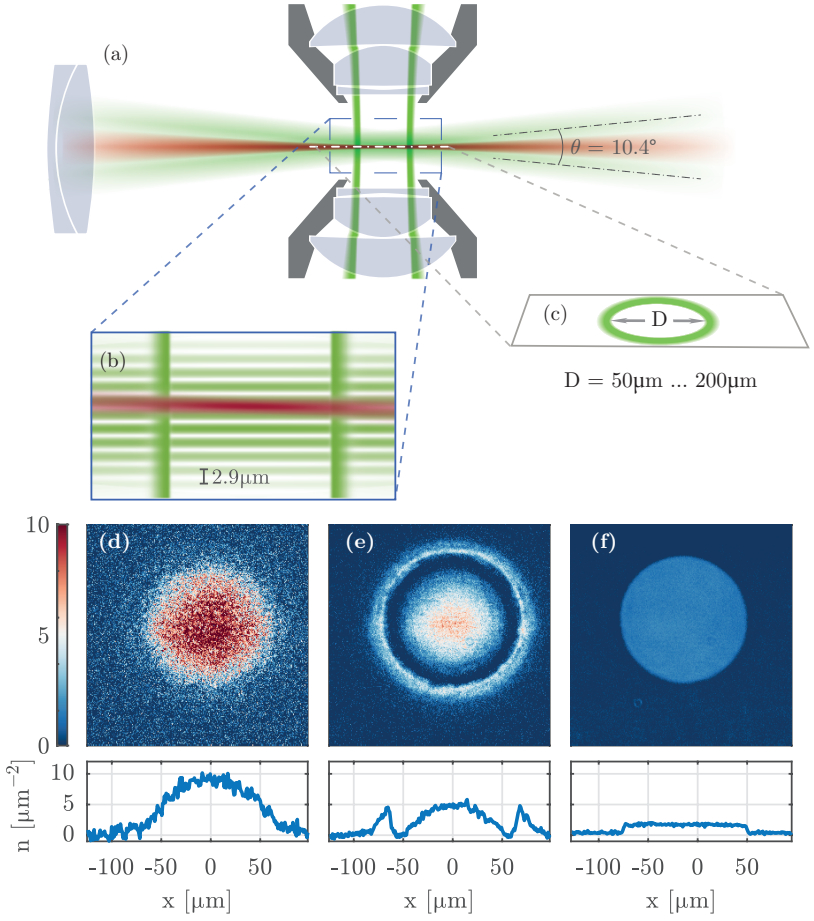

Figure 6.6: Preparation of a homogeneous 2D Fermi gas. (**a**) The atoms are initially prepared in a highly elliptic dipole trap (HEDT, red) that tightly confines the cloud in the z-direction. Then, a ring-shaped repulsive potential with a tunable diameter (**c**) is switched on to confine the atoms in the radial direction. A blue-detuned optical lattice is used to freeze out the motion in the z-direction (**b**). Panels (**d-f**) show the density distribution of the atoms in the HEDT (**d**), with the ring switched on (**e**) and after ramping on the confining lattice (**f**). In these images, the atom number was chosen to be larger to highlight the ring potential in panel (**e**). Figure adapted from [20].

than the chemical potential of the atoms, providing a deep, homogeneous trapping volume in the radial direction. Because the system is in the BEC regime, the chemical potential is small, and the cloud diameter is therefore small enough to be loaded completely into the ring trap at the diameter of $\approx 60\,\mu m$ used throughout this thesis. The laser power of the HEDT is then increased from $P = 25\,mW$ to $P = 800\,mW$, decreasing the diameter of the cloud along the z-direction to $\sim 2\,\mu m$. This tightly confined, already fairly two-dimensional system is then loaded into a single node of a blue-detuned optical lattice potential that is created by interfering two $\lambda = 532\,nm$ beams with a laser power of $P \approx 300\,mW$ each under a shallow angle of approximately 12°. The lattice spacing is approximately $3\,\mu m$, enabling the controlled loading of a single layer. Once the confining lattice has been ramped on, the HEDT is switched off and the system is deeply in the two-dimensional regime. Finally, a last evaporation step is performed by lowering the potential height of the ring to compensate for any residual heating during the transfer as well as set the final atom number, which for most experiments shown in this thesis will be approximately 2200 atoms per spin state. This corresponds to a density per spin state of $n = 0.8\,\mu m^{-2}$, with a typical temperature of around $15\,nK$ and a Fermi energy of $E_F = h \cdot 8.5\,kHz$.

The End

At this point, manipulation schemes will be performed that depend on the specific measurement made. For example, one might use a spatial light modulator to manipulate the density distribution [20] or excite a sound wave [40]. In any case, after the scheme has been performed, the density distribution needs to be imaged to obtain the information we seek. In our experiment, this is done by high-intensity absorption imaging, which we have discussed in detail in [38]. In short, we simultaneously switch off all optical traps and, depending on the measurement made, optionally allow for the atomic cloud to expand in the harmonic potential provided by the curvature of the magnetic offset field. Then, the atoms are illuminated by a resonant light pulse, and the density distribution is extracted from the shadow cast by the atoms onto a CCD camera. When no expansion is performed, the imaged density corresponds to the *in-situ* density distribution of the two-dimensional Fermi gas. If, however, the atoms are left to expand in the harmonic confinement for a quarter of the trap period (i.e. approximately 10 ms), a rotation in phase-space is performed and the imaged density corresponds to the momentum distribution of the trapped system. In any case, the absorption imaging is destructive as the photons scattered remove the atoms from our confinement, and the experimental cycle begins anew at the oven chamber.

Part III

Results

7 OBSERVATION OF SUPERFLUIDITY

In the following chapter, I will present the first main result of this thesis: the observation of superfluidity in two-dimensional Fermi gases. I will discuss how the concept of a critical velocity has shaped our understanding of superfluidity and summarize the different systems in which critical velocities have been measured over the years. I will explain the optical lattice setup used to measure the critical velocity and show how we manipulate and calibrate the potential. Recalling the groundwork laid in the previous chapters, I will discuss how we quantify whether excitations were created in our system before presenting the first measurement of a critical velocity in two-dimensional Fermi gases. Using the momentum selectivity of our measurements, I will show how we separate the different excitation mechanisms that set the critical velocity for the first time. The dependence of the critical velocity on the interaction strength will be discussed and compared to the three-dimensional case. Finally, I will present our measurements of the phase transition to the normal state and compare the results with theoretical predictions.

The results presented in this chapter are adopted from

> *L. Sobirey, N. Luick, M. Bohlen, H. Biss, H. Moritz and T. Lompe*
> *Science* **372** *(6544), 844-846 (2021) [41]*

and are reprinted here with modifications and additions.

As we begin our discussion of critical velocities and superfluidity, let us first talk about the motivation behind this measurement. When we began preparations for the measurements shown in this chapter, pair condensation had already been observed in two-dimensional Fermi gases [28], algebraically scaling correlations had been measured [99], and our own previous measurements had shown that two-dimensional Fermi gases are phase coherent [39]. All of these observations are in good agreement with the theoretical expectation of a quasi-condensate of pairs, superfluid through the BKT mechanism. However, while some publications already referred to 2D Fermi gases as superfluids [86], none of these observations actually show superfluidity. Instead, they show clearly the presence of a quasi-condensate: In [28], a macroscopically occupied low-momentum mode serves as a very direct sign for condensation, in [99], the measured algebraic decay of the first-order correlation function indicates a phase that varied slow enough to be considered locally constant, and in [39], the coherence of the phase was directly shown in the observation of Josephson oscillations, and the critical current could even be used to extract the condensed fraction.

Superfluidity and condensation are not, however, the same. While the two phenomena often go hand in hand, they do not have to appear together, as a non-interacting Bose gas at zero temperature will condense, but not become superfluid, and an infinitely large 2D system might become superfluid through the BKT mechanism without condensing. However, such pathological cases aside, the two terms also

describe different things. Condensation is a static property, referring to a macroscopically occupied state and a phase that is at least locally constant. Superfluidity, on the other hand, is a dynamic property that describes the robustness of a system against excitations. Therefore, for a measurement to show that a system is superfluid, it needs to show this robustness when probing the system over an extended amount of time. Such a measurement is the topic of this chapter: We will show that the 2D Fermi gas flows without friction, even when subjected to a moving obstacle for times much larger than any of its characteristic time scales. Thereby, we will show that 2D Fermi gases fulfill the Landau criterion, establishing their superfluidity firmly.

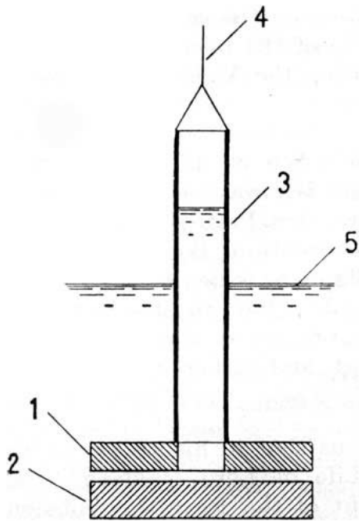

Figure 7.1: Experimental apparatus used by Kapitza. Two glass plates (1,2) are separated from each other by an adjustable gap. The top plate has a hole in the center which is connected to a tube (3). By lifting the tube and plates (4) so that the level of liquid Helium inside is above that of the reservoir (5), the velocity of flow in the small gap can be inferred from the time it takes for the levels to equilibrate. From [106].

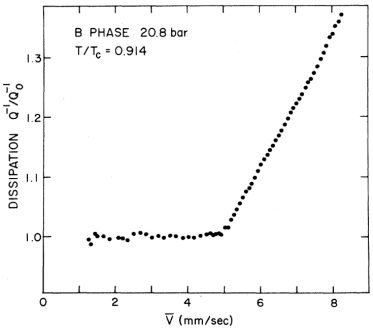

Figure 7.2: Critical velocity of superfluid ^{3}He. The dissipation as a function of velocity, measured using a torsional cell. A clear onset of dissipation is visible at a critical velocity of 5 mm/s. From [110].

7.1 Historic overview

In this section, I will briefly summarize the history of superfluidity, using measurements of critical velocities as the guiding thread. I will begin with the first use of the word superfluid by Kapitza, following research done on liquid Helium before moving on to ultracold quantum gases. There, I will discuss measurements on bosons and fermions in 3D as well as superfluid bosons in 2D.

The first measurement that observed superfluid flow was performed by Kapitza in 1938 [106] and simultaneously by Allen and Misener [107]. Kapitza measured the flow of liquid ^{4}He through a narrow gap between two glass plates (see fig. 7.1), reporting a drop in the viscosity by a factor of at least 1500 as the phase transition was crossed. Due to the analogy to the drop in resistivity in superconductors, he coined the word *superfluid* for this special state of matter.

While these experiments were not the first to report on unusual properties of ^{4}He below the λ-point at 2.17 K, the incredibly low viscosities reported and the close similarities to superconductors sparked a wide interest into this new state of matter. Over the next years, a plethora of measurements on the flow of liquid Helium were performed for different geometries. However, while some experiments found the same vanishing viscosities that Kapitza and Allen and Misener had reported, other experiments found different results, often for measurements at higher pressures or in different geometries (see e.g. [108]). This behavior was explained by Landau in 1941, who introduced the concept of a critical velocity (see section 4.1) as well as the two-fluid model, which succeeded in explaining many of the observations that had been reported.

While superfluid ^{4}He was studied in great detail over the coming years, it would take 32 years until a second neutral superfluid was realized in the laboratory when Osheroff, Richardson and Lee cooled ^{3}He below its transition temperature in 1970 [109]. While they initially presumed to have found a solid phase of fermionic Helium, they quickly realized that the observed phase transition was of a different nature - they had realized the first fermionic superfluid, with a critical temperature of only 2.6 mK.

Soon, this was confirmed by measurements [110] that clearly showed a critical velocity for superfluid flow as described by Landau (see fig.

7.2). In these measurements, the liquid Helium is held in a torsional cell that can be oscillated at variable amplitude using electrostatic forces. A small orifice constricts the flow in one location, causing a single, well defined region in which high flow velocities occur. As the voltage driving the oscillations is increased, the amplitude of oscillations and thereby the maximum flow velocity increases linearly until the critical velocity is reached, where the sudden onset of dissipation requires larger changes in voltage to increase the amplitude further.

Ultracold gases

With both stable isotopes of Helium made superfluid, it took another 25 years until the next neutral superfluid was realized. In 1995, the first Bose-Einstein-Condensate was observed in ultracold ^{87}Rb-atoms [111]. Quickly, it was established that these systems are phase coherent, as two separated condensates were found to interfere [112]. In 1999, Raman and coworkers [113] subjected a sodium BEC to a focused blue detuned laser beam that was moved through the condensate at a variable velocity (see Fig. 7.3). They observed that the temperature of the system increased suddenly as the velocity of the beam exceeded a critical velocity, establishing superfluidity in BECs.

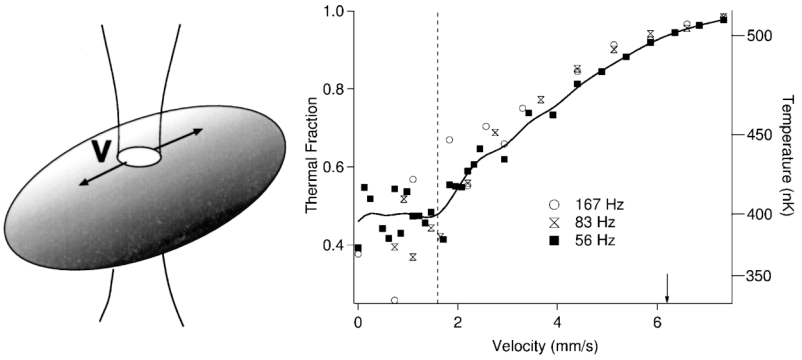

Figure 7.3: Stirring a BEC. Left: A blue detuned laser beam is moved through a cigar-shaped condensate at a variable velocity v. **Right**: The temperature plotted as a function of the velocity of the beam. Below a critical velocity, no dissipation is observed, heralding the presence of a superfluid. From [113].

With the advent of BEC, the number of superfluid materials and studies of the properties of such superfluids quickly skyrocketed. The next expansion of the field occurred a few years later, when the first ultracold Fermi gases were brought to degeneracy. As explained in section 4.3, when fermions of two different spinstates interacting attractively are brought together and cooled to ultracold temperatures, bosonic pairs form from the fermionic atoms, and condensation once again occurs. Once more, superfluidity was observed in ultracold Fermi gases through a measurement of a critical velocity. In 2007, Miller and coworkers [114] subjected a gas of ^{6}Li atoms in the BEC-BCS crossover to an optical lattice, created by interfering two tightly focused beams in the center of the gas (see fig. 7.4). By detuning one of the beams with respect to the other, the interference pattern was made to move at a velocity proportional to the detuning. By measuring the number of atoms that remained in the condensate after sub-

jecting the system to the moving optical lattice for 500 ms, they found clear evidence for a critical velocity and thereby superfluidity. Using a Feshbach resonance to tune the interaction strength, they reported a maximum of the critical velocity around unitarity, where the interactions in the system are strongest.

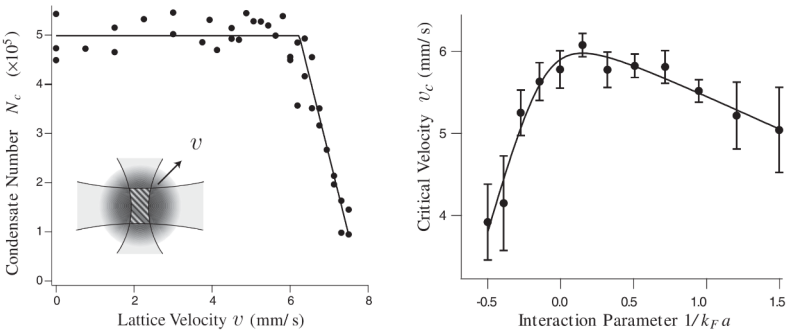

Figure 7.4: Critical velocity of an ultracold Fermi gas. Left: A moving optical lattice is moved through a 3D Fermi gas (inset) for 500 ms. The number of condensed atoms is plotted as a function of velocity, showing a clear onset of dissipation once a critical velocity is reached. **Right**: The critical velocity is plotted as a function of interaction strength. A maximum of the critical velocity is found around unitarity. From [114].

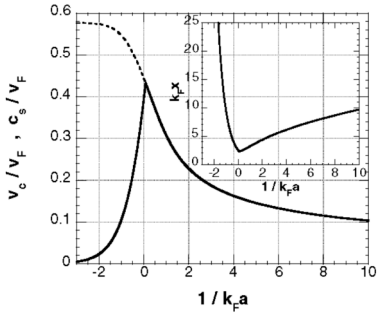

Figure 7.5: Theoretical prediction for the critical velocity. The critical velocity (solid line) follows the speed of sound (dashed line) until pair breaking excitations become available towards the BCS side of the crossover, reducing the critical velocity. The inset shows the coherence length in the crossover. From [67].

This observation was in agreement with theoretical expectations, which predict a maximum in the crossover. However, the quantitative behavior Miller and coworkers observed was quite different from the theoretical prediction (see fig. 7.5). This problem was revisited by Weimer and coworkers in 2015 [115, 116], where the critical velocity was measured by stirring with a laser beam in an oblate geometry and compared to measurements of the speed of sound and theoretical predictions. They found that while the size and wavelength of the stirrer, the temperature of the system and the density inhomogeneity all reduce the critical velocity, when all these effects are taken into account, the critical velocity is in excellent agreement with theoretical expectations throughout the BEC-BCS crossover.

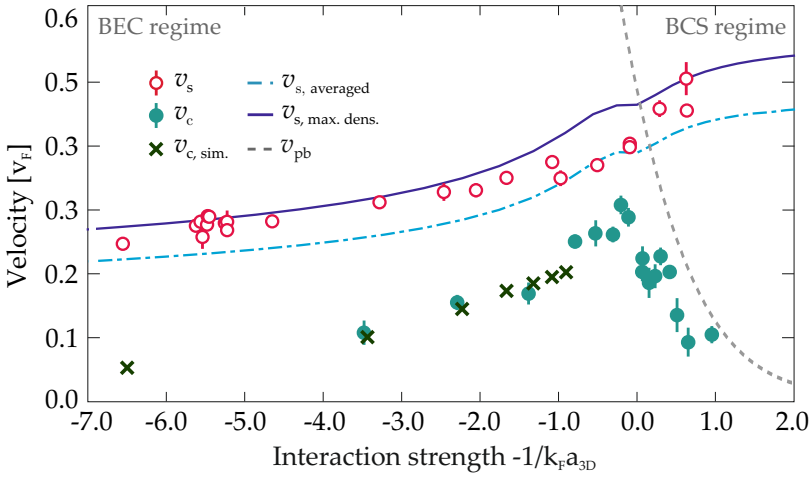

Figure 7.6: Critical velocity in the BEC-BCS crossover. Critical velocity v_c and speed of sound v_s as a function of interaction strength, together with theoretical predictions. The critical velocities are significantly reduced compared to the speed of sound, but the discrepancy is reproduced by calculations considering the finite size of the stirrer, the stirring pattern and the finite temperature ($v_{c,sim}$). $v_{s,averaged}$ and $v_{s,max.dens.}$ denote theoretical calculations for the speed of sound using different definitions of the Fermi velocity, and v_{pb} denotes the expected velocity for pair breaking excitations to occur. Note that the x-axis is defined with a different sign than in the previous figures. From [115].

Two-dimensional systems

When the first ultracold two-dimensional Bose gases were realized, one of the most obvious questions to answer was whether a transition to superfluidity would be observed in these quantum gases. To answer this question, Desbuquois and coworkers employed the now familiar method of stirring with a focused laser beam to verify the Landau criterion [117]. They found that in the central part of the cloud, the stirring beam caused no dissipation below a critical velocity, while in the outer wings of the cloud, no finite critical velocity could be found. Therefore, their stirring experiment not only clearly showed superfluidity in 2D Bose gases, but also probed the phase transition to the normal state.

Note that it later became clear that the precise determination of the location of the phase transition in this fashion is difficult due to the slow thermalization of vortices [118].

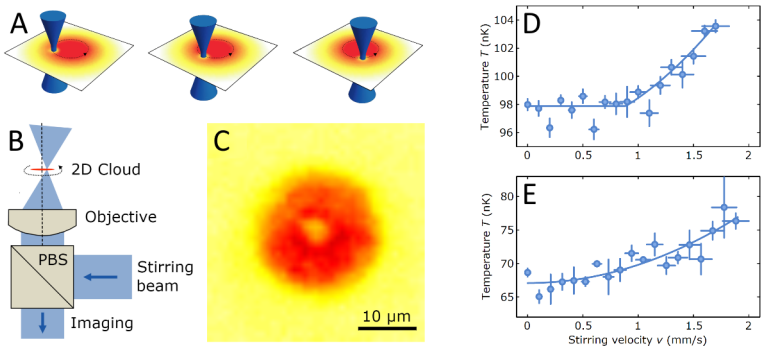

Figure 7.7: Critical velocity in the BEC-BCS crossover. A Illustration of the stirring process used to measure critical velocities. **B** The stirring beam is overlapped with the imaging beams and focused tightly into the gas. **C** Absorption image of a 2D Bose gas with the density suppression caused by the blue-detuned stirring beam visible in the center of the cloud. **D** Temperature after stirring the cloud for a superfluid (**D**) and a normal (**E**) gas. In the superfluid system, a critical velocity is visible below which no dissipation occurs. From [117].

7.2 The moving optical lattice

In this section, I will describe the optical lattice setup we use to measure critical velocities. I will show how the interference pattern is created and how we tune its different parameters. Finally, I will discuss how we calibrate the height of the potential by measuring its influence on the density distribution.

In our experiments, we employ a moving optical lattice instead of a tightly focused laser beam to act as the moving impurity in Landaus thought experiment, similar to the setup used in [114]. We focus two red-detuned laser beams to a size slightly smaller than the system size and overlap them in the center of the trap. The sinusoidal interference pattern then has a wavevector of $q = |\vec{k}_1 - \vec{k}_2|$, where $\vec{k}_1, \vec{k}_2$ are the individual wavevectors of the two beams. If one of the beams is detuned by a frequency difference of $\Delta\nu$ with respect to the other, the interference pattern begins to move at a velocity of $v = \frac{2\pi\Delta\nu}{q}$.

There are a few reasons why we chose to use a moving optical lattice rather than a focused laser beam like many previous experiments. First, the velocity of a moving lattice is very well known, depending only on the frequency detuning, which is highly controllable through acusto-optic modulators, and the wavevector, which can be measured directly. Second, the velocity can also be tuned to arbitrarily large values as opposed to the common piezoelectric-mirror-based setups for focused stirring beams which encounter mechanical resonances and

similar issues. Third, because the interference pattern can be made as large as the system size, the height of the moving lattice can be kept very low without sacrificing signal, whereas a focused beam would have to be stirred for tremendously long times to cause a measurable temperature increase or increased to potential heights where it can no longer be considered a weak perturbation. Finally, as we will see in the following, the moving lattice brings the great advantage of being able to select a specific wavevector of excitations.

7.2.1 Creating the interference pattern

The laser light used to create the optical lattice is generated by a 780 nm diode laser and amplified with a tapered amplifier. Through an optical fiber, the light is transported to the vicinity of the science cell. An acousto-optical modulator before the fiber is used to stabilize and tune the transmitted power, which is measured using a photodiode immediately after the fiber outcoupler. The beam is then split into two parts using a polarizing beam splitter and a $\lambda/2$ waveplate, where the waveplate is adjusted such that both beams are approximately equal in power. After each beam traverses another acousto-optical modulator used for fast switching and frequency detuning, the beams are collimated, one of the beams passes a second $\lambda/2$ waveplate to align their polarizations again, and the beams are adjusted to their final size by telescopes. They then travel over a number of mirrors to reach the microscope. One pair of those mirrors is mounted on motorized translation stages, which allow the distance between the two beams to be tuned from approximately 3 mm to 22 mm. The pair of beams is then focused by a high-resolution (NA=0.62) microscope with a focal length of $f = 26.2$ mm onto the atom plane, causing the two beams to interfere. After the atom plane, the beams traverse a second high-resolution microscope and a set of lenses before ultimately reaching the CCD camera used for absorption imaging.

The translation stages are motorized using two CONEX-TRA12CC linear actuators (Newport).

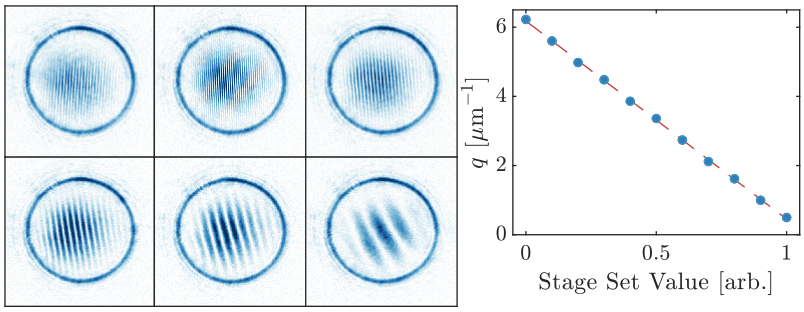

Figure 7.8: Calibration of the lattice wavevector. Left: Exemplary images of the lattice potential, together with the ring potential used for homogeneous confinement, shown for six different lattice wavevectors. The intensity distribution is imaged using an auxiliary imaging system. Right: Calibration of the lattice wavevector, obtained by Fourier transforming the images on the left and fitting the peaks corresponding to the periodicity. The set value used in the experiment is roughly proportional to the separation of the two lattice beams.

As the lattice beams reach the camera together with the ring-shaped confinement beam, adjusting the size, overlap and position of the two beams is straightforward as the resulting interference pattern can be directly imaged and compared to the position of the atom cloud. Calibrating the lattice wavevector is therefore a simple process where the

interference pattern is imaged on the CCD camera for a number of different beam distances. Such a calibration procedure is shown in fig. 7.8. The range of wavevectors available in the experiment is limited by the size of the mirrors and mirror mounts used in the beam path. Larger distances between the beams and therefore higher wavevectors would be possible either by using shorter wavelengths or by replacing some of the $50\,\mathrm{mm}$ circular mirrors with either larger or elliptic mirrors. Shorter distances are more difficult to realize as the beams need to be separated by at least a few Gaussian waists to be manipulated independently, and the current lower bound of $3\,\mathrm{mm}$ beam distance is set by one beam clipping on the mirror mount of the other beam.

To calibrate the potential height of the beams, we employ two complimentary methods. The first method directly projects a lattice with no frequency detuning and the smallest possible wavevector onto the atoms. By measuring how the density is modified by the optical lattice and using the known density equation of state [119], we obtain a potential height per milliwatt total lattice beam power of $\approx \mathrm{h}{\cdot}510\,\mathrm{Hz/mW}$.

The second method projects the two lattice beams individually onto the atoms and measures their potential heights independently. Since the interference pattern shows a contrast $\gtrsim 0.95$, the total potential height should be well approximated by two times the sum of the two individual potential heights. For the two beams, we obtain values of $\approx \mathrm{h} \cdot 108\,\mathrm{Hz/mW}$ and $\approx \mathrm{h} \cdot 122\,\mathrm{Hz/mW}$, resulting in a total potential height of the optical lattice of $\approx \mathrm{h} \cdot 460\,\mathrm{Hz/mW}$. In our analysis, we therefore use the mean of the two results of $\mathrm{h} \cdot 485\,\mathrm{Hz/mW}$ as the potential height per laser power.

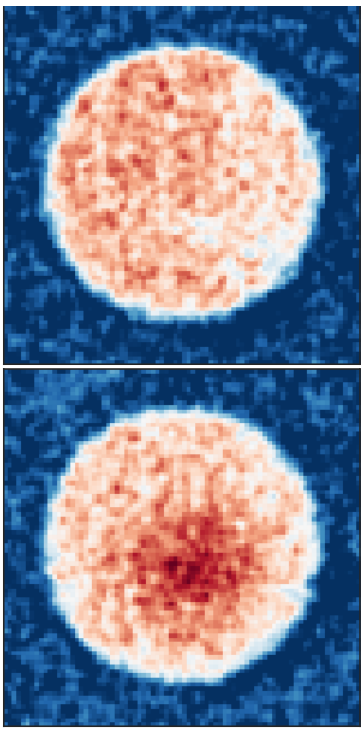

Figure 7.9: Calibrating the potential height. Density distribution of a homogeneous system without (top) and with (bottom) a single lattice beam left on. From the relative change in density and the known density equation of state [119], the potential height of the lattice can be obtained. A slight Gaussian filtering has been applied to the images for visibility.

7.3 Observing excitations

In this section, I describe how we quantify the amount of excitations created by the moving optical lattice. I will explain how the heating rate in the system is related to the dynamic structure factor and further discuss the differences between optical lattices and stirring beams. The different methods of thermometry in ultracold Fermi gases will be discussed, and the occupation of the lowest momentum modes in the BEC regime will be established as a robust proxy for the amount of excitations that was created by the lattice.

To measure a critical velocity, we need to be able to detect if excitations were created in our system. As discussed in section 4.4, there are two possibilities to do so: The first method is to measure the momentum transferred to the system directly, for example by performing a time of flight measurement directly after a short exposure to the moving optical lattice. Due to the very short exposures, however, this method leads to small signal-to-noise ratios in low density systems such as ours. The second method is more promising: In this approach, the system is allowed to thermalize after the exposure to the moving optical lattice, causing any excitations that were created to result in an increase in the temperature of the system. Therefore, the lattice can be kept at a low potential height and the system exposed to it for a long time, remaining well in the linear, weak-perturbation regime.

The heating rate $\frac{dE}{dt}$ resulting from a perturbing potential was derived in [63, 120]. To calculate it, we need to know the Fourier transform $V(k_x, k_y)$ of the perturbing potential. For an optical lattice with wavevector q along the x-direction, we can simply approximate the time-independent part of the lattice potential as

$$V(k_x, k_y) = V_0 \delta_{k_y} (\delta_{k_x - q} + \delta_{k_x + q}),$$

where V_0 quantifies the potential height of the lattice. The heating rate at a detuning of $\omega = 2\pi\Delta\nu$ can then be written as

$$\frac{1}{\omega}\frac{dE}{dt} = 2\left(\frac{V_0}{2}\right)^2 S(q, \omega)\left(1 - e^{\frac{-\hbar\omega}{k_B T}}\right). \tag{7.1}$$

Note that as discussed in section 4.4, the temperature of our 2D Fermi gas is very low compared to $\hbar\omega$, and we therefore neglect the finite temperature correction as $e^{\frac{-\hbar\omega}{k_B T}} \approx 0$.

The heating rate is therefore directly related to the dynamic structure factor, which we have established in section 4.4 as the quantity that describes all possible excitations that maintain the number of particles in a system as a function of transferred momentum and energy. As we can see, a moving optical lattice with tunable wavevector can directly measure the dynamic structure factor by measuring the heating rate. As discussed in section 4.4, this is the principle behind Bragg spectroscopy. However, in this chapter, we will not concern ourselves too much with the shape of the dynamic structure factor beyond the question at which velocity the first excitations are created.

On stirring experiments

Let us make a short excursion to discuss once more the choice of a moving optical lattice over that of a tightly focused laser beam. Intuitively, a stirring beam is a very obvious choice for measurements of critical velocities, as it closely resembles the point-like impurity in Landau's thought experiment. However, there is a very important difference between a point-like impurity and a focused laser beam: The minimum achievable size of a Gaussian stirring beam is limited by the wavelength of the light used, which is on the order of the interparticle spacing k_F^{-1}. Therefore, the Fourier transform of the perturbing potential in the case of a stirring beam is once again a Gaussian with a waist on the order of the Fermi wavevector. The heating rate caused by a stirring beam will then be some sum over the contributions at all wavevectors, but weighted by the Fourier transformation of the lattice potential. Therefore, excitations at high wavevectors are strongly suppressed for realistic stirrer sizes, making it difficult to quantify the contribution of such excitations using a stirring beam. Additionally, since excitations at different wavevectors are summed together, a lot of details of the dynamic structure factor are lost, making it difficult to differentiate between different types of excitations or to extract quantitative information. This is visualized in fig. 7.10, which shows a comparison between the excitations that contribute to the measured heating rates using a moving optical lattice and a stirring beam.

Now, if our only aim were to measure the critical velocity in a bosonic superfluid where all relevant excitations are phonons at low momentum, these considerations need not be made - a stirring beam is well

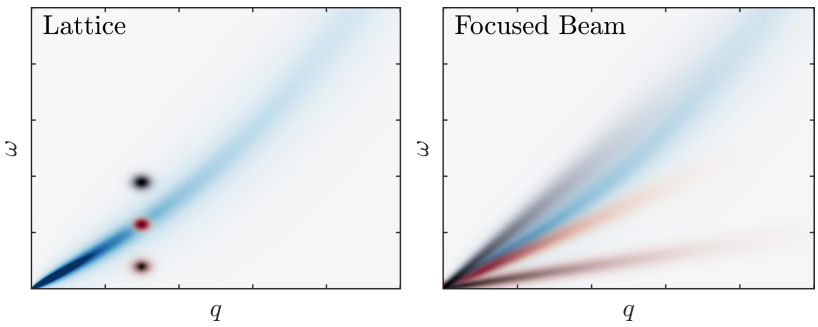

Figure 7.10: Contributions to the heating rate. Left: The red and black spots mark the parts of the dynamic structure factor (blue, shown for a superfluid Bose gas at finite temperature) that contribute to the heating rate caused by a moving optical lattice, for three different velocities and at a constant wavevector. **Right**: The same picture, but for a stirring beam at three different velocities. Where the heating rate caused by a moving optical lattice only considers excitations at the lattice wavevector, the stirring beam averages together contributions from a range of wavevectors. However, excitations at higher wavevector are suppressed due to the finite size of the beam, and it is not possible to separate which kind of excitations contributed to the heating rate.

suited for such a measurement. However, in any more complicated system such as a Fermi gas with the possibility of pair breaking excitations that occur at wavevectors around $2\,k_F$, an optical lattice has significant advantages.

Thermometry

We have established that to quantify whether excitations were created in the system, we will want to measure the heating rate caused by the moving lattice. Therefore, we need to determine the temperature of our 2D Fermi gas, which is not a trivial task. When strong interactions and finite temperatures come together, any theoretical description becomes extremely challenging. Usually, thermometry in such systems is performed by measuring the occupation of high energy states, the population of which is well described by the Boltzmann distribution. One common way to do so is to measure the low-density region of the cloud, where the low density reduces the Fermi temperature far enough for the local temperature T/T_F to be high [93, 96]. However, this method is only really suited to work in harmonically trapped systems, where there will always be such a low density region. In our homogeneous two-dimensional Fermi gases, no low density regions exist *in situ*, precluding the use of this method for thermometry.

Another common approach is to measure the momentum distribution and obtain the temperature from its high momentum tail [28, 96]. However, matter wave focusing (see chapter 5) is affected by interactions during the expansion time, and therefore limited to the BEC regime where the scattering rate becomes low enough. Nevertheless, using this method, we are able to measure the temperature of systems in the BEC regime, see fig. 7.11. While we are able to obtain a temperature from these Boltzmann fits to the momentum distribution, they require a significant amount of statistics. The measurements shown in fig. 7.11 show the average of 50 images for each datapoint, and the obtained temperatures are already quite noisy. For day-to-day measurements, the large number of repetitions required is not feasible for our experiments. Instead, we use the fact that the condensed fraction in the system depends strongly on the temperature. We measure the

Note that the heating rate should in good approximation be constant, and that a linear increase in the temperature as a function of the heating time is therefore expected for these measurements.

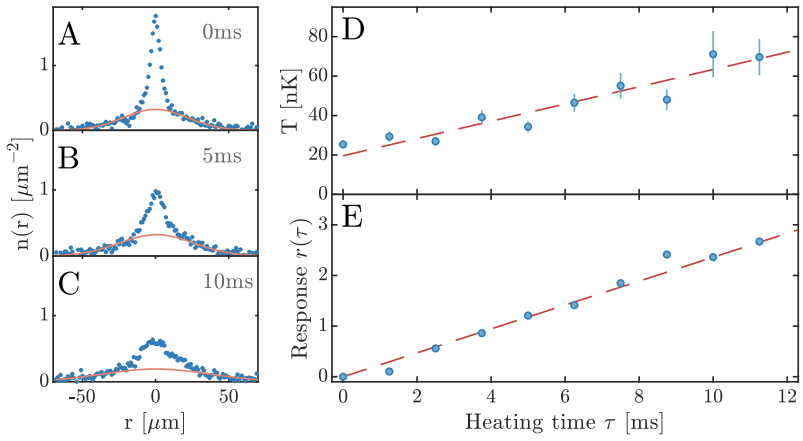

Figure 7.11: Measuring the temperature in the BEC regime. We measure the momentum distribution for a system in the BEC regime ($\log(k_F a_{2D}) = -2.9$) that has been prepared after heating the system for a variable amount of time (see text). Panels **A-C** show cuts through the momentum distribution at different temperatures. In a cold system (**A**), a clear peak is visible, indicating the presence of a pair condensate. It is surrounded by a low density wing well described by a Boltzmann distribution (red line). As the system is heated, the peak becomes less prominent (**B**) and the width of the thermal wing increases. Panel **D** shows the temperatures obtained from a Boltzmann fit. The temperature of the system increases roughly linear in the heating time τ (see text). As this method of thermometry requires a good signal-to-noise ratio in the low density regions of the cloud, it requires a significant amount of statistics (here 50 individual realizations per data point) and is therefore not well suited for our experiments. We therefore make use of the fact that the *response* $r \equiv \frac{n_{k=0,\tau=0}}{n_{k=0,\tau}} - 1$ (Panel **E**) increases linearly with τ and use it as a proxy for the temperature of the system.

height of the pair condensate peak $n_{k=0}$ and define the *response*

$$r \equiv \frac{n_{k=0,\tau=0}}{n_{k=0,\tau}} - 1 \tag{7.2}$$

We find that the response increases in good approximation linearly with the temperature increase in the system in the range of temperatures relevant to our experiments, see fig. 7.11. As the response can be measured with a significantly higher signal-to-noise ratio than the temperature, this enables us to reduce the number of required repetitions by an order of magnitude. In our measurements, we will therefore quantify the temperature and thereby the heating rate in the system by measuring its response r.

Outside the BEC regime, we are not currently able to measure the temperature of our homogeneous 2D Fermi gas as interactions during time of flight prevent us from measuring the pair momentum distribution. For the measurements shown here, however, this is not a significant issue, as we are mostly interested in the qualitative behavior of the heating rate as a function of the lattice velocity. We will therefore slowly ramp the interaction strength back into the BEC regime after exposing the gas to the moving lattice and measure the temperature $\tilde{T}$ at an interaction strength of $\log(k_F a_{2D}) = -2.9$. While the resulting temperatures will not be equal to those before the interaction ramp, an entropy increase before the ramp must nevertheless also correspond to an entropy increase after the ramp relative to the system that was not exposed to the lattice, given that our interaction ramps do not significantly heat or cool the system. The heating rate in the BEC regime can then serve once more as a proxy for the heating rate at arbitrary interaction strengths.

To verify that these interaction ramps do not significantly heat or cool the system, we prepare systems in the crossover and ramp the interaction strength to different values. The system is then exposed to the optical lattice at zero detuning for a time comparable to those used in later experiments. Afterwards, the interaction strength is ramped into the BEC regime and the temperature $\tilde{T}$ of the gas is measured as described above. The result is shown in fig. 7.12. As the temperature

We refer to the temperature measured after an interaction strength ramp into the BEC regime as $\tilde{T}$, while the true temperature of the system at the original interaction strength is denoted by T.

In fact, as long as any heating or cooling due to the interaction ramps is the same in any repetition of the experiment and monotonously scales with the initial temperature (two quite reasonable assumptions to make), our measurements of critical velocities would not be significantly affected.

after the interaction ramp $\tilde{T}$ is mostly independent of the interaction strength at which the system was exposed to the lattice, a change in $\tilde{T}$ as a function of the lattice velocity therefore indicates that excitations were created in the system. In summary, for all measurements shown in this chapter, we will measure the momentum distribution after a slow ramp into the BEC regime and obtain a measure for the amount of excitations created in the system from the response r.

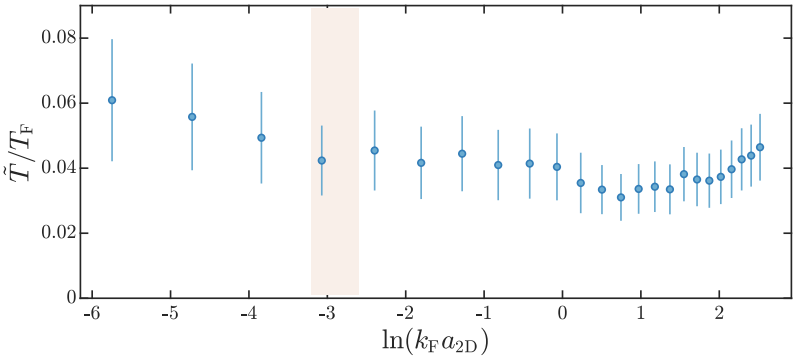

Figure 7.12: Heating during interaction ramps. Shown is the temperature $\tilde{T}$ after an interaction ramp into the BEC regime for systems prepared at different interaction strengths. We find that the resulting temperature $\tilde{T}$ is nearly constant, showing only a small increase in the far BEC regime attributed to collisional losses and some slight evaporation in the crossover region. Therefore, an increase of $\tilde{T}$ can be interpreted as an increase in the temperature T before the interaction ramp.

7.4 Observing superfluidity

Now that I have established how the lattice setup works and how excitations can be detected, it is time to present the first main result of this thesis: the observation of superfluidity in two-dimensional Fermi gases. In this section, I will present clear evidence that 2D Fermi gases are superfluid in the BEC and BCS regimes. Utilizing the momentum-tunability of the moving lattice, I will demonstrate how different types of excitations set the critical velocity in different interaction regimes.

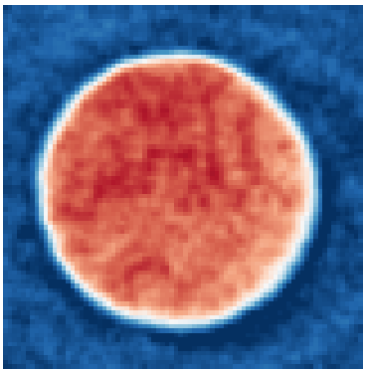

Figure 7.13: A homogeneous 2D Fermi gas. *In situ* density distribution of a homogeneous system, confined by a ring-shaped repulsive potential. Nearly all measurements discussed in this thesis are performed in a system such as this one.

With the motivation and methodology established, we are now ready to probe our systems and attempt to observe a nonzero critical velocity. To do so, we prepare an ultracold 2D Fermi gas at some interaction strength and expose it to the moving optical lattice at variable lattice velocities. We then slowly ramp the interaction strength into the BEC regime and perform matter wave focusing to obtain the momentum distribution. If the system is superfluid and therefore has a critical velocity, we expect the response r to suddenly increase at this velocity. The result of such a measurement is shown in fig. 7.14. We observe a sudden increase of r once the velocity of the moving lattice exceeds a critical velocity v_c, which we determine by fitting the response with the equation $r(v) = A \max(0, v^2 - v_c^2)$ [121]. At higher velocities, the heating rate initially increases further, but decreases again to zero for velocities significantly above the critical velocity.

The reason for this decrease is obvious when we remember that this measurement was performed using an optical lattice with a fixed wavevector of $q = 0.15\, k_F$. As shown in eq. 7.1, the heating rate caused by the moving lattice is proportional to the magnitude of the dynamic structure factor $S(q, vq)$. At this low wavevector, the only feature in

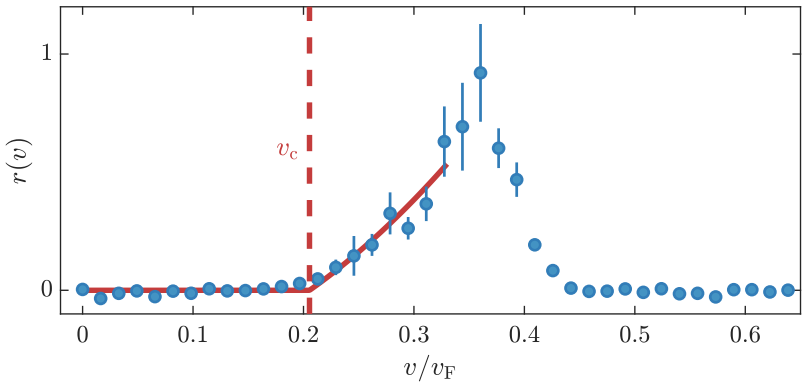

Figure 7.14: Observation of a critical velocity. Response of a homogeneous system at an interaction strength of $\log(k_F a_{2D}) = -0.8$ to the moving optical lattice with $q = 0.15\, k_F$. No dissipation is observed below a critical velocity v_c (red lines). At higher lattice velocities, dissipation decreases again. Error bars denote the standard error of the mean of 10 repetitions.

the dynamic structure factor is the Goldstone mode, which has an energy of $\hbar\omega \approx c_s q$ and is broadened by different effects such as the finite temperature and damping, see section 4.4. Therefore, as the velocity of the lattice increases significantly beyond the speed of sound, $S(q, vq) \to 0$ and no more excitations are created by the moving lattice. The observed behavior hence is exactly what one would expect when performing such a measurement for only one wavevector.

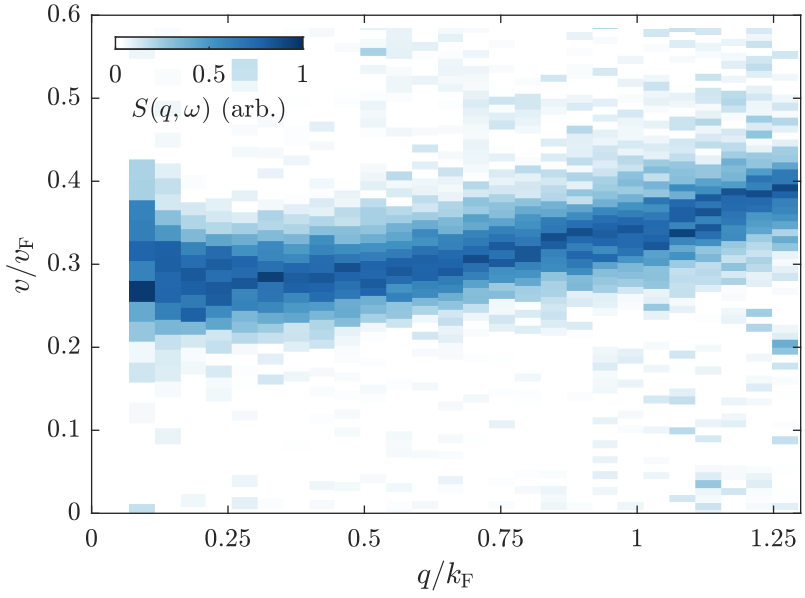

Figure 7.15: Observation of superfluidity in the BEC regime in 2D. Plotted is the heating rate in a bosonic 2D superfluid ($\log(k_F a_{2D}) = -1.8$) as a function of velocity and wavevector, with each column normalized individually for visibility. At low wavevectors, the excitations occur at the speed of sound of $c_s \approx 0.3 v_F$. As the wavevector increases, the mode moves towards higher velocities as excitations start to resemble single particle excitations. We observe no excitations at any wavevector below a critical velocity of $v_c \approx 0.15\, v_F$, establishing the presence of a superfluid.

The obvious remedy must now be to repeat the measurement for a range of different wavevectors. Then, the lowest velocity at which excitations are created will correspond to the critical velocity, and from the observed heating rates, the dynamic structure factor should be obtainable. To verify this expectation, we prepare a system of bosonic molecules, well in the regime where its excitation spectrum should be described by the Bogoliubov dispersion relation. We repeat the measurement above over the whole range of wavevectors that our lattice setup can realize and obtain the result shown in fig. 7.15. We clearly observe a linear branch at low wavevectors, where the excitations are

phonons and the heating rate has a maximum when the velocity of the lattice is equal to the speed of sound. As the wavevector of the lattice is increased and excitations are no longer purely phase fluctuations, their mode velocity increases. For all wavevectors, we clearly observe a critical velocity below which no excitations are created. This observation firmly establishes that two-dimensional Fermi gases in the BEC regime are superfluid.

As we have discussed above, the heating rates shown in fig. 7.15 ultimately reflect the shape of the dynamic structure factor. Neglecting the very minor influence of finite temperature as discussed in section 4.4, the measured heating rate shown in fig. 7.15 directly yields the dynamic structure factor shown in fig. 7.16. Plotted in this fashion, the Bogoliubov dispersion relation is immediately recognizable in its familiar form. However, as this chapter is focused on the presence of superfluidity and the Landau criterion, we will leave more in-depth discussions of the dynamic structure factor for the next chapters.

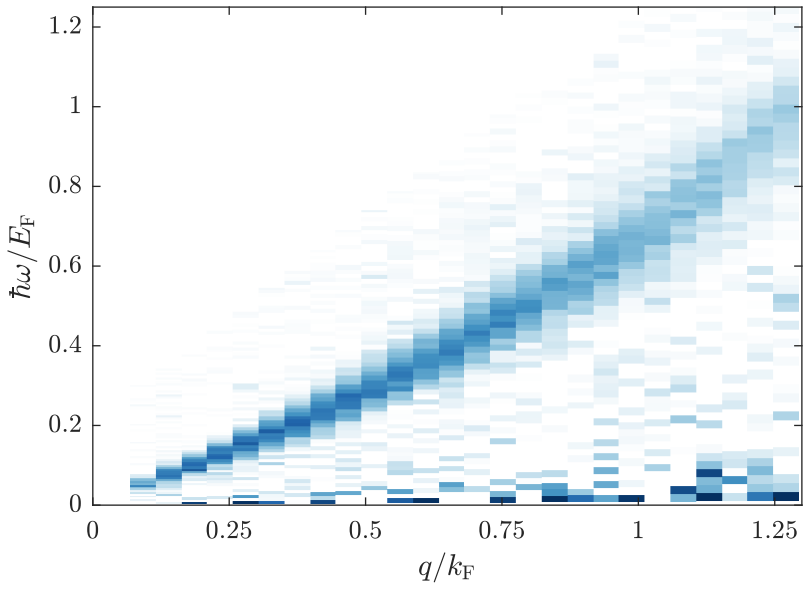

Figure 7.16: Dynamic structure factor of a 2D Bose gas. This figure shows the same data as the previous one, but plotted as a function of transferred energy instead of velocity and divided by ω. The well-known Bogoliubov dispersion relation is immediately recognizable, emphasizing the relation of the heating rate to the dynamic structure factor. The noise at low transferred energy is a result of the division by ω, amplifying measurement noise at low detunings.

After having established superfluidity in two-dimensional Fermi gases on the BEC side of the crossover, the next obvious step is to repeat this measurement towards the BCS side, where pair breaking excitations are known to reduce the critical velocity. As we have discussed in section 4.4, pair breaking excitations can occur when the energy transferred by the probe is $\hbar\omega \geq 2\Delta$, where Δ is the pairing gap. Since the velocity of the lattice is related to the detuning ω as $v = \omega/q$, the lowest velocity for which pairs can be broken is therefore $v_{pb} = \lim_q \frac{2\Delta}{q} \simeq \frac{\Delta}{k_F}$ at a lattice wavevector of $q = 2\,k_F$. Therefore, our momentum selective measurements should allow us to distinguish phononic excitations at low wavevectors and pair breaking excitations which occur around $q = 2\,k_F$.

To verify this prediction, we prepare 2D Fermi gases at an interaction strength of $\log(k_F a_{2D}) = 1.6$, which is on the BCS side of the

Note that when the chemical potential of the atoms $\mu < 0$, the minimum energy for pair breaking to occur is shifted by the interaction energy to $\hbar\omega = \sqrt{\mu^2 + \Delta^2}$ [59].

Since the onset of the continuum increases smoothly for wavevectors above $2\,k_F$, the minimum velocity should in fact be found at slightly higher wavevectors, but the effect should be small and will be neglected here.

crossover. To be able to reach wavevectors of $q = 2\,k_F$, we reduce the density to a value of $n = 0.8\,\mu m^{-2}$ and thereby the Fermi wavevector to a value of approximately half the maximum wavevector we can realize with the optical lattice. We then repeat the same measurement as above and obtain the heating rate shown in fig. 7.17. The result is in

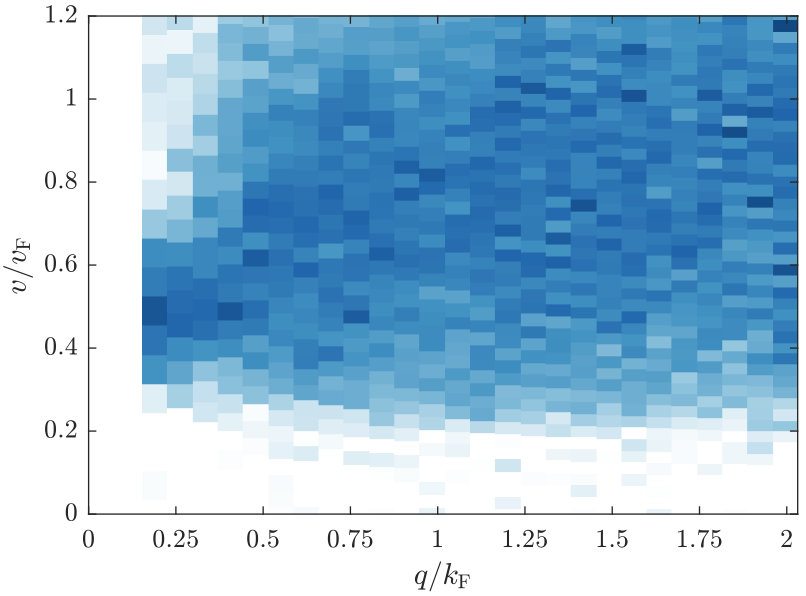

Figure 7.17: Observation of superfluidity in a 2D BCS gas. Plotted is the heating rate in a fermionic 2D superfluid ($\log(k_F a_{2D}) = 1.6$) as a function of velocity and wavevector and with each column normalized individually for visibility. At low wavevectors, excitations are still phononic and linear in wavevector. However, as the wavevector increases, pair breaking excitations become available, resulting in a broad continuum of excitations with a minimum velocity for excitations at $q \approx 2\,k_F$, as expected from BCS theory. Once again, we observe no excitations below a critical velocity for any wavevector, establishing the presence of superfluidity in the BCS regime.

excellent agreement with our expectations, and in stunning contrast to that obtained for a 2D Bose gas: A broad continuum of excitations is visible, with the minimum velocity for excitations to be created found at $2\,k_F$. In addition, a phononic mode is still visible at low momentum, but soon merges with the continuum. Once more, we find that no excitations are created below a critical velocity, which is this time set by the pair breaking continuum as expected. Therefore, this measurement clearly demonstrates that 2D Fermi gases are superfluid on the BCS side of the crossover as well and is the first time the different excitation mechanisms and their role in setting the critical velocity have been directly observed.

For a detailed discussion of the behavior in between the two limits, see the next chapter.

7.5 Interaction dependence of the critical velocity

In this section, I show how the critical velocity evolves between the BEC and BCS limits. I will compare the results to theoretical predictions and discuss what effects reduce the measured critical velocities.

The measurements above have shown that 2D Fermi gases are superfluid, and that the critical velocity is set by different types of excitations at different interaction strengths. We now go on to measure how the critical velocity depends on the interaction strength explicitly, using what we have learned so far. As we know that there are two relevant types of excitations that limit the critical velocity, one being phonons and the other being pair breaking, we do not need to measure

the entire range of wavevectors for every interaction strength. Instead, since the critical velocity will always be limited either by phononic excitations or by pair breaking, it suffices to perform one measurement at a low wavevector, here $q \approx 0.3\,k_F$, and one at $q \approx 2\,k_F$. The critical velocity will then correspond to the lowest velocity at which excitations are created at that interaction strength.

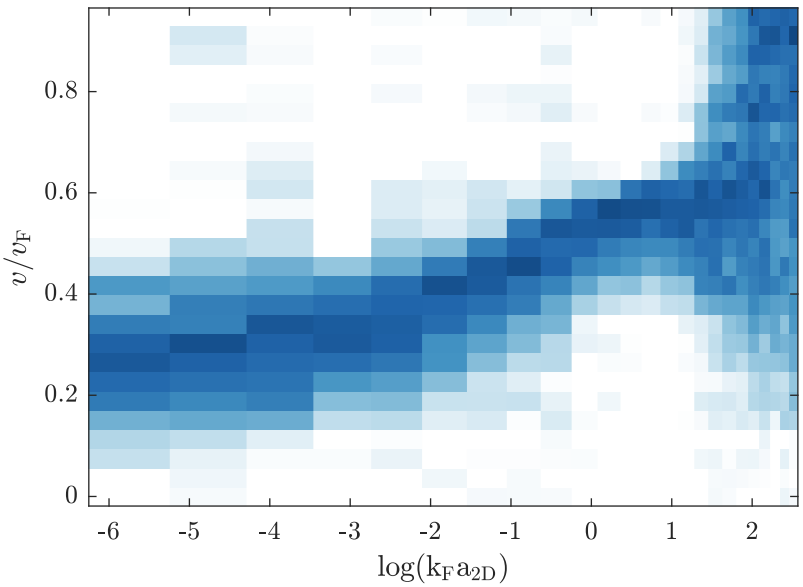

Figure 7.18: Evolution of the phonon mode in the crossover. Heating rate as a function of velocity and interaction strength, measured at a wavevector of $q = 0.3\,k_F$.

Fig. 7.18 shows the heating rate measured for systems that were prepared in the crossover, ramped to a variable interaction strength and exposed to the moving optical lattice with $q \approx 0.3\,k_F$ before slowly being ramped down into the BEC regime for thermometry. As the system approaches the crossover from the BEC side, the phonon mode moves to higher velocities and becomes more narrow. However, in the crossover at $\log(k_F a_{2D}) \approx 1$, the mode suddenly broadens into a continuum as the moving lattice begins to break pairs even at low wavevectors.

When the same measurement is repeated using an optical lattice with a wavevector of $q = 2\,k_F$, the resulting heating rate behaves quite differently, as one would expect (see fig. 7.19). In the BEC regime, the excitations are single particle excitations of dimers, as the moving lattice cannot break the tightly bound pairs. Therefore, these excitations occur at significantly higher velocities than the speed of sound, but the mode is mostly unaffected as the interaction strength changes. However, already at an interaction strength of $\log(k_F a_{2D}) < 0$, the mode broadens and pair breaking excitations become available in a wide continuum. As expected, the onset velocities for pair breaking excitations are significantly lower at $q = 2\,k_F$ than at low wavevectors, and decrease quickly as the BCS regime is approached.

From these two measurements combined, we can immediately see that the two-dimensional Fermi gas is superfluid throughout the BEC-BCS crossover. The velocities at which excitations are first created

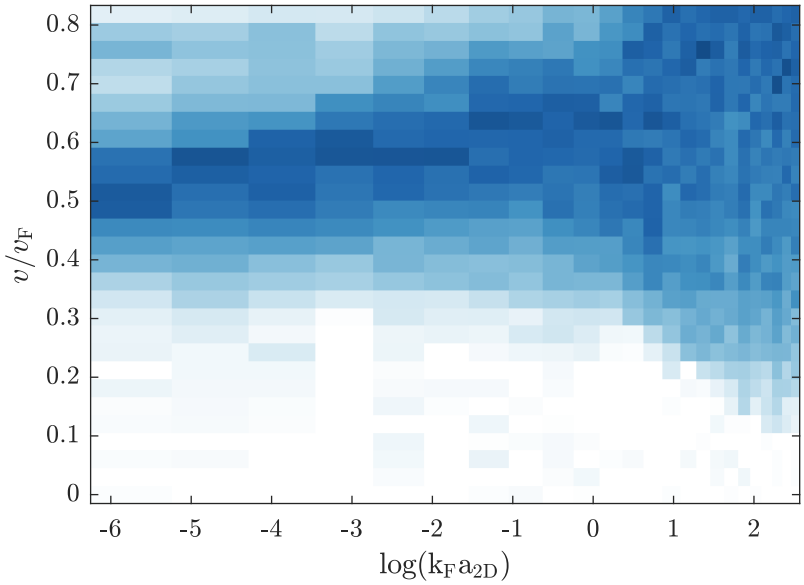

Figure 7.19: Evolution of single particle excitations in the crossover. The same measurement as in the previous figure, repeated at a wavevector of $q = 2\,k_F$. The behavior is qualitatively very different, with the broad continuum of pair breaking excitations starting further in the crossover and at lower velocities.

are plotted in fig. 7.20. We observe that low-wavevector excitations are created at much lower velocities in the BEC regime than high-wavevector excitations, in excellent agreement with theoretical expectations. In the crossover, pair breaking lowers the velocity for excitations to be created at higher wavevectors, and they start to be created before excitations at low wavevector become possible. Interestingly, for the two datapoints furthest in the BCS regime, the onset velocity for heating is lowest at $q \approx 0.3\,k_F$ and is fairly compatible with zero. This very likely indicates that the phase transition for superfluidity has been crossed, and the system is now in the normal state. We will readdress this point in a later section.

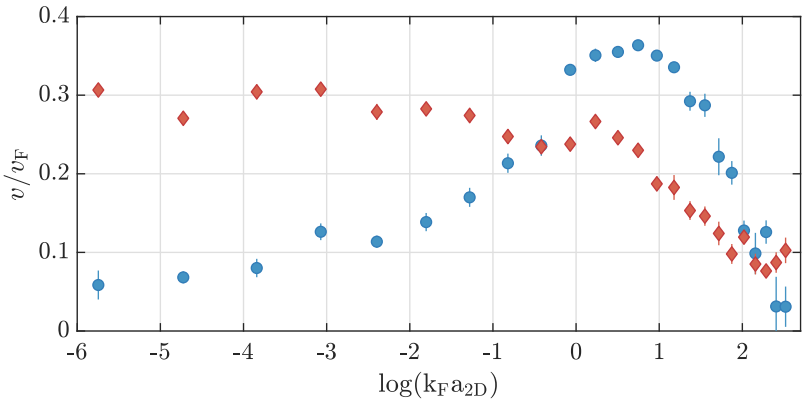

Figure 7.20: Onset velocities for excitations. Plotted is the fitted onset velocity for excitations to be created at $0.3\,k_F$ (**blue circles**) and at $2\,k_F$ (**red diamonds**). In the BEC regime, phononic excitations set the critical velocity, whereas in the BCS limit, it is set by pair breaking excitations. The onset velocity for excitations at $2\,k_F$ shows a small kink where the branch of single-particle excitations of molecules and the pair breaking continuum connect. At interaction parameters of $\log(k_F a_{2D}) > 2.3$, the measured onset velocities at low wavevector are compatible with zero, indicating that the phase transition has been crossed due to the decreasing critical temperature. Error bars denote 1σ confidence intervals of the fit.

Fig. 7.21 shows the resulting critical velocities, which are simply given by the smaller of the two fitted onset velocities. For comparison, the speed of sound c_s in the system is also shown, as well as a mean-field prediction for the pair breaking velocity $v_{pb} = \frac{\Delta}{k_F} = \frac{\sqrt{2E_B E_F}}{k_F}$ [59]. We find that the increase of the critical velocity in the BEC regime

follows the increasing speed of sound, reaching a maximum around $\log(k_F a_{2D}) = 0$ before pair breaking excitation suppress the critical velocity back down towards the BCS regime. The observed behavior is very similar to that reported in 3D Fermi gases, as expected given that the mechanisms at play are the same.

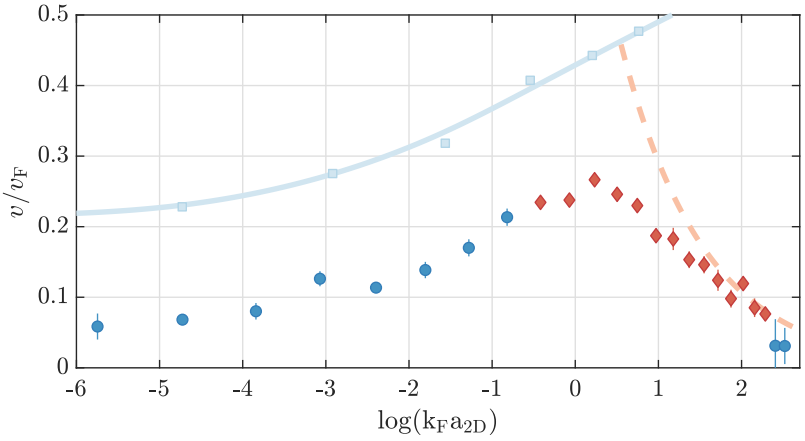

Figure 7.21: Critical velocity in the 2D BEC-BCS crossover. When the critical velocity is set by phononic excitations at low momentum (blue dots), it scales with the speed of sound in the system (light blue squares and solid line) [40]. In the crossover, the critical velocity is lowered by the onset of pair breaking excitations (red diamonds) and the resulting critical velocities approach the mean field prediction (dashed line). Error bars denote 1σ confidence intervals of the fit.

The critical velocities we measure in the BEC regime are, however, significantly below the theoretical limit of c_s also shown in fig. 7.21, a discrepancy which seems to vanish towards the BCS limit. One reason for this is simply the finite linewidth of the phonon mode: As damping of phonons through three- and four-phonon processes will inevitably cause phononic excitations to decay, the quasiparticle acquires a finite lifetime and thereby a non-zero linewidth that depends on the temperature and wavevector. However, the perturbation by the moving lattice also modifies the observed width of the mode, similar to the power-broadening of optical transitions. Especially far in the BEC regime, this effect can be quite severe, as the chemical potential of the dimers becomes very low. To remain in the limit of weak perturbation, we would therefore have to reduce the potential height of the lattice accordingly. To compensate for the loss of signal, we would then have to increase the time for which the system is perturbed by the moving lattice. However, collisional losses in the BEC regime also reduce the lifetime of the system, making such adjustments unfeasible. Therefore, we performed these measurements at a constant potential height, resulting in a width of the mode that is expected to increase towards the BEC regime, which is in good agreement with fig. 7.18, and therefore resulting in lower critical velocities the further in the BEC regime the measurement is performed.

We can find some intuition on how strong this effect would be from numerical simulations. In ref. [122], Singh and Mathey performed classical-field simulations for bosonic systems to study experiments such as the ones discussed in this chapter. The simulation results for the influence of temperature and potential height on the critical velocity are shown in fig. 7.22. Singh and Mathey observe a linear decrease in the critical velocity when the temperature is increased, allowing for

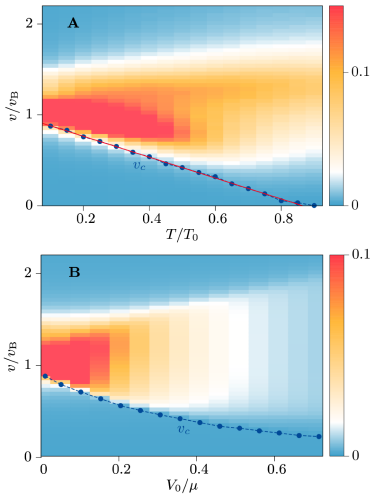

Figure 7.22: Influence of temperature and lattice potential height. Shown is the heating rate in arbitrary units as a function of temperature (A) and lattice potential height V_0 (B). Velocities are given in units of the speed of sound, here written as v_B, and temperatures in units of the BEC transition temperature T_0, which is an upper bound estimate for the critical temperature. Using classical-field simulations, Singh and Mathey simulated an experimental procedure comparable to the one described in this text for a bosonic superfluid at an interaction parameter of $\tilde{g} = 1.6$, comparable to a system far in the BEC regime in this chapter. The fitted critical velocities are found to decrease linearly with the temperature and nonlinearly with the height of the lattice potential. Figure adapted from [122].

an extraction of the critical temperature of the system where $v_c \to 0$. When the potential height of the moving lattice potential is increased, the critical velocity also decreases, but remains nonzero in the range of potential heights probed. From these simulations, we conclude that the observed suppression of v_c visible in fig. 7.21 is most likely the result of a combination of these two factors.

7.6 Measurement of the superfluid phase transition

Here, I show how critical velocity measurements can be used to determine the superfluid phase transition. I will show how we determine the critical temperature in the BEC regime using two independent methods of thermometry. Performing measurements at different interaction strengths, I extract the critical entropy for superfluidity and discuss its compatibility with previous measurements and predictions.

Now that we have established superfluidity in 2D Fermi gases, the natural next step is to ask about the phase transition: At what temperature does the system leave the superfluid phase and enter the normal state? As we have seen above, when the temperature of a system increases, the phonon mode becomes broadened until v_c reaches 0 at the critical temperature T_c. Therefore, measurements of the critical velocity can serve as a flexible tool to directly measure the phase boundary between the superfluid and the normal state.

To perform such measurements, we require a way to heat the system in a controlled fashion. Luckily, we have already found one: Using the moving optical lattice at a velocity equal to the speed of sound in the system, we reliably create phononic excitations that are ultimately converted into an increased temperature after thermalization. Because these excitations can be very long-lived in the crossover [40], we perform this heating procedure in the BEC regime where damping is substantial. This has the added benefit that we are able to calibrate the heating procedure directly, as thermometry is available in this regime. This calibration was already shown in fig. 7.11 D, where the temperature of the system is shown as a function of the heating time τ for which it is exposed to the moving lattice. The approximately linear increase in temperature reported there is in good agreement with eq. 7.1, which predicts a nearly constant heating rate. Therefore, we can control the temperature of the system by tuning the time for which it is exposed to the optical lattice moving at the speed of sound in the BEC regime.

Fig. 7.23 shows a sketch of the experimental sequence for these heating experiments. Note specifically that the potential height V_1 and the time τ' are varied depending on the experiment to achieve a compromise of negligible collisional losses, small potential height V_1 compared to the chemical potential of the pairs, and good signal-to-noise ratio.

While the moving optical lattice allows for a controlled heating process, there is one problem: The maximum velocity of the moving translation stage we use to set the lattice wavevector is quite slow. Travers-

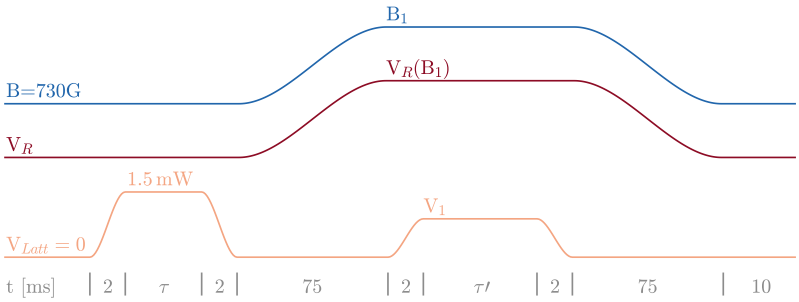

Figure 7.23: Sketch of the experimental sequence. The system is prepared in the BEC regime, at a magnetic field (blue line) of $B = 730\,G$, corresponding to $\log(k_F a_{2D}) \approx -2.8$. The dark red line shows the potential height of the confining ring potential V_R, which is always kept at a constant height relative to the chemical potential of the dimers. The orange line shows the potential height of the moving lattice. After the system has been prepared, the lattice is ramped on for a variable time τ at a constant potential height to heat the system. After heating, the interaction strength is set to the desired value and the moving lattice is ramped on at a variable time and height that depends on the experiment. Finally, the magnetic field is ramped back into the BEC regime to perform thermometry.

ing the full range of motion takes approximately 10 s, which is significantly longer than the time between the heating step and the critical velocity measurements of 75 ms. Therefore, heating has to be performed at the same wavevector q as the final measurement. Because of the difficulty of calibrating the heating procedure for each wavevector, we therefore only work at low wavevectors for these measurements. However, since the phononic excitations at low wavevector set the critical velocity in the BEC regime and parts of the crossover, this decision will only be problematic if we wish to measure further towards the BCS side.

Using the calibrated heating procedure, we can now perform the first measurements of the superfluid phase transition in 2D Fermi gases. For now, we will work at an interaction strength of $\log(k_F a_{2D}) = -2.8$, where our thermometry is accurate. Using a constant lattice wavevector of $q \approx 0.6\,k_F$, we measure the heating rate as a function of temperature and velocity. The result is shown in fig. 7.24. While the overall

The wavevector was chosen at this slightly higher-than-usual value for historical reasons. However, we do not expect this to significantly shift the resulting critical temperatures.

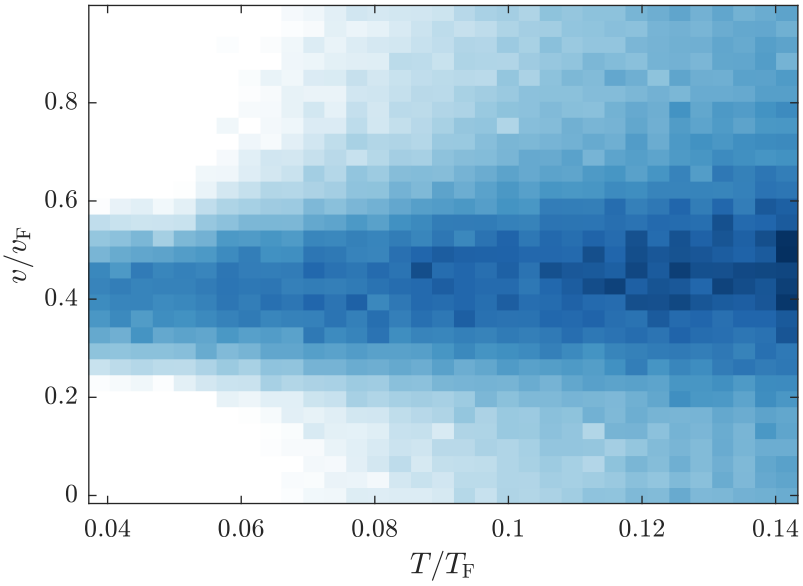

Figure 7.24: Heating rate as a function of temperature at an interaction strength of $\log(k_F a_{2D}) = -2.8$. As the temperature of a bosonic system is increased, the phononic mode remains mostly unaffected. The high velocity at which the mode is found is a result of the wavevector $q \approx 0.6\,k_F$, which is not deep in the phononic regime, but contains some contribution from single particle excitations for historical reasons.

temperature of the system increases as expected, the mode appears to remain mostly unaffected. To quantify this, we subtract the initial temperature as measured for a stationary lattice and fit the mode with

a Gaussian, which describes the lineshape well. The results of the fit are shown in fig. 7.25. We find that as the temperature of the sys-

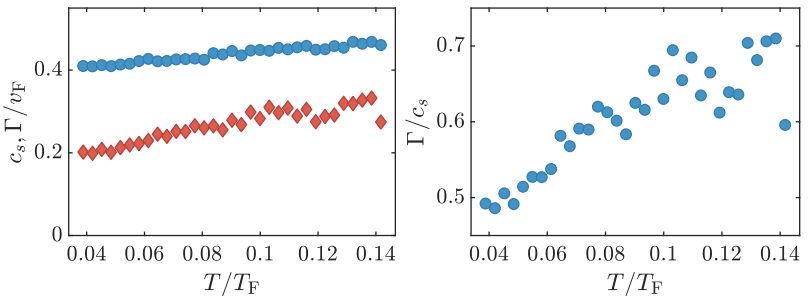

Figure 7.25: Fitted peak position c_s and linewidth Γ of the phonon mode. Left: Both the peak position (blue dots) and the linewidth of the mode (red diamonds, here given by its $1/e^2$ radius) increase with the temperature of the system. However, the increase in the peak position is relatively small. **Right**: The ratio between the linewidth and the peak position shows how the mode becomes less well-defined as the temperature of the system increases. Within the uncertainty of our measurement, the broadening of the mode and its position change continuously.

tem is increased, the phonon mode shifts slightly to higher velocities, indicating a subtle dependence of the speed of sound on the temperature. Additionally, the mode broadens quicker than it shifts, indicating that the phononic quasiparticles become less well-defined as the system is heated. Within the uncertainty of our measurement, we observe no sudden jump in position or damping of the sound mode as for example observed in unitary Fermi gases [123]. However, as the data becomes somewhat noisy at temperatures above $T \approx 0.1\, T_F$, such features may become apparent in more careful measurements in the future. The linear increase in Γ/c_s with temperature in the low temperature regime is in good agreement with theoretical predictions [124, 125], assuming a constant offset which might be a result of the non-negligible potential height of the optical lattice.

As we have discussed above, a simple way to obtain the temperature at which the phase transition occurs would now be to fit the onset velocity at which dissipation first occurs and find the temperature at which it becomes compatible to zero, as shown in fig. 7.22. However,

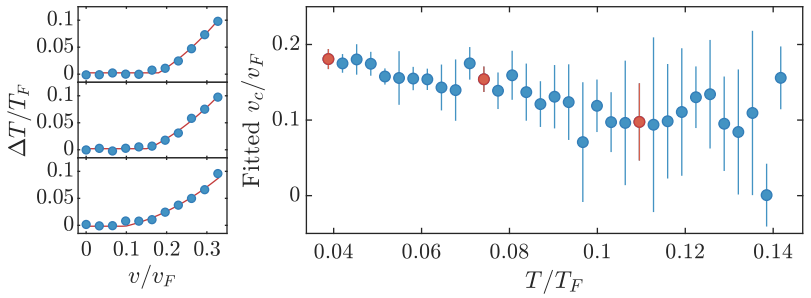

Figure 7.26: Fitting critical velocities. Left: Three exemplary heating rate curves from cold (top row) to hot (bottom row), shown with fits to the expression $r(v) = A \max(0, v^2 - v_c^2)$. As the temperature increases, the system more closely resembles a simple quadratic increase in temperature. However, the additional free parameter provided by a non-zero critical velocity will generally still increase the quality of the fit for realistic signal-to-noise ratios. **Right**: When plotting the fitted onset velocity for dissipation, it becomes immediately apparent that such a fit is not well suited to measure the decreasing critical velocity as the temperature is increased. The increase in the 1σ confidence interval of the fit towards higher temperatures shows the fit loses its predictive power, and the resulting onset velocities are no longer related to a true critical velocity but a mere result of over-fitting.

for signal-to-noise ratios obtained in our experiments, this approach is not as straightforward as it seems. In fig. 7.26, we show the heating rate for velocities below the speed of sound for different temperatures, together with fits to obtain the critical velocities. While for low temperatures, it is not difficult to fit the critical velocity, the predictive power of the fit is significantly reduced for hotter systems. This is due to the fact that the additional free parameter of v_c will almost always be able to to optimize the fit, even when there is no longer a critical

velocity present.

Therefore, we attempt to extract the location of the phase transition by quantifying this decrease in the predictive power of the fit. How well a fit describes a dataset while taking into account the number of free parameters is quantified by the **adjusted coefficient of determination** $\bar{R}^2$. In fig. 7.27, we plot the values of $\bar{R}^2$ for fits with and

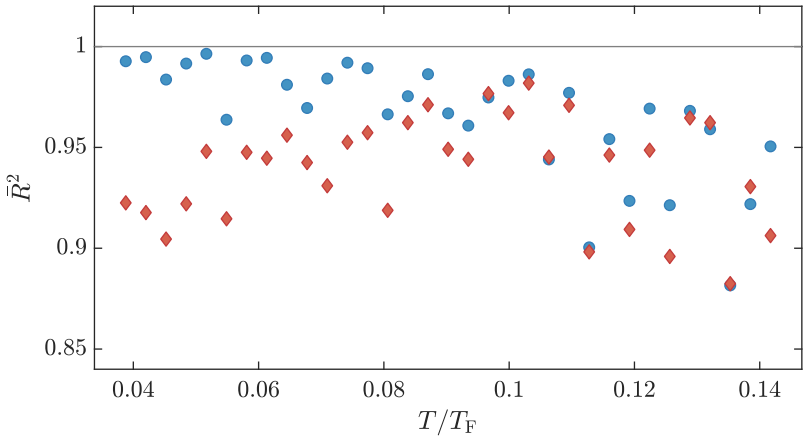

Figure 7.27: Comparing fits with and without v_c. Shown is the adjusted coefficient of determination of fits to the expression $r(v) = A \max(0, v^2 - v_c^2)$ with (blue dots) and without (red diamonds) nonzero v_c. For low temperatures, the data is significantly better described by fits with a critical velocity than by those without. As the temperature increases, this advantage decreases until both fits describe the data equally well when taking into account the different number of coefficients.

without a non-zero critical velocity. While there is quite a bit variation between the different temperatures due to noise, especially at higher temperatures, the fit allowing for a non-zero v_c is clearly better at low temperatures, whereas the difference is negligible at higher temperatures. Comparing the two values of $\bar{R}^2$, we can therefore get an estimate whether the system is well-described without a critical velocity, allowing us to extrapolate at what temperature the superfluid phase transition is crossed.

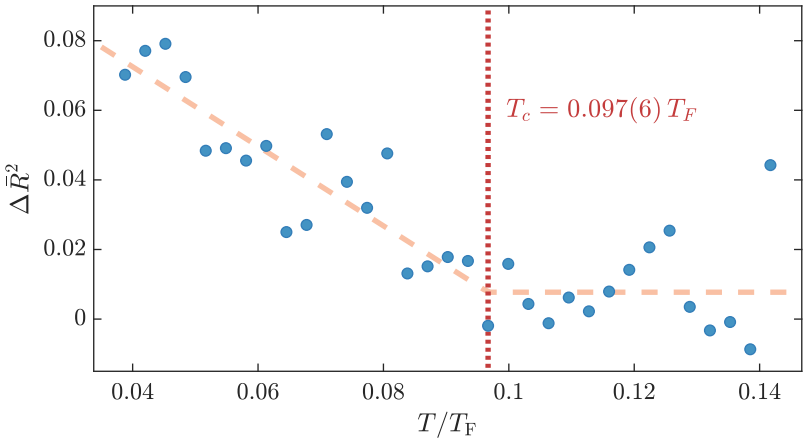

Figure 7.28: Critical temperature in the BEC regime. Plotted is the difference $\Delta\bar{R}^2$ between fits with and without a nonzero critical velocity. We observe a roughly linear decrease in $\Delta\bar{R}^2$ with temperature until it stabilizes close to 0. Performing a bilinear fit (orange dashed line), we obtain an estimate for the critical temperature (red dotted line).

In fig. 7.28, we plot the difference $\Delta\bar{R}^2$ between the adjusted coefficients of determination as a function of temperature. At low temperatures, we find that $\Delta\bar{R}^2$ decreases approximately linearly as the temperature is increased. At higher temperatures, we find negligible difference between the two fits, indicating that no critical velocity is

needed to explain the heating rate. By performing a phenomenological bilinear fit to the data, we obtain an estimate for the temperature at which the phase transition occurs. We find $T_c = 0.097(6)\,T_F$, in very good agreement with the observed onset of pair condensation [28] and theoretical predictions [29, 61, 126]. Furthermore, this critical temperature also appears to match the temperature where the relative width of the mode no longer increased linearly in fig. 7.25 and where the confidence intervals of the fit in fig. 7.26 suddenly increased, indicating a certain robustness of the method.

The error of the critical temperature corresponds to the 1σ confidence interval of the fit.

7.6.1 An alternate approach

While the method described above enables us to extract the critical temperature of our 2D Fermi gas, this measurement can only be as good as the underlying thermometry. Therefore, it is useful to verify the temperatures obtained from the momentum distribution using a different method. As we have established previously, the most common approach for thermometry not using the momentum distribution is to measure the density in regions of the trap where the potential is high, and n is thereby low enough to be thermal. However, our homogeneous systems do not feature a low density region, making such thermometry unfeasible. The reason no low density regions are present is that the gas is confined using a sharp repulsive ring potential significantly higher than the chemical potential of the pairs. Even if we lowered the potential height of the ring and allowed a few atoms to escape, the atoms outside the ring would be disconnected from those inside due to the high potential barrier, and no longer be thermalized.

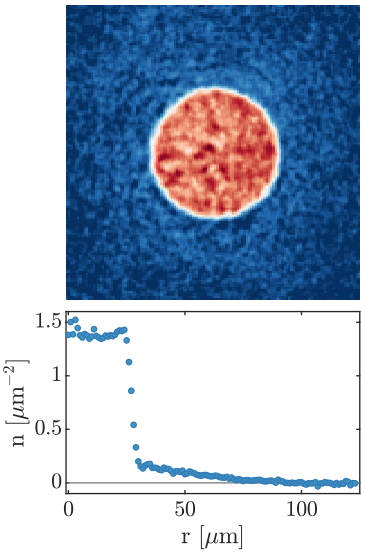

Figure 7.29: Alternative trapping setup
Top: *In situ* density distribution in the red box trap. **Bottom**: Radially averaged density distribution, showing the low density wings.

We circumvent this problem by implementing an alternative trapping setup which creates a homogeneous gas with thermal low density wings without using the ring beam. The new setup, which we will refer to as the red box, consists of a digital micromirror device (DMD) which allows us to realize arbitrary potentials in the atom plane and is illuminated with red-detuned ($\lambda = 780\,\mathrm{nm}$) light. Using this DMD, we create a radially symmetric potential well in the center of the underlying harmonic confinement from the curvature of the magnetic field, realizing a homogeneous density distribution in the center of the trap (see fig. 7.29). If the potential height of this DMD beam is now chosen to be comparable to the chemical potential of the pairs, some atoms can leave the central area and populate the surrounding harmonically confined parts of the trap. By tuning the potential height, we can vary this amount to ensure that only a small fraction of atoms is in the low-density wings. A great advantage of this setup is that as the potential in the low density wings is given by the curvature of the magnetic field, we know the potential energy of the atoms very well, which is of great importance for this method of thermometry. By fitting the *in situ* density distribution with a Boltzmann distribution, we obtain the temperature of the system.

We repeat the measurements shown above in this new trapping ge-

ometry, using this new *in situ* thermometry. The results are shown in fig. 7.30. We observe a similar decrease in the adjusted coefficient

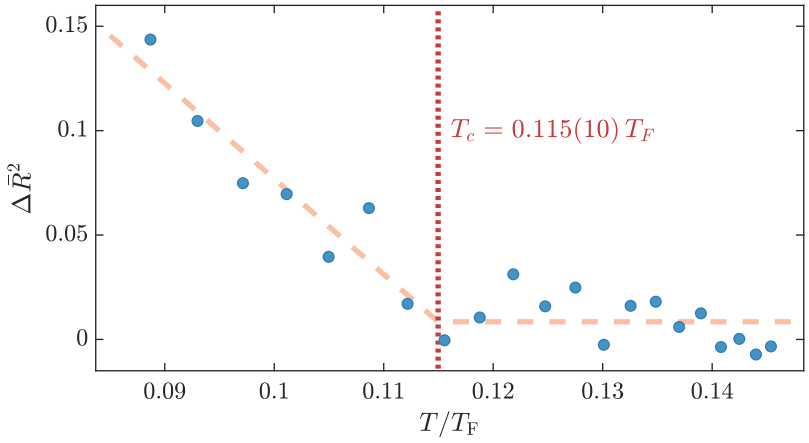

Figure 7.30: Critical temperature measured in situ. The same measurement as described previously, but performed in the red box trap. Thermometry is performed by fitting a Boltzmann distribution to the low density wings. The resulting critical temperature is approximately $0.02\,\mathrm{T_F}$ above than that obtained using time-of-flight thermometry.

of determination, allowing us to extract the temperature at which the phase transition occurs once again. Using this method, we find a critical temperature of $\mathrm{T_c} = 0.115(10)\,\mathrm{T_F}$ using the red box. The discrepancy of $\Delta\mathrm{T_c} \approx 0.02\,\mathrm{T_F}$ could arise from a number of reasons: First, inhomogeneities in the potential due to the optical lattice used for the 2D confinement could systematically shift the fit on the *in situ* data, most likely causing the temperature to be overestimated. Second, collisions during the time-of-flight would cause the temperature extracted from the momentum distribution to appear lower than it is, as momentum is redistributed inwards. Third, if thermalization is slow, the critical temperature obtained using the red box would appear larger than it should be, similar to the case discussed in [118]. Ultimately, it is difficult for us at this point to pinpoint the specific reasons for the discrepancy. However, since the difference between the two results is not too large, we will use it as an estimate for the systematic error on our temperature determination as $\mathrm{T_{err}} \approx 0.02\,\mathrm{T_F}$.

There is another clear difference between the results obtained in our usual homogeneous gas and those obtained using the red box: In the red box, the minimum temperature we were able to achieve appears to be approximately a factor of 2 above that realized in the homogeneous system. This most likely indicates that the ability for atoms to evaporate out of the homogeneous system by tunneling through the repulsive walls contributes significantly to the achievable temperatures. In the red box, where this option does not exist, the temperature is thereby limited to whatever value is achieved during the loading procedure, and is even further increased by photon scattering and intensity noise as the atoms now are confined in a region of high intensity. This leads to temperatures quite close to the critical temperature, making measurements of the phase transition difficult as it is easier to extrapolate if more data far from the transition is available. In fact, for most interaction strengths, we appear to be barely able to realize systems below the critical temperature in the red box. Therefore, while

an important crosscheck and useful to estimate the magnitude of systematic errors in our thermometry, we will be working in the homogeneous system for the remainder of this thesis.

7.6.2 The phase transition in the crossover

Now that we have established how we measure the critical temperature in the BEC regime, we turn to a discussion of the BEC-BCS crossover. However, as we have elaborated above, we are not currently able to measure the temperature for systems outside the BEC regime. Therefore, we will not be able to measure the critical temperature as a function of interaction strength. Nevertheless, the nearly adiabatic interactions strength ramps (see fig. 7.12) enable a different approach where we approximate that systems which have the same temperature after a slow ramp into the BEC regime have the same **entropy**. Preparing a system at its critical temperature and slowly ramping it into the BEC regime then results in a measure of its critical entropy, as the higher the temperature after the ramp back is, the higher the critical entropy of the system must have been.

At this point, the finite temperature equation of state of 2D Fermi gases is not known. Therefore, no statement can be made here on how the ratio between temperature T and entropy S evolves in the crossover and as a function of temperature, and we are henceforth unable to calculate the corresponding entropy S from the temperature $\tilde{T}$ in the BEC regime, and even less the temperature T from the entropy S. However, the evolution of the critical entropy nonetheless encapsulates important information about the robustness of the superfluid phase. This is a hotly debated topic, with a range of different results reported so far: On the experimental side, Ries and coworkers measured the critical temperature for pair condensation [28] and found a distinct maximum of the critical temperature in the crossover, exceeding the critical temperature in the BEC regime by around 50% (see fig. 7.31).

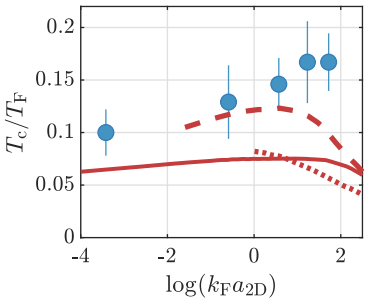

Figure 7.31: Critical temperatures from experiment and theory. Blue dots show the measurements performed in [28], red lines show the theoretical prediction of ref. [60] (dotted), ref. [126] (dashed) and ref. [61] (solid).

Note that as pair breaking excitations become relevant around $\log(k_F a_{2D}) \approx 0$, excitations at $2\,k_F$ might lower the critical temperature. However, as our heating procedure is limited to low wavevectors, we are unable to measure this effect directly. As pairing above T_c is expected to occur in the crossover region, we expect the critical temperature to still be set by phononic excitations, but more work is needed to verify this expectation.

Theoretical predictions [60, 61, 126] on the other hand generally find rather smooth evolutions of the critical temperature at lower values than reported in the experiment. While they still predict the critical temperature to be maximized in the crossover, they tend to predict a broad maximum with critical temperatures similar to those in the BEC regime. A measurement of the critical entropy in the crossover would represent an important piece of this puzzle. While not immediately comparable to previous work, it would provide another independent quantity for a finite-temperature theory to compete against.

We repeat the measurement described above for a range of interaction strengths, using the experimental sequence outlined in fig. 7.23. Fig. 7.32 shows four exemplary measurements in the crossover. We find a clear bilinear feature for all interaction strengths probed. We therefore prepare systems at the phase transition and measure their temperature $\tilde{T}_c$ after ramping back into the BEC regime, obtaining a proxy for the critical entropy in the system. Fig. 7.33 shows the re-

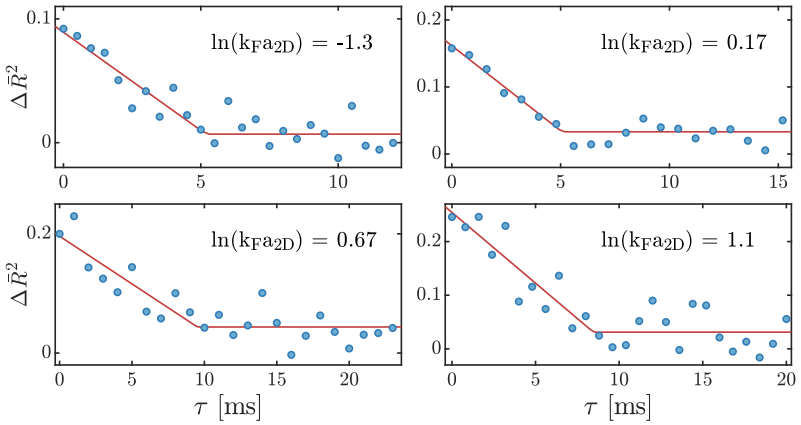

Figure 7.32: Critical temperature measurements in the crossover. Shown is the difference in the adjusted coefficient of determination as a function of heating time for four exemplary interaction strengths in the 2D BEC-BCS crossover. A roughly bilinear feature is observable for all interaction strengths probed, enabling us to locate the phase transition.

sulting values of $\tilde{T}_c$. We find little variation of $\tilde{T}_c$ as the interaction parameter is increased, indicating that the critical entropy does not change much in the 2D BEC-BCS crossover.

This is an intriguing and unexpected result. A constant critical entropy in the crossover would indicate that the robustness of the superfluid phase is not significantly affected by the interaction strength on the BEC side and in the crossover region, but might instead be limited by other effects such as the reduced dimensionality itself. This is reminiscent of the theoretical predictions [61] that predict a somewhat flat critical temperature, although as we have argued above, temperature and entropy cannot be directly compared in this fashion.

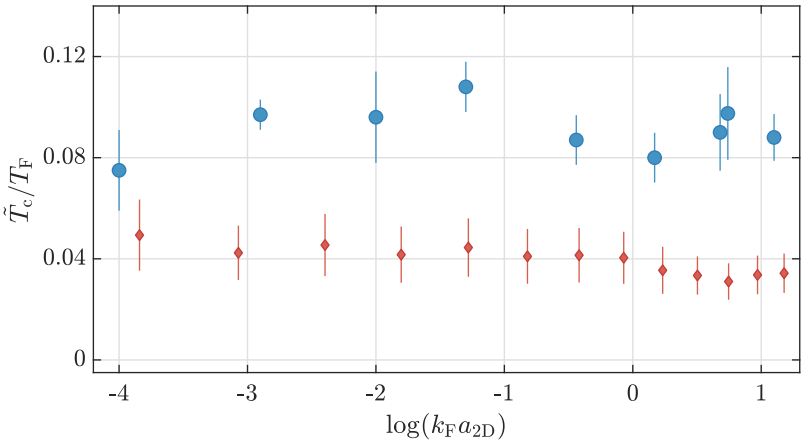

Figure 7.33: The phase transition in the BEC-BCS crossover. Shown is the temperature $\tilde{T}_c$ measured after a system prepared at the superfluid phase transition was slowly ramped into the BEC regime (blue dots), which is a proxy for the critical entropy. Surprisingly, we observe little change in $\tilde{T}_c$, indicating that the critical entropy for superfluidity is nearly constant in the crossover. For comparison, we also show the coldest temperatures $\tilde{T}$ we achieve in the crossover (red diamonds). These temperatures being significantly below the critical values $\tilde{T}_c$ shows that our measurements of the critical velocity in the crossover were performed well below the critical temperature for all but the lowest and highest interaction parameters. Error bars denote the 1σ confidence interval of the fit for $\tilde{T}_c$ and the standard error of the mean for $\tilde{T}$.

Of course, it is not possible for an additional measurement to resolve a discrepancy in qualitative behavior such as the one between refs. [28] and [60, 61, 126]. However, the complicated situation is further highlighted by a recent prediction for the relation between temperature and entropy in the BEC-BCS crossover. In ref. [127], Tononi and coworkers calculated the entropy of a system at constant low temperature of $T = 0.01\,T_F$, see fig. 7.34. They report that the entropy decreases at constant temperature as the system approaches the crossover. Assuming that the behavior is similar at higher tem-

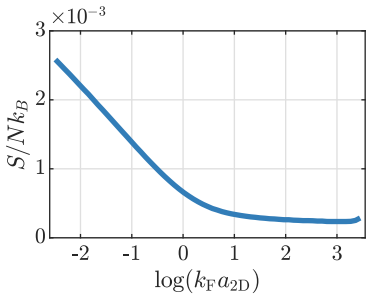

Figure 7.34: Entropy at constant temperature in the crossover. Entropy at constant volume at a fixed temperature of $T/TF = 0.01$ in the 2D BEC-BCS crossover. Figure adapted from [127].

peratures, such a behavior would indicate that the temperature of a system at constant entropy increases as the interaction parameter is increased and the BCS regime approached. Therefore, the mostly constant critical entropy we measure would correspond to an increasing critical temperature, compatible with the reported behavior from ref. [28]. This is a puzzling result especially considering that the calculated relation between entropy and temperature stems from the same theoretical framework used to calculate the flat critical temperatures in ref.[61].

At this point, this conundrum cannot be resolved. More work will have to be done on the finite-temperature equation of state, and on thermometry in the BEC-BCS crossover. One possible measurement would perform critical entropy measurements as described here and also measure the critical temperature for pair condensation as described in [28] to verify whether the two measurements are compatible using rapid ramp measurements for thermometry. An alternate approach could be to improve cooling in the red box trap to obtain a thermometry that should in principle work in the entire crossover. On the theory side, more work on the relation between entropy and temperature at strong interactions would aid in thermometry, and predictions of the critical entropy could be compared to our data and to those for the critical temperature.

Box 7.1: Temperature of the homogeneous system in the crossover

While we have established that it is difficult to measure the temperature in the 2D BEC-BCS crossover, the measurements described here can be used to derive an estimate of the temperature of our systems in the crossover. In the BEC regime, we have shown that our homogeneous Fermi gas is prepared at temperatures of $T = 0.04(1)\,T_F$, compatible with the previously reported value of $T \approx 0.03\,T_F$ [39]. In the BCS regime, we can make use of the fact that we appear to cross the phase transition at $\log(k_F a_{2D}) \approx 2.3$ and therefore $T \approx T_c$. Some publications predict critical temperature of $T \approx 0.07\,T_F$ at $\log(k_F a_{2D}) = 2.3$ [61, 126], but lower values of $T \approx 0.045\,T_F$ have also been reported [60]. As we have argued previously, the entropy of our homogeneous 2D Fermi gases seems to be roughly constant, and we can interpret fig. 7.34 to indicate that the temperature at constant entropy should increase in a monotonous fashion in the crossover. Therefore, by performing this comparison to theoretical predictions, the temperature of our homogeneous superfluids can be assumed to lie between $T \approx 0.04\,T_F$ and $T \approx 0.07\,T_F$ depending on the interaction strength.

8 MEASUREMENT OF THE EXCITATION SPECTRUM

In the following chapter, I will present the second main result of this thesis: the first momentum-resolved measurements of the excitation spectrum of two-dimensional Fermi gases.
I will begin with a brief overview over the different methods commonly used to study the excitation spectrum of ultracold Fermi gases. Employing the methods introduced in the previous chapter, I will present the first measurements of the dynamic structure factor of two-dimensional Fermi gases and its evolution in the BEC-BCS crossover. I will discuss how the Goldstone mode and the pair breaking continuum develop as the system changes from a fermionic to a bosonic superfluid, and comment on the interaction between the two modes. Finally, I will extract the superfluid gap and compare it to theoretical predictions.

The results presented in this chapter are adopted from

> *L. Sobirey, H. Biss, N. Luick, M. Bohlen, H. Moritz and T. Lompe*
> *arXiv:2106.11893 (2021) [12]*

and are reprinted here with modifications and additions.

Over the last decades, much effort has been invested in studying the ground state of ultracold Fermi gases. However, the ground state of a system is only a small part of it, and much of the intriguing physics of strongly correlated systems arises from their dynamics - that is, their response to external perturbations. How a system responds to perturbations is governed by its excitation spectrum, which describes how the system is modified as energy and momentum are added to bring it away from its ground state. Here, we will present the first measurements of the excitation spectrum of two-dimensional Fermi gases.

8.1 Previous work

So far, no measurements have been made on the excitation spectrum of two-dimensional Fermi gases beyond the frequency of the breathing mode in harmonically trapped systems [88, 89]. Therefore, in this section I will summarize some key measurements of the excitation spectrum of three-dimensional Fermi gases, focusing on the superfluid phase and on publications closely related to the results presented in this chapter. For a more thorough overview of spectroscopic measurements on ultracold Fermi gases, see e.g. ref. [128] and references therein.

There are two commonly used methods to study the excitation spectrum of ultracold Fermi gases: Radio-frequency (RF) spectroscopy and Bragg spectroscopy.

RF spectroscopy

The oldest and best established method to study the excitation spectrum of ultracold Fermi gases is RF spectroscopy. In brief, RF photons

of a well-defined energy are used to transfer atoms from one hyperfine state to another. If the final state is sufficiently weakly interacting, this process can be described as the removal of a fermion, and the energy of the RF photon can be related to the single-particle excitation spectrum E_k (see section 4.3). As the momentum of RF photons is negligible, the momentum of the transferred fermion is essentially unchanged during this process. However, the momentum is not always straightforward to measure, and therefore many studies using RF spectroscopy simply record the amount of transferred atoms as a function of the energy of the RF photons.

One key study that exemplarizes RF spectroscopy was performed by Schunck and coworkers in 2008 [130]. They prepared Fermi gases of ultracold ^{6}Li in a mixture between the lowest and third-lowest hyperfine states. This so-called 1-3 mixture has the advantage that close to the location of the Feshbach resonance [19, 84], the final state (the second lowest hyperfine state) is only weakly interacting with the other two, allowing final state interactions to be neglected. Therefore, the resulting RF spectrum can be interpreted in a straightforward fashion as a measurement of the properties of the interacting 1-3 mixture.

Fig. 8.1 shows the resulting RF spectra, together with fits to the theoretically expected lineshape. Roughly speaking, the observed lineshape is mostly set by the superfluid gap, which sets the minimum energy to remove a particle from the interacting many-body system and thereby gives rise to a sharp onset of dissociated pairs. Towards higher energies, the dissociation rate slowly decreases again, which can be interpreted as a result of the finite size of the pairs. This allowed Schunck and coworkers to derive an estimate of the pair size in the BEC-BCS crossover. However, the RF spectrum is subject to Hartree shifts that result from the interaction between the spin states [132]. These shift the onset of the RF spectrum by $U = gn$, and therefore additional input from theory is required to obtain the superfluid gap from the RF spectrum (see section 4.1). This question was revisited by Schirotzek and coworkers in ref. [133]. By introducing a local spin imbalance and using theoretical calculations of the Hartree shift, they were able to obtain the first measurements of the superfluid gap in the BEC-BCS crossover.

A more uncommon variant called spin injection spectroscopy adds a particle to the system by transferring it from a weakly interacting initial state, see e.g. [129]. This method therefore probes the unoccupied states in the system, as opposed to more traditional RF spectroscopy which probes the occupied states.

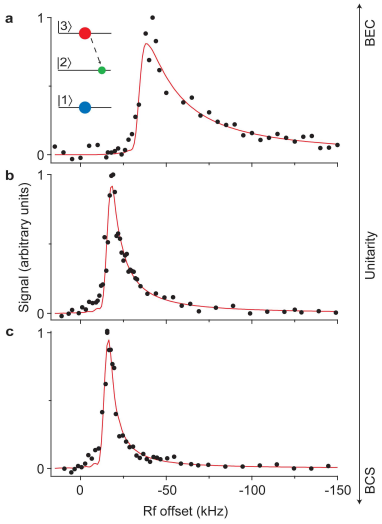

Figure 8.1: RF spectra of gases in the BEC-BCS crossover. Datapoints quantify the amount of atoms transferred from the third to the second lowest hyperfine state by a RF pulse; red lines are fits using the typical lineshape of a pair dissociation spectrum. Adapted from [130].

Note that the magnitude of the pair size obtained in [130] likely requires a correction, as discussed in [131].

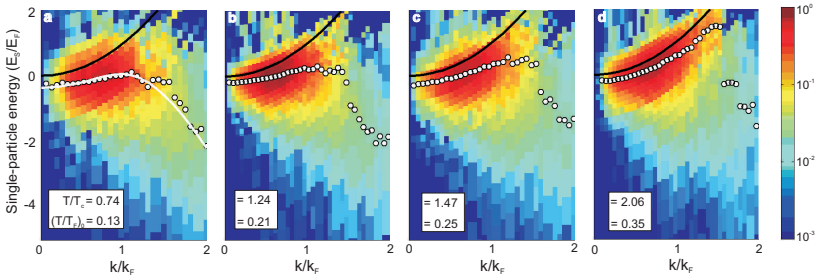

Figure 8.2: Photoemission spectra around the critical temperature. The plotted intensity map describes the number of atoms transferred to a weakly interacting state as a function of energy and momentum for a system at an interaction strength of $1/k_F a_{3D} \approx 0.15$. The white points mark the center of an individual column, extracted by a Gaussian fit; the black line shows the dispersion of an ideal Fermi gas; the white line is a fit to the data with a BCS quasiparticle dispersion. Backbending of the dispersion can be observed well above the critical temperature. Adapted from [134].

While RF spectroscopy as performed in [130, 133] is a powerful tool to study the properties of ultracold Fermi gases, the loss of momentum information often requires substantial theory input to extract quantita-

tive information about the system. This can be a significant limitation of the method in the strongly correlated crossover regime, where theoretical calculations are extremely challenging and hard to verify. In [135], Stewart and coworkers performed RF spectroscopy while additionally measuring the momentum of the transferred fermions. This allowed them to directly observe a BCS-like quasiparticle dispersion in a strongly interacting Fermi gas and later study its temperature-dependence [134] (see Fig. 8.2). Such momentum- and energy resolved RF spectroscopy is sometimes referred to as photoemission spectroscopy due to its close similarity with angle-resolved photoemission spectroscopy (ARPES) measurements performed on superconductors.

For a review of ARPES in cuprate superconductors see [136]; for a more recent review see [36].

Bragg spectroscopy

A different approach commonly used to study the excitation spectrum of ultracold Fermi gases is Bragg spectroscopy, which we have previously introduced in section 4.4. The key difference between RF and Bragg spectroscopy is that RF spectroscopy changes the number of particles in a spin state, while Bragg spectroscopy does not. This fundamentally changes what information is contained in the resulting spectra: RF spectroscopy generally yields information about the energy and momentum the removed atom had before removal, and can therefore be a useful tool to describe the ground state of a system. On the other hand, Bragg spectroscopy yields information about the excited states the atom is transferred to, and can therefore be used to understand correlations and dynamics within the system. Another way to phrase the differences between RF and Bragg spectroscopy is to say that RF spectroscopy contains information on either the occupied or the unoccupied states of the system, whereas Bragg spectroscopy combines information from both. Additionally, because Bragg spectroscopy excites atoms within the many-body system, the initial and final states are subject to the same Hartree shift, enabling measurements of many-body quantities without additional input from theory.

More formally speaking, we can describe RF spectroscopy by a two-operator term $(c_k^\dagger c_k)$, whereas Bragg spectroscopy is described by a four-operator term $(c_{k+q} c_{k+q}^\dagger c_k^\dagger c_k)$.

Note that there exists a variant of Bragg spectroscopy called stimulated Raman spectroscopy where the detuning between the beams is chosen such that particles are transferred from one spin state to another [137]. It is therefore described by a two-operator term much like RF spectroscopy, but retains some of the advantages of Bragg spectroscopy in momentum selectivity and control over the light field.

In ultracold Fermi gases, Bragg spectroscopy has been employed to study quantities such as pair condensation [138] and Tan's contact [77, 139–144]. In ref. [69], Hoinka and coworkers measured the dynamic structure factor at a low momentum transfer of $q \approx 0.5\,k_F$ and observed two distinct features, which they attributed to the pair breaking continuum and the Goldstone mode (see section 4.4 and fig. 8.3). By detecting the onset energy for pair breaking excitations, they were able to perform the first measurements of the superfluid gap in ultracold Fermi gases that did not require input from theory. However, due to the fixed, somewhat small transferred momentum in their experiment, the superfluid gap could only be measured over a small range of interaction strengths.

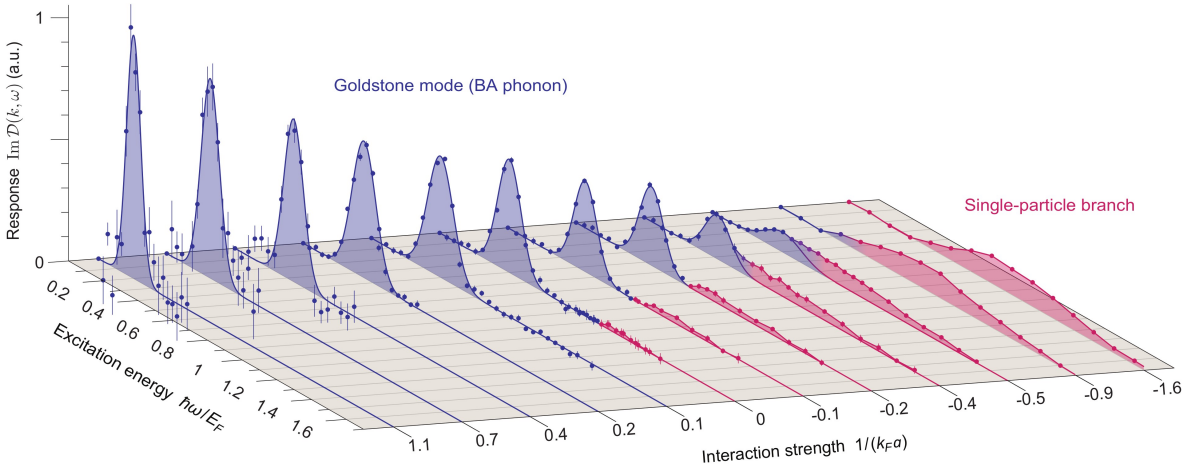

Figure 8.3: Bragg spectra in the BEC-BCS crossover. By performing Bragg spectroscopy at a fixed momentum transfer of $q \approx 0.5\,k_F$, Hoinka *et al.* observed two different features depending on the interaction strength: The Goldstone mode (blue datapoints and fits) and the single-particle or pair breaking continuum (red datapoints and fit). From [69].

8.2 The excitation spectrum in the BEC-BCS crossover

In this section, I will present our results on the momentum-dependent excitation spectrum of two-dimensional ultracold Fermi gases. I will discuss the different types of excitations present in the system and describe their interaction dependence.

As we have discussed in section 4.4, there are two main types of excitations in ultracold Fermi gases in the BEC-BCS crossover. The first are pair breaking excitations, where a single-particle excitation breaks apart a Cooper pair. These excitations should be dominant in the BCS regime, where pairs are weakly bound and large, and get suppressed towards the BEC regime as the pairs become more and more tightly bound. The second are collective excitations, where a fluctuation of the superfluid phase propagates in the form of a phonon. These excitations form the Goldstone mode of the superfluid, as described in section 4.1, and should therefore persist throughout the BEC-BCS crossover as long as the system remains superfluid.

Besides changing how likely pair breaking excitations are to occur, changing the interaction strength must also change where in the dynamic structure factor these two types of excitations can be found. Pair breaking excitations can only occur for energy transfers that exceed 2Δ, where Δ is the superfluid gap. On the other hand, the energy of the Goldstone mode will be a linear function of the momentum transfer at low energies, with a slope that changes in the crossover with the speed of sound in the system. Finally, some additional physics must occur where these two modes meet, as there is no mechanism that would stop a phonon from breaking a Cooper pair and therefore

a coupling between the two types of excitations must exist.

To investigate the evolution of these excitations in the 2D BEC-BCS crossover, we prepare and probe systems as described in chapter 7: We prepare homogeneous two-dimensional Fermi gases and use the moving optical lattice to perform optical Bragg spectroscopy [75, 120, 145–147], which measures the dynamic structure factor $S(q, \omega)$ of the system as discussed in section 4.4.

8.2.1 The dynamic structure factor of a strongly interacting 2D Fermi gas

Fig. 8.4 shows the measured dynamic structure factor in the strongly interacting crossover regime at an interaction strength of $\log(k_F a_{2D}) = 1.1$. The two types of excitations can clearly be identified in this measurement: A well-defined Goldstone mode at low momenta, as well as a continuum of pair breaking excitation at higher momenta.

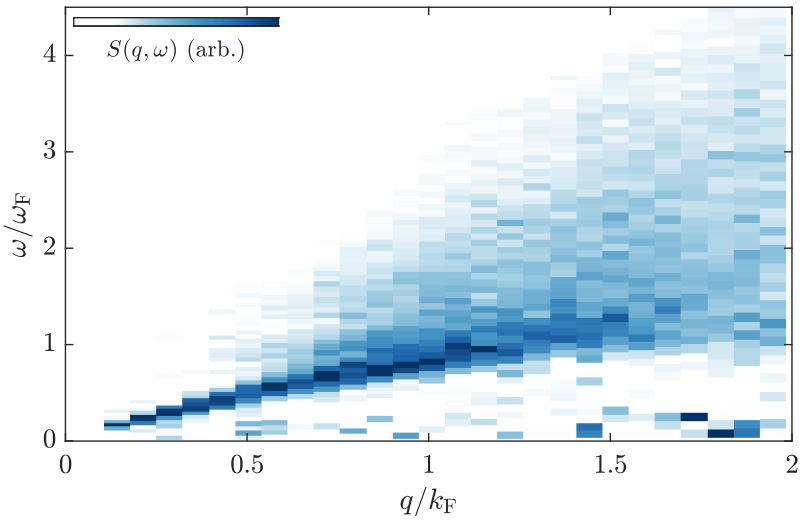

Figure 8.4: $S(q, \omega)$ **measured at** $\log(k_F a_{2D}) = 1.1$**.** We observe a broad continuum of pair breaking excitations as well as a well-defined Goldstone mode. Where the two modes meet, the Goldstone mode appears to bend down.

Note that the noise at low detunings in all measurements of the dynamic structure factor presented here arises as a result of dividing the measured heating rate by the detuning ω to obtain $S(q, \omega)$.

At low momentum and energy, our measurements feature a clear Bogoliubov-Anderson phonon, with a linear dispersion $\omega = c_s q$ set by the speed of sound c_s in the system. The width of the phonon mode is small compared to its energy, indicating well-defined phononic quasiparticles and therefore superfluidity [123]. As the phononic mode approaches the pair breaking continuum, we observe a pronounced downbending, reminiscent of an avoided crossing with the continuum. This behavior had been predicted to occur in three-dimensional Fermi gases [67, 148] and appears in RPA calculations of the dynamic structure factor of two-dimensional [66] and three-dimensional [68, 69] Fermi gases, but had not previously been observed. It clearly demonstrates a coupling between phonons and broken Cooper pairs.

Broken Cooper pairs are themselves quasiparticles and correspond to a bound state of a particle and a hole. They are sometimes called Bogoliubov quasiparticles or Bogoliubons in condensed matter physics.

At higher energies and momenta, the measured dynamic structure factor features the broad continuum of pair breaking excitations expected for a superfluid that consists of paired fermions. Although the

sharp onset of the continuum at 2Δ is masked by the presence of the Goldstone mode, fig. 8.4 nevertheless directly shows a suppression of pair breaking excitations for detunings $\omega \lesssim \omega_F$, most clearly visible at momentum transfers around $q \approx 2\,k_F$. We also observe that the pair breaking continuum is suppressed at low transferred momentum. This suppression can be interpreted as the result of a size mismatch between the low momentum (long wavelength) excitations and the size of the Cooper pairs [149, 150]: If the pairs are much smaller than the wavelength of the optical lattice, there is little differential force acting on the fermions, and the pairs experience the optical lattice as one particle. Intuitively speaking, we can say that the optical lattice no longer resolves the constituents of the pairs. We will revisit this effect in section 10.1.

8.2.2 Changing the interaction strength

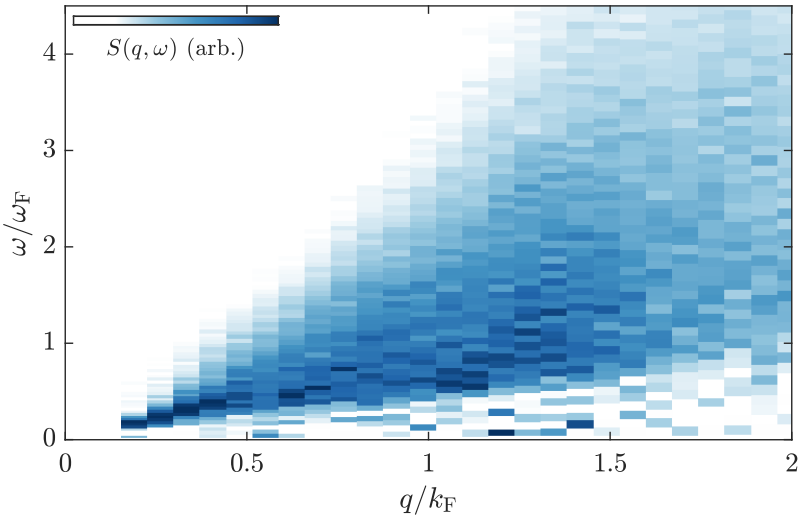

Figure 8.5: $S(q,\omega)$ **measured at** $\log(k_F a_{2D}) = 1.6$**.** Towards the BCS regime, the pair breaking continuum expands towards lower energies and momenta. While the Goldstone mode still persists, it is heavily broadened at intermediate momenta, leading to a seemingly momentum-dependent onset of the pair breaking continuum.

Next, we prepare systems with weaker attractive interatomic interactions. Fig. 8.5 shows the measured dynamic structure factor at an interaction strength of $\log(k_F a_{2D}) = 1.6$. Compared to the measurement performed at $\log(k_F a_{2D}) = 1.1$, we can directly see that the pair breaking continuum has become more prominent, extending over a wider range of momenta and energies. Furthermore, while the Goldstone mode is still present at low momentum and energy transfer, it appears to vanish quickly into the continuum. However, when looking at large transferred momentum, it becomes clear that the onset of the pair breaking continuum does not occur until $\omega \approx (0.7 - 0.8)\,\omega_F$. Consequently, the phononic mode is still present for a sizeable range of momenta, but appears to be so heavily broadened that it is no longer possible to visually separate it from the pair breaking continuum anywhere except at the lowest transferred momentum. While so far not understood, possible reasons for this broadening could include an increase in the coupling between the two modes towards the

BCS regime, a change in the available damping mechanisms of phononic excitations, or an increase in T/T_c.

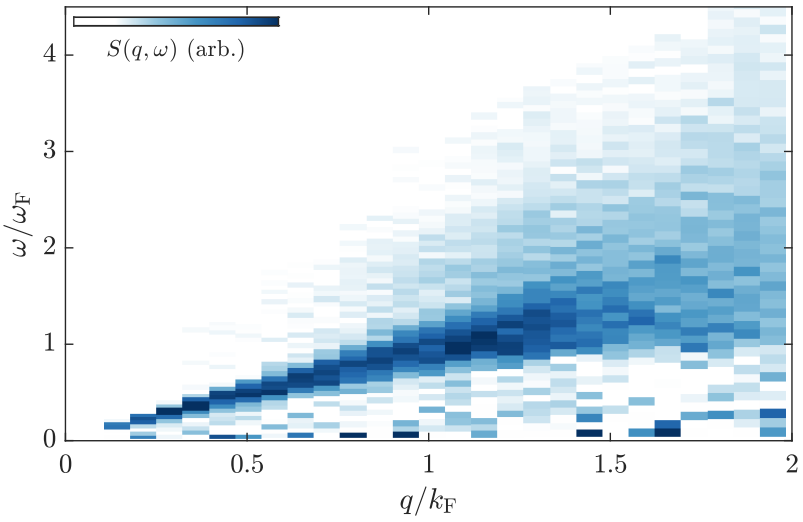

Figure 8.6: $S(q,\omega)$ **measured at** $\log(k_F a_{2D}) = 0.7$**.** Towards the BEC regime, the Goldstone mode gains relative weight as the pair breaking continuum is suppressed everywhere except at high energy and momentum transfers. The downbending of the Goldstone mode is still visible, but much weaker than further towards the BCS regime.

If we instead prepare systems with stronger attractive interatomic interactions, we see the opposite trend: Fig. 8.6 shows the result of a measurement performed at an interaction strength of $\log(k_F a_{2D}) = 0.7$. Compared to fig. 8.4, we can observe a significantly more pronounced Goldstone mode that no longer appears to cross into the continuum, but rather seems to partially coexist with it. The continuum itself is significantly less pronounced, and only found at higher energies and momenta. Interestingly, we still observe some downbending of the phononic mode, showing that the coupling between the two modes still persists at this interaction strength. However, the effect of the continuum on the phononic dispersion has significantly diminished compared to the measurements performed further in the crossover regime, indicating that this coupling becomes weaker towards the BEC side of the crossover.

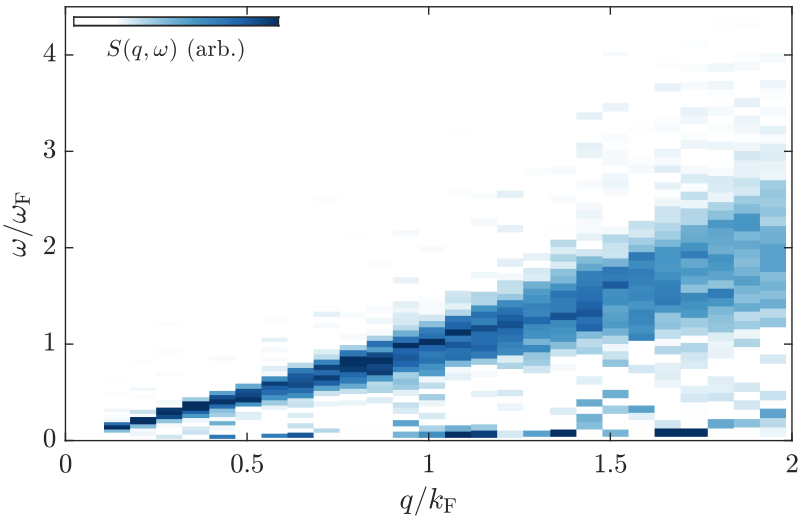

Figure 8.7: $S(q,\omega)$ **measured at** $\log(k_F a_{2D}) = -0.1$**.** Even further towards the BEC side, no more pair breaking continuum is visible.

Fig. 8.7 shows a measurement performed at an interaction strength of $\log(k_F a_{2D}) = -0.1$. At this interaction strength, the phonon mode has a nearly linear dispersion over the entire momentum range probed. The pair breaking continuum is no longer directly visible. However, the increasing width of the phonon mode towards higher momenta is most likely still a result of a coupling to pair breaking excitations.

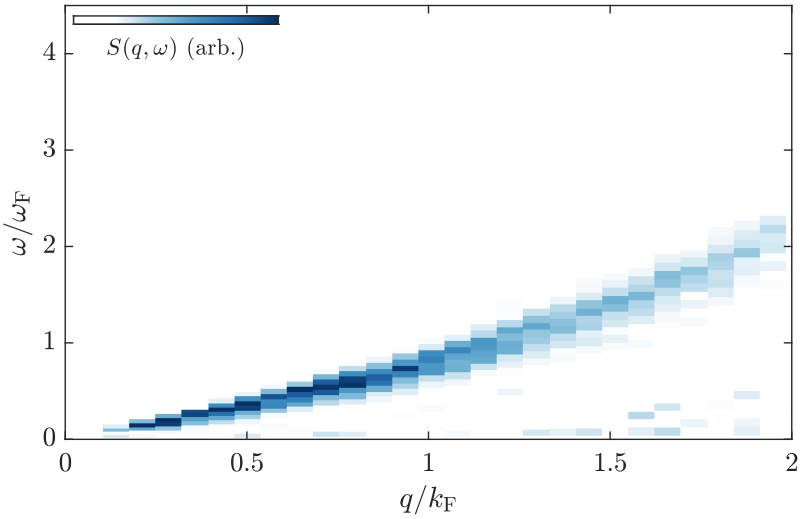

Figure 8.8: $S(q,\omega)$ **measured at** $\log(k_F a_{2D}) = -1.8$**.** Well in the BEC regime, we observe the Bogoliubov dispersion relation of a strongly interacting Bose gas.

Finally, fig. 8.8 shows the measured dynamic structure factor at an interaction strength of $\log(k_F a_{2D}) = -1.8$, well in the BEC regime. Here, the pairs are bound tightly, and pair breaking excitations due to the moving optical lattice can no longer occur at the energies and momenta probed here. Instead, the pairs are excited as single particles, and we observe a free particle dispersion of pairs at larger momentum transfers. The system is therefore well described as a strongly interacting Bose gas, and the dynamic structure factor simply shows the expected Bogoliubov dispersion relation, see section 4.1.

Fig. 8.9 displays the complete set of measured dynamic structure factors, spanning the entire 2D BEC-BCS crossover. The red lines at low momentum show the speed of sound in the system and are taken from the measurements we performed in ref. [40]. As expected, they are in excellent agreement with the slope of the Goldstone mode.

Fig. 8.9 clearly shows the smooth evolution from BEC to BCS superfluidity that occurs in the crossover. With increasing $\log(k_F a_{2D})$, we observe how the Goldstone mode increases in slope, but at the same time bends down and becomes more broadened as the pair breaking continuum gains in prominence. At the same time, these measurements reveal the smooth expansion of the pair breaking continuum towards lower energies and momenta. The momentum-dependence of the pair breaking continuum gives rise to an interesting observation: At low momentum transfer (and thereby long wavelengths), pair breaking excitations have little relevance for the dynamics and correlations of a system in the crossover, even though there is a significant amount of pair breaking excitations already available at larger mo-

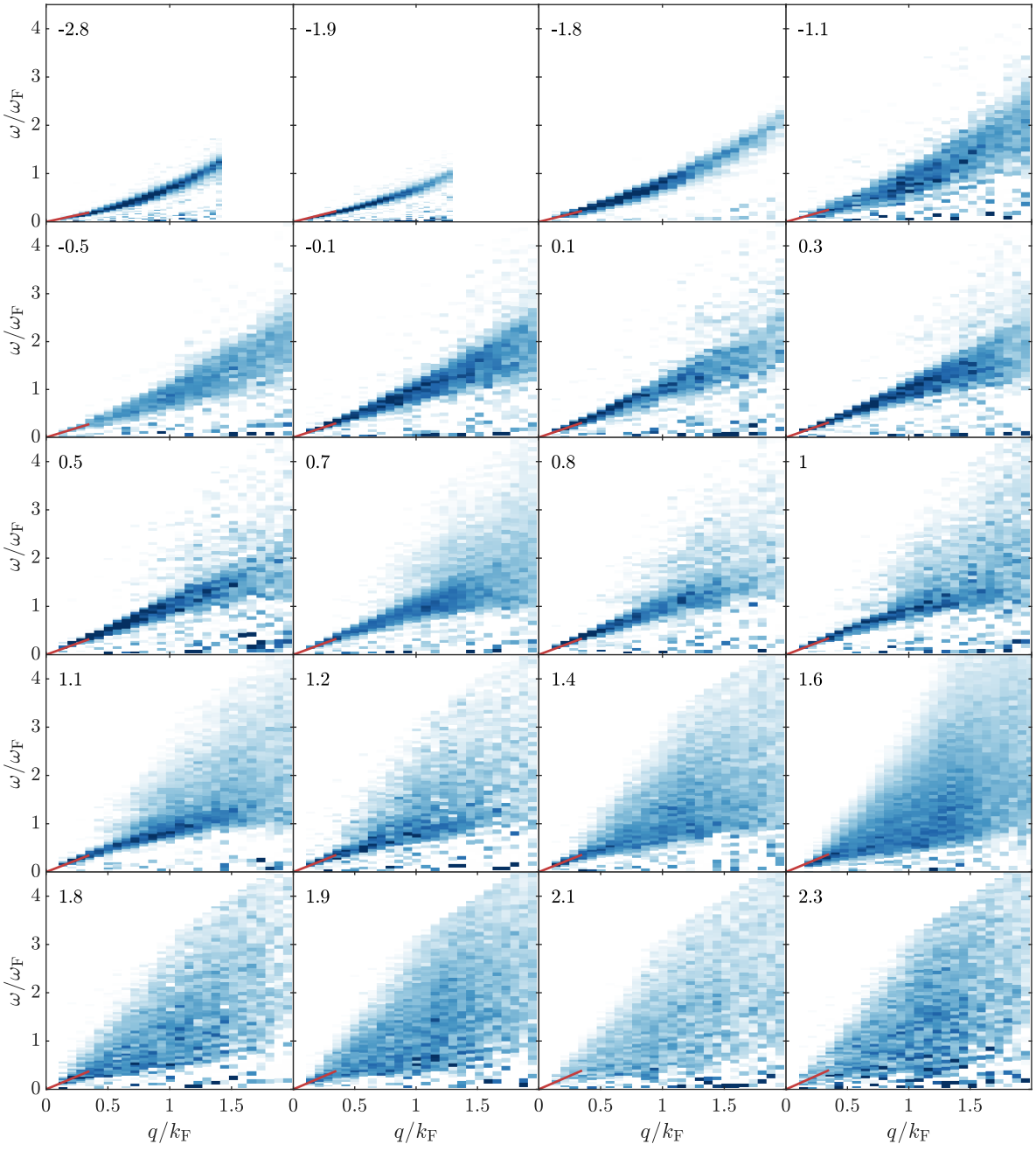

Figure 8.9: Full overview over all measurements of $S(q, \omega)$. The numbers in the top left corner denote the interaction parameter $\log(k_F a_{2D})$. The red lines are derived from an independent measurement of the speed of sound performed in [40] and show excellent agreement with the slope of the Goldstone mode. The smooth evolution of the excitation spectrum in the 2D BEC-BCS crossover is clearly visible. Note that the first two panels were measured with a higher density, leading to a smaller probed momentum range when normalizing with the Fermi wavevector. On the BCS side of the crossover, the pair breaking continuum is cut off as larger detunings were not measured.

mentum transfers (shorter wavelengths). This observation also holds for small and large energy transfers, corresponding to long or short timescales of observations. Whether a fermionic superfluid resembles a system of bosons or a system of paired fermions therefore depends entirely on the distance and time over which it is probed [151].

8.3 The superfluid gap

In this section, I will discuss how we extract the superfluid gap Δ from our measurements of the dynamic structure factor. I will introduce the two different methods we use to obtain Δ and discuss their limitations. Finally, I will present our results on the superfluid gap in the 2D BEC-BCS crossover and compare the results to predictions from theory.

The superfluid gap is one of the central quantities in the description of fermionic superfluids. It is one of the two key parameters derived in BEC-BCS theory (see section 4.3), sets the energy cost required to break apart the pairs that form the superfluid, and in the BCS limit is directly proportional to the critical temperature and the critical current. Therefore, we can consider it to be a key parameter that quantifies the stability of the superfluid phase.

Here, we use our Bragg spectroscopy measurements to obtain the superfluid gap in the two-dimensional BEC-BCS crossover. This is complicated by the presence of the Goldstone mode at energies below the onset of the continuum at 2Δ, which prevents us from directly reading off the gap from our measurements of $S(q, \omega)$. In the following, we will therefore present two different methods used to circumvent this problem and obtain the superfluid gap.

8.3.1 Integrating out the momentum dependence

The first method we use to extract the superfluid gap from measurements of $S(q, \omega)$ was motivated by electronic Raman scattering (ERS) in solid state physics (see box below). In s-wave BCS superconductors, the Raman response (quantifying the probability of creating an excitation as a function of the transferred energy) is expected to show a sharp onset at 2Δ [152], with some momentum dependence in the shape at larger energy transfers. Most measurements of the Raman response in solid state systems essentially sum together contributions from different momenta, and due to experimental broadening, the sharp onset then generally appears as maximum in the measured Raman response.

While ultracold quantum gases do not need to worry about many of the different excitation modes particular to solid state systems like lattice phonons and magnons, they feature a Goldstone mode below 2Δ, which is absent in charged superfluids [65]. However, the pair breaking continuum extends over a wide range of transferred momenta, whereas the Goldstone mode is only present at a specific momentum transfer given by its dispersion $\omega(q)$. Therefore, we decided to integrate over the available momentum range in our measurements

to obtain

$$S(\omega) = \int_{q_{exp,min}}^{q_{exp,max}} S(q,\omega)\, q\, dq \quad , \tag{8.1}$$

which we shall refer to as the Raman response for simplicity. Here, we have carried out the integration in polar coordinates as ultracold quantum gases are isotropic due to their contact interactions, but our measurements only probe excitations in the direction of the moving optical lattice. The Raman response as given by eq. 8.1 therefore quantifies the probability to create an excitation at a given detuning ω, regardless of the direction in space. However, we note that the conclusions drawn in the following are not significantly affected if the integration is performed only along the direction of the lattice.

Since all measurements in this chapter are presented in arbitrary units, we have omitted constant prefactors for clarity.

Box 8.1: Electronic Raman scattering

Electronic Raman scattering (ERS) is a technique used in solid state physics that, similar to Bragg spectroscopy in ultracold quantum gases, essentially measures the dynamic structure factor of a material. It is described in detail in [153]. In short, light with a well-defined wavelength is directed at the material and inelastically scattered by the electrons in the solid. By detecting the wavelength difference of the scattered photons, the energy transferred to the electrons can be inferred. Choosing specific polarizations of the incident and measured light additionally enables some degree of momentum selectivity.

Presented to the right is an exemplary result of such a measurement, showing the Raman response (which is proportional to the dynamic structure factor, integrated over a range of momenta) as a function of the energy transfer at different temperatures. The sharp feature at low energy transfer corresponds to the excitation of a lattice phonon, whereas the two broad maxima correspond to the superconducting gaps of the inner and outer copper-oxide planes in a bismuth-based cuprate superconductor. Note how experimental broadening and gap anisotropy smooth out the sharp features expected from the superconducting gap.

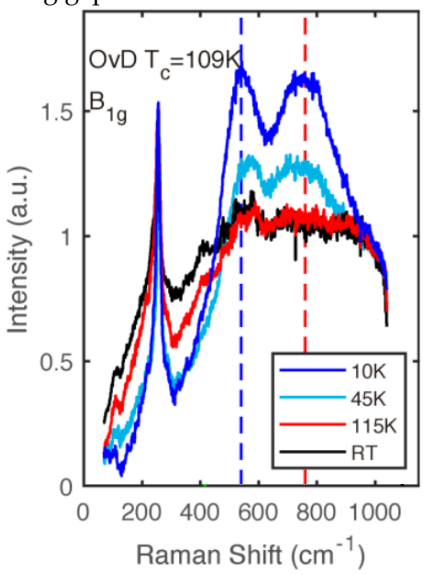

Image adapted from [154].

Fig. 8.10 shows exemplary Raman responses at different interaction strenghts. We observe a clear maximum in $S(\omega)$ that moves to lower detunings as the system is tuned towards the BCS limit. However, the onset at 2Δ is occluded by the presence of the Goldstone mode. Additionally, the shape of $S(\omega)$ changes from a distinct peak in the crossover to a broader feature with a slower decay in the BCS regime, making the maximum a somewhat poorly defined quantity to fit. We therefore chose to fit the edge of the continuum as a well-defined feature, using the phenomenological fitting function

$$S(\omega) = \begin{cases} \max(0, a\omega + b) & \text{for } \omega < 2\Delta \\ (2a\Delta + b)\exp(-(\omega - 2\Delta)^2/c^2) & \text{for } \omega \geq 2\Delta \end{cases} \tag{8.2}$$

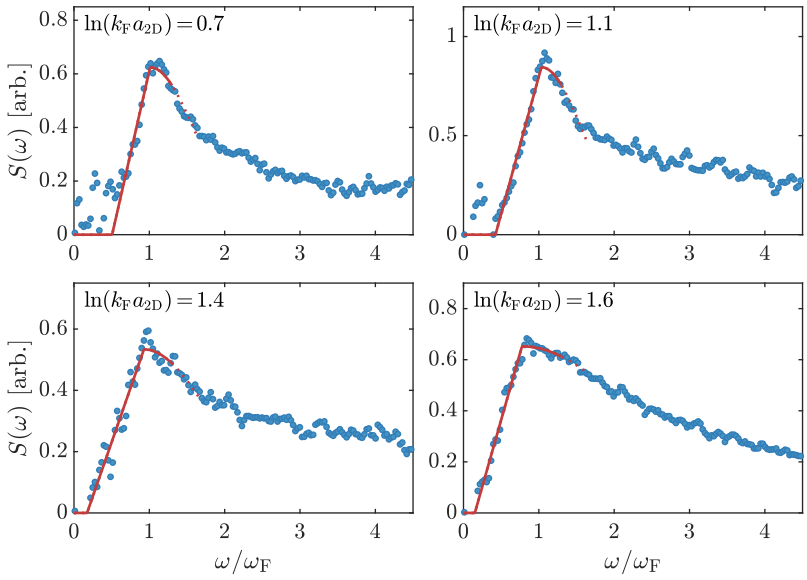

Figure 8.10: Examples for the Raman response $S(\omega)$**.** Shown are typical Raman responses obtained by integrating the measured dynamic structure factors over the momentum axis. While the presence of the Goldstone mode obscures the onset of the pair breaking continuum, a clear feature is still visible. The red lines show the fit used to extract the gap (see below).

with a, b, c and Δ as free parameters of the fit. As a Gaussian decay does not capture the slow decay of the Raman response at larger detunings, fitting is restricted to the interval $\omega \in [0, 1.6\,\omega_F]$. This produces good agreement with the measured $S(\omega)$ and allows us to extract an estimate of the superfluid gap.

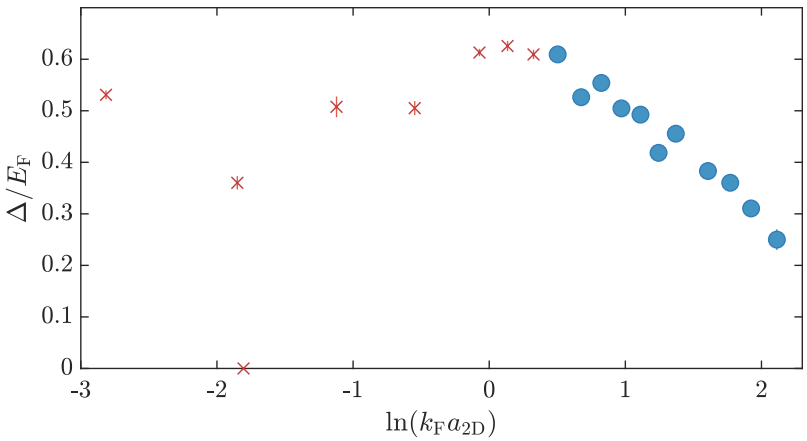

Figure 8.11: Fitted superfluid gaps from $S(\omega)$**.** Blue dots show the fitted values of Δ. Red crosses mark interaction strengths where the dynamic structure factor does not show a visible pair breaking continuum and therefore does not allow for the extraction of the superfluid gap, as the fit captures only the Goldstone mode. Error bars describe 1σ confidence intervals of the fit and are mostly smaller than the symbol size.

Fig. 8.11 shows the fitted values of $S(\omega)$ as a function of the interaction strength. We initially observe a continuous increase from the BCS towards the BEC limit, as expected from theoretical predictions [59, 155–158]. However, in the BEC regime, the superfluid gap obtained using the phenomenological fit to $S(\omega)$ starts to become unphysical as the pair breaking continuum is no longer visible. For interaction strengths $\log(k_F a_{2D}) < 0.5$, $S(\omega)$ is instead dominated by the Goldstone mode and thereby contains little information about the superfluid gap.

8.3.2 Strong driving at lower momentum transfers

The second method is better suited to measurements in the BEC regime and was initially developed in ref. [69]. We probe the system at low momentum transfers $q \lesssim 0.5\,k_F$, where the energy of the Goldstone mode is well below the onset of pair breaking excitations at 2Δ. As shown above, the pair breaking continuum is already strongly suppressed at these low momenta and interaction strengths. However, because these excitations are more strongly suppressed, we are also able to drive the system stronger while still remaining in the linear regime. While strong driving leads to a sizeable broadening of the Goldstone mode, it is usually possible to find a combination of lattice potential height and momentum transfer for which the two modes are well separated.

While the height of the lattice potential has to be adjusted for each interaction strength and momentum transfer, it is generally approximately a factor of 8 larger than for the measurements in the previous section.

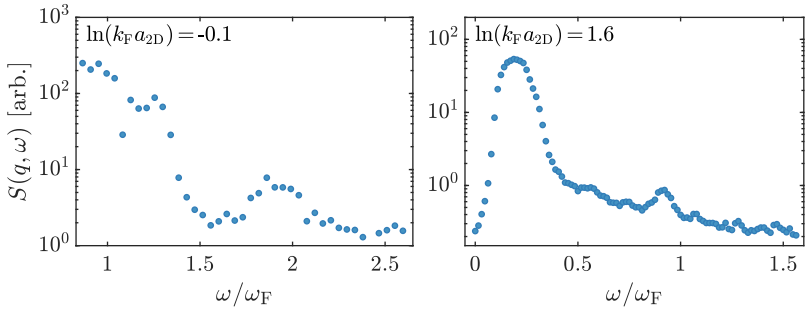

Figure 8.12: Examples for the strongly driven dynamic structure factor. Shown are typical spectra obtained by strongly driving the system at low momentum transfers. The Goldstone mode is heavily broadened, but a second, smaller feature corresponding to pair breaking excitations is clearly visible.

Fig. 8.12 shows two exemplary measurements of the superfluid gap using this method. Even though the Goldstone mode is broadened heavily by the strong drive, the pair breaking mode is still clearly visible. Since the two modes are well separated, fitting the superfluid gap is straightforward: We simply perform a bilinear fit to the pair breaking mode and identify the onset as 2Δ.

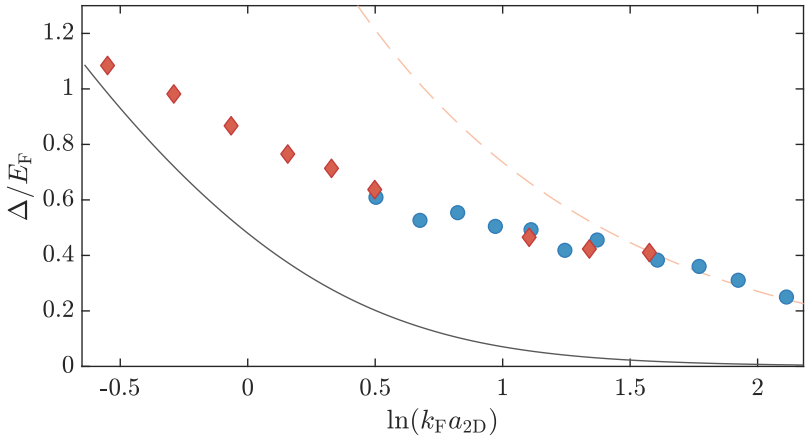

Figure 8.13: Superfluid gap in the 2D BEC-BCS crossover. Blue dots show gaps extracted obtained from $S(\omega)$, red diamonds show data obtained from strong driving at low q. Both methods show excellent agreement with each other. The black solid line shows the energy of the trivial two-body bound state [29]; the orange dashed line is the prediction from BEC-BCS mean field theory [59, 155].

The result of these measurements is shown in fig. 8.13, together with the values obtained in the previous section. Both methods are in excellent agreement with each other in the parameter region where

both methods can be applied, and paint a clear picture of the evolution of the superfluid gap in the BEC-BCS crossover. Our measurements span a wide range of interaction strengths: On the BCS side of the crossover our data is in good agreement with mean field calculations, while on the BEC side of the crossover we obtain gaps that are dominated by the trivial two-body binding energy (see section 4.5).

8.3.3 Comparison to theoretical predictions

To compare our measurements with theoretical predictions, it is important to remember one of the particularities of quasi-2D Fermi gases. As discussed in section 4.5, there are some modifications on short length scales to the physics of tightly confined ultracold Fermi gases that cause them to differ from purely 2D models. The most important modification in the context of this chapter is a modification of the binding energy, which arises as the two-body bound state undergoes a transformation from purely two-dimensional in the BCS limit (where the pairs are large compared to the confinement) to purely three-dimensional in the BEC limit (where the pairs are much smaller than the confinement).

This modification of the bound state has important consequences for the superfluid gap: If we imagine building a superfluid Fermi gas pair by pair, the cost of breaking a pair will initially just be given by the two-body binding energy. As the number of pairs increases, the system may eventually condense into a coherent many-body state and become superfluid. This many-body state protects the pairs, increasing the energy required to break them apart. Therefore, the superfluid gap forms as a combination of the two-body binding energy and the additional effect of the many-body system.

All current theoretical calculations of the superfluid gap in the two-dimensional BEC-BCS crossover are performed using purely 2D models. Therefore, their results will trivially disagree with our measurements, because the 2D and quasi-2D two-body binding energies are already significantly different on the BEC side of the crossover. To compensate for this discrepancy, we subtract the known binding energies from our measured values and the theoretical predictions to compare the more interesting many-body part of the superfluid gap $\Delta - E_B/2$.

Fig. 8.14 shows this comparison between our measurements of the superfluid gap and predictions from mean field BEC-BCS theory [59], diffusion Monte Carlo (DMC) [156, 158, 159] and auxiliary-field quantum Monte Carlo (AFQMC) [157]. Remarkably, our measurements are in significant disagreement with quantum Monte Carlo predictions: In the BCS regime, our results lie significantly above the predicted many-body contribution, irrespective of the specific method, and are in surprisingly good agreement with mean field theory. At the same time, our measurements show that the many-body contribution decays faster towards the BEC regime than predicted: We find a broad maximum of the many-body contribution around $\log(k_F a_{2D}) \approx 1$,

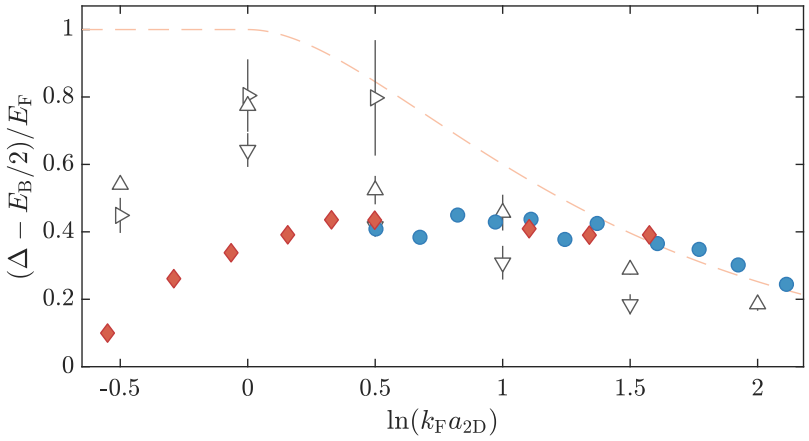

Figure 8.14: Many-body contribution to the gap with theoretical predictions. Blue dots correspond to data obtained from $S(\omega)$, red diamonds are obtained using strong driving at low q. Dashed orange line: BEC-BCS mean field theory [59, 155]; right facing triangles: fixed-node Diffusion Monte Carlo [156]; downwards facing triangles: auxiliary-field quantum Monte Carlo [157]; upwards facing triangles: fixed-node Diffusion Monte Carlo [158]. Our measurements clearly deviate from the QMC predictions, which tend to show a maximum further in the BEC regime and with a larger magnitude.

whereas DMC and AFQMC suggest a sharper maximum closer to $\log(k_F a_{2D}) \approx 0$ with a somewhat larger magnitude.

The reason for this discrepancy is not immediately obvious. One possibility is that the influence of the third dimension is not fully taken into account by subtracting the appropriate binding energy, but that there are higher order effects that further modify the superfluid gap. However, since realistic two-dimensional systems will generally feature some three-dimensional contributions, this would indicate that purely two-dimensional theories are not adequate to describe realistic strongly correlated superfluids like 2D quantum gases and likely also layered superconductors, requiring computationally more challenging calculations on three-dimensional lattices. Another possibility is that the particle numbers used in DMC and AFQMC calculations, which are generally on the order of 50 fermions, are not enough to describe the thermodynamic limit (or the closer approximation thereof our ≈ 5000 fermions represent). At this point, we are unable to resolve this open question, and further work on experiment and theory will be required.

While there are significant discrepancies between the different quantum Monte Carlo methods, we note that the authors of ref. [157] (AFQMC) present their calculations as exact results from first principles.

9 THE EXCITATION SPECTRUM OF 3D FERMI GASES

In this short chapter, I will summarize closely related measurement we performed on the excitation spectrum of three-dimensional Fermi gases.
I will introduce the modifications we made to the setup to allow for the creation of three-dimensional gases and present our results on the dynamic structure factor in the 3D BEC-BCS crossover. Similar to our work on two-dimensional Fermi gases, I will describe how we extract the superfluid gap from the measured excitation spectrum and briefly discuss the results.

The results presented in this chapter are adopted from

> *H. Biss, L. Sobirey, N. Luick, M. Bohlen, J.J. Kinnunen, G.M. Bruun, T. Lompe and H. Moritz*
> *arXiv:2105.09820 (2021) [42]*

and are summarized here with modifications. They will be discussed in more detail in the PhD thesis of Hauke Biss. I contributed to this project mainly by performing and analyzing measurements of the dynamic structure factor, by establishing and implementing the methodology for determining the temperature and density of the system, and in the interpretation of the results.

One of the great advantages of ultracold Fermi gases is the high degree of control available over the experimental environment. In most materials, the dimensionality is predetermined and cannot be changed, as changing it would result in a completely different material. However, in ultracold Fermi gases, the dimensionality is simply determined by the shape of the confining potential. Therefore, an experimental setup designed to create ultracold 2D Fermi gases only requires some minor changes to create ultracold 3D Fermi gases. Here, we will expand the setup described in previous chapters in a straightforward fashion to prepare 3D systems and to measure their excitation spectrum using the same Bragg spectroscopy setup.

9.1 Three-dimensional homogeneous Fermi gases

In this section, I will describe how we use the existing setup designed for creating two-dimensional Fermi gases and expand it to prepare three-dimensional Fermi gases. Additionally, I will briefly summarize how we can perform thermometry in these systems by using existing measurements of the equation of state at unitarity.

To create homogeneous three-dimensional Fermi gases, we must do away with the vertical optical lattice used to provide the tight harmonic confinement that brings our systems into the two-dimensional regime. Instead, we use two tightly focused, elliptical, blue-detuned laser beams a distance of $\approx 40\,\mu\mathrm{m}$ apart. This creates a box-shaped potential along the axial direction, which we can combine with our ring potential to create an approximately cylindrical confinement, inside of which the density is approximately homogeneous.

A similar setup was used to create the first homogeneous 3D Fermi gases [160]. Other homogeneous quantum gases often make use of spatial light modulators, for a recent review see e.g. [161].

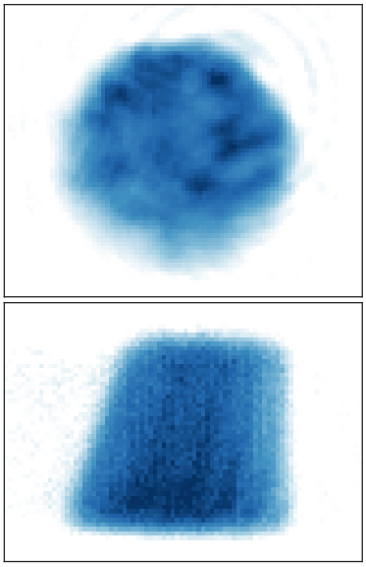

Figure 9.1: Absorption images of the 3D Fermi gas. The top image is taken along the axial direction; the bottom image is taken from the side.

We verified the adiabacity of our interaction ramps by performing different interaction ramps through the crossover, all ending at the same value deep in the BEC regime. By measuring the momentum distribution using matter wave focusing, we were able to confirm that the condensate fraction was unaffected by our interaction ramps, indicating that the entropy per particle had not changed.

Fig. 9.1 shows characteristic absorption images of the resulting homogeneous 3D Fermi gas with a density per spin state of $n \approx 0.4\,\mu m^{-3}$. We can observe a small divergence of the ring beam, resulting in a shape that more closely resembles a truncated cone than a cylinder. This results in some smearing out of the density distribution when imaged along the axial direction, as regions of different radii are imaged together. Additionally, the extent of the gas along the axial direction is larger than the depth of field of the imaging setup, leading to further distortions. However, the absorption image taken along the radial direction clearly shows that the density distribution is homogeneous.

To perform thermometry at unitarity, we follow the procedure outlined in [162] and switch off the ring trap, allowing the gas to expand into the underlying harmonic trap. As the system is homogeneous in the axial direction, we can obtain the total internal energy in a straightforward fashion using the virial theorem and the known trapping frequency of the harmonic trap. Comparing with previous measurements of the equation of state at unitarity [163], we can calculate the temperature and entropy per particle of the system before the expansion. Away from unitarity, knowledge of Tan's contact [139–141] and the equation of state would be required to apply this method of thermometry. However, we can make use of the fact that adiabatic interaction ramps do not change the entropy per particle of homogeneous quantum gases. Therefore, we can obtain the entropy per particle for systems at arbitrary interaction strengths by ramping to unitarity and performing measurements as outline above.

9.2 Measuring their excitation spectrum

In this section, I will present our measurements of the momentum-resolved dynamic structure factor in three-dimensional Fermi gases and discuss their evolution in the 3D BEC-BCS crossover.

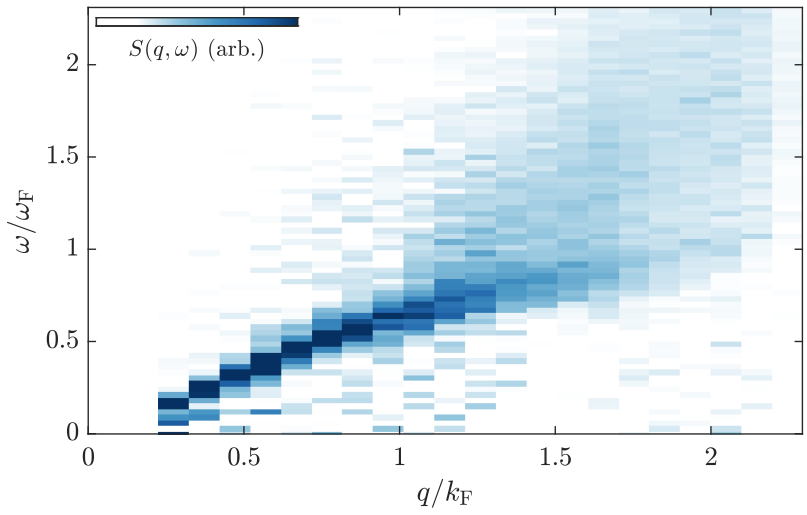

Figure 9.2: $S(q,\omega)$ **measured at** $(k_F a_{3D})^{-1} = 0$**.** Similar to the measurements performed in 2D Fermi gases, we observe a well-defined Goldstone mode as well as a distinct pair breaking continuum.

The same Bragg spectroscopy setup used in chapters 7 and 8 can be

used without further modifications to measure the dynamic structure factor of three-dimensional Fermi gases. In Fig. 9.2, we show the first momentum-resolved measurement of the dynamic structure factor at unitarity. The excitation spectrum of the 3D Fermi gas is remarkably similar to our measurements performed on 2D Fermi gases, featuring the same well-defined Goldstone mode at low momentum transfer and a pronounced pair breaking continuum at large detunings. As the homogeneous 3D Fermi gases we prepare feature slightly larger values of the Fermi wavevector k_F than in 2D, we are able to observe the onset of the pair breaking continuum bending up at large momentum transfers, as expected from theory (see section 4.4).

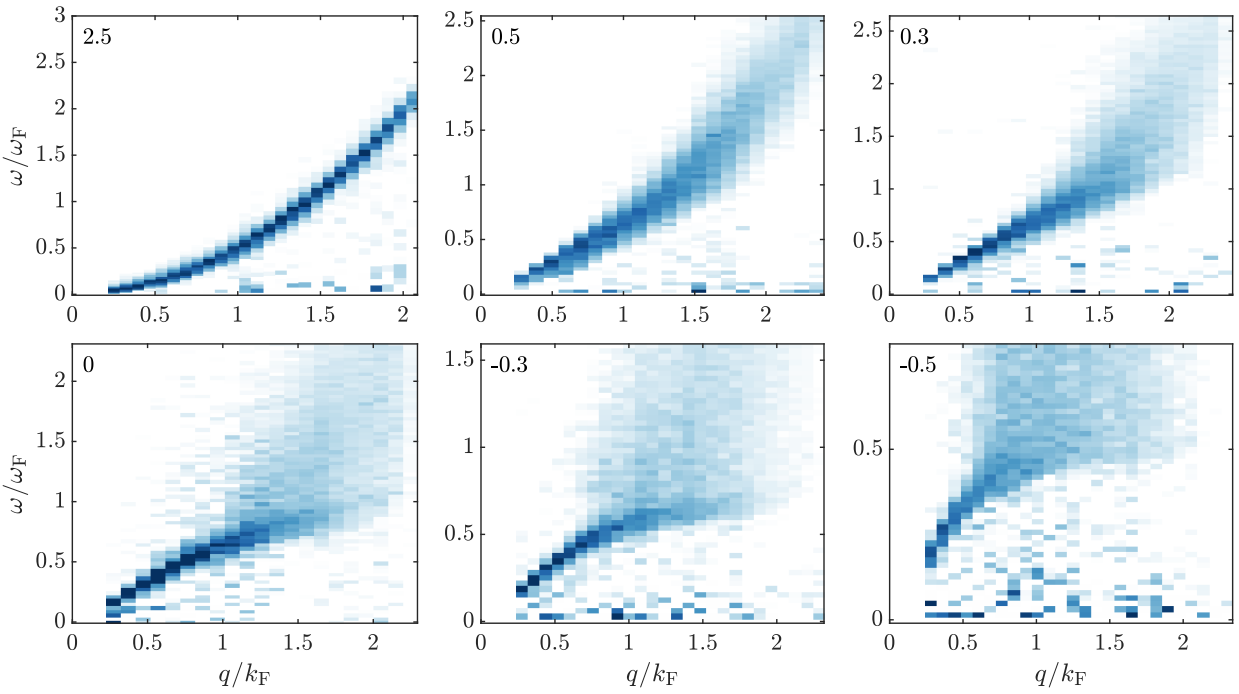

Figure 9.3: Measurements of $S(q,\omega)$ in the 3D BEC-BCS crossover. The numbers in the top left corner denote the value of the interaction parameter $(k_F a_{3D})^{-1}$. We observe a smooth crossover from BEC to BCS superfluidity as the interaction strength is tuned. The Goldstone mode remains well-defined throughout the crossover, whereas the pair breaking continuum gains in strength towards the BCS regime. Note the different scaling on the y-axis.

As in the case of the 2D Fermi gas, upon tuning the interaction strength the dynamic structure factor reveals the smooth evolution from BEC to BCS superfluidity that occurs in the crossover, see fig. 9.3. However, we do not observe a strong broadening of the Goldstone mode as it approaches the continuum on the BCS side of the resonance, which was clearly present in 2D. Instead, well-defined phononic quasiparticles seem to persist deep into the BCS regime. This might indicate that the reason for this broadening is specific to the systems probed in 2D and not of general nature.

9.3 The superfluid gap

Finally, I will describe how we extract the superfluid gap from our measurements of the excitation spectrum. I will present the evolution of the superfluid gap in the 3D BEC-BCS crossover and compare it to predictions from theory.

Much like in 2D Fermi gases, obtaining the superfluid gap from our measurements of the dynamic structure factors is fairly straightforward. However, in 3D Fermi gases, we are able to employ a different method on the BCS side of the crossover: Because the Goldstone mode is not heavily broadened and because the range of momentum transfers probed extends further, we are able to make out a clear, constant-energy onset of the pair breaking continuum in the BCS regime at larger momentum transfers. Therefore, we can obtain the superfluid gap in a straightforward fashion by fitting the dynamic structure factor at large momentum transfer with a line shape obtained from QRPA calculations. At the same time, we find that strong driving at low momentum transfers still represents a robust and efficient way to measure the superfluid gap in the crossover and towards the BEC regime.

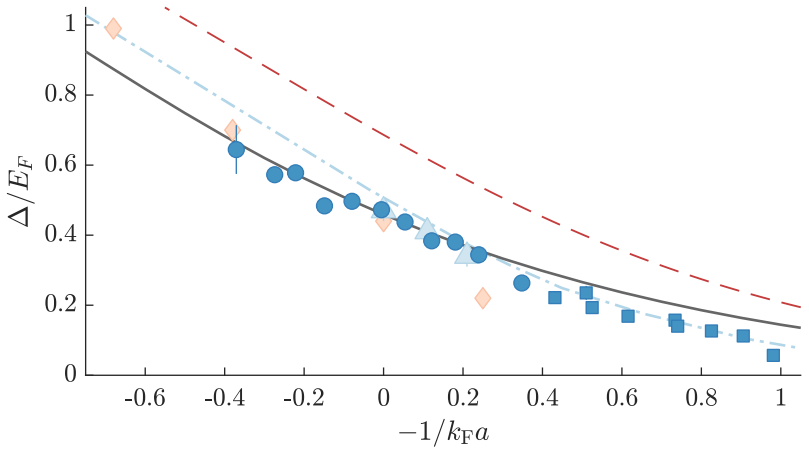

Figure 9.4: The superfluid gap Δ in the 3D BEC-BCS crossover. Blue dots and squares denote our results, obtained using strong driving at low momentum transfers and fitting with QRPA calculations at higher momenta, respectively. Orange diamonds [133] and light blue triangles [69] show the results of previous measurements. The red dashed line shows the 3D BEC-BCS mean field prediction [55]; the black solid line shows a prediction from self-consistent T-matrix calculations [151]; the blue dash-dotted line shows a prediction including particle-hole interactions [164].

Fig. 9.4 presents our measurements of the superfluid gap in the 3D BEC-BCS crossover. Much like in 2D, we observe a smooth decrease of Δ towards the BCS regime. Our results are in excellent agreement with previous measurements [69, 133], but span significantly further into the BCS regime. We find excellent agreement with self-consistent T-matrix calculations [151] of the superfluid gap in the crossover and on the BEC side of the crossover, but find results below their $\mathrm{T} = 0$ predictions in the BCS regime. Calculations including particle-hole interactions [164] show better agreement in the BCS regime, but disagree with our measurements in the BEC regime. Further work will be required to determine whether particle-hole effects are already relevant at these interaction strengths or whether other effects such as finite temperature contribute to the observed decrease of the gap in the BCS regime.

The suppression of the gap due to particle-hole interactions is commonly referred to as the GMB corrections after Gor'kov and Melik-Barkhudarov, who first calculated it for the case of a BCS superconductor [165].

10 COMPARING FERMIONIC SUPERFLUIDS IN 2D AND 3D

In this chapter, I will describe how we compare two- and three-dimensional fermionic superfluids to investigate the influence of reduced dimensionality on the stability of the superfluid phase.
I will discuss different ways how the interaction strength can be parameterized in a way that is applicable both to 2D and 3D systems to facilitate a comparison. Comparing our results on the superfluid gap in 2D to 3D Fermi gases, I will show that the dimensionality does not seem affect the stability of the superfluid phase. Finally, I will compare our results to different solid state materials and show that this trend appears to hold for a wide range of superconducting materials.

The results presented in this chapter are adopted from

> *L. Sobirey, H. Biss, N. Luick, M. Bohlen, H. Moritz and T. Lompe*
> *arXiv:2106.11893* (2021) [12]

and are reprinted here with modifications and additions.

Now that we have performed measurements of the dynamic structure factor and the superfluid gap in 2D and 3D Fermi gases, the obvious open question is how the two dimensionalities compare. However, comparing different dimensionalities is not a trivial task, as a meaningful comparison requires all relevant parameters except for the dimensionality to be the same. Luckily for us, there are not too many parameters that present a challenge: By normalizing all quantities with the Fermi energy (or the Fermi wavevector where appropriate), we can compare systems with different densities. We will also mostly be able to neglect the temperature, because the systems we prepare both in 2D and in 3D are mostly well below the critical temperature and should therefore be a reasonable approximation of the zero-temperature limit. However, the most important parameter that needs to be the same is the interaction strength. Therefore, we will begin this chapter with a discussion of different parameterizations of the interaction strength.

10.1 Parameterizing the interaction strength

In this section, I will discuss how the interaction strength of two- and three-dimensional systems can be compared. I will introduce two different interaction parameters that are applicable to both 2D and 3D superfluids, namely the dimensionless chemical potential and the dimensionless pair size and discuss their advantages and disadvantages. I will furthermore show how our measurements of the dynamic structure factor can be used to estimate the pair size of our ultracold Fermi gases.

The reason why we need to discuss different parameterizations of the interaction strength is that the commonly used interaction parameters

See section 4.5 for our previous discussion about interaction parameters and the motivation behind $1/k_F a_{3D}$ and $\log(k_F a_{2D})$.

$1/k_F a_{3D}$ and $\log(k_F a_{2D})$ cannot be directly compared. While both parameters ultimately relate the phase shift incurred during a scattering event to the interparticle spacing, the different relations between the phase shift and the scattering length in the two dimensionalities results in interaction parameters without a clear mapping from one to the other. In the following, we will therefore discuss two different possibilities to perform such a mapping in the form of alternative parameters that quantify the interaction strength. These parameters need to fulfill three requirements: First, they should describe a fundamental physical quantity that is well-defined independent of the dimensionality of the system. This will ensure that the mapping relates similar systems to each other. Second, they need to be dimensionless by relating such a fundamental quantity to the appropriate scale set by the interparticle spacing, so that we can compare systems with different densities. Third, they need to be known reasonably well - there is no use in a parameter that would perform a mapping, but which we do not know the value of.

10.1.1 The dimensionless chemical potential

The first interaction parameter we propose is the dimensionless chemical potential μ/E_F. This choice is motivated by BEC-BCS theory (see section 4.3), where solving the gap and number equations ultimately results in two parameters: the gap Δ and the chemical potential μ. Having measured the superfluid gap in both dimensionalities, the chemical potential therefore seems like an appropriate pairing. It is also a fundamental, thermodynamic quantity which is well-defined in any (grand canonical) system. Furthermore, μ/E_F evolves smoothly in the crossover, approaching a value of 1 in the BCS limit and $-E_B/2E_F$ in the BEC limit, independent of the dimensionality. Finally, μ/E_F has been studied extensively in the BEC-BCS crossover, both theoretically [119, 151, 156, 159, 166] and experimentally [40, 96, 163, 167]. This greatly simplifies the use of μ/E_F as an interaction parameter, as it allows us to use the theoretical prediction for the reduced chemical potential $\tilde{\mu} = \mu - E_B/2$ as calculated in [119] and the two-body binding energy as given in [29] to calculate μ/E_F for our two-dimensional Fermi gases with no measurements required.

We note that while it would also be possible to measure the chemical potential in our experimental setup instead of simply using the theoretical prediction, previous experiments have found very good agreement with the calculation results, and measuring μ/E_F to the required precision is not exactly trivial, see e.g. [40, 96].

One final argument for μ/E_F can be made based on the location of the BEC-BCS crossover. In 3D Fermi gases, we can clearly identify unitarity to be a special point that defines the most strongly interacting regime. In 2D Fermi gases, the choice is not this obvious. Early studies pointed out that a weak singularity exists where $\mu = 0$, and suggested that this marked the interaction strength that separated the BEC and BCS regimes [59, 155]. However, experimental studies of the 2D BEC-BCS crossover clearly indicate that the strongest many-body effects are found around $\log(k_F a_{2D}) = 1$, see e.g. refs. [28, 86, 87]. If we calculate the dimensionless chemical potential μ/E_F at $\log(k_F a_{2D}) = 1$, we obtain a value of $\mu/E_F = 0.36$, in remarkable agreement with the value of $\mu/E_F = 0.37$ measured at unitarity in 3D Fermi gases [84,

163]. This excellent agreement strongly supports the choice of μ/E_F as a parameterization of the interaction strength that connects comparable two-dimensional and three-dimensional Fermi gases.

10.1.2 The dimensionless pair size

The second interaction parameter was proposed by Pistolesi and Strinati in 1993 [168], long before ultracold Fermi gases were first realized. Their aim was to find a parameter in BEC-BCS theory that could be measured in superconducting materials. Their suggested parameterization of the interaction strength was the parameter ξk_F. Here, ξ is the size of the Cooper pairs in the system, which is equivalent to the phase coherence length in BCS theory. This choice was inspired by the observation that superconductors with large critical temperatures T_c generally feature surprisingly short coherence lengths [8], and by the fact that both the Fermi wavevector and the coherence length can be measured in condensed matter systems.

Note that while there are many different definitions of pair sizes and coherence lengths, they all coincide up to small factors of order unity on the BCS side of the crossover where all known superconductors are found. In the BEC regime, the coherence length is no longer equivalent to the pair size [169] and increases again, but the pair size remains a useful parameterization as it continues to decrease towards the BEC limit.

The parameter ξk_F also holds up reasonably well when faced with the requirements posited earlier: The size of the Cooper pairs is also a fundamental physical quantity that is well-defined independent of the dimensionality. The normalization with k_F ensures that the parameter is dimensionless and applicable for systems with different densities. However, ξk_F has a weakness in that it is not particularly well known for ultracold Fermi gases. While theoretical calculations of ξ exist for 3D Fermi gases (see e.g. refs. [131, 169, 170]), only one experiment has extracted the pair size [130], and only few interaction strengths were probed. Furthermore, some open questions remain about the magnitude of the results obtained in ref. [130] (see box below.) For 2D Fermi gases, the situation is even more dire: no measurements of the pair size have been performed to date, and the only theoretical prediction is that obtained from BEC-BCS mean field theory [59, 155]. Therefore, before we can use ξk_F as a parameterization of the interaction strength for ultracold Fermi gases, we need a better estimate of the value of ξ in the 2D and 3D BEC-BCS crossover first.

Box 10.1: The pair size measured in ref. [130]

We would like to point out that there are some open questions regarding the extraction of the pair size performed in ref. [130], which will be relevant for our comparison with their work below.

First, the authors state that the pair size can be inferred both from the onset of pair dissociation and from the width of the pair dissociation spectrum. They define expressions for the pair size from both, introducing a numerical constant in the definition of the pair size from the width to ensure both expressions result in the same value when applied to a theoretical prediction for the line shape in the BEC limit. However, the authors show in their Fig. 1 that the two definitions of the pair size nevertheless produce different results outside the BEC regime. The authors then later state that the definition of the pair size using the onset of pair dissociation cannot be used in their experiments as the onset is subject to Hartree shifts. The definition of the pair size from the width therefore contains a numerical prefactor that is ill-motivated outside the BEC limit and cannot be verified experimentally.

Second, the authors show in their Fig. 1 that when chosen to agree in the BEC limit, this definition of the pair size from the width is a factor of ≈ 2.44 different from the theoretical prediction of the pair size towards the BCS limit. However, the authors fail to compensate for this effect, stating that as their uncompensated measurements yield pair sizes below the interparticle spacing, they may assume their definition of the pair size from the width to be equivalent to the real pair size, as this supposedly indicates the measurement was performed close enough to the BEC limit. This is a rather surprising statement, given that at least one of their measurements is performed on the BCS side of the crossover, where their Fig. 1 prescribes a correction factor of ≈ 2 already.

This discrepancy was pointed out by Palestini and coworkers [131], who showed that when a correction factor is applied as suggested by Fig. 1 of ref. [130], the resulting pair sizes are in good agreement with theoretical predictions. As an aside, this discussion is further complicated by a calculation of the pair size in ref. [171], which finds a compatible pair size to the uncorrected value from ref. [130], but does so using a definition of the Pippard coherence length in the BCS regime that differs from the definition used in ref. [130] by a factor of ≈ 2.7.

In summary, there are still many open questions regarding the value of the Cooper pair size in the 3D BEC-BCS crossover. When we compare our results to that of ref. [130], we will therefore assume the correct method of extracting the pair size from the RF spectra to be that including the correction pointed out in ref. [131].

10.1.3 Estimating the pair size

In the following, we will obtain an estimate of the pair size ξ from our measurements of the dynamic structure factor. To this end, we will focus on the suppression of the pair breaking continuum at low momentum transfers, which we have previously argued to be the result of a size mismatch between the wavelength of the Bragg lattice and the size of the Cooper pairs. However, the connection between the dynamic structure factor and the pair size is rarely explicitly made, and if so only in approximate terms. In ref. [150], Büchler and coworkers state that for momenta $q \ll 1/\xi$, the phonon mode exhausts the sum rules, implying that the continuum must therefore be absent at these low momentum transfers. In ref. [149], Leggett also states that the density response function (which is closely related to the dynamic structure factor) should tend to zero on a scale on the order of $1/\xi$. We will therefore use the onset of the pair breaking continuum in the momentum axis to estimate the pair size.

In our measurements, the onset of the continuum has an additional dependence on the detuning. To not further complicate things, we focus only on a small window around 2Δ where the onset momentum is lowest. This also ensures that our measurement is unaffected by the presence of the Goldstone mode.

Fig. 10.1 shows the typical onset of the pair breaking continuum as it is visible in $S(q, 2\Delta/\hbar)$. To obtain an estimate of the pair size, we perform a bilinear fit to obtain the onset wavevector of the continuum k_o. Building on refs. [149, 150], we estimate the pair size to be $\xi \approx \alpha_{2D}/k_o$, where α_{2D} is some so far undetermined prefactor.

At this point, we are unaware of any explicit expression from which we could derive the magnitude of α_{2D}. Therefore, we turn to theory to obtain an estimate. We fit our data to the theoretical mean-field prediction from refs. [59, 155], leaving α_{2D} as a free parameter. This fit results in $\alpha_{2D} = 0.60$.

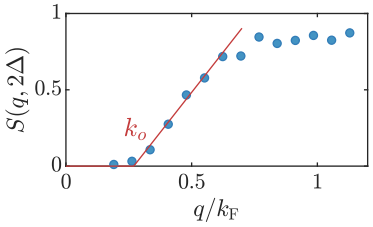

Figure 10.1: Onset of the continuum. Shown is $S(q, 2\Delta/\hbar)$, measured at an interaction strength of $\log(k_F a_{2D}) = 1.6$. The red line shows the bilinear fit used to extract the onset wavevector k_o. Note that we have averaged together a small range of detunings ($[1.8\Delta, 2.2\Delta]$) to obtain this data.

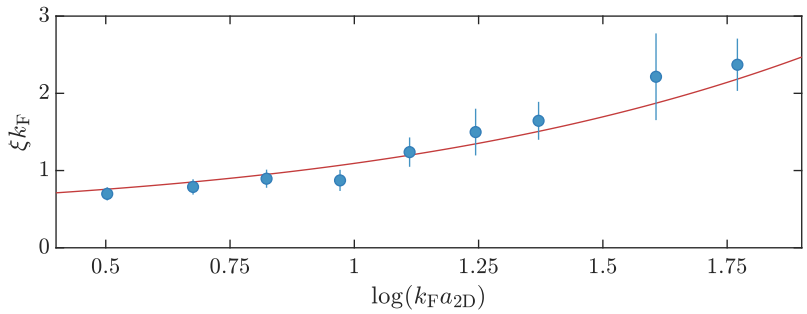

Figure 10.2: Estimate of the pair size ξ in 2D. The datapoints show our estimate of the pair size, obtained from the measured dynamic structure factors for the 2D Fermi gas. The red line is the theoretical prediction from refs. [59, 155] that was used to calibrate the prefactor α_{2D}. Errorbars denote 1σ confidence intervals of the fit. We find excellent agreement with the prediction from mean field theory.

Fig. 10.2 shows our resulting estimate of ξ, together with the prediction from mean field theory. We find surprisingly good agreement with the theoretical prediction, further supporting the link between the dynamic structure factor and the pair size. As in the case of the superfluid gap, this method is only applicable for $\log(k_F a_{2D}) \gtrsim 0.5$ as no pair breaking continuum is visible further in the BEC regime.

Encouraged by the good agreement for 2D Fermi gases, we use the same method to obtain an estimate for the pair size in 3D Fermi gases. As fewer measurements of the full dynamic structure factor were made, we perform an additional measurement, recording just $S(q, 2\Delta/\hbar)$ for a wide range of interaction strengths, combine the data from both methods and proceed as for the 2D Fermi gas. This time, the fit to the prediction from ref. [170] results in $\alpha_{3D} = 0.83$.

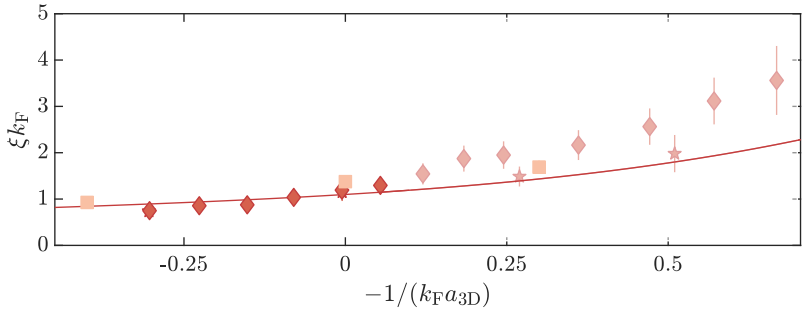

Figure 10.3: Estimate of the pair size ξ in 3D. Stars show the pair size estimate obtained from averaging a small window of $S(q, \omega)$ around 2Δ; Diamonds were obtained using the separate measurement at $\hbar\omega \approx 2\Delta$. The red line is the theoretical prediction from ref. [170] that was used to calibrate the prefactor α_{3D}. Orange squares show the previous measurement of ref. [130], corrected as described in ref. [131]. Errorbars denote 1σ confidence intervals of the fit. We find good agreement with previous measurements and theory in the BEC- and crossover regimes, but our measurements disagree in the BCS regime for unknown reasons.

The results are shown in fig. 10.3, together with the theoretical prediction from ref. [170] and the results from ref. [130], which have been corrected using the ratio shown in the inset of fig. 1c of ref. [130] as described in ref. [131] and discussed in the box above. Towards the BEC limit and in the crossover, we find good agreement with previous measurements and theoretical predictions. However, in the BCS regime our two measurements deviate from each other. The datapoints obtained from the original measurements continue to show good agreement with previous measurements and theoretical predictions. However, the independent measurements performed at a fixed detuning of 2Δ suggest larger values of the pair size.

Due to these discrepancies in the BCS regime, the fit to determine α_{3D} was limited to $-1/k_F a_{3D} < 0.1$.

It is not immediately clear what effects could be responsible for this discrepancy. We note that fitting the onset momentum k_o is difficult in the BCS regime, as k_o quickly approaches the smallest momentum transfers available in our setup. It is possible that this effect gets mitigated somewhat due to the higher signal to noise ratio obtained by averaging together a range of detunings in the original measurements, and therefore larger systematic errors could affect the determination of k_o from the second measurement at fixed detuning. However, at this point this possibility is purely speculative, and we are not able to determine with certainty which one of the two measurements is closer to the true value of the pair size. We will therefore proceed using the data from both measurements.

10.1.4 Comparing μ/E_F and ξk_F

Now that we have introduced two different parameterizations of the interaction strength, the final step required is to compare them. As we have established early in this section, a useful mapping should connect similar systems to each other. If the two interaction parameters we in-

troduced fulfill our requirements, they should therefore map the same systems onto another, or any comparison we do will be ill defined.

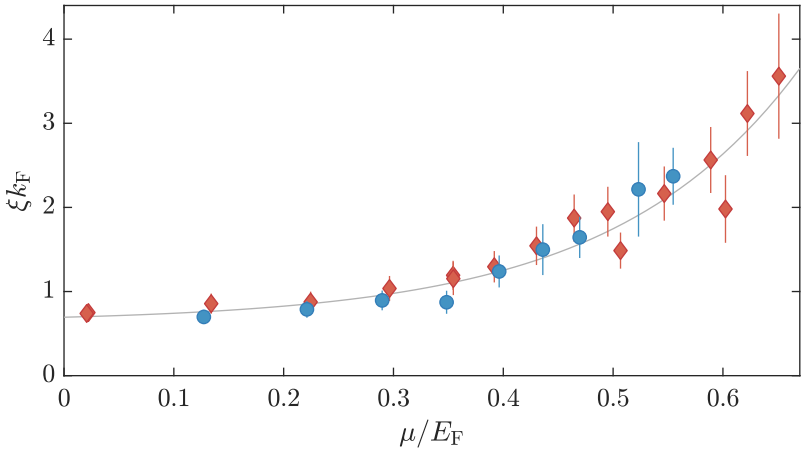

Figure 10.4: Comparison between interaction parameters. Plotted is our estimate of ξk_F against the calculated value of μ/E_F. Blue points correspond to the 2D Fermi gas; red diamonds to the 3D Fermi gas. We observe that within the accuracy of our measurement, the values from 2D and 3D collapse onto a single curve, indicating that ξk_F and μ/E_F represent equivalent mappings between 2D and 3D Fermi gases. The solid grey line marks an interpolating fit to the data used to obtain ξk_F for a given value of μ/E_F.

Therefore, we take our estimates of ξk_F for 2D and 3D Fermi gases and calculate the value of μ/E_F at that interaction strength. For the two-dimensional systems, we calculate μ using the value of $\tilde{\mu} = \mu + E_B/2$ obtained in QMC calculations in ref. [119] and subtract the appropriate binding energy given in ref. [29] as stated previously. For the three-dimensional system, we use the value of $\tilde{\mu}$ obtained from QMC calculations in ref. [166].

The resulting comparison between the two interaction parameters is shown in fig. 10.4. We find that when plotted against μ/E_F, our estimates of ξk_F obtained for 2D and 3D Fermi gases collapse onto a single curve within the accuracy of our measurement. Both interaction parameters therefore describe the same mapping between two-dimensional and three-dimensional systems, which is shown in fig. 10.5. This excellent agreement further justifies our choices of μ/E_F and ξk_F and supports the assumptions we have made in our estimate of the pair size.

We note that while the value of $\mu/E_F \approx 0.44$ at unitarity in ref. [166] is somewhat above the value of $\mu/E_F = 0.37$ found in state of the art measurements [84, 163], this difference is not significant in the context of the comparisons we perform in this thesis.

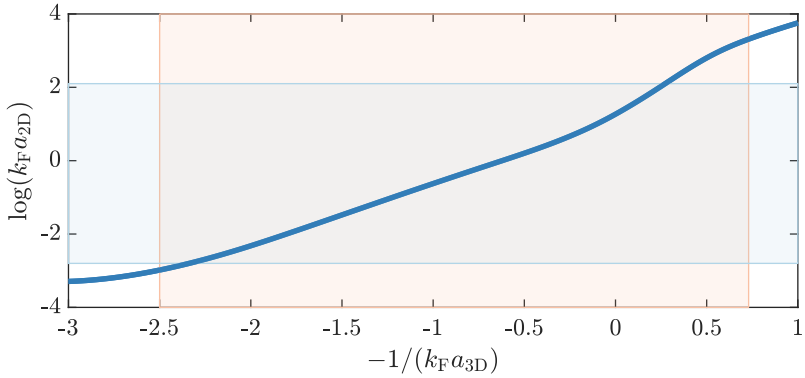

Figure 10.5: Mapping between 2D and 3D using μ/E_F as an interaction parameter. The shaded areas show the range of interaction strengths for which measurements of $S(q, \omega)$ were performed in this thesis. Remarkably, although our measurements in 2D were performed over a significantly larger range of magnetic fields than in 3D (730 G − 940 G in 2D, 730 G − 890 G in 3D), our measurements on 3D Fermi gases reached significantly further into the BCS regime.

Finally, we note that given the accessible range of interaction strengths in our experiment (see fig. 10.5), our measurements on 3D Fermi gases appear to reach significantly further into the BCS regime than

those performed on 2D Fermi gases, although our measurements on 2D Fermi gases were performed up to higher magnetic fields. This could be the result of the two-dimensional confinement, which favors pairing since a bound state exists for arbitrarily small interaction strengths. The difference in the accessible interaction range would thereby essentially arise from a tendency towards smaller pair sizes in 2D geometries, which is interesting in the context of high-temperature superconductivity. However, other effects such as a different scaling of T/T_c at constant entropy could also be responsible for this discrepancy.

10.2 Comparing two- and three-dimensional Fermi gases

In this section, I will perform a comparison between 2D and 3D Fermi gases. Using the dimensionless chemical potential as an interaction parameter, I will discuss the similarities and differences in their excitation spectra. Comparing the superfluid gaps measured in 2D and 3D, I will show a remarkable collapse onto a universal function that is independent of the dimensionality.

Now that we have established a mapping between two-dimensional and three-dimensional Fermi gases, we may proceed to compare the measurements we have presented in chapters 8 and 9. While we have shown that μ/E_F and ξk_F are to some degree interchangeable parameters, μ/E_F is known to much greater accuracy than the pair size for ultracold Fermi gases. Therefore, we will use it to parameterize the interaction strength in this section.

10.2.1 Comparing the excitation spectrum

As we have already pointed out in chapter 9, our measurements of the dynamic structure factor in 3D Fermi gases look remarkably similar to those performed on 2D Fermi gases; a side-by-side comparison is shown in fig. 10.6. Those similarities do not come as a surprise, as the fundamental excitation modes available in the two systems are the same. Both are neutral superfluids, and therefore both are expected to show a well-defined Goldstone mode; and as both consist of paired fermions, we expect both to show a clear pair breaking continuum.

Nevertheless, while the two dimensionalities are similar in many regards, there are some differences: First, as we have mentioned previously, the Goldstone mode appears heavily broadened towards the BCS regime in 2D Fermi gases. Our measurements on 3D Fermi gases do not show such a broadening, indicating that it stems from an effect particular to our two-dimensional systems. Second, the different prefactors α_{3D} and α_{2D} introduced in the previous section already indicate that the onset of the pair breaking continuum appears at slightly lower momentum transfers in 2D than in 3D. This is especially visible in the fourth row in fig. 10.6, and leads to some changes to the behavior of the dynamic structure factor at high momentum transfers. A good example for this is visible in the second row, where the continuum is still absent in the 3D Fermi gas and we observe a dynamic structure factor

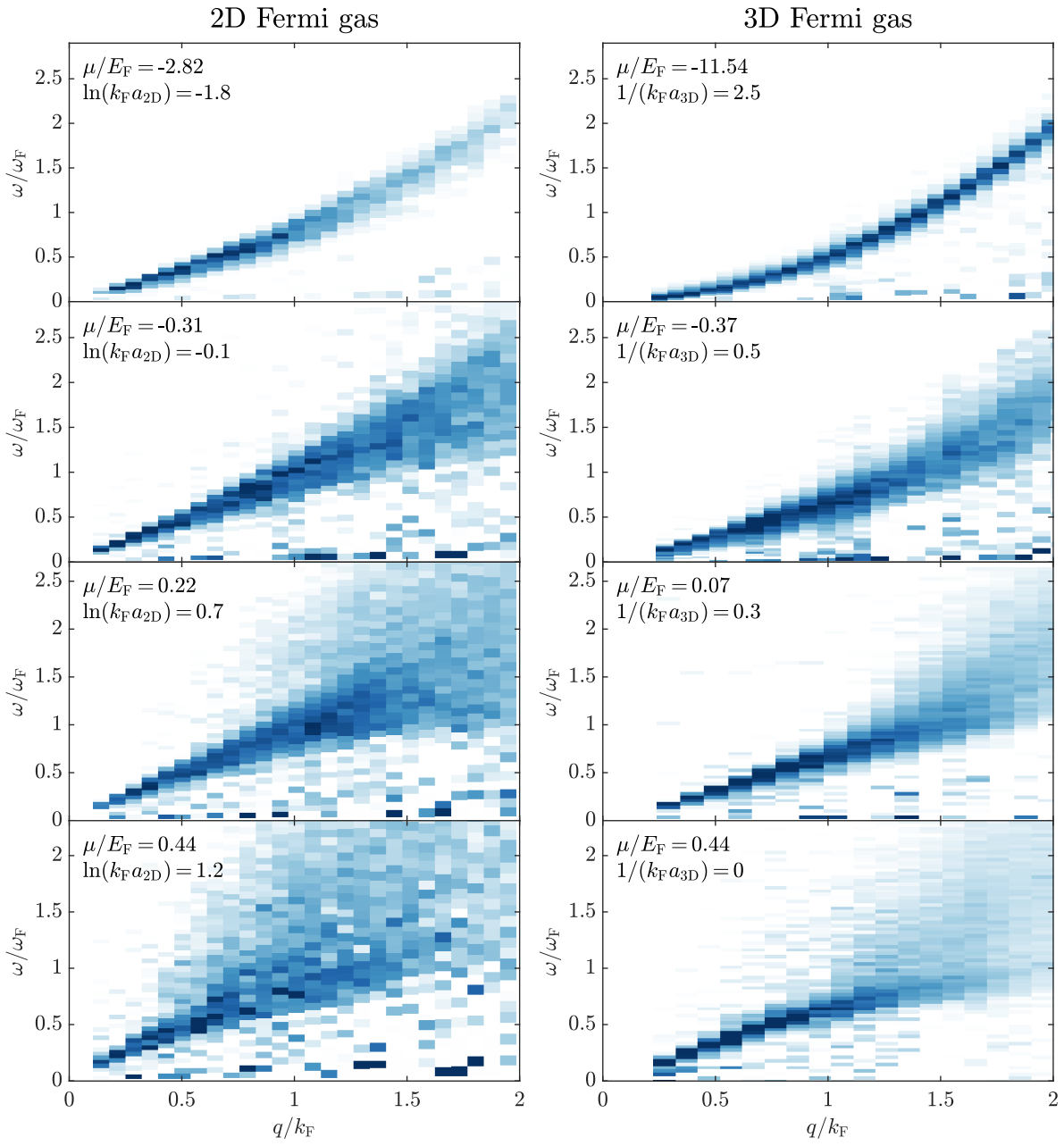

Figure 10.6: Comparison between results from 2D and 3D Shown are four typical dynamic structure factors from chapters 8 and 9 with somewhat similar values of the interaction parameter μ/E_F. The momentum and energy range shown has been restricted to a common area to enable a fair comparison. For the two dynamic structure factors shown in the top row, no measurements with closer values of μ/E_F were taken.

that still closely resembles the Bogoliubov dispersion relation. However, in the 2D Fermi gas, we already observe an almost completely straight mode with some first hints of downbending, as the effect of the pair breaking continuum can already be seen.

10.2.2 Comparing the superfluid gap

As we have discussed previously, the superfluid gap is one of the most important parameters in the description of fermionic superfluids, essentially capturing the stability of the superfluid phase. Therefore, and given our measurements of the superfluid gap in 2D and 3D Fermi gases, it is only natural to ask how the gap is affected by reducing the dimensionality from 3D to 2D. There are two different effects that might play a role: On the one hand, the two-body bound state exists for arbitrarily weak interactions in 2D, whereas in 3D it only exists on the BEC side of the resonance. As the superfluid gap consists of both the two-body binding energy and the additional contribution from the many-body state (see chapter 8), we could therefore expect the gap to be larger in 2D. On the other hand, there is no long range order in 2D (see section 4.2), and we know that the critical temperature for superfluidity should therefore be reduced to the BKT transition temperature T_{BKT}. While it is not clear what effect this reduction should have on the superfluid gap, we might nevertheless expect BKT superfluidity to be less robust.

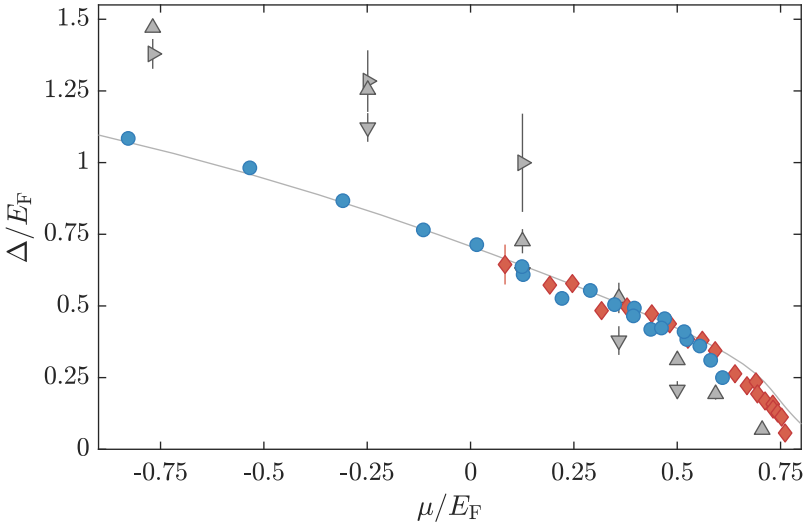

Figure 10.7: Comparing the gap of 2D and 3D Fermi gases. Blue points show our measurement of the gap in 2D Fermi gases; red diamonds show our results for 3D Fermi gases. The grey line is the prediction from ref. [151] for 3D Fermi gases; grey triangles show the predictions from 2D DMC (right facing, [156] and up facing, [158]) and 2D AFQMC (down facing, [157]). Our measurements from 2D and 3D collapse onto a single curve that is independent of the dimensionality of the system and in good agreement with theoretical predictions for 3D Fermi gases. Note that for the predictions from 2D QMC, we have used their results for $\Delta - E_B/2$ and added the appropriate binding energy for quasi-2D Fermi gases from ref. [29] to facilitate a fair comparison. Using just their calculations for Δ, the disagreement with our data would be significantly more pronounced in the BEC regime.

To resolve this question, we plot our previous measurements of the gap Δ/E_F against our new interaction parameter μ/E_F. The results are shown in fig. 10.7. Remarkably, we find that within the experimental precision, our measurements of the gap in 2D and 3D Fermi gases collapse onto a single curve. Our observations therefore suggest that the superfluid gap follows a single, universal function of the interaction strength that is independent of the dimensionality of

the system. This function seems be reasonably well described by self-consistent T-matrix calculations carried out for 3D Fermi gases in ref. [151], whereas 2D QMC calculations show very little agreement with our data as discussed previously.

This collapse is unlikely to be the result of experimental imperfections. While the gap should be reduced as T/T_c approaches 1, our 2D Fermi gases are well below the critical temperature for most of the BEC-BCS crossover, as discussed in chapter 7. Only the measurements furthest in the BCS regime were performed close to T_c, which could explain their slight deviation from the 3D measurements. Therefore, thermal excitations are unlikely to have significantly shifted the gap measured in 2D Fermi gases. For the case of the 3D Fermi gas, finite temperature might be the reason why our measurement of the gap in the BCS regime lies below the prediction from ref. [151] as discussed in chapter 9, but is very unlikely to be of relevance in the interaction range where our 2D and 3D results overlap.

Populated excited states in the axial direction are also unlikely to have affected our measurement of the gap, as they would be expected to be the more relevant the larger $\mu/\hbar\omega_z$ becomes. As ω_z is constant in our measurements, such effects would therefore also most strongly affect the data furthest in the BCS regime, where our measurements in 2D are not far from theoretical predictions. Trivial explanations such that our 2D Fermi gases actually behave like three-dimensional gases (and in consequence should be treated as such) because $\hbar\omega_z$ is not sufficiently large compared to the relevant energy scales can be ruled out by analyzing the data using this assumption. Assuming the system to be a purely 3D Fermi gas with an extent of l_z in the vertical direction, our measurements of the gap remain unaffected, but one obtains Fermi energies which are roughly twice as large, shifting the measured values of Δ/E_F far below those obtained for 3D systems.

The final possibility to be discussed is the modified two-body bound state in our quasi-2D geometry, which was already commented on in previous chapters (see especially fig. 4.18 and its discussion in section 4.5.2). The resulting change in E_B could certainly be of relevance for our measurement of the gap in 2D. The modification of the bound state and therefore the binding energy increases smoothly from the BCS- to the BEC limit, and we would expect a corresponding change in the superfluid gap to follow this trend. However, our measurements of the gap in 2D and 3D Fermi gases collapse over the entire range of interaction strengths probed, as is particularly evident from the remarkable agreement between the measured gaps in 2D and the prediction from ref. [151] in 3D even far in the BEC regime. Therefore, if this collapse was only a coincidence caused by the reduced two-body binding energy, it would have to be a case of truly remarkable accidental finetuning.

Consequently, these observations suggest that the stability of the superfluid phase in ultracold Fermi gases is remarkably robust with regard to changing the dimensionality of the system. A possible interpretation of this result is to say that μ/E_F and Δ/E_F (and ξk_F, for that

Note that we use the same conversion of $(k_F a_{3D})^{-1}$ to μ/E_F for the calculations of ref. [151] as we do for our data, although ref. [151] also yields results for the chemical potential. This choice is made to ensure that all data shown in fig. 10.7 is treated equally. However, we verified that using the chemical potential obtained in ref. [151] does not significantly affect the conclusions drawn here.

matter) are essentially the same quantity, describing the strength of pairing in the BEC-BCS crossover. In this interpretation, any change to the stability of the superfluid phase would be expressed purely in a modification of the critical temperature, whereas the zero-temperature parameters of the system would remain unaffected. However, current state of the art measurements of the critical temperature in the strongly interacting regime yield $T_c = 0.167(13)\,T_F$ for 3D Fermi gases [163] and $T_c = 0.167(39)\,T_F$ for 2D Fermi gases [28]. More work is therefore needed to see how the reduced dimensionality affects the critical temperature, and whether all other parameters of the system indeed remain unaffected.

Note that the measurement of the critical temperature in 2D [28] probed the critical temperature for pair condensation as opposed to superfluidity. However, as of the time of writing, no measurements of the critical temperature for superfluidity exist for strongly interacting 2D Fermi gases.

10.3 Comparing different fermionic superfluids

In this final section, I will extend our comparison beyond ultracold quantum gases and compare our systems to different superconducting materials. I will highlight the surprising relevance of weak coupling theory even towards the strongly correlated regime and show how our conclusions from ultracold Fermi gases seem to apply to fermionic superfluids in general.

Finally, it is time to return to the topic with which we have motivated this entire study: the question to what extent dimensionality matters in high-temperature superconductors. Here, the interaction parameter ξk_F which we have established in section 10.1 becomes useful due to its original design intent of parameterizing the interaction strength in superconductors: As ξ can be inferred for superconducting materials from measurements of the upper critical field, ξk_F presents us with the opportunity to perform the first direct comparison between ultracold Fermi gases and solid state superconductors. As in the previous section, we will investigate the influence of the reduced dimensionality on the superfluid gap as a probe for the stability of the superfluid phase.

The upper critical field H_{c2} refers to the magnetic field at which type-II superconductivity breaks down at 0 K. At this field, the magnetic flux through the superconductor is so large that the Abrikosov vortices that carry the magnetic flux quanta are separated exactly by their diameter, which is given by the coherence length ξ. Any further increase in the magnetic flux can no longer be accommodated, and superconductivity breaks down.

To this end, we surveyed publications from solid state physics that cited the seminal papers by Uemura and coworkers [7–10, 172] to find materials for which ξ, Δ, k_F and E_F had been reported. Whenever a material had additional tuneable parameters such as the doping level, we only selected data for optimally doped samples (corresponding to the highest critical temperatures). In cases such as cuprate superconductors where multiple gaps exist, we focused on the one most closely related to superconductivity (as opposed to e.g. the pseudogap state). In total, we were able to find 31 materials that fulfilled these requirements, of which 9 materials feature layered, two-dimensional structures. These materials are summarized in table 10.1.

Note that if only either k_F or E_F is known, the effective mass m^* can be used to obtain the other as $E_F = \frac{\hbar^2 k_F^2}{2m^*}$ for superconducting materials.

For our measurements of the gap in 2D and 3D Fermi gases, we interpolated our joint estimates of ξk_F in 2D and 3D shown in fig. 10.4 and discarded all measurements of the gap outside the interaction range for which estimates of ξk_F are available. The resulting comparison between 2D Fermi gases, 3D Fermi gases, various superconducting materials and liquid ^{3}He is shown in fig. 10.8. Our comparison spans five orders of magnitude in Δ/E_F and ξk_F, reaching from the

Material	Δ/k_B [K]	E_F/k_B [K]	ξ [Å]	k_F [Å^{-1}]	Ref.
$Bi_2Sr_2CaCu_2O_8$	140	970	7.0	0.41	[173, 174]
$Tl_2Ba_2Ca_2Cu_3O_{10}$	270	1800	7.3	0.49	[173, 175, 176]
$La_{1.85}Sr_{0.15}CuO_4$	84	1100	11	0.46	[173, 174]
$YBa_2Cu_3O_7$	470	8800	15	0.45	[173, 177, 178]
$RbCa_2Fe_4As_4F_2$	95	730	10	0.20	[179]
FeSe/STO	240	6200	6.7	0.61	[13, 180]
Pb	13	120000	830	1.6	[181]
Sn	6.6	110000	2300	1.6	[181]
Al	2.1	110000	16000	1.6	[181]
Nb	18	13000	111	0.54	[182–184]
$BaKBiO_3$	61	2900	53	0.26	[181, 185]
κ-$(ET)_2Cu(NCS)_2$	25	210	23	0.17	[173, 186]
$NbSe_2$	15	810	80	0.54	[187, 188]
$PbMo_6S_8$	36	1600	9.8	0.31	[173, 189]
YB_6	16	2400	330	0.41	[190]
YNi_2B_2C	21	4200	80	0.94	[190]
$LuRuB_2$	16	4100	180	0.85	[191, 192]
$YRuB_2$	13	2400	110	0.84	[191, 192]
K_3C_{60}	33	470	26	0.34	[10, 193]
Rb_3C_{60}	62	2900	29	0.49	[181, 193, 194]
Re_3Ta	8.6	640	110	0.46	[195]
$Re_{5.5}Ta$	16	2000	45	0.44	[196]
$Nb_{0.5}Os_{0.5}$	5.6	660	78	0.15	[197]
La_7Ir_3	4.3	520	190	0.40	[198]
LaPtGe	4.9	1200	59	0.43	[199]
BeAu	5.8	18000	1900	1.1	[200]
TaOs	3.5	900	74	0.50	[201]
Zr_3Ir	4.1	1700	46	0.75	[202]
$NbOs_2$	4.8	620	90	0.43	[203]
^3He	0.0046	0.89	200	0.78	[168, 204]
Li_xZrNCl		tuneable			[184]

Table 10.1: Parameters for different superconducting materials. Values and references for the superconducting gap Δ, the Fermi energy E_F, the coherence length ξ and the Fermi wavevector k_F used in fig. 10.8. We note that there are different extrapolation methods and definitions of the coherence length, leading to different values between references. However, the differences are generally on the order of unity and therefore do not affect the conclusions drawn below.

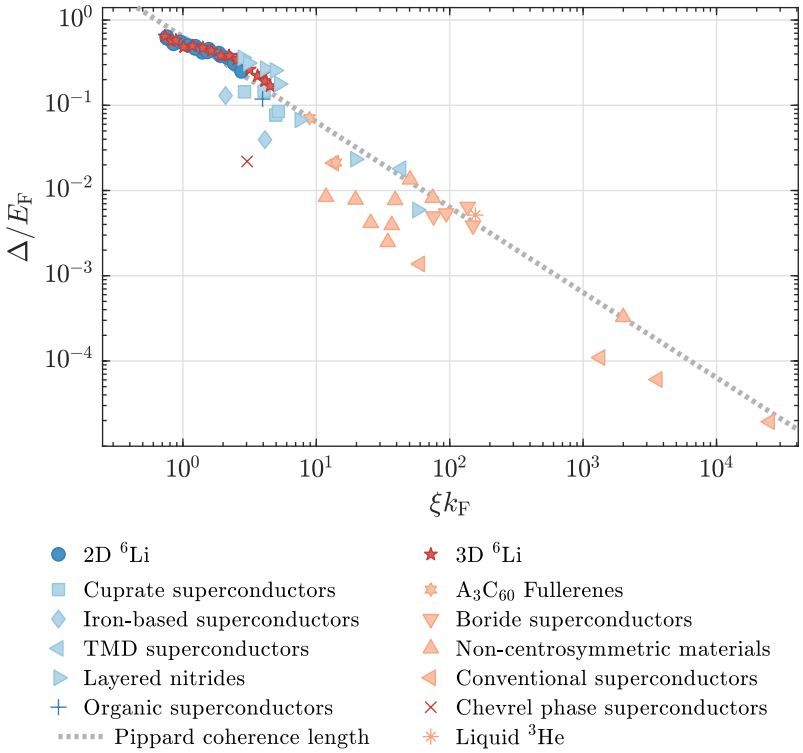

Figure 10.8: Comparing the gap of ultracold Fermi gases and superconducting materials. We find a clear correlation between large gaps Δ/E_F and short coherence lengths / pair sizes ξk_F that holds independent of the dimensionality of the system, and for superconductors and Fermi gases alike. Even at strong interactions, this correlation is well described by the weak coupling prediction of the Pippard coherence length.

The Pippard coherence length can intuitively be understood as the length scale associated with the softening of the Fermi edge due to pairing in BCS superfluids.

The large scatter of datapoints visible for superconducting materials most likely stems from effects such as disorder, competing order parameters and extrapolation errors in the determination of the upper critical field.

strongly correlated regime all the way into the weak coupling limit. We observe that all materials surveyed fall into a single band, which follows the Pippard coherence length $\xi_p = \frac{\hbar v_F}{\pi \Delta}$ [74, 205]. This expression, which is only expected to be valid in the weak coupling limit, holds surprisingly far into the strongly correlated regime, where our measurements finally appear to deviate as the system enters the BEC regime.

As pointed out by Uemura and coworkers [8], two-dimensional superconductors tend to feature larger values of Δ/E_F and correspondingly smaller values of the interaction parameter ξk_F. However, both two-dimensional and three-dimensional materials ultimately fall into the same band - the correlation between shorter pair sizes and larger superconducting gaps appears to be independent of the dimensionality. Consequently, fig. 10.8 suggests that there is no inherent change in the stability of fermionic superfluids in two dimensions compared to three-dimensional systems with the same interaction strength. This observation is in excellent agreement with our findings on ultracold Fermi gases, and strongly implies that dimensionality in itself does little to strengthen the superfluid phase in fermionic superfluids, independent of the material.

Part IV

Conclusion

11 CONCLUSION AND OUTLOOK

In this thesis, I have presented experiments on ultracold Fermi gases that have allowed us to perform the first quantitative comparison between two-dimensional and three-dimensional fermionic superfluids.

As the first main result, we established the presence of a critical velocity in the 2D BEC-BCS crossover, demonstrating superfluidity in two-dimensional Fermi gases. To this end, we subjected homogeneous two-dimensional Fermi gases to a moving optical lattice and showed that dissipation due to the lattice was absent below a critical lattice velocity. By tuning the wavevector of the moving lattice, we were able to demonstrate how different excitation mechanisms set the critical velocity in the BEC- and BCS regimes and measure the critical velocity throughout the crossover. Using the same lattice to heat the system, we observed the phase transition to the normal state and showed that the critical entropy is approximately constant from the BEC limit into the crossover.

As the second main result, we utilized this momentum-tunable moving optical lattice to perform Bragg spectroscopy on two-dimensional Fermi gases. This allowed us to map out their excitation spectrum in the crossover, which demonstrated the smooth evolution from BEC to BCS superfluidity in the crossover. We were able to clearly observe the distinct contributions from the Goldstone mode and the pair breaking continuum, and for the first time directly observed the interaction between the two modes. From the onset of pair breaking excitations, we obtained the superfluid gap as a function of the interaction strength, finding a remarkable deviation from state-of-the-art numerical calculations. We were furthermore able to expand our experimental setup to allow us to create three-dimensional homogeneous Fermi gases and measured their excitation spectrum using the same method as for two-dimensional Fermi gases. This allowed us to obtain the superfluid gap of 3D Fermi gases over a wide range of interaction strengths.

The third and final main result of this thesis is the comparison between 2D and 3D fermionic superfluids. To this end, we established two interaction parameters that are applicable to both 2D and 3D systems, namely the dimensionless chemical potential and the dimensionless pair size, and demonstrated that they are approximately equivalent. Having demonstrated superfluidity in 2D Fermi gases, and having performed similar measurements on the superfluid gap in both dimensionalities, we were able to perform the first direct comparison between two-dimensional and three-dimensional superfluids. We observed a remarkable collapse of the superfluid gaps measured in 2D and 3D onto a single, universal function of the interaction strength throughout the BEC-BCS crossover. Our parameterization of the interaction strength furthermore allowed us to compare ultracold Fermi

gases to superconducting materials for the first time. We observed a clear correlation between large superconducting gaps and short coherence lengths that holds independent of the dimensionality of the system, in excellent agreement with our observations on ultracold Fermi gases. Therefore, our experiments strongly suggest that the stability of the superfluid phase is remarkably unaffected by the dimensionality of the system in fermionic superfluids in general.

Outlook

In this thesis, we have restricted ourselves to studying of the influence of reduced dimensionality on the superfluid gap, and have found that the gap remains remarkably unaffected. However, in the context of high temperature superconductivity, the critical temperature should clearly be the more relevant quantity for their usefulness. Therefore, it would be of great interest to study how our results extend to the influence of reduced dimensionality on the critical temperature. So far, the best estimates for the critical temperature in 2D and 3D Fermi gases agree at the point of strongest interactions [28, 163]. However, little data exists away from unitarity in 3D, and the measurements performed in 2D have large uncertainties associated with them. Therefore, reliable measurements of the critical temperature for superfluidity in 2D and 3D would represent a significant increase in our understanding of fermionic superfluids.

However, thermometry of ultracold systems with strong interactions is by no means a trivial task. One comparatively simple path to reliable thermometry in 3D is to expand the method we have used in 3D Fermi gases. Currently, this method is limited to unitarity because the virial theorem requires knowledge of the internal energy density, which is difficult to calculate away from unitarity. However, by measuring Tan's contact [139–141] for different interaction strengths, the energy of the unitary Fermi gas could be related to that at different interaction strengths using the adiabatic sweep theorem. This approach has the advantage that it does not require significant modifications of the experimental setup as would be required e.g. for measuring the temperature using impurities of a different atomic species. The only necessary modification would be a second Bragg lattice at a very large wavevector, so that Tan's contact can be obtained from the high-energy tail of the dynamic structure factor [142, 143, 206].

We note that extending this proposed technique to 2D is not straightforward. First, one would have to find an interaction strength where the energy can be precisely measured, as no unitary point exists where the internal energy density can be trivially calculated. Then, the contact would have to be measured [207], and an additional measurement would need to connect the energy to the temperature at one interaction strength, e.g. following the procedure of ref. [93].

Besides measuring the critical temperature, a robust method of thermometry in the BEC-BCS crossover would also enable a wide range of additional measurements on finite-temperature fermionic superfluids. One very promising avenue of further research would be to study the strongly correlated normal state of fermionic superfluids. Historically, the trivial presence of pairs above the critical temperature in the strongly correlated regime has been compared by some to the pseudogap state in cuprate superconductors (see e.g. refs. [60, 95, 134, 208, 209]). However, current experimental evidence associates the pseudogap in cuprate superconductors with a competing

order parameter corresponding to a density-wave ordered state [36], which is not expected to be present in ultracold Fermi gases. Nevertheless, the onset of pairing in the normal state has been suggested to be relevant in setting the critical temperature for superconductivity, see e.g. refs. [210, 211]. Furthermore, initial studies performed using RF spectroscopy have shown density-dependent many-body pairing in the strongly correlated regime [87]. Consequently, it would be of great interest to measure how the dynamic structure factor evolves as the phase transition is crossed. Given our capacity of preparing and probing 2D and 3D Fermi gases, it could furthermore be interesting to see if this evolution occurs differently depending on the dimensionality [212].

However, not all future studies need to focus on finite-temperature physics. A recent upgrade added an accordion lattice to our setup (see e.g. ref. [91]), enabling continuous tuning from two-dimensional confinement to three-dimensional Fermi gases. Using this accordion lattice, studies could probe the evolution from 2D to quasi-2D to oblate 3D geometries to further study the influence of reduced dimensionality on fermionic superfluids. Another advantage of such a tunable lattice is that it is much better suited for loading systems with large chemical potentials such as spin-imbalanced gases. This could be helpful to prepare exotic phases of matter such as the elusive Fulde-Ferrel-Larkin-Ovchinnikov (FFLO) phase [213].

Another possibility would be to focus on our Bragg spectroscopy. Using near-detuned Bragg beams, our experimental setup would be perfectly suited to investigate the dynamic spin structure factor [206] as a complement to the dynamic (density) structure factor we have studied in this thesis. Because the spin response is unaffected by the Goldstone mode, such measurements could measure the superfluid gap further into the BEC regime. Furthermore, it has been suggested that the spin structure factor is the ideal tool to measure the Higgs mode [66], which is otherwise difficult to probe as it lies within or very close to the pair breaking continuum.

Finally, while not the main subject of this thesis, over the last years we have made significant improvements in creating systems with arbitrary potentials, which enabled us to e.g. implement an ideal Josephson junction in a 2D Fermi gas. Using a combination of digital micromirror devices (DMDs) to create a tunnel junction and to measure its conductivity, our experiment is perfectly suited to implement a recent proposal [214] to create a quantum gas analogue to the enhancement of interlayer transport in high-temperature superconductors [215, 216].

To summarize, at the end of my PhD thesis, our experimental apparatus is in a great spot: After many years of work, we are able to reliably prepare homogeneous superfluid Fermi gases in 2D and 3D over a wide range of interaction strengths [20, 42]. Besides directly imaging their density- and momentum distribution [20, 38], we are able to manipulate them using DMDs [39, 40] and probe their excitation spectrum using Bragg spectroscopy [12, 41, 42]. We have established

methods to control the temperature and entropy in these systems [20, 39, 41, 42] and to probe the phase transition to the normal state [41]. Therefore, our experimental apparatus is positioned well to investigate a wide range of problems, and will serve as a strong basis no matter in what direction the future will take our research.

BIBLIOGRAPHY

[1] J. G. Bednorz and K. A. Müller: *Possible high T c superconductivity in the Ba- La- Cu- O system*, "Z. Phys. B: Condens. Matter" vol. 64, no. 2, 189–193 (1986) (cited on page 7).

[2] B. Keimer, S. A. Kivelson, M. R. Norman, S. Uchida, and J. Zaanen: *From quantum matter to high-temperature superconductivity in copper oxides*, "Nature" vol. 518, no. 7538, 179–186 (2015) (cited on pages 7, 9).

[3] P. C. Hohenberg: *Existence of Long-Range Order in One and Two Dimensions*, "Physical Review" vol. 158, no. 2, 383–386 (1967) (cited on pages 7, 25).

[4] V. L. Berezinskii: *Destruction of long-range order in one-dimensional and two-dimensional systems having a continuous symmetry group I. Classical systems*, "Sov. Phys. JETP" vol. 32, no. 3, 493–500 (1971) (cited on pages 7, 26).

[5] V. L. Berezinskii: *Destruction of long-range order in one-dimensional and two-dimensional systems possessing a continuous symmetry group. ii. quantum systems*, "Sov. Phys. JETP" vol. 34, no. 3, 610–616 (1972) (cited on pages 7, 26).

[6] J. M. Kosterlitz and D. J. Thouless: *Ordering, metastability and phase transitions in two-dimensional systems*, "J. Phys. C: Solid State Phys." vol. 6, no. 7, 1181 (1973) (cited on pages 7, 26).

[7] Y. J. Uemura, G. M. Luke, B. J. Sternlieb, J. H. Brewer, J. F. Carolan, W. N. Hardy, R. Kadono, J. R. Kempton, R. F. Kiefl, S. R. Kreitzman, P. Mulhern, T. M. Riseman, D. L. Williams, B. X. Yang, S. Uchida, H. Takagi, J. Gopalakrishnan, A. W. Sleight, M. A. Subramanian, C. L. Chien, M. Z. Cieplak, G. Xiao, V. Y. Lee, B. W. Statt, C. E. Stronach, W. J. Kossler, and X. H. Yu: *Universal correlations between Tc and ns/m (carrier density over effective mass) in high-Tc cuprate superconductors*, "Phys. Rev. Lett." vol. 62, no. 19, 2317–2320 (1989) (cited on pages 7, 126).

[8] Y. J. Uemura, L. P. Le, G. M. Luke, B. J. Sternlieb, W. D. Wu, J. H. Brewer, T. M. Riseman, C. L. Seaman, M. B. Maple, M. Ishikawa, D. G. Hinks, J. D. Jorgensen, G. Saito, and H. Yamochi: *Basic similarities among cuprate, bismuthate, organic, Chevrel-phase, and heavy-fermion superconductors shown by penetration-depth measurements*, "Phys. Rev. Lett." vol. 66, no. 20, 2665–2668 (1991) (cited on pages 7, 8, 117, 126, 128).

[9] Y. J. Uemura: *Muon spin relaxation studies on high-Tc organic, heavy-fermion, and Chevrel phase superconductors*, "Phys. B" vol. 169, 99–106 (1991) (cited on pages 7, 126).

[10]Y. J. Uemura, A. Keren, L. P. Le, G. M. Luke, B. J. Sternlieb, W. D. Wu, J. H. Brewer, R. L. Whetten, S. M. Huang, S. Lin, R. B. Kaner, F. Diederich, S. Donovan, G. Grüner, and K. Holczer: *Magnetic-field penetration depth in K 3 C 60 measured by muon spin relaxation*, "Nature" vol. 352, no. 6336, 605–607 (1991) (cited on pages 7, 126, 127).

[11]J. Bardeen, L. N. Cooper, and J. R. Schrieffer: *Theory of Superconductivity*, "Phys. Rev." vol. 108, no. 5, 1175–1204 (1957) (cited on pages 7, 29).

[12]L. Sobirey, H. Biss, N. Luick, M. Bohlen, H. Moritz, and T. Lompe: *Comparing fermionic superfluids in two and three dimensions*, "arXiv: 2106.11893" (2021) (cited on pages 8, 9, 12, 95, 115, 133).

[13]J.-F. Ge, Z.-L. Liu, C. Liu, C.-L. Gao, D. Qian, Q.-K. Xue, Y. Liu, and J.-F. Jia: *Superconductivity above 100 K in single-layer FeSe films on doped SrTiO3*, "Nat. Mater." vol. 14, no. 3, 285–289 (2015) (cited on pages 8, 127).

[14]Y. Yu, L. Ma, P. Cai, R. Zhong, C. Ye, J. Shen, G. D. Gu, X. H. Chen, and Y. Zhang: *High-temperature superconductivity in monolayer Bi2Sr2 CaCu2O8+δ*, "Nature" vol. 575, no. 7781, 156–163 (2019) (cited on page 8).

[15]I. Bloch, J. Dalibard, and W. Zwerger: *Many-body physics with ultracold gases*, "Rev. Mod. Phys." vol. 80, no. 3, 885–964 (2008) (cited on page 8).

[16]W. Zwerger: *The BCS-BEC Crossover and the Unitary Fermi Gas*, Sprin ger Science & Business Media Oct. 2011 (cited on page 8).

[17]W. Ketterle and M. W. Zwierlein: *Making, probing and understanding ultracold Fermi gases*, in *Proceedings of the International School of Physics-Enrico Fermi*, edited by M Inguscio, S Stringari, Jan. 2008 (cited on pages 8, 9).

[18]S. Giorgini, L. P. Pitaevskii, and S. Stringari: *Theory of ultracold atomic Fermi gases*, "Rev. Mod. Phys." vol. 80, no. 4, 1215–1274 (2008) (cited on page 8).

[19]C. Chin, R. Grimm, P. Julienne, and E. Tiesinga: *Feshbach resonances in ultracold gases*, "Rev. Mod. Phys." vol. 82, no. 2, 1225–1286 (2010) (cited on pages 8, 49, 50, 96).

[20]K. Hueck, N. Luick, L. Sobirey, J. Siegl, T. Lompe, and H. Moritz: *Two-Dimensional Homogeneous Fermi Gases*, "Phys. Rev. Lett." vol. 120, no. 6, 060402 (2018) (cited on pages 8, 9, 14, 57, 58, 60, 65, 66, 133, 134).

[21]C. Gross and W. S. Bakr: *Quantum gas microscopy for single atom and spin detection*, "arXiv:2010.15407" (2020) (cited on page 8).

[22]H. Moritz, T. Stöferle, K. Günter, M. Köhl, and T. Esslinger: *Confinement induced molecules in a 1D Fermi gas*, "Phys. Rev. Lett." vol. 94, no. 21, 210401 (2005) (cited on page 9).

[23]X.-W. Guan, M. T. Batchelor, and C. Lee: *Fermi gases in one dimension: From Bethe ansatz to experiments*, "Rev. Mod. Phys." vol. 85, no. 4, 1633–1691 (2013) (cited on page 9).

[24]K. Martiyanov, V. Makhalov, and A. Turlapov: *Observation of a two-dimensional fermi gas of atoms*, "Phys. Rev. Lett." vol. 105, no. 3, 030404 (2010) (cited on pages 9, 57, 58).

[25]B. Fröhlich, M. Feld, E. Vogt, M. Koschorreck, W. Zwerger, and M. Köhl: *Radio-Frequency Spectroscopy of a Strongly Interacting Two-Dimensional Fermi Gas*, "Phys. Rev. Lett." vol. 106, no. 10 (2011) (cited on pages 9, 57, 59).

[26]A. T. Sommer, L. W. Cheuk, M. J. H. Ku, W. S. Bakr, and M. W. Zwierlein: *Evolution of fermion pairing from three to two dimensions*, "Phys. Rev. Lett." vol. 108, no. 4, 045302 (2012) (cited on pages 9, 57, 59).

[27]W. Ong, C. Cheng, I. Arakelyan, and J. E. Thomas: *Spin-imbalanced quasi-two-dimensional Fermi gases*, "Phys. Rev. Lett." vol. 114, no. 11, 110403 (2015) (cited on pages 9, 59).

[28]M. G. Ries, A. N. Wenz, G. Zürn, L. Bayha, I. Boettcher, D. Kedar, P. A. Murthy, M. Neidig, T. Lompe, and S. Jochim: *Observation of Pair Condensation in the Quasi-2D BEC-BCS Crossover*, "Phys. Rev. Lett." vol. 114, no. 23, 230401 (2015) (cited on pages 9, 57–60, 69, 77, 90, 92–94, 116, 126, 132).

[29]J. Levinsen and M. M. Parish: *Strongly Interacting Two-Dimensional Fermi Gases*, in *Annual Review of Cold Atoms and Molecules*, Vol. 3, Annual Review of Cold Atoms and Molecules, World Scientific Feb. 2015, pp. 1–75 (cited on pages 9, 51, 53, 90, 107, 116, 121, 124).

[30]A. V. Turlapov and M. Yu Kagan: *Fermi-to-Bose crossover in a trapped quasi-2D gas of fermionic atoms*, "J. Phys. Condens. Matter" vol. 29, no. 38, 383004 (2017) (cited on pages 9, 51, 54).

[31]B. DeMarco and D. S. Jin: *Onset of fermi degeneracy in a trapped atomic Gas*, "Science" vol. 285, no. 5434, 1703–1706 (1999) (cited on page 9).

[32]C. A. Regal, C. Ticknor, J. L. Bohn, and D. S. Jin: *Creation of ultracold molecules from a Fermi gas of atoms*, "Nature" vol. 424, no. 6944, 47–50 (2003) (cited on page 9).

[33]M. Greiner, C. A. Regal, and D. S. Jin: *Emergence of a molecular Bose–Einstein condensate from a Fermi gas*, "Nature" vol. 426, no. 6966, 537–540 (2003) (cited on page 9).

[34]P. A. Lee, N. Nagaosa, and X.-G. Wen: *Doping a Mott insulator: Physics of high-temperature superconductivity*, "Rev. Mod. Phys." vol. 78, no. 1, 17–85 (2006) (cited on page 9).

[35]P. A. Lee: *From high temperature superconductivity to quantum spin liquid: progress in strong correlation physics*, "Rep. Prog. Phys." vol. 71, no. 1, 012501 (2007) (cited on page 9).

[36]M. Hashimoto, I. M. Vishik, R.-H. He, T. P. Devereaux, and Z.-X. Shen: *Energy gaps in high-transition-temperature cuprate superconductors*, "Nat. Phys." vol. 10, no. 7, 483–495 (2014) (cited on pages 9, 97, 133).

[37]P. A. Lee and T. V. Ramakrishnan: *Disordered electronic systems*, "Rev. Mod. Phys." vol. 57, no. 2, 287–337 (1985) (cited on page 9).

[38]K. Hueck, N. Luick, L. Sobirey, J. Siegl, T. Lompe, H. Moritz, L. W. Clark, and C. Chin: *Calibrating high intensity absorption imaging of ultracold atoms*, "Opt. Express" vol. 25, no. 8, 8670–8679 (2017) (cited on pages 9, 14, 66, 133).

[39]N. Luick, L. Sobirey, M. Bohlen, V. P. Singh, L. Mathey, T. Lompe, and H. Moritz: *An ideal Josephson junction in an ultracold two-dimension al Fermi gas*, "Science" vol. 369, no. 6499, 89–91 (2020) (cited on pages 9, 13, 60, 69, 94, 133, 134).

[40]M. Bohlen, L. Sobirey, N. Luick, H. Biss, T. Enss, T. Lompe, and H. Moritz: *Sound Propagation and Quantum-Limited Damping in a Two-Dimensional Fermi Gas*, "Phys. Rev. Lett." vol. 124, no. 24, 240403 (2020) (cited on pages 9, 13, 60, 66, 85, 86, 102, 103, 116, 133).

[41]L. Sobirey, N. Luick, M. Bohlen, H. Biss, H. Moritz, and T. Lompe: *Observation of superfluidity in a strongly correlated two-dimensional Fermi gas*, "Science" vol. 372, no. 6544, 844–846 (2021) (cited on pages 9, 11, 69, 133, 134).

[42]H. Biss, L. Sobirey, N. Luick, M. Bohlen, J. J. Kinnunen, G. M. Bruun, T. Lompe, and H. Moritz: *Excitation Spectrum and Superfluid Gap of an Ultracold Fermi Gas*, "arXiv:2105.09820" (2021) (cited on pages 9, 13, 111, 133, 134).

[43]N. Luick: *An ideal Josephson junction in an ultracold two-dimensional Fermi gas*, PhD thesis, Universität Hamburg (cited on pages 13, 54, 61–64).

[44]M. Bohlen: *Sound Propagation and Quantum-Limited Damping in an Ultracold Two-Dimensional Fermi Gas*, PhD thesis, Ecole Normale Superieure Paris (cited on page 13).

[45]V. P. Singh, N. Luick, L. Sobirey, and L. Mathey: *Josephson junction dynamics in a two-dimensional ultracold Bose gas*, "Phys. Rev. Research" vol. 2, no. 3, 033298 (2020) (cited on page 14).

[46]K. Hueck: *A homogeneous, two-dimensional Fermi gas*, PhD thesis, Universität Hamburg (cited on pages 14, 58, 61, 64).

[47]G. V. Shlyapnikov: *Lecture on Ultracold quantum gases, Part 1: Bose-condensed gases* (cited on page 19).

[48]Y. Nambu: *Quasi-Particles and Gauge Invariance in the Theory of Superconductivity*, "Phys. Rev." vol. 117, no. 3, 648–663 (1960) (cited on page 24).

[49]J. Goldstone: *Field theories with Superconductor solutions*, "Il Nuovo Cimento (1955-1965)" vol. 19, no. 1, 154–164 (1961) (cited on page 24).

[50]L. Landau: *Theory of the Superfluidity of Helium II*, "Phys. Rev." vol. 60, no. 4, 356–358 (1941) (cited on page 24).

[51]Z. Hadzibabic and J. Dalibard: *Two-dimensional Bose fluids: An atomic physics perspective*, "La Rivista Del Nuovo Cimento", no. 6 (2011) (cited on page 25).

[52]H. Moritz: *One-dimensional Atomic gases*, PhD thesis, ETH Zürich (cited on page 25).

[53]J. Michael Kosterlitz: *Kosterlitz–Thouless physics: a review of key issues*, "Rep. Prog. Phys." vol. 79, no. 2, 026001 (2016) (cited on page 26).

[54]C. Mora and Y. Castin: *Extension of Bogoliubov theory to quasicondensates*, "Phys. Rev. A" vol. 67, no. 5, 053615 (2003) (cited on page 27).

[55]M. W. Zwierlein: *High-Temperature Superfluidity in an Ultracold Fermi Gas*, PhD thesis, MIT (cited on pages 29, 30, 42, 114).

[56]K. Onnes and H: *The superconductivity of mercury*, "Comm. Phys. Lab. Univ. Leiden" vol. 122, 122–124 (1911) (cited on page 29).

[57]L. N. Cooper: *Bound Electron Pairs in a Degenerate Fermi Gas*, "Phys. Rev." vol. 104, no. 4, 1189–1190 (1956) (cited on page 29).

[58]A. J. Leggett: *Modern trends in the theory of condensed matter*, "Modern Trends in the Theory of Condensed Matter, Proc. XVI Karpacz Winter School of Theoretical Physics, 1980" (1980) (cited on page 30).

[59]M. Randeria, J. M. Duan, and L. Y. Shieh: *Bound states, Cooper pairing, and Bose condensation in two dimensions*, "Phys. Rev. Lett." vol. 62, no. 9, 981–984 (1989) (cited on pages 35, 81, 84, 106–109, 116, 117, 119).

[60]M. Bauer, M. M. Parish, and T. Enss: *Universal equation of state and pseudogap in the two-dimensional Fermi gas*, "Phys. Rev. Lett." vol. 112, no. 13, 135302 (2014) (cited on pages 35, 92–94, 132).

[61]G. Bighin and L. Salasnich: *Renormalization of the superfluid density in the two-dimensional BCS-BEC crossover*, "Int. J. Mod. Phys. B" vol. 32, no. 17, 1840022 (2018) (cited on pages 35, 90, 92–94).

[62]F. Wu, J. Hu, L. He, X.-J. Liu, and H. Hu: *Effective theory for ultracold strongly interacting fermionic atoms in two dimensions*, "arXiv:1906.08578" (2019) (cited on pages 35, 53).

[63]E. Kuhnle: *Studies of Universality in Strongly Interacting 6Li Fermi Gases with Bragg Spectroscopy*, PhD thesis, Swinbourne (cited on pages 37, 44, 76).

[64]L. Van Hove: *Correlations in Space and Time and Born Approximation Scattering in Systems of Interacting Particles*, "Phys. Rev." vol. 95, no. 1, 249–262 (1954) (cited on page 39).

[65]P. W. Anderson: *Random-Phase Approximation in the Theory of Superconductivity*, "Physical Review" vol. 112, no. 6, 1900–1916 (1958) (cited on pages 44, 104).

[66]H. Zhao, X. Gao, W. Liang, P. Zou, and F. Yuan: *Dynamical structure factors of a two-dimensional Fermi superfluid within random phase approximation*, "New J. Phys." vol. 22, no. 9, 093012 (2020) (cited on pages 44, 99, 133).

[67]R. Combescot, M. Y. Kagan, and S. Stringari: *Collective mode of homogeneous superfluid Fermi gases in the BEC-BCS crossover*, "Phys. Rev. A" vol. 74, no. 4, 042717 (2006) (cited on pages 44, 72, 99).

[68]P. Zou, F. Dalfovo, R. Sharma, X.-J. Liu, and H. Hu: *Dynamic structure factor of a strongly correlated Fermi superfluid within a density functional theory approach*, "New J. Phys." vol. 18, no. 11, 113044 (2016) (cited on pages 44, 99).

[69]S. Hoinka, P. Dyke, M. G. Lingham, J. J. Kinnunen, G. M. Bruun, and C. J. Vale: *Goldstone mode and pair-breaking excitations in atomic Fermi superfluids*, "Nat. Phys." vol. 13, no. 10, 943–946 (2017) (cited on pages 44–46, 97–99, 107, 114).

[70]L. D. Landau and I. M. Khalatnikov: *Theory of viscosity of Hellium II. 1. Collissions of elementary excitations in Hellium II*, "Zhurnal Eksperimentalnoi I Teoreticheskoi Fiziki" vol. 19, no. 7, 637–650 (1949) (cited on page 44).

[71]H. Kurkjian, Y. Castin, and A. Sinatra: *Three-Phonon and Four-Phonon Interaction Processes in a Pair-Condensed Fermi Gas*, "Ann. Phys." vol. 529, no. 9, 1600352 (2017) (cited on page 44).

[72]G. Bighin and L. Salasnich: *Finite-temperature quantum fluctuations in two-dimensional Fermi superfluids*, "Phys. Rev. B Condens. Matter" vol. 93, no. 1, 014519 (2016) (cited on page 45).

[73]E. Babaev and H. Kleinert: *Crossover from Weak- to Strong-Coupling Superconductivity and to Normal State with Pseudogap*, "arXiv:9804206" (1998) (cited on page 45).

[74]N. W. Ashcroft and N. D. Mermin: *Solid state physics*, New York: Holt, Rinehart and Winston, 1976 (cited on pages 45, 128).

[75]J. Stenger, S. Inouye, A. P. Chikkatur, D. M. Stamper-Kurn, D. E. Pritchard, and W. Ketterle: *Bragg Spectroscopy of a Bose-Einstein Condensate*, "Phys. Rev. Lett." vol. 82, no. 23, 4569–4573 (1999) (cited on pages 45, 99).

[76]D. M. Stamper-Kurn, A. P. Chikkatur, A. Görlitz, S. Inouye, S. Gupta, D. E. Pritchard, and W. Ketterle: *Excitation of Phonons in a Bose-Einstein Condensate by Light Scattering*, "Phys. Rev. Lett." vol. 83, no. 15, 2876–2879 (1999) (cited on page 45).

[77]C. Carcy, S. Hoinka, M. G. Lingham, P. Dyke, C. C. N. Kuhn, H. Hu, and C. J. Vale: *Contact and Sum Rules in a Near-Uniform Fermi Gas at Unitarity*, "Phys. Rev. Lett." vol. 122, no. 20, 203401 (2019) (cited on pages 45, 97).

[78]P. T. Ernst, S. Götze, J. S. Krauser, K. Pyka, D.-S. Lühmann, D. Pfannkuche, and K. Sengstock: *Probing superfluids in optical lattices by momentum-resolved Bragg spectroscopy*, "Nat. Phys." vol. 6, no. 1, 56–61 (2010) (cited on page 45).

[79]D. Clément, N. Fabbri, L. Fallani, C. Fort, and M. Inguscio: *Exploring Correlated 1D Bose Gases from the Superfluid to the Mott-Insulator State by Inelastic Light Scattering*, "Phys. Rev. Lett." vol. 102, no. 15 (2009) (cited on page 46).

[80]D. Clément, N. Fabbri, L. Fallani, C. Fort, and M. Inguscio: *Multiband spectroscopy of inhomogeneous Mott-insulator states of ultracold bosons*, "New J. Phys." vol. 11, no. 10, 103030 (2009) (cited on page 46).

[81]T. Lompe: *Efimov physics in a three-component Fermi gas*, PhD thesis, Universität Heidelberg (cited on pages 47, 49).

[82]J. Dalibard: *Collisional dynamics of ultra-cold atomic gases*, in *Proceedings of the International School of Physics-Enrico Fermi*, Vol. 321, edited by M Inguscio, S Stringari, 1999, p. 14 (cited on page 47).

[83]R. J. Le Roy, N. S. Dattani, J. A. Coxon, A. J. Ross, P. Crozet, and C. Linton: *Accurate analytic potentials for Li2($X\,\Sigma 1g+$) and Li2($A\,\Sigma 1u+$) from 2 to 90 Å, and the radiative lifetime of Li(2p)*, "J. Chem. Phys." vol. 131, no. 20, 204309 (2009) (cited on page 51).

[84]G. Zürn, T. Lompe, A. N. Wenz, S. Jochim, P. S. Julienne, and J. M. Hutson: *Precise Characterization of Li 6 Feshbach Resonances Using Trap-Sideband-Resolved RF Spectroscopy of Weakly Bound Molecules*, "Phys. Rev. Lett." vol. 110, no. 13 (2013) (cited on pages 51, 96, 116, 121).

[85]D. S. Petrov and G. V. Shlyapnikov: *Interatomic collisions in a tightly confined Bose gas*, "Phys. Rev. A" vol. 64, no. 1, 012706 (2001) (cited on page 52).

[86]P. A. Murthy, N. Defenu, L. Bayha, M. Holten, P. M. Preiss, T. Enss, and S. Jochim: *Quantum scale anomaly and spatial coherence in a 2D Fermi superfluid*, "Science" vol. 365, no. 6450, 268–272 (2019) (cited on pages 52, 55, 59, 60, 69, 116).

[87]P. A. Murthy, M. Neidig, R. Klemt, L. Bayha, I. Boettcher, T. Enss, M. Holten, G. Zürn, P. M. Preiss, and S. Jochim: *High-temperature pairing in a strongly interacting two-dimensional Fermi gas*, "Science" vol. 359, no. 6374, 452–455 (2018) (cited on pages 52, 59, 116, 133).

[88]T. Peppler, P. Dyke, M. Zamorano, I. Herrera, S. Hoinka, and C. J. Vale: *Quantum Anomaly and 2D-3D Crossover in Strongly Interacting Fermi Gases*, "Phys. Rev. Lett." vol. 121, no. 12, 120402 (2018) (cited on pages 55, 60, 95).

[89]M. Holten, L. Bayha, A. C. Klein, P. A. Murthy, P. M. Preiss, and S. Jochim: *Anomalous Breaking of Scale Invariance in a Two-Dimensional Fermi Gas*, "Phys. Rev. Lett." vol. 121, no. 12, 120401 (2018) (cited on pages 55, 60, 95).

[90]Y. Zhang, W. Ong, I. Arakelyan, and J. E. Thomas: *Polaron-to-polaron transitions in the radio-frequency spectrum of a quasi-two-dimensional Fermi gas*, "Phys. Rev. Lett." vol. 108, no. 23, 235302 (2012) (cited on pages 57, 59).

[91]D. Mitra, P. T. Brown, P. Schauß, S. S. Kondov, and W. S. Bakr: *Phase Separation and Pair Condensation in a Spin-Imbalanced 2D Fermi Gas*, "Phys. Rev. Lett." vol. 117, no. 9, 093601 (2016) (cited on pages 57, 59, 133).

[92]P. Dyke, K. Fenech, T. Peppler, M. G. Lingham, S. Hoinka, W. Zhang, S.-G. Peng, B. Mulkerin, H. Hu, X.-J. Liu, and C. J. Vale: *Criteria for two-dimensional kinematics in an interacting Fermi gas*, "Phys. Rev. A" vol. 93, no. 1, 011603 (2016) (cited on pages 58, 60).

[93]K. Fenech, P. Dyke, T. Peppler, M. G. Lingham, S. Hoinka, H. Hu, and C. J. Vale: *Thermodynamics of an Attractive 2D Fermi Gas*, "Phys. Rev. Lett." vol. 116, no. 4, 045302 (2016) (cited on pages 58, 59, 77, 132).

[94]S. K. Baur, B. Fröhlich, M. Feld, E. Vogt, D. Pertot, M. Koschorreck, and M. Köhl: *Radio-frequency spectra of Feshbach molecules in quasi-two-dimensional geometries*, "Phys. Rev. A" vol. 85, no. 6, 061604 (2012) (cited on page 59).

[95]M. Feld, B. Fröhlich, E. Vogt, M. Koschorreck, and M. Köhl: *Observation of a pairing pseudogap in a two-dimensional Fermi gas*, "Nature" vol. 480, no. 7375, 75–78 (2011) (cited on pages 59, 132).

[96]I. Boettcher, L. Bayha, D. Kedar, P. A. Murthy, M. Neidig, M. G. Ries, A. N. Wenz, G. Zürn, S. Jochim, and T. Enss: *Equation of State of Ultracold Fermions in the 2D BEC-BCS Crossover Region*, "Phys. Rev. Lett." vol. 116, no. 4, 045303 (2016) (cited on pages 59, 77, 116).

[97]V. Makhalov, K. Martiyanov, and A. Turlapov: *Ground-state pressure of quasi-2D Fermi and Bose gases*, "Phys. Rev. Lett." vol. 112, no. 4, 045301 (2014) (cited on page 59).

[98]P. A. Murthy, D. Kedar, T. Lompe, M. Neidig, M. G. Ries, A. N. Wenz, G. Zürn, and S. Jochim: *Matter-wave Fourier optics with a strongly interacting two-dimensional Fermi gas*, "Phys. Rev. A" vol. 90, no. 4, 043611 (2014) (cited on page 59).

[99]P. A. Murthy, I. Boettcher, L. Bayha, M. Holzmann, D. Kedar, M. Neidig, M. G. Ries, A. N. Wenz, G. Zürn, and S. Jochim: *Observation of the Berezinskii-Kosterlitz-Thouless Phase Transition in an Ultracold Fermi Gas*, "Phys. Rev. Lett." vol. 115, no. 1, 010401 (2015) (cited on pages 59, 60, 69).

[100]W. Weimer: *Probing superfluid properties in strongly correlated Fermi gases with high spatial resolution*, PhD thesis, Universität Hamburg (cited on page 61).

[101]K. H. Morgener: *Microscopy of 2D Fermi Gases: Exploring excitations and thermodynamics*, PhD thesis, Univ. Hamburg (cited on pages 61–63).

[102]J. Siegl: *Probing coherence properties of strongly interacting Bose gases*, PhD thesis, Universität Hamburg (cited on page 61).

[103]H. J. Metcalf and P. van der Straten: *Laser Cooling and Trapping*, Springer Science & Business Media Nov. 2001 (cited on page 61).

[104]M Inguscio, S Stringari, ed.: *Bose-Einstein Condensation in Atomic Gases*, IOS Press 1999 (cited on page 61).

[105]S. Jochim: *Bose-Einstein Condensation of Molecules*, PhD thesis, Universität Innsbruck (cited on page 61).

[106]P. Kapitza: *Viscosity of liquid helium below the λ-point*, "Nature" (1938) (cited on page 70).

[107]J. F. Allen and A. D. Misener: *Flow of Liquid Helium II*, "Nature" vol. 141, no. 3558, 75–75 (1938) (cited on page 70).

[108]J. F. Allen and A. D. Misener: *The properties of flow of liquid He ll*, "Proceedings of the Royal Society" (1939) (cited on page 70).

[109]D. D. Osheroff, R. C. Richardson, and D. M. Lee: *Evidence for a new phase of solid He 3*, "Phys. Rev. Lett." vol. 28, no. 14, 885 (1972) (cited on page 70).

[110]J. M. Parpia and J. D. Reppy: *Critical Velocities in Superfluid He 3*, "Phys. Rev. Lett." vol. 43, no. 18, 1332 (1979) (cited on page 70).

[111]M. H. Anderson, J. R. Ensher, M. R. Matthews, C. E. Wieman, and E. A. Cornell: *Observation of bose-einstein condensation in a dilute atomic vapor*, "Science" vol. 269, no. 5221, 198–201 (1995) (cited on page 71).

[112]M. R. Andrews, C. G. Townsend, H. Miesner, D. S. Durfee, D. M. Kurn, and W. Ketterle: *Observation of Interference Between Two Bose Condensates*, "Science" vol. 275, no. 5300, 637–641 (1997) (cited on page 71).

[113]C. Raman, M. Köhl, R. Onofrio, D. S. Durfee, C. E. Kuklewicz, Z. Hadzibabic, and W. Ketterle: *Evidence for a Critical Velocity in a Bose-Einstein Condensed Gas*, "Phys. Rev. Lett." vol. 83, no. 13, 2502–2505 (1999) (cited on page 71).

[114]D. E. Miller, J. K. Chin, C. A. Stan, Y. Liu, W. Setiawan, C. Sanner, and W. Ketterle: *Critical velocity for superfluid flow across the BEC-BCS crossover*, "Phys. Rev. Lett." vol. 99, no. 7, 070402 (2007) (cited on pages 71–73).

[115]W. Weimer, K. Morgener, V. P. Singh, J. Siegl, K. Hueck, N. Luick, L. Mathey, and H. Moritz: *Critical velocity in the BEC-BCS crossover*, "Phys. Rev. Lett." vol. 114, no. 9, 095301 (2015) (cited on page 72).

[116]V. P. Singh, W. Weimer, K. Morgener, J. Siegl, K. Hueck, N. Luick, H. Moritz, and L. Mathey: *Probing superfluidity of Bose-Einstein condensates via laser stirring*, "Phys. Rev. A" vol. 93, no. 2, 023634 (2016) (cited on page 72).

[117]R. Desbuquois, L. Chomaz, T. Yefsah, J. Léonard, J. Beugnon, C. Weitenberg, and J. Dalibard: *Superfluid behaviour of a two-dimensional Bose gas*, "Nature Physics" vol. 8, 645–648 (2012) (cited on page 73).

[118]V. P. Singh, C. Weitenberg, J. Dalibard, and L. Mathey: *Superfluidity and relaxation dynamics of a laser-stirred two-dimensional Bose gas*, "Phys. Rev. A" (2017) (cited on pages 73, 91).

[119]H. Shi, S. Chiesa, and S. Zhang: *Ground-state properties of strongly interacting Fermi gases in two dimensions*, "Phys. Rev. A" vol. 92, no. 3, 033603 (2015) (cited on pages 75, 116, 121).

[120]A. Brunello, F. Dalfovo, L. Pitaevskii, S. Stringari, and F. Zambelli: *Momentum transferred to a trapped Bose-Einstein condensate by stimulated light scattering*, "Phys. Rev. A" vol. 64, no. 6, 063614 (2001) (cited on pages 76, 99).

[121]G. E. Astrakharchik and L. P. Pitaevskii: *Motion of a heavy impurity through a Bose-Einstein condensate*, "Phys. Rev. A" vol. 70, no. 1, 013608 (2004) (cited on page 79).

[122]V. P. Singh and L. Mathey: *Collective modes and superfluidity of a two-dimensional ultracold Bose gas*, "Phys. Rev. Research" vol. 3, no. 2, 023112 (2021) (cited on pages 85, 86).

[123]C. C. N. Kuhn, S. Hoinka, I. Herrera, P. Dyke, J. J. Kinnunen, G. M. Bruun, and C. J. Vale: *High-Frequency Sound in a Unitary Fermi Gas*, "Phys. Rev. Lett." vol. 124, no. 15, 150401 (2020) (cited on pages 88, 99).

[124]M.-C. Chung and A. B. Bhattacherjee: *Damping in 2D and 3D dilute Bose gases*, "New J. Phys." vol. 11, no. 12, 123012 (2009) (cited on page 88).

[125]V. Pastukhov: *Damping of Bogoliubov excitations at finite temperatures*, "J. Phys. A: Math. Theor." vol. 48, no. 40, 405002 (2015) (cited on page 88).

[126]B. C. Mulkerin, L. He, P. Dyke, C. J. Vale, X.-J. Liu, and H. Hu: *Superfluid density and critical velocity near the Berezinskii-Kosterlitz-Thouless transition in a two-dimensional strongly interacting Fermi gas*, "Phys. Rev. A" vol. 96, no. 5, 053608 (2017) (cited on pages 90, 92–94).

[127]A. Tononi, A. Cappellaro, G. Bighin, and L. Salasnich: *Propagation of first and second sound in a two-dimensional Fermi superfluid*, "arXiv: 2009.06491" (2020) (cited on pages 93, 94).

[128]P. Törmä: *Physics of ultracold Fermi gases revealed by spectroscopies*, "Phys. Scr." (2016) (cited on page 95).

[129]L. W. Cheuk, A. T. Sommer, Z. Hadzibabic, T. Yefsah, W. S. Bakr, and M. W. Zwierlein: *Spin-injection spectroscopy of a spin-orbit coupled Fermi gas*, "Phys. Rev. Lett." vol. 109, no. 9, 095302 (2012) (cited on page 96).

[130]C. H. Schunck, Y.-I. Shin, A. Schirotzek, and W. Ketterle: *Determination of the fermion pair size in a resonantly interacting superfluid*, "Nature" vol. 454, no. 7205, 739–743 (2008) (cited on pages 96, 117, 118, 120).

[131]F. Palestini and G. C. Strinati: *Temperature dependence of the pair coherence and healing lengths for a fermionic superfluid throughout the BCS-BEC crossover*, "Phys. Rev. B Condens. Matter" vol. 89, no. 22, 224508 (2014) (cited on pages 96, 117, 118, 120).

[132]Y. Castin: *Basic theory tools for degenerate Fermi gases*, "arXiv:0612613", 349 (2006) (cited on page 96).

[133]A. Schirotzek, Y.-I. Shin, C. H. Schunck, and W. Ketterle: *Determination of the superfluid gap in atomic Fermi gases by quasiparticle spectroscopy*, "Phys. Rev. Lett." vol. 101, no. 14, 140403 (2008) (cited on pages 96, 114).

[134]J. P. Gaebler, J. T. Stewart, T. E. Drake, D. S. Jin, A. Perali, P. Pieri, and G. C. Strinati: *Observation of pseudogap behaviour in a strongly interacting Fermi gas*, "Nat. Phys." vol. 6, no. 8, 569–573 (2010) (cited on pages 96, 97, 132).

[135]J. T. Stewart, J. P. Gaebler, and D. S. Jin: *Using photoemission spectroscopy to probe a strongly interacting Fermi gas*, "Nature" vol. 454, no. 7205, 744–747 (2008) (cited on page 97).

[136] A. Damascelli, Z. Hussain, and Z.-X. Shen: *Angle-resolved photoemission studies of the cuprate superconductors*, "Rev. Mod. Phys." vol. 75, no. 2, 473–541 (2003) (cited on page 97).

[137] T.-L. Dao, A. Georges, J. Dalibard, C. Salomon, and I. Carusotto: *Measuring the one-particle excitations of ultracold fermionic atoms by stimulated Raman spectroscopy*, "Phys. Rev. Lett." vol. 98, no. 24, 240402 (2007) (cited on page 97).

[138] M. G. Lingham, K. Fenech, S. Hoinka, and C. J. Vale: *Local observation of pair condensation in a Fermi gas at unitarity*, "Phys. Rev. Lett." vol. 112, no. 10, 100404 (2014) (cited on page 97).

[139] S. Tan: *Generalized virial theorem and pressure relation for a strongly correlated Fermi gas*, "Ann. Phys." vol. 323, no. 12, 2987–2990 (2008) (cited on pages 97, 112, 132).

[140] S. Tan: *Energetics of a strongly correlated Fermi gas*, "Ann. Phys." vol. 323, no. 12, 2952–2970 (2008) (cited on pages 97, 112, 132).

[141] S. Tan: *Large momentum part of a strongly correlated Fermi gas*, "Ann. Phys." vol. 323, no. 12, 2971–2986 (2008) (cited on pages 97, 112, 132).

[142] E. D. Kuhnle, S. Hoinka, H. Hu, P. Dyke, P. Hannaford, and C. J. Vale: *Studies of the universal contact in a strongly interacting Fermi gas using Bragg spectroscopy*, "New J. Phys." vol. 13, no. 5, 055010 (2011) (cited on pages 97, 132).

[143] E. D. Kuhnle, S. Hoinka, P. Dyke, H. Hu, P. Hannaford, and C. J. Vale: *Temperature dependence of the universal contact parameter in a unitary Fermi gas*, "Phys. Rev. Lett." vol. 106, no. 17, 170402 (2011) (cited on pages 97, 132).

[144] S. Hoinka, M. Lingham, K. Fenech, H. Hu, C. J. Vale, J. E. Drut, and S. Gandolfi: *Precise determination of the structure factor and contact in a unitary Fermi gas*, "Phys. Rev. Lett." vol. 110, no. 5, 055305 (2013) (cited on page 97).

[145] P. J. Martin, B. G. Oldaker, A. H. Miklich, and D. E. Pritchard: *Bragg scattering of atoms from a standing light wave*, "Phys. Rev. Lett." vol. 60, no. 6, 515–518 (1988) (cited on page 99).

[146] P. R. Berman and B. Bian: *Pump-probe spectroscopy approach to Bragg scattering*, "Phys. Rev. A" vol. 55, no. 6, 4382–4385 (1997) (cited on page 99).

[147] M. G. Lingham, K. Fenech, T. Peppler, S. Hoinka, P. Dyke, P. Hannaford, and C. J. Vale: *Bragg spectroscopy of strongly interacting Fermi gases*, "J. Mod. Opt." vol. 63, no. 18, 1783–1794 (2016) (cited on page 99).

[148] P. Pieri, L. Pisani, and G. C. Strinati: *BCS-BEC crossover at finite temperature in the broken-symmetry phase*, "Phys. Rev. B Condens. Matter" vol. 70, no. 9, 094508 (2004) (cited on page 99).

[149] A. J. Leggett: *WHERE is the energy saved in cuprate superconductivity?*, "J. Phys. Chem. Solids" vol. 59, no. 10-12, 1729–1732 (1998) (cited on pages 100, 119).

[150]H. P. Büchler, P. Zoller, and W. Zwerger: *Spectroscopy of superfluid pairing in atomic fermi gases*, "Phys. Rev. Lett." vol. 93, no. 8, 080401 (2004) (cited on pages 100, 119).

[151]R. Haussmann, W. Rantner, S. Cerrito, and W. Zwerger: *Thermodynamics of the BCS-BEC crossover*, "Phys. Rev. A" vol. 75, no. 2, 023610 (2007) (cited on pages 104, 114, 116, 124, 125).

[152]M. V. Klein and S. B. Dierker: *Theory of Raman scattering in superconductors*, "Phys. Rev. B Condens. Matter" vol. 29, no. 9, 4976–4991 (1984) (cited on page 104).

[153]T. P. Devereaux and R. Hackl: *Inelastic light scattering from correlated electrons*, "Rev. Mod. Phys." vol. 79, no. 1, 175–233 (2007) (cited on page 105).

[154]G. Vincini, K. Tanaka, T. Adachi, L. Sobirey, S. Miyasaka, S. Tajima, S. Adachi, N. Sasaki, and T. Watanabe: *Double pair breaking peak in Raman scattering spectra of the triple-layer cuprate $Bi_2Sr_2Ca_2Cu_3O_z$*, "Phys. Rev. B Condens. Matter" vol. 98, no. 14, 144503 (2018) (cited on page 105).

[155]M. Randeria, J. M. Duan, and L. Y. Shieh: *Superconductivity in a two-dimensional Fermi gas: Evolution from Cooper pairing to Bose condensation*, "Phys. Rev. B Condens. Matter" vol. 41, no. 1, 327–343 (1990) (cited on pages 106, 107, 109, 116, 117, 119).

[156]G. Bertaina and S. Giorgini: *BCS-BEC crossover in a two-dimensional Fermi gas*, "Phys. Rev. Lett." vol. 106, no. 11, 110403 (2011) (cited on pages 106, 108, 109, 116, 124).

[157]E. Vitali, H. Shi, M. Qin, and S. Zhang: *Visualizing the BEC-BCS crossover in a two-dimensional Fermi gas: Pairing gaps and dynamical response functions from ab initio computations*, "Phys. Rev. A" vol. 96, no. 6, 061601 (2017) (cited on pages 106, 108, 109, 124).

[158]T. Zielinski, B. Ross, and A. Gezerlis: *Pairing in two-dimensional Fermi gases with a coordinate-space potential*, "Phys. Rev. A" vol. 101, no. 3, 033601 (2020) (cited on pages 106, 108, 109, 124).

[159]A. Galea, H. Dawkins, S. Gandolfi, and A. Gezerlis: *Diffusion Monte Carlo study of strongly interacting two-dimensional Fermi gases*, "Phys. Rev. A" vol. 93, no. 2, 023602 (2016) (cited on pages 108, 116).

[160]B. Mukherjee, Z. Yan, P. B. Patel, Z. Hadzibabic, T. Yefsah, J. Struck, and M. W. Zwierlein: *Homogeneous Atomic Fermi Gases*, "Phys. Rev. Lett." vol. 118, no. 12, 123401 (2017) (cited on page 111).

[161]N. Navon, R. P. Smith, and Z. Hadzibabic: *Quantum Gases in Optical Boxes*, "arXiv:2106.09716" (2021) (cited on page 111).

[162]Z. Yan, P. B. Patel, B. Mukherjee, R. J. Fletcher, J. Struck, and M. W. Zwierlein: *Boiling a Unitary Fermi Liquid*, "Phys. Rev. Lett." vol. 122, no. 9, 093401 (2019) (cited on page 112).

[163]M. J. H. Ku, A. T. Sommer, L. W. Cheuk, and M. W. Zwierlein: *Revealing the superfluid lambda transition in the universal thermodynamics of a unitary Fermi gas*, "Science" vol. 335, no. 6068, 563–567 (2012) (cited on pages 112, 116, 121, 126, 132).

[164]L. Pisani, P. Pieri, and G. C. Strinati: *Gap equation with pairing correlations beyond the mean-field approximation and its equivalence to a Hugenholtz-Pines condition for fermion pairs*, "Phys. Rev. B Condens. Matter" vol. 98, no. 10, 104507 (2018) (cited on page 114).

[165]L. P. Gor'kov and T. K. Melik-Barkhudarov: *Contribution to the theory of superfluidity in an imperfect Fermi gas*, "Sov. Phys. JETP" vol. 13, no. 5, 1018 (1961) (cited on page 114).

[166]G. E. Astrakharchik, J. Boronat, J. Casulleras, Giorgini, and S: *Equation of state of a Fermi gas in the BEC-BCS crossover: a quantum Monte Carlo study*, "Phys. Rev. Lett." vol. 93, no. 20, 200404 (2004) (cited on pages 116, 121).

[167]N. Navon, S. Nascimbène, F. Chevy, and C. Salomon: *The equation of state of a low-temperature Fermi gas with tunable interactions*, "Science" vol. 328, no. 5979, 729–732 (2010) (cited on page 116).

[168]F. Pistolesi and G. C. Strinati: *Evolution from BCS superconductivity to Bose condensation: Role of the parameter kF xi*, "Phys. Rev. B Condens. Matter" vol. 49, no. 9, 6356–6359 (1994) (cited on pages 117, 127).

[169]F. Pistolesi and G. C. Strinati: *Evolution from BCS superconductivity to Bose condensation: Calculation of the zero-temperature phase coherence length*, "Phys. Rev. B Condens. Matter" vol. 53, no. 22, 15168–15192 (1996) (cited on page 117).

[170]M. Marini, F. Pistolesi, and G. C. Strinati: *Evolution from BCS superconductivity to Bose condensation: analytic results for the crossover in three dimensions*, "Eur. Phys. J. B" vol. 1, 151–159 (1998) (cited on pages 117, 120).

[171]R. Haussmann, M. Punk, and W. Zwerger: *Spectral functions and rf response of ultracold fermionic atoms*, "Phys. Rev. A" vol. 80, no. 6, 063612 (2009) (cited on page 118).

[172]Y. J. Uemura: *Bose-Einstein to BCS crossover picture for high-Tc cuprates*, "Physica C SC" vol. 282-287, 194–197 (1997) (cited on page 126).

[173]D. R. Harshman and A. P. Mills: *Concerning the nature of high-T_c superconductivity: Survey of experimental properties and implications for interlayer coupling*, "Phys. Rev. B Condens. Matter" vol. 45, no. 18, 10684–10712 (1992) (cited on page 127).

[174]T. Yoshida, M. Hashimoto, S. Ideta, A. Fujimori, K. Tanaka, N. Mannella, Z. Hussain, Z.-X. Shen, M. Kubota, K. Ono, et al.: *Universal versus material-dependent two-gap behaviors of the high-T c cuprate superconductors: Angle-resolved photoemission study of La 2- x Sr x CuO 4*, "Phys. Rev. Lett." vol. 103, no. 3, 037004 (2009) (cited on page 127).

[175]E. E. M. Chia, J.-X. Zhu, D. Talbayev, and A. J. Taylor: *Competing energy scales in high-temperature superconductors: Ultrafast pump-probe studies: Competing energy scales in high-temperature superconductors: Ultrafast pump-probe studies*, "Phys. Stat. Solidi. Rapid Res. Lett." vol. 5, no. 1, 1–9 (2011) (cited on page 127).

[176]Y. G. Ponomarev, V. A. Alyoshin, E. V. Antipov, T. E. Oskina, A. Krapf, S. V. Kulbachinskii, M. G. Mikheev, M. V. Sudakova, S. N. Tchesnokov, and L. M. Fisher: *Multigap superconductivity in doped p-type cuprates*, "JETP Lett." vol. 100, no. 2, 126–132 (2014) (cited on page 127).

[177]G. Grissonnanche, O. Cyr-Choinière, F. Laliberté, S. René de Cotret, A. Juneau-Fecteau, S. Dufour-Beauséjour, M.-È. Delage, D. LeBoeuf, J. Chang, B. J. Ramshaw, D. A. Bonn, W. N. Hardy, R. Liang, S. Adachi, N. E. Hussey, B. Vignolle, C. Proust, M. Sutherland, S. Krämer, J.-H. Park, D. Graf, N. Doiron-Leyraud, and L. Taillefer: *Direct measurement of the upper critical field in cuprate superconductors*, "Nat. Commun." vol. 5, 3280 (2014) (cited on page 127).

[178]Y. Dagan, R. Krupke, and G. Deutscher: *Determination of the superconducting gap in YBa 2 Cu 3 O 7- δ by tunneling experiments under magnetic fields*, "Phys. Rev. B: Condens. Matter Mater. Phys." vol. 62, no. 1, 146 (2000) (cited on page 127).

[179]D. T. Adroja, F. K. K. Kirschner, F. Lang, M. Smidman, A. D. Hillier, Z.-C. Wang, G.-H. Cao, G. B. G. Stenning, and S. J. Blundell: *Multigap Superconductivity in RbCa2Fe4As4F2 Investigated Using μSR Measurements*, "J. Phys. Soc. Jpn." vol. 87, no. 12, 124705 (2018) (cited on page 127).

[180]P. K. Biswas, Z. Salman, Q. Song, R. Peng, J. Zhang, L. Shu, D. L. Feng, T. Prokscha, and E. Morenzoni: *Direct evidence of superconductivity and determination of the superfluid density in buried ultrathin FeSe grown on $SrTiO_3$*, "Phys. Rev. B Condens. Matter" vol. 97, no. 17, 174509 (2018) (cited on page 127).

[181]R. M. Carter, M. Casas, J. M. Getino, de Llano M, A. Puente, H. Rubio, and van der Walt DM: *Coherence lengths for three-dimensional superconductors in the BCS-Bose picture*, "Phys. Rev. B Condens. Matter" vol. 52, no. 22, 16149–16154 (1995) (cited on page 127).

[182]P. L. Richards and M. Tinkham: *Far-infrared energy gap measurements in bulk superconducting in, Sn, Hg, ta, V, Pb, and Nb*, "Phys. Rev." vol. 119, no. 2, 575–590 (1960) (cited on page 127).

[183]P. Townsend and J. Sutton: *Investigation by electron tunneling of the superconducting energy gaps in Nb, ta, Sn, and Pb*, "Phys. Rev." vol. 128, no. 2, 591–595 (1962) (cited on page 127).

[184]Y. Nakagawa, Y. Kasahara, T. Nomoto, R. Arita, T. Nojima, and Y. Iwasa: *Gate-controlled BCS-BEC crossover in a two-dimensional superconductor*, "Science" vol. 372, no. 6538, 190–195 (2021) (cited on page 127).

[185]R. Escudero, E. Verdin, and F. Morales: *Electron tunneling in oxide superconductors*, "J. Supercond." vol. 7, no. 2, 381–385 (1994) (cited on page 127).

[186]J. Wosnitza, S. Wanka, J. Hagel, M. Reibelt, D. Schweitzer, and J. A. Schlueter: *Thermodynamic properties of quasi-two-dimensional organic superconductors*, "Synth. Met." vol. 133-134, 201–203 (2003) (cited on page 127).

[187] L. P. Le, G. M. Luke, B. J. Sternlieb, W. D. Wu, Y. J. Uemura, J. W. Brill, and H. Drulis: *Magnetic penetration depth in layered compound NbSe2 measured by muon spin relaxation*, "Physica C Supercond." vol. 185-189, 2715–2716 (1991) (cited on page 127).

[188] T. Dvir, F. Massee, L. Attias, M. Khodas, M. Aprili, C. H. L. Quay, and H. Steinberg: *Spectroscopy of bulk and few-layer superconducting NbSe 2 with van der Waals tunnel junctions*, "Nat. Commun." vol. 9, no. 1, 1–6 (2018) (cited on page 127).

[189] A. P. Petrović, R. Lortz, G. Santi, C. Berthod, C. Dubois, M. Decroux, A. Demuer, A. B. Antunes, A. Paré, D. Salloum, et al.: *Multiband superconductivity in the Chevrel phases SnMo 6 S 8 and PbMo 6 S 8*, "Phys. Rev. Lett." vol. 106, no. 1, 017003 (2011) (cited on page 127).

[190] A. D. Hillier and R. Cywinski: *The classification of superconductors using muon spin rotation*, "Appl. Magn. Reson." vol. 13, no. 1-2, 95–109 (1997) (cited on page 127).

[191] W. H. Lee, S. Appl, and R. N. Shelton: *Comparative critical field study of superconducting ternary borides*, "J. Low Temp. Phys." vol. 68, no. 1, 147–157 (1987) (cited on page 127).

[192] J. A. T. Barker, R. P. Singh, A. D. Hillier, and D. M. Paul: *Probing the superconducting ground state of the rare-earth ternary boride superconductors RuB_2 (R= Lu,Y) using muon-spin rotation and relaxation*, "Phys. Rev. B Condens. Matter" vol. 97, no. 9, 094506 (2018) (cited on page 127).

[193] L. Degiorgi, G. Briceno, M. S. Fuhrer, A. Zettl, and P. Wachter: *Optical measurements of the superconducting gap in single-crystal K 3 C 60 and Rb 3 C 60*, "Nature" vol. 369, no. 6481, 541–543 (1994) (cited on page 127).

[194] D. Varshney, R. Jain, and N. Singh: *Phonon-induced superconductivity and physical properties in intercalated fullerides Rb3C60*, "Journal of Theoretical and Applied Physics" vol. 6, no. 1, 25 (2012) (cited on page 127).

[195] J. A. T. Barker, B. D. Breen, R. Hanson, A. D. Hillier, M. R. Lees, G. Balakrishnan, D. M. Paul, and R. P. Singh: *Superconducting and normal-state properties of the noncentrosymmetric superconductor Re 3 Ta*, "Phys. Rev. B: Condens. Matter Mater. Phys." vol. 98, no. 10, 104506 (2018) (cited on page 127).

[196] D. Singh, P. K. Biswas, A. D. Hillier, R. P. Singh, et al.: *Unconventional superconducting properties of noncentrosymmetric Re 5.5 Ta*, "Phys. Rev. B: Condens. Matter Mater. Phys." vol. 101, no. 14, 144508 (2020) (cited on page 127).

[197] D. Singh, J. A. T. Barker, A. Thamizhavel, A. D. Hillier, D. M. Paul, and R. P. Singh: *Superconducting properties and μSR study of the noncentrosymmetric superconductor Nbo.5Oso.5*, "J. Phys. Condens. Matter" vol. 30, no. 7, 075601 (2018) (cited on page 127).

[198]J. A. T. Barker, D. Singh, A. Thamizhavel, A. D. Hillier, M. R. Lees, G. Balakrishnan, D. M. Paul, and R. P. Singh: *Unconventional superconductivity in La 7 Ir 3 revealed by muon spin relaxation: Introducing a new family of noncentrosymmetric superconductor that breaks time-reversal symmetry*, "Phys. Rev. Lett." vol. 115, no. 26, 267001 (2015) (cited on page 127).

[199]K. P. Sajilesh, D. Singh, P. K. Biswas, A. D. Hillier, and R. P. Singh: *Superconducting properties of the noncentrosymmetric superconductor LaPtGe*, "Phys. Rev. B Condens. Matter" vol. 98, no. 21, 214505 (2018) (cited on page 127).

[200]D. Singh, A. D. Hillier, and R. P. Singh: *Type-I superconductivity in the noncentrosymmetric superconductor BeAu*, "Phys. Rev. B Condens. Matter" vol. 99, no. 13, 134509 (2019) (cited on page 127).

[201]D. Singh, K. P. Sajilesh, S. Marik, A. D. Hillier, and R. P. Singh: *Superconducting properties of the noncentrosymmetric superconductor TaOs*, "Supercond. Sci. Technol." vol. 30, no. 12, 125003 (2017) (cited on page 127).

[202]D. Singh, P. K. Biswas, G. B. G. Stenning, A. D. Hillier, R. P. Singh, et al.: *Investigations of the superconducting ground state of Zr 3 Ir: Introducing a new noncentrosymmetric superconductor*, "Physical Review Materials" vol. 3, no. 10, 104802 (2019) (cited on page 127).

[203]D. Singh, S. K. P., S. Marik, A. D. Hillier, and R. P. Singh: *Superconducting and normal state properties of the noncentrosymmetric superconductor $NbOs_2$ investigated by muon spin relaxation and rotation*, "Phys. Rev. B Condens. Matter" vol. 99, no. 1, 014516 (2019) (cited on page 127).

[204]R. Movshovich, N. Kim, and D. M. Lee: *Pair-breaking edge of superfluid 3He-B in a magnetic field*, "Phys. Rev. Lett." vol. 64, no. 4, 431–434 (1990) (cited on page 127).

[205]A. B. Pippard and W. L. Bragg: *An experimental and theoretical study of the relation between magnetic field and current in a superconductor*, "Proc. R. Soc. Lond. A Math. Phys. Sci." vol. 216, no. 1127, 547–568 (1953) (cited on page 128).

[206]S. Hoinka, M. Lingham, M. Delehaye, and C. J. Vale: *Dynamic spin response of a strongly interacting Fermi gas*, "Phys. Rev. Lett." vol. 109, no. 5, 050403 (2012) (cited on pages 132, 133).

[207]A. A. Orel, P. Dyke, M. Delehaye, C. J. Vale, and H. Hu: *Density distribution of a trapped two-dimensional strongly interacting Fermi gas*, "New J. Phys." vol. 13, no. 11, 113032 (2011) (cited on page 132).

[208]Q. Chen, J. Stajic, S. Tan, and K. Levin: *BCS–BEC crossover: From high temperature superconductors to ultracold superfluids*, "Phys. Rep." vol. 412, no. 1, 1–88 (2005) (cited on page 132).

[209]Q. Chen, K. Levin, and J. Stajic: *Applying BCS–BEC crossover theory to high-temperature superconductors and ultracold atomic Fermi gases* (*Review Article*), "Low Temp. Phys." vol. 32, no. 4, 406–423 (2006) (cited on page 132).

[210]T. Kondo, Y. Hamaya, A. D. Palczewski, T. Takeuchi, J. S. Wen, Z. J. Xu, G. Gu, J. Schmalian, and A. Kaminski: *Disentangling Cooper-pair formation above the transition temperature from the pseudogap state in the cuprates*, "Nat. Phys." vol. 7, no. 1, 21–25 (2011) (cited on page 133).

[211]T. Kondo, A. D. Palczewski, Y. Hamaya, T. Takeuchi, J. S. Wen, Z. J. Xu, G. Gu, and A. Kaminski: *Formation of gapless Fermi arcs and fingerprints of order in the pseudogap state of cuprate superconductors*, "Phys. Rev. Lett." vol. 111, no. 15, 157003 (2013) (cited on page 133).

[212]F. Marsiglio, P. Pieri, A. Perali, F. Palestini, and G. C. Strinati: *Pairing effects in the normal phase of a two-dimensional Fermi gas*, "Phys. Rev. B Condens. Matter" vol. 91, no. 5, 054509 (2015) (cited on page 133).

[213]J. J. Kinnunen, J. E. Baarsma, J.-P. Martikainen, and P. Törmä: *The Fulde-Ferrell-Larkin-Ovchinnikov state for ultracold fermions in lattice and harmonic potentials: a review*, "Rep. Prog. Phys." vol. 81, no. 4, 046401 (2018) (cited on page 133).

[214]B. Zhu, V. P. Singh, J. Okamoto, and L. Mathey: *Dynamical control of the conductivity of an atomic Josephson junction*, "Phys. Rev. Research" vol. 3, no. 1 (2021) (cited on page 133).

[215]W. Hu, S. Kaiser, D. Nicoletti, C. R. Hunt, I. Gierz, M. C. Hoffmann, M. Le Tacon, T. Loew, B. Keimer, and A. Cavalleri: *Optically enhanced coherent transport in YBa2Cu3O6.5 by ultrafast redistribution of interlayer coupling*, "Nat. Mater." vol. 13, no. 7, 705–711 (2014) (cited on page 133).

[216]G. Homann, J. G. Cosme, J. Okamoto, and L. Mathey: *Higgs mode mediated enhancement of interlayer transport in high- Tc cuprate superconductors*, "Phys. Rev. B Condens. Matter" vol. 103, no. 22 (2021) (cited on page 133).

ACKNOWLEDGEMENTS

This thesis would not have been possible without many people, of whom I shall acknowledge a select few here.

First and foremost, I would like to thank Henning. Your enthusiasm was what first got me interested in physics beyond the superficial during my bachelors, and your mentoring has made me the scientist I am today. At every point, you make sure that your students feel taken serious and you do whatever is needed to support them. I could not have asked for a better supervisor or role model.

Thank you, Niclas and Thomas, for six wonderful and invigorating years. From Clouds Rest to opening the main vacuum, we faced a number of obstacles together that seemed almost insurmountable at the time. Both inside and outside the lab, I have always enjoyed our discussions about physics, politics and random nonsense, and I am truly happy how well we always complemented each other.

I would also like to thank Klaus and Jonas. From during my bachelor thesis to the first years of my PhD, you were not only always helpful and full of knowledge, but have also both taught me a number of important things outside of physics. I also want to thank Wolf, Kai, Phillip, Martin, Alex, Markus and Hauke, because this group would not have been the same without our noodle mondays, cake get-togethers, ice cream in winter and the uncounted discussions over lunch or any other opportunity. You have been wonderful colleagues to me, and I am very grateful that I got to get to know you all.

I also want to thank Vijay and Ludwig for all of our discussions and their patience. Thank you Ludwig in particular for allowing me to keep you occupied during the coffee break at that theory symposium in 2019, when you had many other things you wanted to do, but I just really needed to know if I had understood where our mistake was. I would furthermore like to thank Klaus Sengstock, Reinhard Mielck, Ralf Lühr, Ellen Gloy, Janina Neubert, Loreen Tornier and Stephan Fleig as well as all the other employees in workshop and administration that have enabled our work with patience and dedication for all these years.

I want to thank my friends, who have stuck with me over many changes in time zone and many periods of little communication. My most special thanks go out to Max and Sebi for being the most excellent friends one can ask for, and to Halgrim, Fiana, Fiorella and Luciano for keeping me entertained in their continuous struggle. I would also like to thank my family. Sabine, Wolf and Bea, you have always been incredibly supportive and just reliably wonderful, and I am blessed to have you. And finally, I want to thank Margo, who came to Hamburg with me, explored the world with me, and ultimately even married me. I am deeply grateful to have such wonderful people around me - you make it all feel easy.

EIDESSTATTLICHE VERSICHERUNG

Hiermit versichere ich an Eides statt, die vorliegende Dissertationsschrift selbst verfasst und keine anderen als die angegebenen Hilfsmittel und Quellen benutzt zu haben. Die eingereichte schriftliche Fassung entspricht der auf dem elektronischen Speichermedium. Die Dissertation wurde in der vorgelegten oder einer ähnlichen Form nicht schon einmal in einem früheren Promotionsverfahren angenommen oder als ungenügend beurteilt.

Hamburg, den 10.09.2021

Lennart Sobirey